Mutually Coupled Lasers on a Photonic Integrated Circuit

Alison H. Perrott
BSc
111380271

Thesis submitted for the degree of Doctor of Philosophy

NATIONAL UNIVERSITY OF IRELAND, CORK

SCHOOL OF SCIENCE, ENGINEERING & FOOD SCIENCE

DEPARTMENT OF PHYSICS

TYNDALL NATIONAL INSTITUTE

INTEGRATED PHOTONICS GROUP

October 2020

Head of Department: Prof. John McInerney

Supervisor: Prof. Frank H. Peters

Research supported by Science Foundation Ireland

Contents

List of Figures

List of Tables

I, Alison H. Perrott, certify that this thesis is my own work and has not been submitted for another degree at University College Cork or elsewhere.

Alison H. Perrott

I shall be telling this with a sigh
Somewhere ages and ages hence:
Two roads diverged in a wood, and I-
I took the one less travelled by,
And that has made all the difference.

Robert Frost

Acknowledgements

First, I would like to thank my supervisor Frank for allowing me to do this PhD and welcoming me into the Integrated Photonics Group (IPG) at Tyndall. Thank you for your constant guidance throughout my degree and PhD, and for believing that I could do it. Many thanks to his wife, Jo, for having the group over for many delicious meals and hours of entertaining board games. Also, thank you to the Science Foundation of Ireland for funding this project.

A big thank you to IPG members past and present who welcomed me into the group and have taught and helped me so much. Thank you for showing me a glimpse of what it would have been like to have siblings! A massive thank you to the fabricators in IPG who fabricated the PICs for me. Without you, I would have no results to put in this thesis. Many thanks also to our lunch crew, who've been so supportive, together we've celebrated the highs and struggled through the lows. Thank you also to the wider community in Tyndall and the Physics Department in UCC who have helped me along this journey. A special thank you to the Laser Dynamics Group in UCC for collaborating with me.

I would also like to acknowledge all of my past teachers and lecturers, who taught me much and inspired me to follow a career in physics, especially my Junior Cert science teacher, who said she'd make a scientist out of me, when all I wanted to do was give up science, and my Leaving Cert physics teacher, whose passion for the subject inspired my own. Who knows where I'd be now if it wasn't for them.

Thank you also to my family and friends who've supported me and provided the necessary distraction when things weren't going well. A reluctant thank you for all the times I've been asked "aren't you finished yet?" that pushed me to keep going!

Last but certainly not least, I would like to express my gratitude to my parents for their love and support. I know I don't show my appreciation often but thank you for putting up with me and my ever changing moods throughout this journey.

Thank You!

Abstract

The number of internet users and the internet traffic are growing exponentially year-on-year, leading to an ever-increasing demand for data. This demand risks saturating the current network and is, therefore, driving research into technologies to increase the total data throughput of a single optical fibre. To further increase the data rate through a fibre and keep ahead of demand, the channel spectral density must be increased. One solution is to use super-channels to increase the spectral density and hence the number of channels. Many of the proposed methods for creating super-channels use optical combs. These combs must be demultiplexed so that each channel can be modulated separately. Demultiplexing can be achieved by injection locking a laser to each of the comb lines. It has been shown that for any cost-effective implementation of Tbps super-channels, photonic integration of the source of the super-channel, i.e. the optical comb, and the demultiplexer is necessary. Consequently, the optical comb must then be generated, and a laser injection locked to each of the comb lines, on a photonic integrated circuit (PIC). However, it has long been assumed that different lasers cannot coexist on a PIC without using an optical isolator, but this has never been investigated or proven. The work in this thesis aims to disprove this theory.

This work experimentally investigates mutual injection locking between different lasers on a PIC. For this study, two tuneable slotted Fabry-Pérot lasers were integrated together through a variable optical attenuator/amplifier (VOA). The bias and length of the VOA controlled the coupling and time delay between the lasers, respectively. These, along with the detuning between the lasers, were the variable parameters investigated. The mutual and injection locking characteristics of the integrated lasers were compared, both off and on-chip, which established a baseline for more complex behavioural studies. This also led to the development of a measurement technique, using an optical spectrum analyser, an electrical spectrum analyser and a high speed oscilloscope, for examining the different operational regimes arising from optically locking a semiconductor diode laser.

It was found that the coupling between the lasers is critical in obtaining stable mutual injection locking: if the coupling is too low, the lasers do not interact sufficiently to obtain mutual locking and if the coupling is too high, the full device from facet-to-facet behaves as a compound laser and mutual locking is not achieved. Additionally, it was shown that if the detuning between the lasers is small, the wavelength of both lasers can be fixed, and mutual locking can be attained by varying the coupling between the lasers. Various types of dynamical behaviour were also observed as a function of the coupling and detuning between the lasers. These include: symmetric and asymmetric beating, non-linear interactions, period doubling, pulsing and aperiodic behaviour. The coupling between the lasers was also measured as a function of the VOA bias and compared for different VOA lengths. This work experimentally verifies that two lasers

can indeed coexist on a PIC without an optical isolator and stable mutual injection locking between the lasers can be obtained.

In the short term, this work provides a baseline to support further theoretical studies and in the long term, contributes to enabling the development of integrated high data-rate transmitters that will support the internet traffic growth.

List of Publications

Journal Articles

[1] Niall P. Kelly, Mohamad Dernaika, Ludovic Caro, Padraic E. Morrissey, Alison H. Perrott, Justin K. Alexander and Frank H. Peters, "Regrowth-Free Single Mode Laser Based on Dual Port Multimode Interference Reflector", IEEE Photonics Technology Letters, 29(3): 279-282 (2017)

[2] Fabien M. Dubois, Masoud Seifikar, Alison H. Perrott and Frank H. Peters, "Modelling Mutually Coupled Non-Identical Semiconductor Lasers on Photonic Integrated Circuits", Journal of Applied Optics, 57(22): 154-162 (2018)

[3] Kevin Shortiss, Maryam Shayesteh, William Cotter, Alison H. Perrott, Mohamad Dernaika and Frank H. Peters, "Mode Suppression in Injection Locked Multi-Mode and Single Mode Lasers for Optical Demultiplexing", Photonics, 6(1): 27 (2019)

[4] A.H. Perrott, L. Caro, M. Dernaika and F.H. Peters, "A Comparison between Off and On-Chip Injection Locking in a Photonic Integrated Circuit", Photonics, 6(4): 103 (2019)

[5] B. Lingnau, A.H. Perrott, L. Caro, M. Dernaika, F.H. Peters and B. Kelleher, "Dynamics of On-Chip Asymmetrically Coupled Semiconductor Lasers", Optics Letters, 45(8): 2223-2226 (2020)

[6] Z. Jia, H. Yang, A.H. Perrott, H. Wang and F.H. Peters, "Study on the Proximity of QWI in InP-based AlInGaAs MQWs using the IFVD Method and its Application in Single Frequency Teardrop Laser Diodes", Optics Express, (2020)

Conference Proceedings

[1] A.H. Perrott, P.E. Morrissey, F.M. Dubois, M. Dernaika, L. Caro, N. Kelly and F.H. Peters, "Injection Locking of Mutually Coupled SFP Lasers on a PIC", Photon16, Leeds, UK, (2016)

[2] K. Shortiss, W. Cotter, M. Shayesteh, A. H. Perrott and F. H. Peters, "Modelling Injection Locked Semiconductor Lasers", Photon16, Leeds, UK, (2016)

[3] A.H. Perrott, L. Caro, M. Dernaika, N.P. Kelly, F.M. Dubois and F.H. Peters, "Mutual Injection Locking of Lasers in a Photonic Integrated Circuit", IOP Spring Meet, Dublin, (2017)

[4] Maryam Shayesteh, Kevin Shortiss, William Cotter, Padraic E. Morrissey, Alison H. Perrott, Niall P. Kelly and Frank H. Peters, "De-multiplexing coherent optical combs within Photonic Integrated Circuits", Integrated Optics, European Conference on (ECIO), (2017)

[5] A.H. Perrott, L. Caro, M. Dernaika, N.P. Kelly, P.E. Morrissey and F.H. Peters, "Mutual Injection Locking of Lasers in a Photonic Integrated Circuit", Integrated Optics, European Conference on (ECIO), (2017)

[6] Hua Yang, Mingqi Yang, Alison H. Perrott, Zhengkai Jia and Frank H. Peters, "Photonic integrated circuit based on 1x2 multimode-interferometer-Fabry-Pérot laser diode", Proceedings SPIE 10249, Integrated Photonics: Materials, Devices, and Applications IV, 102490U, (2017)

[7] Fabien M. Dubois, Masoud Seifikar, Alison H. Perrott and Frank H. Peters, "Modelling Mutually Coupled Non-Identical Semiconductor Lasers on Photonic Integrated Circuits", Numerical Simulation of Optoelectronic Devices, International Conference on (NUSOD), (2017)

[8] A.H. Perrott, M. Dernaika, L. Caro, N.P. Kelly, P.E. Morrissey and F.H. Peters, "Injection Locking Mutually Coupled Lasers in a Photonic Integrated Circuit", Photonics Ireland, (2017)

[9] K.J. Shortiss, M. Shayesteh, A.H. Perrott, W. Cotter and F.H. Peters, "Effect of Comb Spacing and Slave Laser Gain on Filtering Properties of Injection Locked Lasers", Photonics Ireland, (2017)

[10] A.H. Perrott, L. Caro, M. Dernaika and F.H. Peters, "Mutual Coupled Lasers in a Photonic Integrated Circuit", IOP Spring Meet, Limerick, (2018)

[11] Masoud Seifikar, Andreas Amann, Fabien M. Dubois, Alison H. Perrott and Frank H. Peters, "Dynamics of two Mutually Coupled Semiconductor Lasers in Low Coupling Regions", Numerical Simulation of Optoelectronic Devices, International Conference on (NUSOD), (2018)

[12] Fabien M. Dubois, Masoud Seifikar, Alison H. Perrott and Frank H. Peters, "A Multimode Approach to Modelling Mutually Coupled Lasers in Photonic Integrated Circuits", Photonics North Conference, (2018)

[13] A.H. Perrott, L. Caro, M. Dernaika and F.H. Peters, "Coupled Lasers on a Photonic Integrated Circuit", Photonics North Conference, (2018)

[14] K. Shortiss, A.H. Perrott, M. Shayesteh, M Dernaika, F. Dubois and F.H. Peters, "Integrated Optical Demultiplexing by Injection Locking", Photonics Ireland, (2018)

[15] F.M. Dubois, M. Seifikar, A.H. Perrott and F.H. Peters, "A Multimode Approach to Modelling Mutually Coupled Lasers in Photonic Integrated Circuits", Photonics Ireland, (2018)

[16] A.H. Perrott, M. Dernaika, L. Caro and F.H. Peters, "Coupled Lasers on a Photonic Integrated Circuit", Photonics Ireland, (2018)

[17] Masoud Seifikar, Andreas Amann, Fabien M. Dubois, A.H. Perrott and F.H. Peters, "Two Mutually Identical Delay-Coupled Semiconductor Lasers in Photonic Integrated Circuits", Photonics Ireland, (2018)

[18] A.H. Perrott, M. Dernaika, L. Caro and F.H. Peters, "Investigation of the Dynamical Behaviour of Mutually Coupled Lasers in a Photonic Integrated Circuit", Integrated Optics, European Conference on (ECIO), (2019)

List of Acronyms

AWG	Arrayed Waveguide Grating
CB	Conduction Band
CoWDM	Coherent Wavelength Division Multiplexing
DFB	Distributed Feedback
DH	Double-Heterostructure
DUT	Device Under Test
EDFA	Erbium Doped Fibre Amplifier
ESA	Electrical Spectrum Analyser
FFT	Fast Fourier Transform
FP	Fabry Pérot
FWM	Four Wave Mixing
HSO	High Speed Oscilloscope
IC	Integrated Circuit
LI	Power-Current Curve
NLI	Non-Linear Interactions
MMI	Multimode Interference Coupler
MQW	Multi-Quantum Well
OFDM	Orthogonal Frequency Division Multiplexing
OSA	Optical Spectrum Analyser
PD	Photo Detector
PIC	Photonic Integrated Circuit
PM	Power Meter
QWI	Quantum Well Intermixing
RO	Relaxation Oscillation
SFP	Slotted Fabry Pérot
SF-SFP	Single Facet Slotted Fabry Pérot
SMSR	Side Mode Suppression Ratio
SOA	Semiconductor Optical Amplifier
TE	Transverse-Electric

TEC	Thermoelectric Cooler
TLS	Tunable Laser Source
TM	Transverse-Magnetic
VB	Valence Band
VI	Voltage-Current Curve
VOA	Variable Optical Attenuator/Amplifier
WDM	Wavelength Division Multiplexing

Chapter 1

Introduction

This thesis investigates mutual injection locking between lasers on a photonic integrated circuit (PIC). The mutual and injection locking characteristics of the integrated lasers were compared, both off and on-chip. The dynamical behaviour of the lasers as a function of the coupling and detuning between the lasers was also investigated. The following sections will first introduce optical communications and integrated photonics. Then Section 1.6 will outline the work done as part of this thesis.

1.1 Internet Growth

The development of optical communication systems in the 1970's changed how people communicated. Long-haul communications were no longer restricted by the limitations of electronic communication systems. The introduction of personal computers in the late 1980's and early 1990's brought the internet, and in particular the *World Wide Web*, to the home for the first time and signalled a rapid growth in Internet traffic. The development of the smartphone and the introduction of the iPhone and the Android operating system in the late 2010's caused Internet traffic to grow even more rapidly. Figure 1.1 shows how the number of Internet users has been steadily increasing over the last 25 years, from 16 million users in 1995 to 4.5 billion users today [1].

The break down of today's Internet users by geographical region is plotted in Figure 1.2. These statistics indicate that half of the internet users are from Asia with Europe lagging considerably behind at 16%. However, taking into account the Internet penetration in each region, this clearly reflects the socioeconomic climate in each area, where wealthier regions such as Europe, North America and Oceania / Australia show high Internet penetration values between 60 and 80% while typically poorer regions such as Africa show a mere 30% Internet penetration.

Total Internet traffic has experienced dramatic growth in the past two decades. 28 years

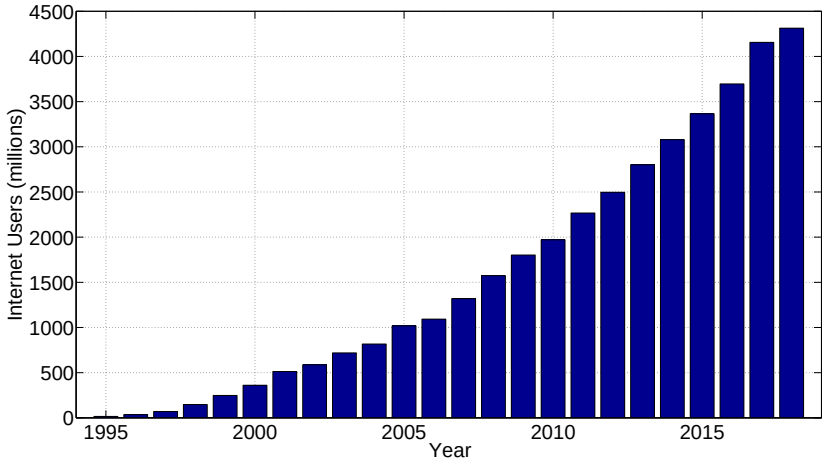

Figure 1.1: Growth of internet users per year [1].

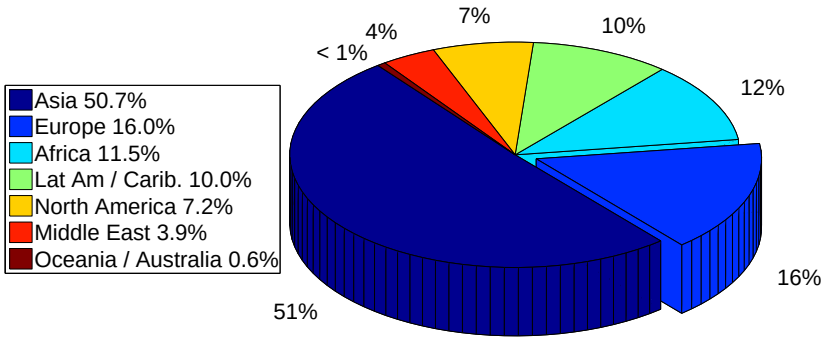

Figure 1.2: Internet users in the world by geographical region - June 30, 2019 based on 4.5 billion users [1].

ago, in 1992, global Internet networks carried approximately 100 GB of traffic per day. In 2017, global Internet traffic amounted to almost 46,600 gigabytes per second (GBps) and is projected to reach 150,700 GBps in 2022 [2]. Figure 1.3 shows how Internet traffic has grown since 1984 and its the projected growth up to 2022.

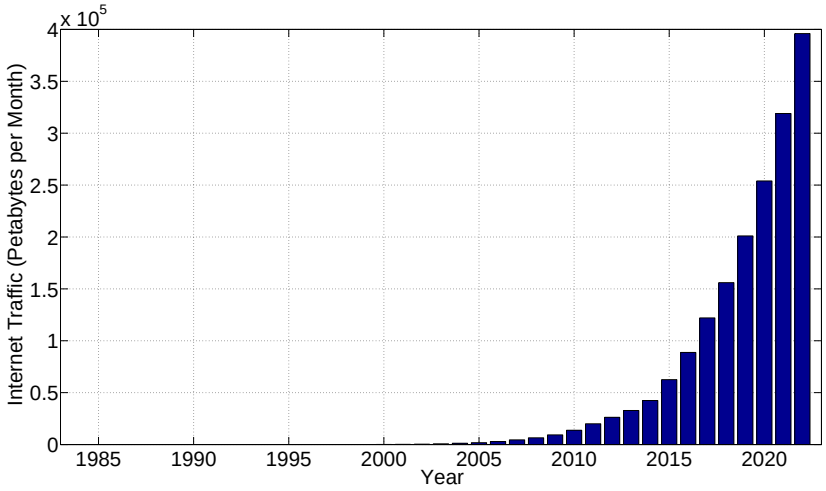

Figure 1.3: Growth of Internet traffic per year [2].

Global Internet traffic is projected to increase threefold from 2017 to 2022. Monthly Internet traffic will reach 50 GB per capita by 2022, up from 16 GB per capita in 2017. Busy-hour Internet traffic is growing even more rapidly than average Internet traffic. Busy-hour (or the busiest 60-minute period in a day) Internet traffic is expected to increase by a factor of 4.8 between 2017 and 2022, while average Internet traffic will increase by a factor of 3.7 [2]. In 2015, wired devices accounted for the majority of Internet traffic, at 52%. However by 2022, wired devices will account for only 29% of Internet traffic, while Wi-Fi and mobile devices are predicted to account for 71% of Internet traffic.

Fibre optical transmission systems play a key role in satisfying the ever-increasing demand for data bandwidth. They form the backbone for long-haul communication systems, where high bandwidth and low-loss transmission is required for transmission over tens of thousands of kilometers. Such systems continue to be improved by lowering the cost of optical to electrical (and vice-versa) conversions and by maximising data transfers. These improvements have been enabled by significant advancements in the area of photonic systems, where highly sophisticated systems have been developed to improve speed, reliability and signal quality during optical transmission. Such improvements were essential in the realisation of current communication systems, and will play a key role in satisfying the ever increasing demand for bandwidth during the next two decades [3].

1.2 Photonics & Photonic Systems

Similar to how electronics is the study of the properties of electrons, photonics is the study of the properties of light and how it can be manipulated. Photonics deals with the generation of light and also the development of optical amplifiers, photodetectors for detecting and measuring light and importantly, optical modulators. These photonic devices are now key components of current optical systems and are required in forming the backbone of the next generation optical networks.

Single-mode fibres are used for long-haul applications. The low-loss of silica fibres for wavelengths between 1530 nm and 1624 nm allows long distance communications in this wavelength range. To fully use this low-loss spectral envelope data is transmitted using many different wavelengths. This is called wavelength division multiplexing (WDM) [4]. Each wavelength represents a different channel and can be used to transmit data independently. The simplified schematic shown in Figure 1.4 best describes WDM.

Three laser sources are shown in Figure 1.4, each operating at a single wavelength; λ_1, λ_2 and λ_3. Each signal is individually modulated at 10 GBps or greater and then

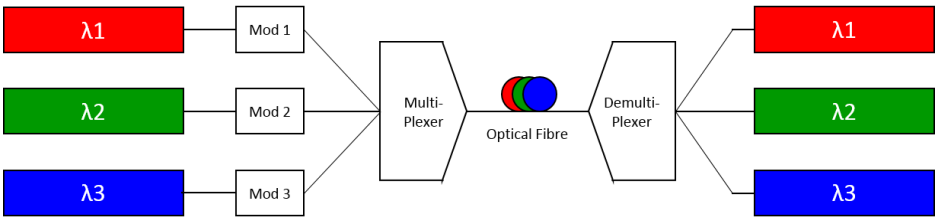

Figure 1.4: Schematic outline of a WDM system with three channels. The signal from each of the three laser sources is individually modulated then combined into an optical fibre using an optical multiplexer. The optical signal is then transmitted across the network before being demultiplexed at the receiving end to re-acquire the original modulated signals.

combined together into a single optical fibre using a wavelength multiplexer. The optical signal is then transmitted across the network where it can be amplified as required. At the receiving end, the optical signal is demultiplexed and the original modulated signals are re-acquired.

In order to increase the total data throughput of a single fibre, the number of channels or the data rates of each channel are increased. An increase in the number of channels in historical experiments is shown in Figure 1.5. By 2002 the full C and L bands, corresponding to the low absorption spectrum of modern optical fibre from 1530 nm to 1624 nm, were being used. Therefore, to further increase the number of channels, the channel spacing must be decreased.

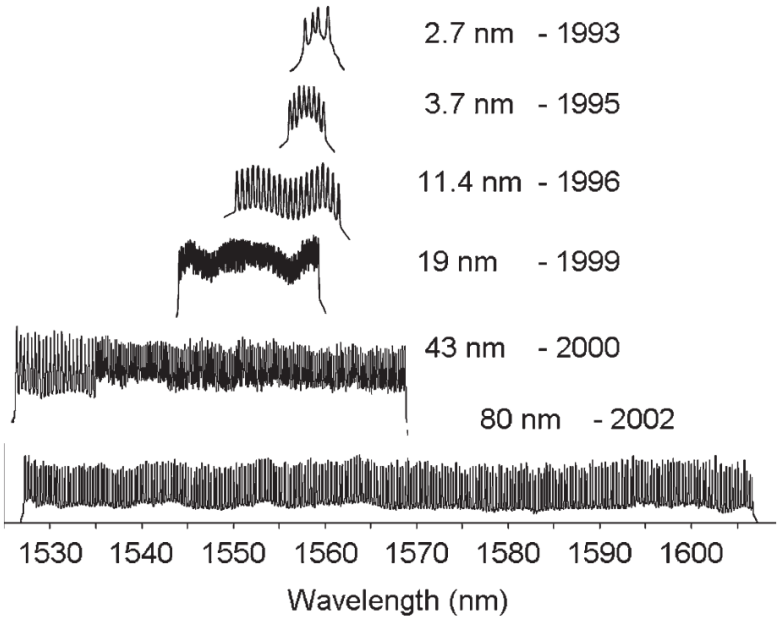

Figure 1.5: Plot from [5] showing the optical spectrum from WDM for the years 1993 to 2002. The spectrum from the experiment in 2002 shows full use of both the C and L bands.

Figure 1.6a shows how current WDM systems have dead zones to allow for optical fil-

tering of individual wavelengths. These dead zones or guard bands are narrow wavelength ranges used to separate two wider wavelength ranges to ensure that both can transmit simultaneously without interfering with each other. 40-50% of the spectrum is used for guard bands [6]. Removing per-channel guard bands allows for tighter spacing, or higher data rate per channel. This is shown in Figure 1.6b, where only 5% of the spectrum is used for guard bands [6].

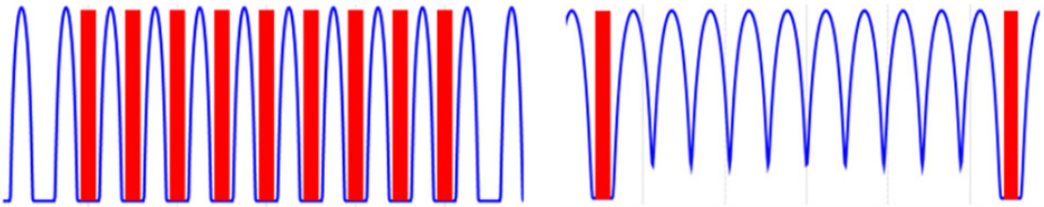

(a) (b)

Figure 1.6: Current WDM systems have dead zones to allow for optical filtering of individual wavelengths. Removing per-channel guard bands allows for tighter spacing, or higher data rate per channel [6].

As data rates increase or channel spacing decreases, incoherent interference occurs. This becomes a problem when adjacent channels fall within the receiver bandwidth [7], and has the effect of increasing error rates where the source of each channel is an independent laser, as in traditional WDM systems.

Coherent WDM (CoWDM) has been shown to allow for crosstalk to occur, without the associated errors [7]. By adjusting the relative phase of the channels making up the coherent signal, the interference can be made to occur in the transition between bits thereby reducing the error rate due to interference cross-talk [7]. In orthogonal frequency-division multiplexing (OFDM) digital processing is used to reduce the error rate instead of adjusting the phases. The advantage of CoWDM is that the eyes can be seen using a simple receiver (rather than a coherent receiver) and without any digital processing [8, 9].

A set of coherent channels is referred to as a coherent super-channel and an optical comb source is a key component in creating the coherent super-channel [6]. The coherent super-channel must be demultiplexed to allow each channel to be modulated separately, as seen in Figure 1.4. Arrayed-waveguide gratings (AWGs) can be used for demultiplexing but have a large footprint and require sub-nanometer fabrication resolution, [10, 11, 12]. Another alternative demultiplexer, the Echelle grating while smaller than an AWG (a few 10s of millimetres squared) is still quite large for an integrated circuit and with nanometre spacing between the channels, a low fabrication tolerance is still required, [13, 14, 15].

An alternate solution to a grating demultiplexer is to use injection locking to filter the comb lines [16]. In this method the comb signal is split evenly between the channels (one for each comb line). At each channel a laser is injection locked to one of the

comb lines. Each laser is locked to a different comb line thus de-multiplexing the comb, see Figure 1.7. The signal from each laser is then modulated individually before recombining the signal again to a coherent comb. Cross-talk between the channels is no longer an issue since each channel originated from the same coherent optical comb, and therefore the phase between each channel is fixed. This demultiplexer does not require a fabrication tolerance lower than 1 μm and is easily scalable to large numbers of channels.

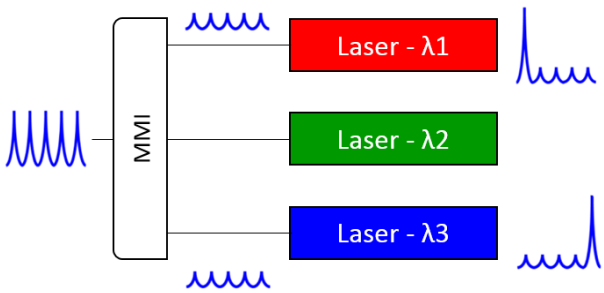

Figure 1.7: Schematic outline of demultiplexing an optical comb using injection locked lasers. The optical comb is split between the channels using an MMI. At each channel a laser is injection locked to a different comb line thus de-multiplexing the comb.

It has been shown in [17] that for any cost-effective implementation of Tbps super-channels, photonic integration of the source of the super-channel, i.e. the optical comb, and the demultiplexer is necessary. Therefore, the viability of injection locking as an integrable demultiplexer must be investigated.

1.3 Photonic Integration

In the electronics industry, the development of chip scale integrated circuits (ICs) allowed for a dramatic increase in the performance of everyday electronic devices. The prospect of developing similar technologies with photonic integration offers huge growth potential in the area. However, due to the larger number of sub-components in photonic devices, research and development of photonic integrated circuits (PICs) has progressed at a far slower rate than its electrical counterpart. In any single PIC, there may be lasers, attenuators, modulators, couplers and detectors, and each may also be based on a vastly different material structure (binary, quaternary alloys III-V semiconductors, etc.) which requires non-standard wafer processing techniques.

The main advantages of photonic integration and PICs are:

- Lower cost
- System simplification
- Increased reliability
- Lower power consumption

Photonic integration can take large power hungry system setups and reduce then to compact and reliable PICs, for example [18] demonstrates a fully integrated 240-GHz direct-conversion quadrature transmitter and receiver chipset in SiGe technology.

Since PICs are typically comprised of many different sub-devices e.g. lasers, modulators, filters, optical splitters and combiners, etc., integration is a challenge. This can be overcome through expensive and time consuming fabrication or by dealing with the challenges on the device packaging side. Hybrid and monolithic integration are the two primary solutions to overcome the difficulties posed by photonic integration.

1.3.1 Hybrid Integration

Hybrid integration [19] allows multiple discrete single function optical devices to be integrated together on a common substrate. The discrete components are then linked together through optical couplings to form a single PIC, typically by using flip-chip bonding techniques [20]. The low tolerances required when creating the interconnects between the devices, make this a very complex and time consuming process and thus expensive.

1.3.2 Monolithic Integration

In monolithic integration, each optical device is fabricated on a PIC with the same material substrate. The light is guided in the substrate medium, therefore optical interconnects linking each component are no longer required. Many different techniques exist for monolithic integration based on current technologies [21]. These methods often use regrowth and etching to form photonic devices on a single substrate, as shown in Figure 1.8.

In butt-joint regrowth, the selective removal of waveguide core material is followed by the regrowth of an alternate waveguide core using different material composition. This process involves a precise etch of the original waveguide core, followed by a regrowth of waveguide material with composition and thickness variables, which is inherently difficult [22].

The selective area regrowth process involves selective growth using a mask - a mask is patterned on the surface of the wafer prior to epitaxial growth [23]. In this method the confinement factor cannot be independently optimised since the thickness is not independent of the bandgap in the areas of regrowth.

For offset and dual quantum well configuration, the quantum wells are grown above the waveguide and selectively removed in various regions post-growth [22]. The drawback of this method, however, is the limitation of each integrated component to one of two

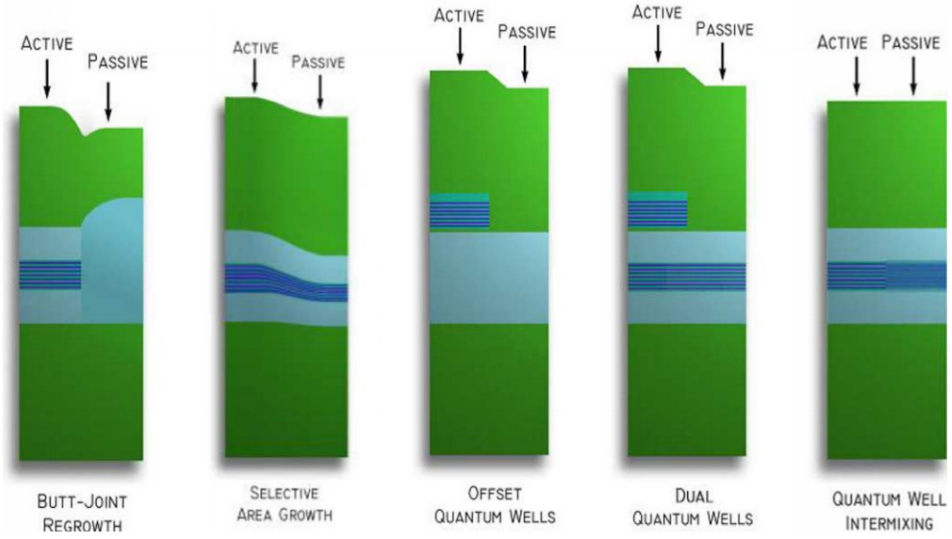

Figure 1.8: Plot from [21] showing different techniques for monolithic photonic integration.

band edges, not allowing for the flexibility necessary for the fabrication of complex, high-performance PICs.

The quantum-well-intermixed (QWI) active-passive configuration is fabricated with an unpatterned cladding regrowth, but in this case the common waveguide contains the multi-quantum well (MQW)-active region, and the bandgap of the MQW region has been selectively increased by a patterned implant and one or more annealing steps to selectively intermix the quantum-well barriers and wells in regions that are to become passive, or perhaps modulator sections [21].

QWI can also be carried out post-growth, where the diffusion of different atoms into the quantum well changes the material composition of the well [24]. The band gap of the QW typically increases as a result of the QWI. Several QWI techniques including impurity induced disordering, photo-absorption-induced disordering and impurity-free vacancy-disordering have been reported [25].

Regrowth steps can significantly increase the cost and complexity of fabrication processes, therefore this work investigates regrowth free monolithic integration, where "passive" sections were defined by areas where less injection current was used. This small amount of current negates any losses incurred by the light propagating through the active material.

1.4 Semiconductor Lasers

The term laser is an acronym for ***L**ight **A**mplification by **S**timulated **E**mission of **R**adiation* and was originally coined by Gould in 1959 [26]. Lasers have been formed from many

materials, including solids, liquids, gasses and free electrons. The lasers investigated during this thesis were formed from semiconductors. Semiconductor lasers, where the gain material is the semiconductor material itself, are used for photonic integration. The first semiconductor laser was developed simultaneously by four research groups in 1962 [27, 28, 29, 30]. These lasers consisted of a GaAs p-n junction operated in forward bias. Most early semiconductor devices had very poor optical confinement and only operated in pulsed mode. The development of the heterostructure device in 1963 [31] allowed for continuous wave operation and the double heterostructure device in 1969 [32, 33] brought the first laser operating at room temperature. Heterostructures will be disscussed further in section 1.4.2.

1.4.1 Band Structure in Semiconductor Lasers

The solution of the Schrödinger equation for electron energies in the periodic potential, created by the collection of atoms in a crystal lattice, results in the broadening of the atomic energy levels and the formation of energy bands. The highest occupied and lowest vacant energy bands at 0 K are the valence and conduction bands, respectively. The forbidden energy region between the valence and conduction bands is known as the band-gap and the size of this energy gap is the band gap energy, E_g. Electrical insulators have a filled valence band and a large energy gap ($E_g > 3$ eV). Conductors have a very small or non-existent energy gap. Semiconductor materials generally have energy gaps of 0.1 eV to 3 eV. A simple parabolic band model for the band structure of a bulk semiconductor material is shown in Figure 1.9. The parabolic band model relates the energy, E to the wavevector, k. The $E - k$ relationship in semiconductors is much more complicated due to the various number of valence bands (e.g. light hole and heavy hole) in the material.

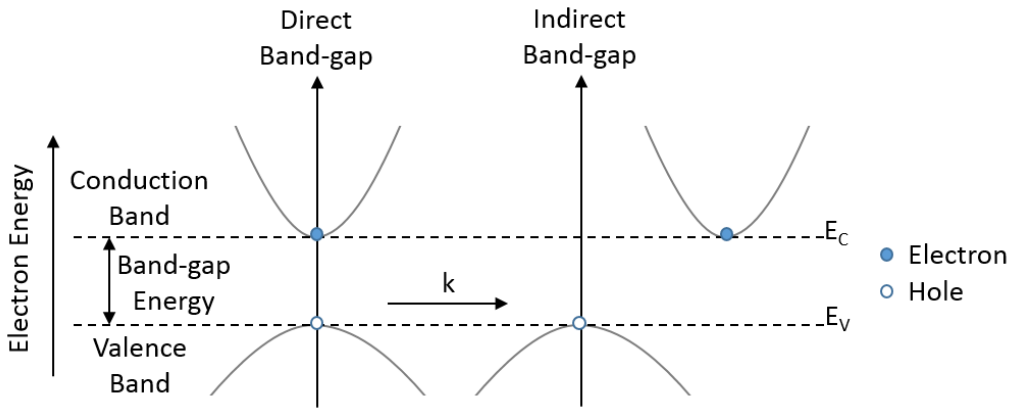

Figure 1.9: Band-gap energy diagram for both direct (left) and indirect (right) band-gap semiconductor materials, at $T > 0$ K.

All semiconductors can be classified as either direct or indirect band-gap materials. Figure 1.9 also shows plots of direct and indirect band-gap materials. In direct band-gap

materials, the maximum of the valence band (VB) and the minimum of the conduction band (CB) lie at the same k-vector value. Energy and momentum ($p = \hbar k$) must be conserved during optical transitions. Therefore, radiative transitions are favoured, where a photon is created when an electron and a hole combine, resulting in the electron and hole momenta annihilating each other.

There is an offset between the maximum of the VB and the minimum of the CB in indirect band-gap materials e.g. Silicon. Since momentum must be conserved in a radiative transition and the momentum change cannot be accounted for by the creation of a photon in an indirect band-gap material, the probability of an electron, hole and photon being involved in a radiative process is very low. Hence, indirect band-gap materials are generally inefficient light emitting devices and are not usually used for semiconductor lasers.

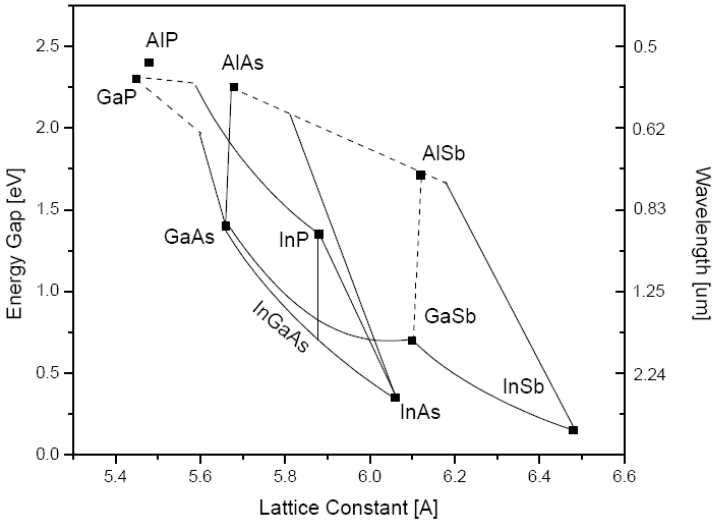

Figure 1.10: Band-gap energy vs. lattice constant for some III-V semiconductors [34]. Direct energy gaps and indirect energy gaps are indicated by the continuous and dashed lines, respectively.

Figure 1.10 is a plot of various band-gap energies as a function of lattice constant for a number of III-V semiconductor families. These compounds generate light with wavelengths ranging from 0.7-1.6 μm. To convert the band-gap energy, E_g, to wavelength, λ, it is assumed that the photon energy is equal to the band-gap energy, giving

$$E_g = hf = \frac{hc}{\lambda} \Rightarrow \lambda(\mu m) = \frac{1.24}{E_g(eV)} \tag{1.1}$$

where h is Planck's constant, f is frequency and c is the speed of light. The laser wavelength can be selected by combining two materials with similar lattice constants, for example InP is typically used in lasers for telecommunications as lattice matched alloys exist, which have bandgap energies corresponding to wavelengths of 1.55 μm, the wavelength of minimum optical fibre loss.

The concentration of mobile charge carriers in a semiconductor can be altered significantly by the addition of controlled amounts of impurities, called dopants. When a majority of mobile electrons are created via doping the material is called an n-type semiconductor. In a p-doped material there is a deficiency of valence electrons and the material is referred to as a p-type semiconductor.

1.4.2 Heterostructures

When a junction exists between differently doped regions of the same semiconductor material it is referred to as a homojunction. A common example of this is the simple p-n junction. When the junction is forward biased with a voltage approximately equal to the energy gap voltage, E_g/e, where e is the electron charge, electrons and holes are injected across the junction to create a population inversion in the active region. When the injected carrier concentration is high enough, stimulated emission exceeds absorption resulting in optical gain. If the gain is larger than the total cavity and mirror losses, lasing occurs. The structure of the homojunction provides little carrier or optical confinement, therefore the losses for a homojunction laser are extremely high and intense pumping is required to achieve lasing.

The development of the double-heterostructure (DH) brought significant improvements in laser performance by reducing the threshold current density and increasing carrier and optical confinement. A DH consists of a thin slab of undoped active material, sandwiched between two higher band-gap p-type and n-type cladding layers [35]. Each of the interfaces is labelled as a heterojunction. For Type I heterojunctions, where the conduction band edge is energetically higher, while the valence band edge is lower in one material than in the other, the difference in the band-gap energies between the materials form potential barriers in both the conduction and valence bands, which significantly increases the carrier confinement [36]. Similarly, the step change in the refractive index leads to a much more efficient waveguide and as a result the radiation is confined to the active region and the optical radiation travelling outside the active region is not strongly absorbed since it is of a higher band-gap energy.

1.4.3 Recombination Processes

Figure 1.11 is a schematic of the three main processes by which electrons and photons interact: absorption, spontaneous emission and stimulated emission. An incident photon of energy $\hbar\omega = E_C - E_V$ will be absorbed if there is an electron in the valence band and a free electron state in the conduction band. The electron will then be excited to the conduction band leaving behind a hole in the valence band. Spontaneous emission occurs when an electron in the conduction band spontaneously relaxes to fill a hole in the valance band. A photon of energy $E \approx E_g$ is then emitted in a random direction.

Spontaneous emission events can be manipulated to produce an efficient light source known as the light emitting diode (LED).

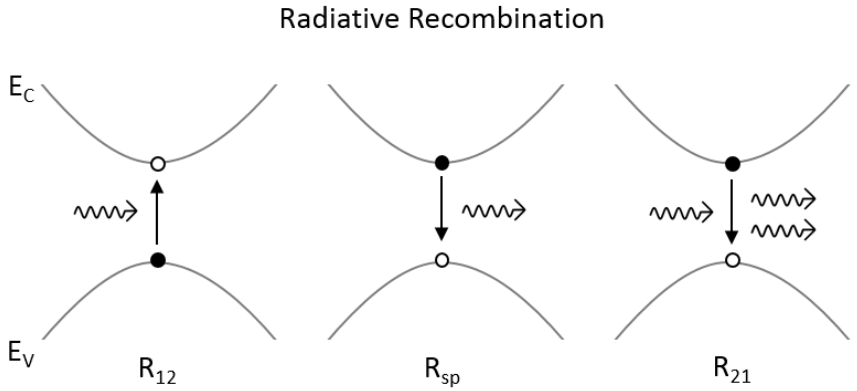

Figure 1.11: Schematic of some recombination processes: stimulated absorption R_{12}, spontaneous emission R_{sp} and stimulated emission R_{21}.

Stimulated emission occurs when an incident photon stimulates an electron in the conduction band to relax and fill a hole in the valance band, resulting in the emission of a second photon of the same energy, phase and direction as the incident photon. This process is the basis of light generation in lasers and laser diodes. The medium exhibits gain when the rate of such radiative transitions is sufficiently high. Since one of the conditions for lasing is that the round trip gain must exceed the losses, non-radiative recombinations must also be considered. Auger recombination (whereby the electron-hole recombination energy is transferred to another electron or hole), the creation of phonons from the transfer of energy to lattice vibrations and recombination via traps or defect centres are some examples of non-radiative processes [35]. Section 2.3 will further discuss the types of semiconductor lasers designed, fabricated and tested as part of this thesis.

1.5 Injection Locking

Injection locking [37, 38, 39] involves coupling an external optical signal from one laser into another. Injection locking is separate from mutual coupling [40, 41, 42] in that the light only propagates in one direction. Therefore the source of the external optical signal is isolated from the injected laser. The source laser is usually referred to as the master laser while the laser to which light is injected is referred to as the slave laser. For sufficiently close frequency/wavelength detuning between the master laser and one of the resonant modes of the slave laser, the slave laser is found to lock to the master laser. In this way, it is possible to force one of the other modes of the slave to lase, which causes the suppression of all the other free-running modes.

In a typical situation, the discrete lasers of the master-slave system are coupled to-

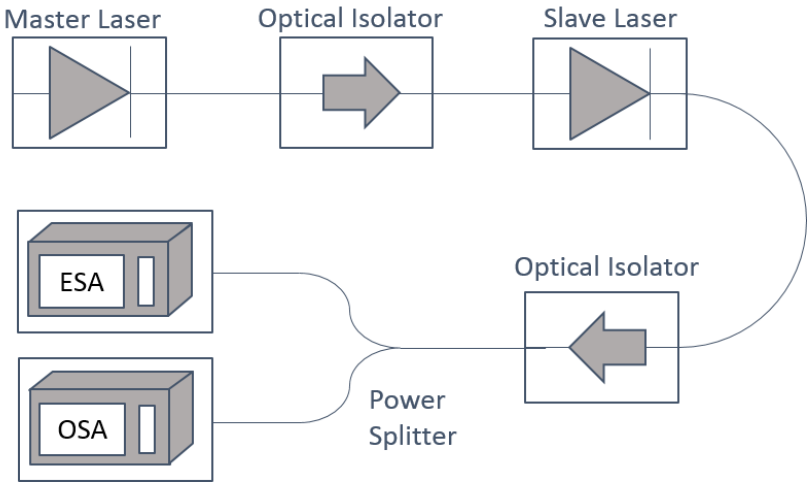

Figure 1.12: Schematic of a typical injection locking experimental setup used to investigate a master-slave system. The master laser is injected into the slave laser via an optical isolator and the output of the slave laser is observed on an ESA and OSA. A second optical isolator prevents any reflections back into the slave laser.

gether using free-space optics or via optical fibre as in Figure 1.12. The requirement of photonic integration for the implementation of super-channels and the use of injection locking to demultiplex the comb source has driven research into injection locking within PICs. It is highly complex to design an optical isolator suitable for integration and the isolator demonstrated in [43] requires a magnetic field for operation. Therefore, injection locking in a system where both the master and slave lasers are integrated together, is highly complex due to mutual feedback between the lasers. Yet, stable optical-phase locking between two integrated SFP lasers has been demonstrated for the case where the master laser is much higher powered than the slave laser [44]. Simultaneous injection locking of two integrated slave lasers to a single master laser has also been obtained [45]. These experiments have relied on a master-slave system to obtain injection locking. This work for the first time investigates mutual injection locking outside of the highly asymmetric operating regime and investigates the limits of stable locking as a function of the detuning, coupling and delay between the lasers.

1.6 Thesis Outline

The aim of this work is to understand mutual injection locking between integrated lasers through experimental testing. The work on injection locking integrated slotted Fabry Pérot (SFP) lasers in [44, 45] was used as a starting point. In these papers, one laser, the master, was much higher powered than the other, the slave. The master laser was used to injection lock the slave(s). The work presented here verifies the work in these papers and then examines the case where both lasers are equally powered. The injection locking properties of a system of two integrated SFP lasers is also investigated

for various detuning and coupling conditions.

Chapter 1 gave a brief introduction to WDM and the push towards increasing the total data throughput of a single optical fibre to allow for the continuous increase in demand for bandwidth from the consumer end. To further increase the number of channels in the fibre, super-channels are required which in turn require photonic integration. The work in this thesis investigates the limits of stable injection locking between integrated lasers which we propose as a potential solution for the creation of super-channels.

Chapter 2 begins by reviewing past experimental studies of mutually coupled semiconductor lasers. The parameters used in theoretical simulations are introduced and how they relate to the experiment is described. The photonic components investigated during this work are described and the material and fabrication steps used for these devices are outlined. The experimental setup used to test the integrated devices is also described.

A block of simple Fabry Pérot (FP) lasers were the first devices examined. Chapter 3 describes the characterisation of a FP laser and demonstrates injection locking a FP laser to an external master laser. The output of the FP laser was examined on an optical spectrum analyser and an electrical spectrum analyser. The characterisation of a slotted Fabry Pérot (SFP) laser is also described. The side mode suppression ratio, wavelength and power of the main lasing mode, modal behaviour (single mode or multimode) and output power of the laser along with the relaxation oscillations were examined for various bias conditions. Injection locking a SFP laser to an external master laser is also demonstrated.

Having characterised a SFP laser, chapter 4 introduces the first fully integrated device where two SFP lasers were integrated together through a 650 μm waveguide interconnect section. Injection locking between the two SFPs was considered for two different coupling schemes: "off-chip"; where the interconnect section between the lasers was reverse biased to make it absorbing thus isolating the lasers and the light from the master SFP was coupled into the slave SFP via an optical circulator, and "on-chip"; where the interconnect section was forward biased to make it transparent, allowing light to couple between the lasers on-chip. In the "on-chip" case, feedback between the lasers was encountered for the first time.

Chapter 5 describes the characterisation of the interconnect section and the effect of its bias on the ability to obtain stable injection locking. Mutually coupled lasers were investigated, where both SFPs were equally biased. Therefore, both lasers had the same optical spectra and output power. The coupling between the lasers (bias of the interconnect section) was varied to investigate its effect on the injection locking properties of the system. The issue of substrate coupling is introduced in this chapter.

Three different waveguide interconnect designs; curved, S-bend and U-bend were in-

vestigated as methods for coupling the two lasers. The U-bend design proved to be the most effective in eliminating the effect of substrate coupling. In Chapter 6, three different length U-bend waveguide interconnect PICs were investigated; 385 μm, 1100 μm and 1285 μm. The dynamical behaviour of the lasers as a function of the coupling and detuning between the lasers was examined. Five types of dynamical behaviour were identified; uncoupled, beating, frequency locked, aperiodic and period doubling. The coupling between the lasers was measured and compared for the different waveguide interconnect lengths.

Chapter 7 summarises the results and conclusions from this thesis, where the key discoveries are outlined. The thesis concludes by giving an outlook into future work that may arise from this study.

Chapter 2

Background

Optical injection locking of semiconductor lasers has been an area of great interest since the early 1980s [37]. The theoretical and experimental study of injection locked semiconductor lasers has resulted in many applications. For example, injection locking can be used, as mentioned previously, to demultiplex an optical comb and to generate multiple phase locked coherent outputs [45], which are required for many modern day modulation formats [46]. Optical injection has also been used with directly modulated lasers in order to reduce the relative intensity noise [47] and enhance resonance frequency and modulation bandwidth [48], while mutual coupling has been shown to dramatically decrease the optical linewidth [40].

Many studies have been carried out to investigate the properties of discrete semiconductor lasers during injection locking and mutual coupling. In these experiments the lasers were either free space or fibre coupled. In one experiment, two commercially available single mode lasers were coupled over a distance of 20 cm [49, 50]. Two collimating lenses were used to mode-match the beams of the two lasers. The coupling strength was controlled by a set of three polarisers so that less than 10^{-4} of the intensity of one laser was injected into the other. Through adjustments of the temperature, the lasers were tuned to the same optical frequency, but their pump levels were kept dissimilar. This study demonstrated a form of local synchronisation, where one laser is forced to oscillate at the relaxation oscillation frequency of the other laser. A regime of self-initiated and self-sustained oscillations was also discovered.

A pair of coupled lasers can also be created by splitting a single output into two beams. The output of an Ar-laser-pumped $LiNdP_4O_{12}$ (LNP) laser was divided into two beams by a beam splitter and focused on the input surface of the LNP crystal by the common focusing lens [51]. In this experiment through the variation of the attenuation of one beam and the coupling distance, a regime of chaos synchronisation was discovered, where the power of both lasers fluctuated chaotically, but with a high level synchronicity.

In another study, two identical semiconductor lasers were pumped at a constant level and coherently coupled via the dominant TE component of the optical field [52]. The delay time between the lasers was varied between 3.8 and 5 ns and the coupling strength was approximately 5%. A regime of time delayed synchronisation was observed, where the leading laser synchronised its lagging counterpart and the synchronised lagging laser drove coupling-induced instabilities.

Regions of locking have also been observed between coupled lasers. Two InGaAsP distributed feedback (DFB) lasers, coupled over a distance of 51 mm using collimating lenses, with a coupling strength of a few percent, locked to the same frequency and exhibited stable emission for small spectral detuning [53]. Oscillatory behaviour was obtained at larger detuning. In another study, using a similar setup and a coupling strength of 5%, stable compound laser modes, where both lasers lock onto a common frequency and emit continuous wave output were demonstrated for small spectral detuning [54]. As detuning increased, this stable output was replaced with oscillatory behaviour. It was found that the width of the locked regime was not symmetric in detuning, i.e. different width for positive and negative detuning.

Mutually coupled and unidirectional coupled lasers have also been compared [55]. Commercially available semiconductor lasers were coupled over a distance of 120 cm. The synchronisation of the lasers for both coupling cases were studied while varying self-feedback, coupling and detuning. It was found that the mutual coupling showed high quality synchronisation in a broad range of self-feedback and coupling strengths. It was tolerant to significant parameter mismatch which for unidirectional coupling would result in loss of synchronisation.

Larger separations between the lasers have also been studied. Two semiconductor lasers were coupled through a system of fibres and attenuators, obtaining a separation of 12.6 m [56]. The maximum coupling strength obtained was 40%. Varying the bias currents and the coupling strength of the lasers resulted in a number of different dynamical regimes. Distinct synchronisation scenarios for two bias currents: 1.02 and 1.25 times the threshold bias current of the solitary laser were obtained. For the low bias current and strong coupling, the lasers exhibited dynamical bistability, i.e. the coexistence of low-frequency fluctuations and stable continuous-wave emission.

The effect of asymmetric coupling between mutually coupled lasers has also been investigated [57]. The lasers were separated by approximately 15 ns. Faraday rotators were used to make the coupling from laser A to laser B different to the coupling from laser B to laser A. Laser B also received self-feedback. Similarly to previous studies, a regime of highly synchronised chaotic fluctuations was observed. The level of synchronicity was studied for varying feedback levels received by laser B and various levels of asymmetry of the coupling.

There have been a small number of studies on mutually coupled semiconductor lasers

fabricated on the same chip. In one study, an integrated colliding-pulse mode-locked semiconductor laser was used to demonstrate the existence of non-linear dynamics, such as period-four, period-three and period-one limit cycles, and chaos in photonic integrated circuits [58].

In another work, a distributed Bragg reflector laser pair fabricated on the same chip was used to investigate non-linear effects, characteristic of mutual optical coupling, in an ultra-short coupling regime [59]. Optical coupling was introduced via back reflection from a cleave-ended fibre. The coupling strength was varied changing the distance of the fibre from the output of the chip, without significantly affecting the coupling time of 30 ps. By adjusting the detuning between the lasers, various non-linear phenomena were observed, such as four wave mixing (FWM), locking, period doubling and chaotic behaviour.

Another device studied, consisted of two monolithically integrated distributed feedback lasers in a face-to-face arrangement, separated by a 400 μm phase section [60]. Similar to the previous work, various behaviours, such as mutually stable locking, period-1 oscillation, frequency locking, quasi-periodicity and chaos, were observed by varying the detuning between the lasers.

Stable phase locking was also demonstrated between two SFP lasers coupled on chip via a variable gain waveguide section [44]. The two lasers were biased asymmetrically, one just above the threshold current of the device with the other at three times this value. The coupling between the lasers was controlled using the variable gain section which acted as a variable optical attenuator or amplifier depending on bias. Using this, the width of the stable phase locking region on chip was shown to be variable. In another work by the same author, a multimode interference coupler was monolithically integrated with single facet slotted Fabry Pérot lasers at its input and output arms [45]. The light from the master SFP laser was used to injection lock both output slave lasers.

Many of the experimental investigations above also contained theoretical studies to match the experiments. There have also been many purely theoretical studies of mutually coupled lasers [37, 61, 62, 63, 64, 65, 66, 67].

The focus of this thesis is solely on experimentally investigating a system of two integrated semiconductor lasers. However this work has been carried out in tandem with theoretical studies of the system [68, 69]. The model used by the theoreticians was a modified version of the Lang–Kobayashi equations for single-mode lasers under feedback, and is shown in the following equations;

$$E_1'(t) = i\Delta E_1 + (1 + i\alpha)E_1 N_1 + \kappa e^{-iC_p} E_2(t - \tau), \tag{2.1}$$

$$E_2'(t) = (1 + i\alpha)E_2 N_2 + \kappa e^{-iC_p} E_1(t - \tau), \tag{2.2}$$

$$N_1'(t) = \epsilon[J - N_1 - (N_1 + \nu)|E_1|^2], \tag{2.3}$$

$$N_2'(t) = \epsilon[J - N_2 - (N_2 + \nu)|E_2|^2]. \tag{2.4}$$

These equations describe the temporal evolution of the complex electric fields, $E_{1,2}$, and excess carrier densities, $N_{1,2}$, of lasers 1 and 2, respectively. α is the linewidth enhancement factor of the lasers, J is the injection parameter, ϵ is the ratio of the carrier and photon lifetimes, ν is simply a scaling constant, κ is the coupling coefficient, which describes the fraction of light reaching one laser from the other, and vice versa, C_p is the coupling phase, described by the phase difference caused by the intermediate section, Δ is the frequency detuning of the laser and τ is the delay time between the lasers. α, J and ϵ are all fixed parameters, as they are either a material property or a non-varying experimental parameter. The four parameters that vary experimentally are Δ, κ, τ and C_p.

The goal of this work is to experimentally investigate mutual injection locking of two integrated semiconductor lasers in order to provide a set of experimental results to aid theoretical work.

2.1 Theoretical Parameters

The four parameters used in theoretical simulations that vary experimentally are (i) the detuning, Δ (ii) the coupling ratio, κ, (iii) the delay, τ and (iv) the coupling phase, C_p between the lasers. The following sections describe what these are and how they relate to the experiment.

2.1.1 Detuning Δ between the Lasers

The detuning Δ between the lasers is the wavelength (or frequency) difference between the lasing wavelengths of the two lasers, Figure 2.1. The lasing wavelength of the lasers is determined by their bias and is widely tuneable. Experimentally varying the detuning between the lasers should be easy in principle, but is somewhat challenging in practice due to mode-hopping in the lasers. Both lasers were designed to be identical but the fabricated lasers were not always identical due to the variability in the cleaved facets and hence did not mode-hop together. Therefore, finding a range of biases where both lasers were tuneable over a range of ideally a few 10s of GHz while the detuning between the two lasers is also less than a few 10s of GHz was challenging.

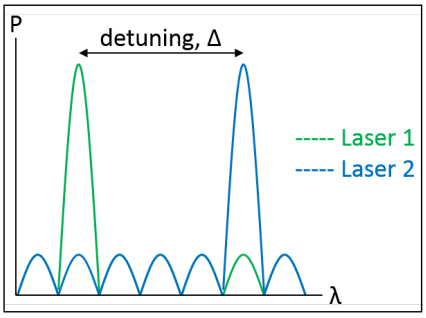

Figure 2.1: Illustration of the wavelength detuning, Δ between two lasers.

2.1.2 Coupling Ratio κ between the Lasers

The coupling ratio κ between the lasers is the percentage of the light emitted by one laser that enters the other laser. κ is determined by the bias of the waveguide interconnect. κ as a function of applied bias can be measured by the following steps;

1. The first laser was set lasing and its total output power was measured by applying a reverse bias of -2 V to the waveguide interconnect and the photocurrent generated by the light being emitted from the laser, $I_{Tot,M}$ was recorded, Figure 2.2a.
2. The laser was turned off and the dark current, $I_{Tot,D}$ in the waveguide interconnect was measured, Figure 2.2c.
3. The total photocurrent generated by the laser was calculated: $I_{Tot} = I_{Tot,M} - I_{Tot,D}$.
4. The photocurrent was converted to optical power using the equation $P(W) = h\,c\,I_{ph}/e\,\lambda$, where I_{ph} is the photocurrent, h is Planck's constant, c is the speed of light and e is the electron charge.
5. The laser was set lasing again and the bias of the waveguide interconnect was swept from -2 V to 2 V. The amount of the output of the laser that entered the second laser was measured by reverse biasing the second laser to -2 V and the photocurrent generated by the light being emitted from the laser, $I_{1\to2,M}$ was recorded, Figure 2.2b.
6. The laser was turned off and the dark current, $I_{1\to2,D}$ in the second laser was measured while the bias of the waveguide interconnect was swept from -2 V to 2 V, Figure 2.2d.
7. The photocurrent generated in the second laser was calculated: $I_{1\to2} = I_{1\to2,M} - I_{1\to2,D}$.
8. The photocurrent was again converted to optical power.
9. The coupling ratio, $\kappa_{1\to2}$ was calculated using $\kappa_{1\to2} = P_{1\to2}/P_{Tot} = I_{1\to2}/I_{Tot}$.
10. The above steps were repeated to obtain $\kappa_{2\to1}$.

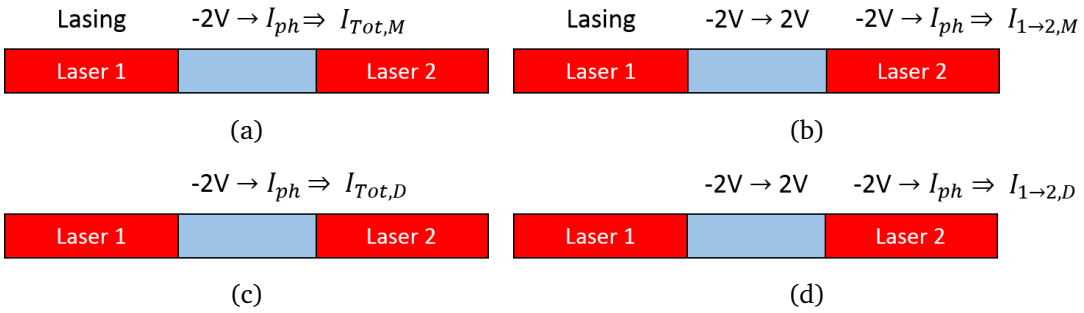

Figure 2.2: Schematic of the method used to measure the coupling, κ between the lasers. (a) Laser 1 was set lasing and its total output power was measured by applying a bias of -2 V to the waveguide interconnect and recording the generated photocurrent, $I_{Tot,M}$. (b) With Laser 1 lasing, the bias of the waveguide interconnect was swept from -2 V to 2 V. The amount of the output of Laser 1 that entered Laser 2 was measured by reverse biasing Laser 2 to -2 V and recording the photocurrent generated by the light being emitted from Laser 1, $I_{1\rightarrow 2,M}$. (c) Laser 1 was turned off and the dark current, $I_{Tot,D}$ in the waveguide interconnect was measured by applying a bias of -2 V to it and recording the photocurrent. (d) With Laser 1 off, the dark current, $I_{1\rightarrow 2,D}$ in Laser 2 was measured while the bias of the waveguide interconnect was swept from -2 V to 2 V.

2.1.3 Delay τ between the Lasers

The time delay τ between the lasers is related to the length of the waveguide interconnect, D, between the lasers (Figure 2.3) by $\tau = nD/c$, where n is the refractive index of the material and c is the speed of light. Therefore τ is fixed in each PIC. In order to investigate the injection locking properties of two integrated lasers as a function of τ, a set of PICs with various length waveguide interconnects is required.

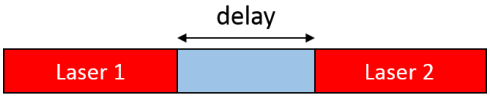

Figure 2.3: Illustration of the delay, τ between the lasers.

2.1.4 Coupling Phase Cp between the Lasers

The coupling phase Cp between the lasers is the phase difference caused by the waveguide interconnect. C_p is unknown experimentally. However, the change in phase due to the bias of the waveguide interconnect can be approximated by calculating how the optical path length changes with applied bias and converting this to change in phase using $C_p = 2\pi(nD \bmod \lambda)$, where nD is the optical path length and λ is the free-running emission wavelength.

2.2 Lab Equipment

The three main pieces of measurement equipment used in the lab to study the laser interactions are (i) the optical spectrum analyser, (ii) the high speed oscilloscope and (iii) the electrical spectrum analyser.

2.2.1 Optical Spectrum Analyser

The optical spectrum analyser (OSA) gives the wavelength information of the lasers. Once the optical spectra from both lasers have been recorded, the detuning between the lasers can be calculated. The OSA also shows if the lasers are single or multi-moded.

2.2.2 High Speed Oscilloscope

The high speed oscilloscope (HSO) shows the temporal behaviour of the system, by displaying the voltage signal received by a photodiode, which is $|E|^2$, where E is the electric field.

2.2.3 Electrical Spectrum Analyser

The electrical spectrum analyser (ESA) gives the Fourier transform of the voltage signal received by a photodiode or the Fourier transform of the signal obtained on the HSO. Therefore the ESA displays the Fourier transform of $|E|^2$, which are the frequencies present in the system.

The goal of this thesis is to experimentally study the mutual injection locking properties of two integrated lasers and create a map of the dynamical behaviours present in the system as a function of Δ, κ and τ. The following section discusses the photonic devices and integrated circuits used in this study.

2.3 Photonic Components

Similar to electronic integrated circuits, PICs are made up of multiple components. The three main photonic components investigated during this work are (i) the Fabry-Pérot laser, (ii) the Slotted Fabry-Pérot laser and (iii) the Variable Optical Amplifier/Attenuator. The following sections give a brief introduction to each.

2.3.1 The Fabry-Pérot Laser

A schematic of the simplest semiconductor laser, the Fabry-Pérot (FP) laser is shown in Figure 2.4. This is a Fabry-Pérot resonator where the sides of the etalon i.e. the mirrors are formed through the change in index from the gain material to air. The structure is composed of one material (i.e. the gain material) sandwiched between the outer material i.e. air. The refractive index of air is 1.0 and the index of the material, used in this work, is approximately 3.5 (based on an approximation of the refractive index of InP based materials).

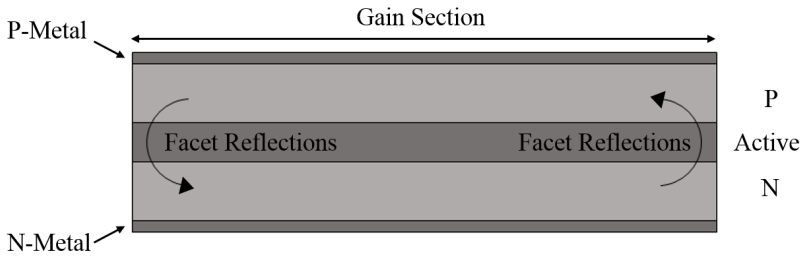

Figure 2.4: Schematic of a semiconductor FP laser where the mirrors are formed through the change in index from the gain material to air.

To fabricate a FP laser a ridge waveguide structure is cleaved at a specific length, where the cavity is formed due to reflections from the cleaved facets. A p-n junction is formed between deposited metal on top of the FP ridges (the P side) and deposited metal on the back of the FP (N-side). A bias is applied across this junction to provide the gain needed to electrically drive the laser.

2.3.2 The Slotted Fabry-Pérot Laser

FP lasers are not easily integrated with other components due to their dependence on the feedback from both cleaved facets for lasing. In the Slotted Fabry-Pérot (SFP) laser, one or both of the cleaved facets (mirrors) was replaced by a sequence of partially reflective slots etched into the active ridge waveguide [70]. A schematic of the laser employing etched slots as the front and back mirrors is shown in Figure 2.5.

In Figure 2.5b, the slot is assumed to be etched to the same depth as the waveguiding ridge. In practice, the slot depth can be accurately and independently controlled by the use of etch stop layers and be used to adjust the reflection and transmission of the individual slots. The reflectivity spectrum of the mirror can be designed with specific spectral properties to allow the realisation of singlemode lasers, multimode lasers with specified mode spacing, or tunable lasers [70]. The single facet lasers used in this work, consisted of a 650 μm long gain section and a 760 μm long mirror section, comprised of seven etched slots, each with a gap of 1.0 μm and 108 μm separation between the slots. The SFPs were controlled by independently biasing their respective mirror and

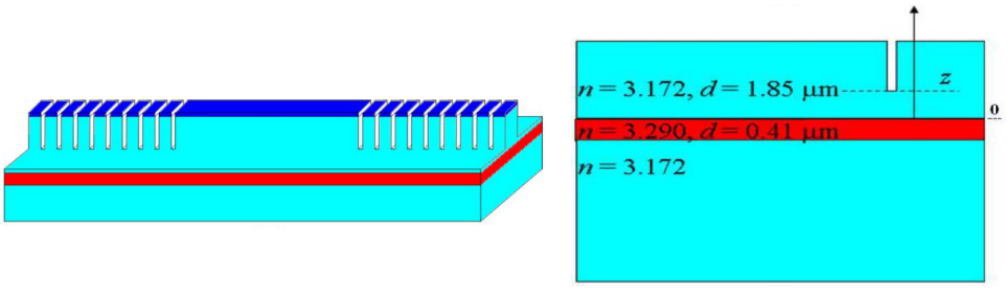

(a) (b)

Figure 2.5: (a) Schematic diagram of a laser with a series of slots as the front and back mirrors and (b) cross-section of a single slot from [70].

gain sections.

2.3.3 The Variable Optical Amplifier/Attenuator

The Variable Optical Amplifier/Attenuator (VOA) is a simple waveguide structure but since it is fabricated on an active substrate, it requires an electrical bias to overcome the loss due to the high absorption of the material at 1550 nm. Left unbiased the VOA attenuates any optical signal that passes through it. Applying a reverse bias to the VOA will further attenuate the signal. The VOA can be forward biased to reduce losses or driven to produce extra optical gain (amplification) to any light propagating through it, thus acting like a semiconductor optical amplifier (SOA).

The photonic integrated circuits designed, fabricated and tested during this work consisted of two single facet SFP lasers integrated together through a VOA section. Varying the length of the VOA section, varied the delay, τ between the lasers.

2.4 PIC Fabrication and Design

The fabrication of all devices tested during this work was based on a monolithic process with a single epitaxial growth step. A substrate based on an active material is required for the lasers to lase, however, this posed a significant problem for the passive devices. High absorption losses would occur in the passive waveguides since they have an identical bandgap to that of the laser sections. To overcome this problem, the passive structures were treated as *pseudo-passive*, which could be electrically biased. Applying an electrical bias to these sections provided sufficient optical gain to overcome the inherent material losses caused by absorption. Hence, each waveguide section of the devices could not only be reverse biased to increase losses or forward biased to reduce losses, but also driven to produce extra optical gain to any light propagating through it. In this way, each waveguide on the integrated devices could be treated as a simple waveguide

or variable optical amplifier/attenuator (VOA) where the amplification/attenuation of the light could be controlled.

2.4.1 Material Structure

The material structure used was commercially grown (IQE) 1550 nm lasing material. It consisted of five compressively strained AlInGaAs quantum wells, grown on an N-doped (100) InP substrate, with a total active region thickness of 0.41 μm. The exact layer structure is shown in Table 2.1. Layer 12 was used as an etch-stop layer during selective etching of the InP in layer 13. This allowed the formation of a 1.85 μm high ridge waveguide structure. The N doped layers 3 and 4, and P doped layer 10, were used as separate confinement heterostructure layers allowing for variations of the mode position and optical confinement.

Table 2.1: Layer structure of the laser material used for all PICs investigated in this thesis.

Layer	Material	x	y	Thickness (μm)	Type
15	GaIn(x)Ax	0.53	-	0.200	P
14	GaIn(x)AsP	0.71	0.62	0.050	P
13	InP	-	-	1.600	P
12	GaIn(x)AsP	0.85	0.33	0.020	P
11	InP	-	-	0.050	P
10	Al(x)GaIn(y)As	0.9	0.53	0.060	P
9	Al(x)GaIn(y)As	0.72	0.53	0.060	U/D
8	Al(x)GaIn(y)As	0.44	0.49	0.010	U/D
7 x 5	Al(x)GaIn(y)As	0.24	0.71	0.060	U/D
6 x 5	Al(x)GaIn(y)As	0.44	0.49	0.040	U/D
5	Al(x)GaIn(y)As	0.9	0.53	0.060	U/D
4	Al(x)GaIn(y)As	0.9	0.53	0.060	N
3	Al(x)GaIn(y)As	0.86	0.53	0.010	N
2	InP	-	-	0.500	N
1	InP	-	-	0.300	N

Standard lithographic techniques were used to define the ridge and slot features, with a ridge width of 2.5 μm, ridge height 1.85 μm, and a slot width of 1.0 μm, with the ridge etch stopping above the quantum wells. To ensure electrical isolation between sections, a deep etch region of 2.4 μm deep, that penetrated through the intrinsic region into

the n-doped layers was performed around the slot separating the sections. Both etches were performed using a Cl_2/CH_4H_2 (10:8:4) inductively coupled plasma etch. The sidewalls of each device were passivated using a 300 nm thick layer of SiO_2. Titanium and gold were deposited using standard lift-off lithography and e-beam evaporation to form the P and (top) N metal contacts. A 360° rotational tool was used to ensure the metal ran continuously up the sidewalls, reducing potential metal breaks. The wafer was then chemically thinned using a bromine methanol solution in order to cleave a high quality facet. The back side N metal was deposited and the devices cleaved [71].

2.4.2 Design/Layout of Photonic Integrated Devices

The software tool developed previously in the IPG at Tyndall for mask design is referred to as *PICDraw*, and generates mask layout files completely mathematically. The main advantage of defining each device mathematically is how efficiently alterations can be made to complex layouts. Any changes to waveguide width, waveguide length, bend radius or other such design parameter can automatically update the entire layout with no extra designing or alterations from the designer. Hence, when designed correctly, changes to the length of the VOA integrating the two SFP lasers could be made by changing just a single parameter.

The fabrication process briefly described above required four main lithographical steps during fabrication: (1) the waveguide etch (ridge and slots), (2) the deep etch (isolation slots and bends), (3) oxide opening and (4) metal deposition to form contact pads. A different mask is required for each lithographical step. Each of these mask layers was designed using PICDraw. Figure 2.6 is a schematic of the 4 layers required to fabricate a single facet SFP laser. The gain section is on the left and the slotted mirror section on the right ending with a deep etched slot for isolation between the SFP and the next device (the VOA). The device is cleaved on the left hand side to create the second mirror. A zoom in of the right hand side of the SFP is shown in Figure 2.7, where the different layers can be seen more clearly.

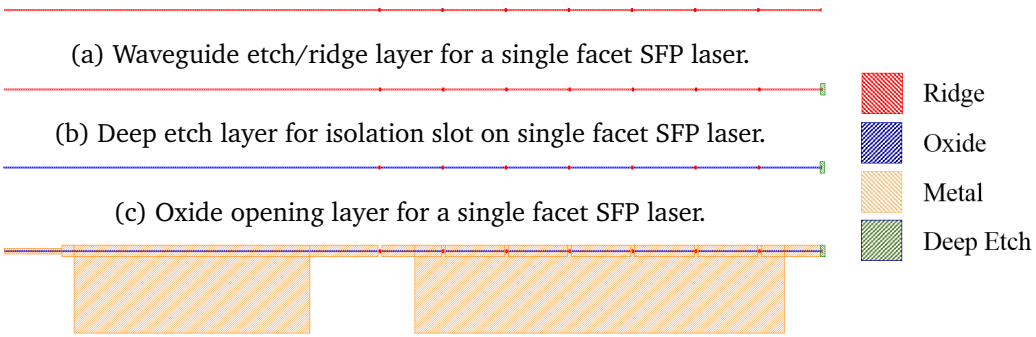

(d) Metal layer for contact pads on a single facet SFP laser.

Figure 2.6: Schematic of the lithographic layers for a single facet SFP laser.

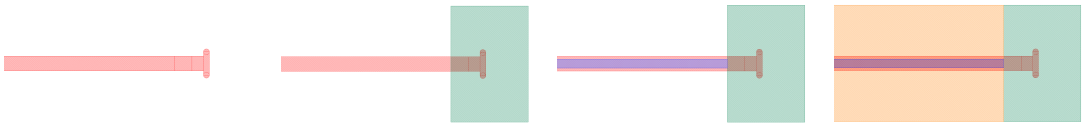

(a) (b) (c) (d)

Figure 2.7: A closer look at the lithographic layers for a single facet SFP laser showing only the right hand side of Figure 2.6a-d.

Figures 2.6a and 2.7a are the waveguide etch/ridge layer, which defines the ridges and slots. At this step SiO_2 is deposited on the sample and patterned using this mask defining the regions that will remain unetched throughout. SiN_x is then deposited on the sample and patterned using the deep etch mask and a dry etch defining the deep etched regions. In Figures 2.6b and 2.7b, the deep layer has been added to the ridge layer. The only deep etched region on the SF-SFP laser is the isolation slot to the right of the device.

The next stage of the process is to dry etch the semiconductive material to a depth just above the intrinsic region. The silicon nitride is then stripped using a dry etch, exposing any underlying SiO_2. Afterwards, the semiconductor dry etch is continued, simultaneously defining the ridge waveguide structures while extending the pre-existing deep etch. Upon completion of this step, the waveguide has a depth just above the intrinsic region while the deep etch has penetrated through the quantum wells and into the n doped layers. The SiO_2 is then removed.

A layer of SiO_2 is deposited over the entire sample and openings are created using the oxide opening mask. The oxide opening mask has been added to the schematic in Figures 2.6c and 2.7c. The SiO_2 passivates the sidewalls of the structures to prevent the metal of the contact pads from shorting the various semiconductor layers.

Titanium and gold are deposited by standard lift-off lithography and e-beam evaporation to form contacts on the surface of the sample. The metal mask is used to define the areas for lift-off. Figures 2.6d and 2.7d show the metal layer added to the SF-SFP schematic. The sample is then thinned to allow for cleaving. The n contact metal is deposited on the backside of the wafer and finally the sample is cleaved to form the cleaved facets necessary for reflection and to get light out of the devices.

A quad mask output from PICDraw is shown in Figure 2.8a, where four mask layers are printed on a single mask plate. On the mask plate data is chrome. Since the fabrication of all devices tested during this work was based on a monolithic process with a single epitaxial growth step, many other devices for various projects are included on the mask. Figure 2.8b shows the full mask layout with four layers; ridge, deep, oxide, and metal, overlapped showing the full device layout. The devices designed as part of the work for this thesis have a black border.

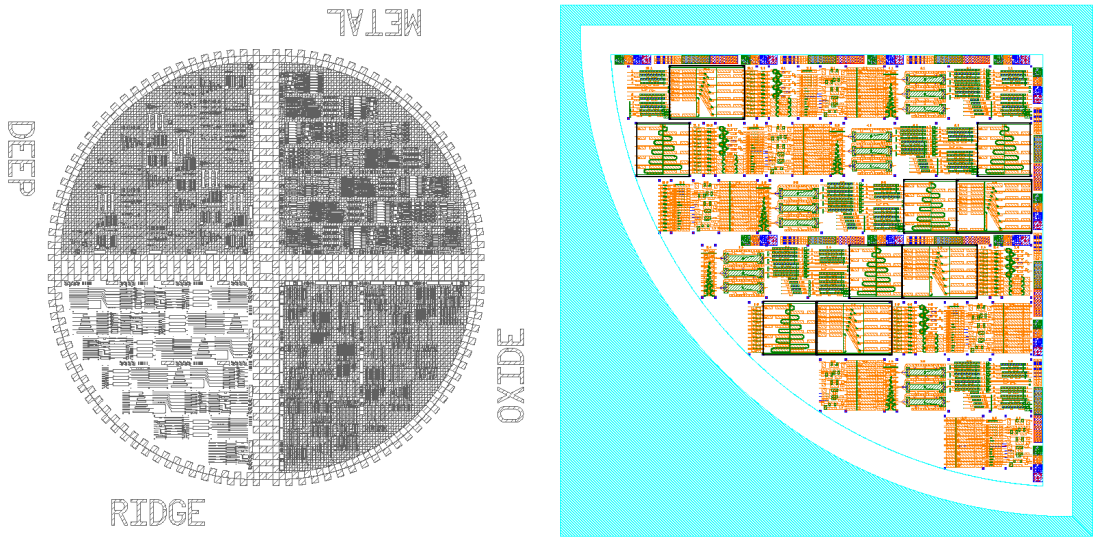

(a) (b)

Figure 2.8: (a) Quad mask output from PICDraw software. Four mask layers printed on a single mask plate for use with a quarter 2" wafer process. (b) Full mask layout with four layers; ridge, deep, oxide, and metal, overlapped showing the full device layout. Devices designed as part of the work for this thesis have a black border.

2.5 Experimental Testing

The probe station used to test the integrated devices is shown in Figure 2.9. A custom mount is shown at the centre with a series of probe manipulators positioned in a “U” shape around it. The manipulators allowed precise positioning of the probes on the chip. The bases of the manipulators were magnetic and placed on the steel platform which kept them from moving and damaging the device under test (DUT). A thermo-electric cooler (TEC) was placed in between the custom mount and a large aluminium heat sink to control the temperature of the DUT. Lensed fibre manipulators can be seen under the steel platform at both sides of the heat sink, which allowed the position of the lensed fibre to be varied in the x-, y- and z-directions. One of the fibre manipulators was controlled via a nanotrak piezo cotroller which allowed for fine control over the fibre position. The nanotrak piezo cotroller was programmed to track the optical power output from the device which compensated for any drift in the fibre. Hence, the lensed fibre remained coupled throughout experiments. Without the nanotrak the fibre tended to drift and lose coupling due to changes in temperature, humidity and air-conditioning in the lab during long experiments. On the other side of the setup, a manual controller was used to adjust the position of the lensed fibre.

This chapter gave an overview of past experimental studies of mutually coupled semiconductor lasers. The parameters used in theoretical simulations were introduced and how they relate to the experiment was described. The photonic components inves-

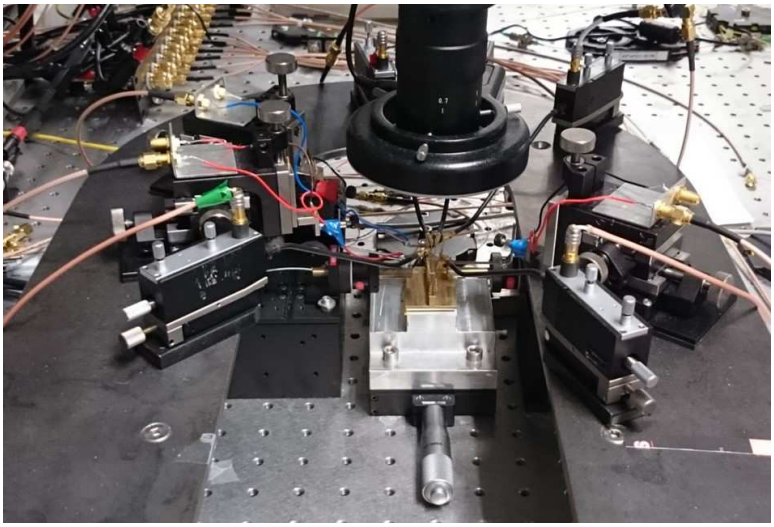

(a)

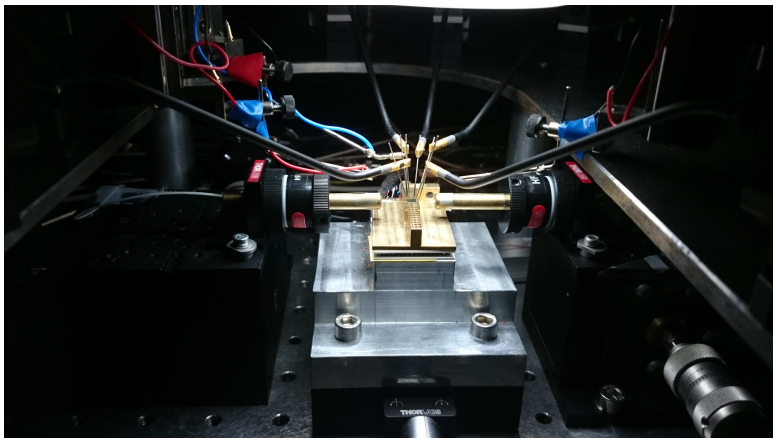

(b)

Figure 2.9: Experimental setup showing external probe manipulators placed around an integrated device under test, with lensed fibres on both sides.

tigated during this work were described and the material and fabrication steps used for these devices were outlined. The experimental setup used to test the integrated devices was also described. The next chapter will describe characterising FP and SFP lasers, and injection locking using an external tunable laser will be introduced. The following chapters will then discuss the investigation of mutual injection locking of two integrated SFP lasers.

Chapter 3

Fabry Pérot and Slotted Fabry Pérot Lasers

Before investigating the mutual injection locking of two integrated SFP lasers, both Fabry Pérot lasers and slotted Fabry Pérot lasers were characterised. Injection locking of the lasers to an external tunable laser was also demonstrated. The Fabry Pérot (FP) laser is the simplest semiconductor laser, therefore the first devices examined were the block of FPs shown in Figure 3.1. The lasers were approximately 2.1 mm in length.

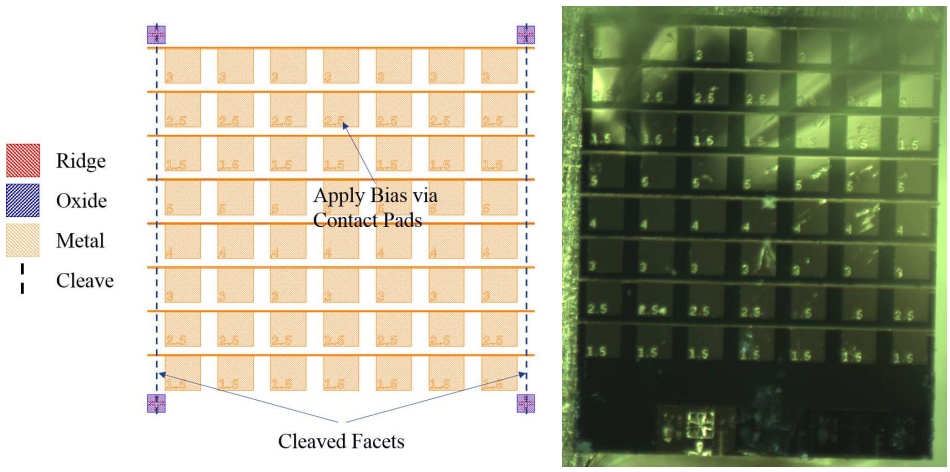

(a) (b)

Figure 3.1: (a) Schematic and (b) microscope image of a block of Fabry Pérot lasers of various ridge widths.

Current was applied to the FP laser using a probe positioned on the large contact pad. The backside of the chip was coated in N-metal and the brass mount was grounded, therefore only one probe was required to apply bias across the FP laser. A lensed fibre was brought towards the cleaved facet of the laser, where it allowed the light to be taken and examined externally on an Optical Spectrum Analyser (OSA), Electrical Spectrum Analyser (ESA) or a power meter (PM).

3.1 Fabry-Pérot Laser Characterisation

The bias of the laser was stepped from 0 mA to 70 mA and a Power-Current (LI) curve for the FP laser was generated. The curve is shown in Figure 3.2. Typical behaviour was observed and the threshold current, I_{th}, of the laser was found to be ∼55 mA. Below this current the laser did not lase.

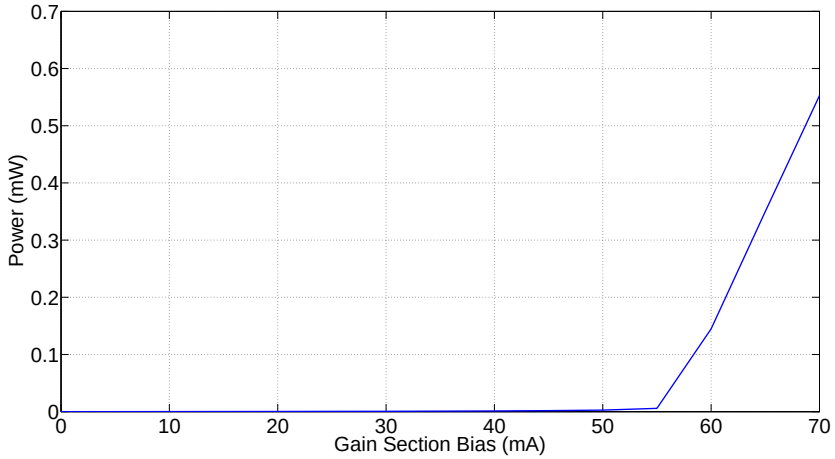

Figure 3.2: LI curve of the FP.

A typical spectrum from the FP laser is shown in Figure 3.3.

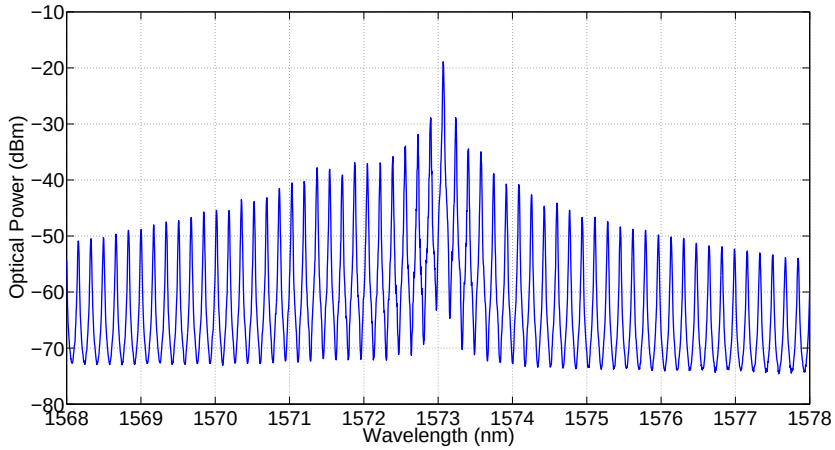

Figure 3.3: Free-running optical spectrum of the FP laser.

The wavelength spacing between modes in a cavity of length L can be written as:

$$\Delta\lambda = \frac{\lambda^2}{2n_{gr}L}. \tag{3.1}$$

where λ is the wavelength and n_{gr} is the group index [72].

The average wavelength separation between the modes of the FP laser was calculated as 1.6 nm. Taking the group index to be approximately 3.5 and using Equation 3.1, the cavity length of the laser was found to be 2.1 mm, which matches the actual length of

the lasers.

3.2 Injection Locking of FP Laser to a Tuneable Laser Source

Next, the optical injection locking of a single FP laser by a commercial external cavity tunable laser, the tunable laser (TLS), was investigated. The TLS used had a linewidth < 100 kHz and was tuneable in steps of 1 pm. A schematic outline of this experiment is shown in Figure 3.4.

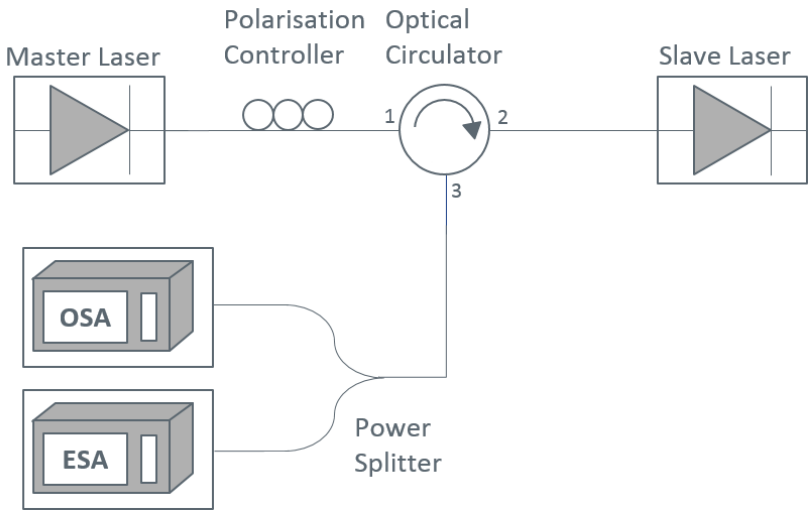

Figure 3.4: Outline of a typical injection locking setup. The output of the master laser is passed through a polarisation controller before being injected into the slave laser via an optical circulator. The output of the slave laser is then observed on an OSA and an ESA.

The TLS (master laser) output, was guided in single mode fibre through a polarisation controller to port 1 of the circulator, which provided greater than 40 dB isolation. The light from the TLS was injected into the FP laser via port 2 of the circulator through the lensed fibre positioned at the laser facet. Light from the FP was then decoupled via the same lensed fibre and examined on an OSA or ESA at port 3. The circulator allowed light to pass from the master laser to the slave laser but prevented light travelling in the reverse. Light can have either TE (transverse-electric) or TM (transverse-magnetic) polarisation. If the light from the master and the slave lasers do not have the same polarisation, injection locking will be difficult. The polarisation controller is used to control the polarisation of the light from the master laser, the TLS. Thus, ensuring that it has the same polarisation as the light from the slave laser.

3.2.1 Injection Locking FP to TLS by Sweeping TLS Wavelength

The TLS wavelength was set close to that of the main mode of the FP laser output and injected into the FP cavity via the circulator. The power of the TLS was set to 0 dBm. The TLS wavelength was then swept across resonance with the chosen mode of the FP while OSA and ESA traces were recorded at each swept wavelength. The resulting plots were concatenated in Matlab and the colour intensity plots obtained are shown in Figures 3.5 and 3.6. The TLS power was then decreased to -7 dBm and the above steps were repeated. Figure 3.5 shows colour intensity plots of the optical spectrum of the FP as the wavelength of the master laser was tuned across the FP for each of the master powers chosen.

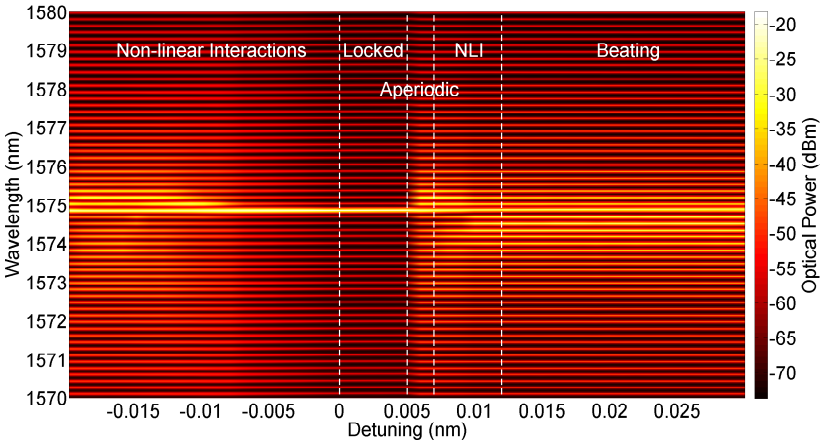

(a) Injected TLS power at 0 dBm.

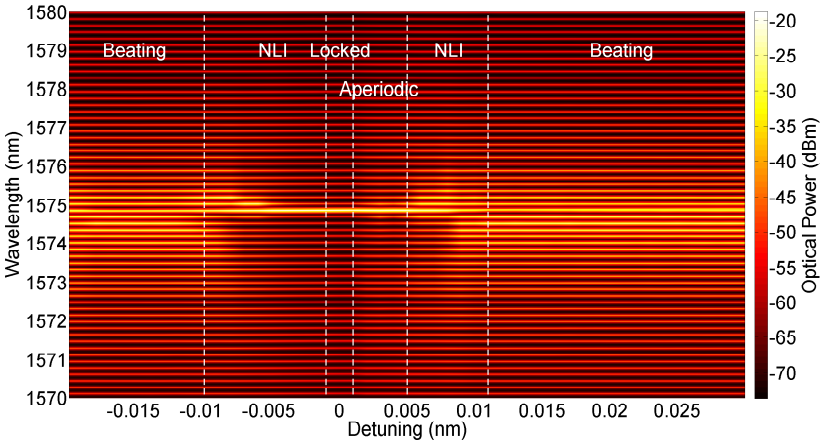

(b) Injected TLS power at -7 dBm.

Figure 3.5: OSA traces from the FP laser as the TLS wavelength was swept across resonance with the main mode of the FP. Two different TLS powers are shown where the effect of higher injected power can be seen. For close to zero detuning in both cases, significant suppression of the side modes of the FP was observed and the FP lased strongly at the injected wavelength.

Detuning is defined as the frequency of the master laser minus the free-running frequency of the slave laser, in this case the FP. As the detuning between the master and

slave lasers became smaller, suppression of the modes occured and the FP laser operated with a single lasing mode at the injected master laser wavelength of 1574.9 nm.

The width of the region where the suppression of the side modes occurred, increased with higher injected powers. Figure 3.5 clearly shows this, where for an injected power of 0 dBm (Figure 3.5a) the detuning could extend to almost 0.005 nm before the output returned to that of a free running FP, whereas for an injected power of -7 dBm (Figure 3.5b) the detuning only extended to ∼0.002 nm. The injected power determines the level of suppression of the side modes of the FP during injection locking; the higher the coupled TLS power the larger the suppression. The maximum side mode suppression ratio (SMSR) obtained for a TLS power of 0 dBm was 33.35 dB and for -7 dBm was 27.66 dB.

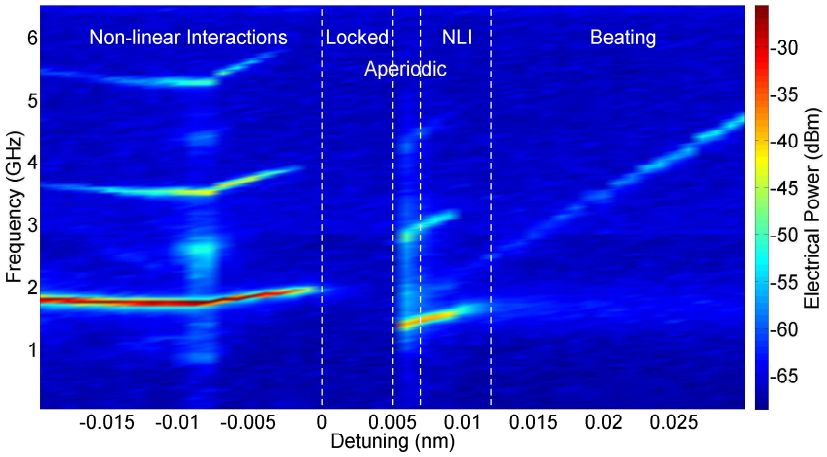

(a) Injected TLS power at 0 dBm.

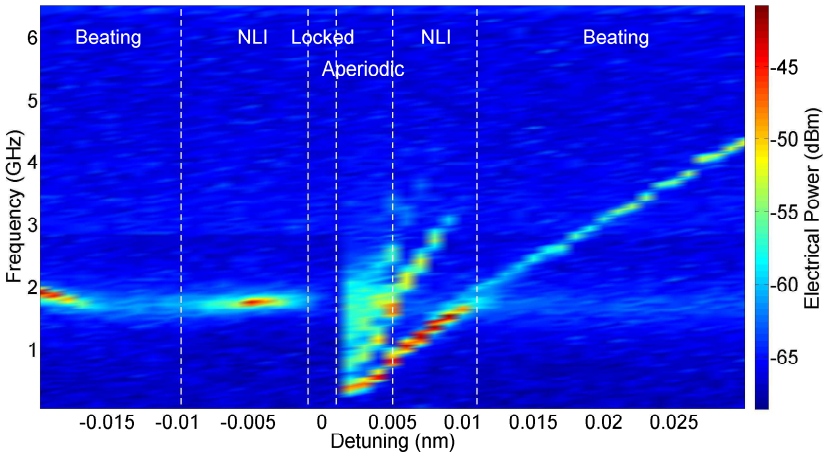

(b) Injected TLS power at -7 dBm.

Figure 3.6: ESA traces from the FP laser as the TLS wavelength was swept across resonance with the main mode of the FP. The beat note between the two signals is observed and a quiet region close to zero detuning.

The power spectrum of the FP, as the wavelength of the master laser was swept across resonance with the slave, shows more clearly whether or not the FP had undergone op-

tical injection locking in the region of small wavelength detunings between the master and slave lasers. These are shown in Figure 3.6.

Four regions of distinct behaviour are observed in Figure 3.6a: (i) a quiet region close to zero detuning where the FP was shown to be injection locked to the external master laser; (ii) an unlocked region for both large negative and positive detuning where the ESA displayed a beat note corresponding to the frequency difference between the lasers; (iii) a region of non-linear interaction (NLI) between the lasers at small detunings; and (iv) a region of aperiodic dynamics close to the positive detuning boundary (i.e. higher external master laser wavelength). Similar regions are observed in Figure 3.6b for the lower master laser injected power, but the quiet region close to zero detuning is much smaller and a narrower stable injection locking region is present. Suppression of the lasing modes of the FP is observed at the same wavelength detunings in the optical spectra in Figure 3.5.

The experiment was repeated for TLS powers between 0 and -20 dBm. The locking width and SMSR are plotted in Figure 3.7 as a function of TLS power. Injection locking was not obtained for TLS powers less than -16 dBm, even though some suppression of the FP side modes was obtained at lower TLS powers. The SMSR decreases linearly with injected power to -16 dBm where it then drops dramatically as expected since injection locking was not achieved. However, the SMSR increases again for a TLS power of -18 dBm. The lensed fibre may have begun to drift at this point in the experiment, therefore the injected power may not be accurate. The locking width also decreases with TLS power.

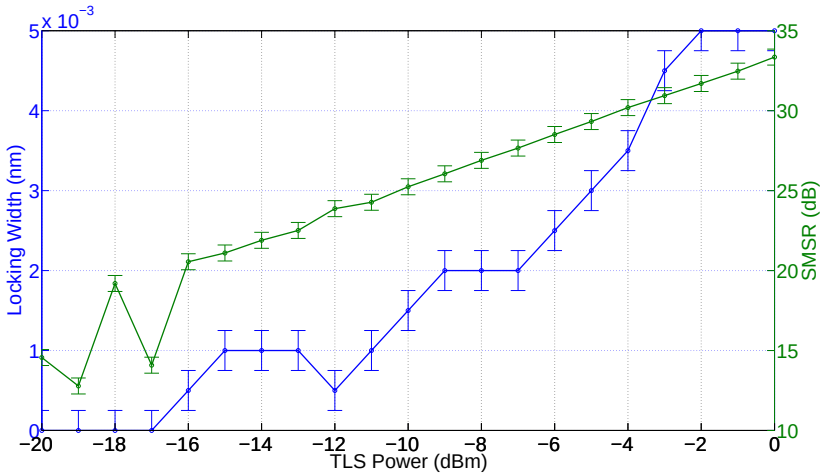

Figure 3.7: The locking width and SMSR obtained while injection locking the FP laser to the TLS, as a function of the TLS power.

Figure 3.8 is a summary of each of the four types of behaviour as a function of detuning and TLS power. As the TLS power decreases a smaller negative detuning is required before the lasers begin to interact non-linearly. For TLS powers of -15 and -16 dBm a small positive detuning is required for the non-linear interactions to begin. Below

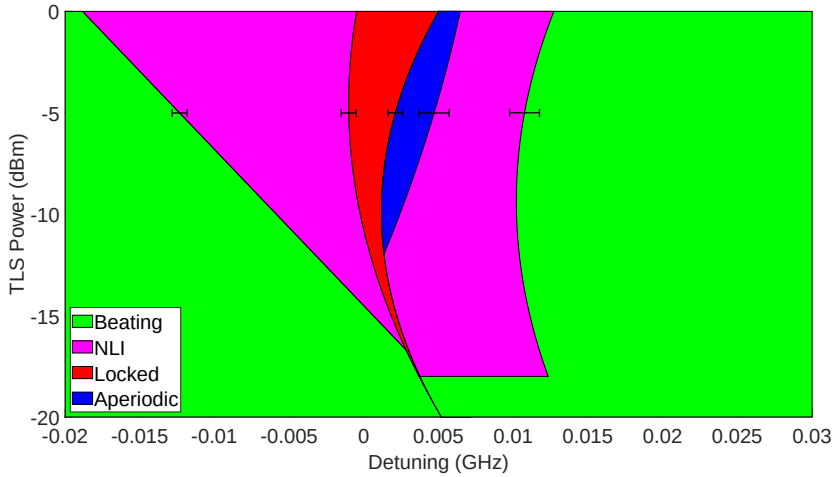

Figure 3.8: Summary of the types of behaviour obtained while injection locking the FP laser to the TLS, as a function of the TLS power. The errors associated with the data fitting is shown on each line.

this no NLI are observed. The narrow region of aperiodic behaviour obtained close to the positive detuning boundary disappears for TLS powers below -12 dBm and there is no NLI observed for TLS powers less than -18 dBm. Injection locking was not obtained for TLS powers less than -16 dBm. The shape of the region of injection locking obtained qualitatively matches that of the well-known bifurcation diagram for semiconductor lasers [35]. The behaviour referred to here (and throughout this thesis) as *Beating* is four wave mixing (FWM). FWM is a non-linear process in which two or more frequencies interact to create one or two more frequencies. The behaviour referred to as *Non-Linear Interactions* is made up of non-linear period 1 and period 2 oscillations. Period 1 oscillations occur when the slave's limit cycle is no longer at a stationary point and an extra oscillation frequency is added to the slave laser's field and phase [73]. As the detuning continues to grow, the period 1 oscillations undergo period doubling, becoming period 2 oscillations. An in-depth study of the complex non-linear behaviour of a semiconductor laser with optical injection can be found in [73].

3.2.2 Injection Locking by Sweeping FP Bias

Varying the bias of the FP tuned the output wavelength of the laser. Therefore, optical injection locking of the FP to the master laser (the TLS) could also be obtained by keeping the wavelength of the TLS constant and sweeping the bias of the FP and hence its wavelength. The TLS wavelength was set close to that of the main mode of the FP and the FP bias was swept from 64 mA to 68 mA. The TLS power was fixed at 0 dBm. The resulting optical and electrical spectra of the FP are shown in Figure 3.9.

Suppression of the side modes of the FP was obtained between 64.75 mA and 66.5 mA. As expected, similar behaviour to that in Figure 3.6 is observed, with a quiet region occurring between 64.75 mA and 65.25 mA where the FP was injection locked to the

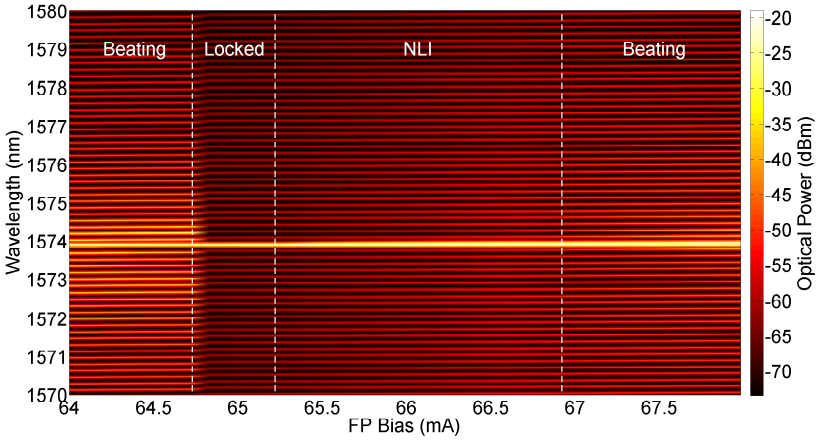

(a) Optical spectra.

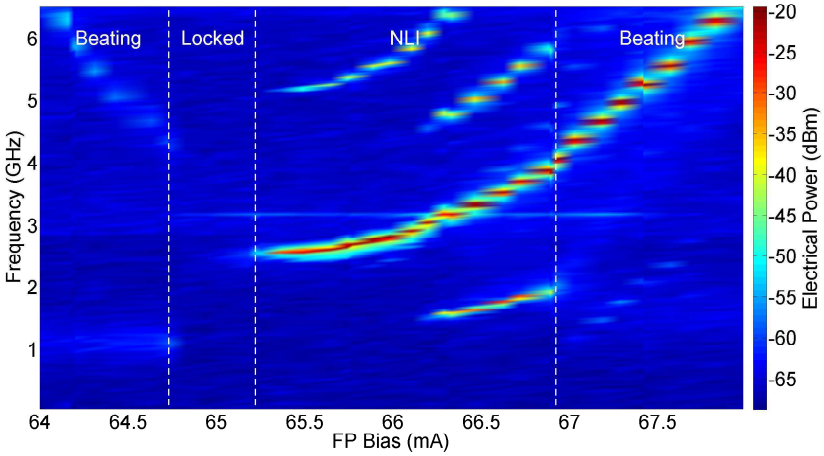

(b) Electrical spectra.

Figure 3.9: OSA and ESA traces from the FP laser as the TLS wavelength was kept fixed while the bias of the FP was swept. The beat note between the two signals is observed and a quiet region around 65 mA where the side modes of the FP are suppressed.

TLS. Beating between the various modes of the FP and the TLS can be clearly seen for positive detunings.

This section discussed the characterisation of a FP laser. Injection locking of the FP laser to an external TLS was demonstrated using two different methods. In the first method, the bias, and hence the wavelength, of the FP was fixed and the wavelength of the TLS was swept across resonance with the chosen mode of the FP to obtain injection locking. In the second method, the wavelength of the TLS was set close to the chosen mode of the FP and the bias, and hence the wavelength, of the FP was swept to obtain injection locking. FP lasers are not suitable for integration since their operation depends on the feedback from both cleaved facets and they are not single mode. The aim of this work is to investigate integrated single mode lasers, therefore it was necessary to move to a slotted Fabry Pérot laser (SFP). In the single facet slotted Fabry Pérot (SF-SFP) laser, one of the cleaved facets in the FP laser is replaced by a slotted mirror, making it

suitable for integration. Therefore, a single facet slotted Fabry Pérot (SF-SFP) laser was next examined and is discussed in detail in the next section. A schematic of a SF-SFP is shown in Figure 3.10.

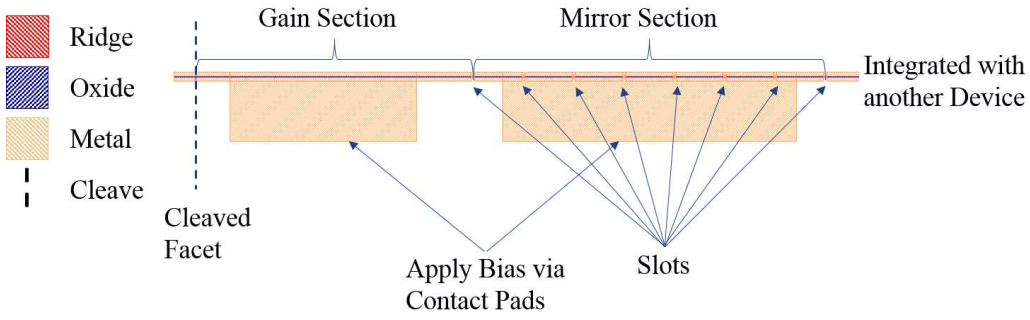

Figure 3.10: Schematic of a SF-SFP showing mirror and gain sections.

The SF-SFP operation depends on feedback from the cleaved facet of the device and a series of equally spaced slots which form a mirror section. Figure 3.11 shows a schematic and a SEM image of a T-bar slot. If the device was also cleaved after the slotted section, (to test the laser independent from other devices) an extra cavity may have been formed which would affect the laser performance. Therefore, it was necessary to characterise the SF-SFP laser while integrated with an unbiased or reverse biased MMI (Multimode Interference Coupler) and/or SOA (Semiconductor Optical Amplifier) or VOA (Variable Optical Attenuator/Amplifier). The device was tested using the experimental setup described previously.

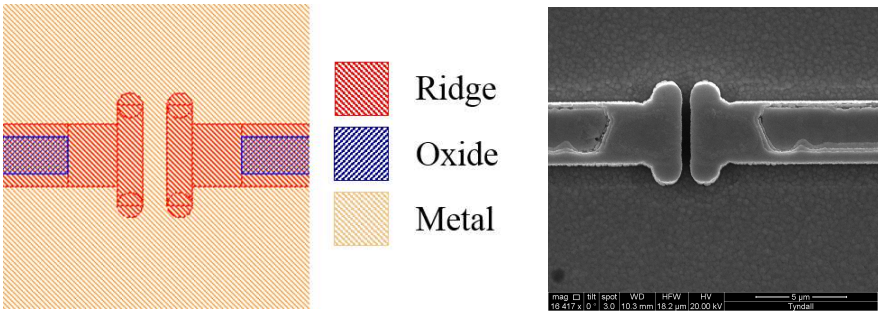

(a) (b)

Figure 3.11: (a) Schematic and (b) SEM image of a T-bar slot.

3.3 Slotted Fabry-Pérot Laser Characterisation

The laser while under test can be seen in Figure 3.12. The gain and mirror sections of the SFP were biased independently using probes positioned on the large contact pads, as seen in Figure 3.12. Lensed fibre was brought towards the cleaved facet of the laser from the left, where it allowed the light from the laser to be fibre coupled and examined on a PM or OSA.

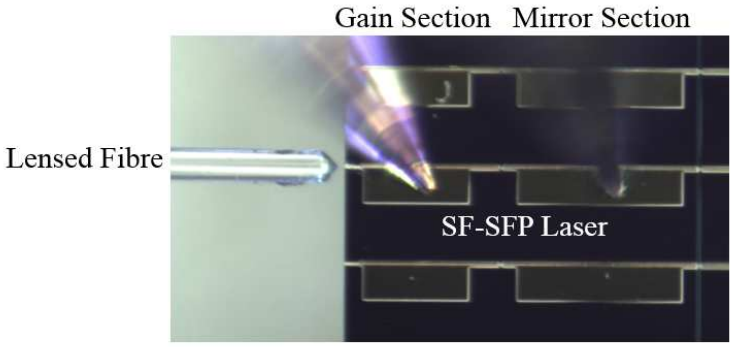

Figure 3.12: Fabricated single facet slotted Fabry Pérot laser under test. Probes are in contact with metal contact pads to apply bias across the mirror and gain sections of the laser. A lensed fibre is also shown where it is positioned close to the waveguide facet to collect the output light.

Probing the gain and mirror sections of the SFP independently allowed various operating currents to be examined. LabView code was written to perform standard characterisation of the SFP lasers. Voltage-Current (VI) curves for the SFP laser were generated as the current in the gain section was stepped from 0 mA to 100 mA, with the mirror section biased from 5 mA to 50 mA. These VI curves are shown in Figure 3.13. Typical behaviour is observed with a turn on voltage of ∼0.85 V seen.

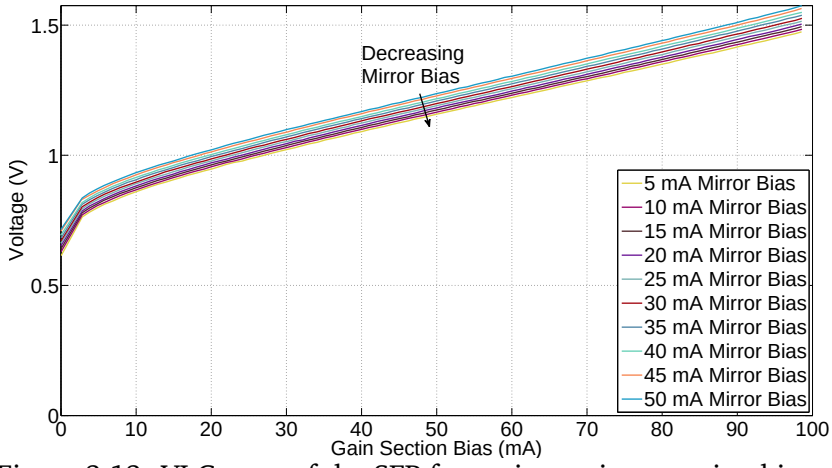

Figure 3.13: VI Curves of the SFP for various mirror section biases.

For the same current sweeps of the mirror and gain sections of the SFP laser, the optical power output versus current was examined. Figure 3.14 shows the LI curves of the

laser. The LI curves allow the role of the mirror section bias on the lasing threshold, I_{th}, to be determined. Higher mirror section currents provide extra gain resulting in a decrease in the gain section current required for lasing. For a mirror bias of 5 mA, I_{th} was found to be ∼65 mA whereas for a mirror bias of 50 mA, lasing began at ∼30 mA.

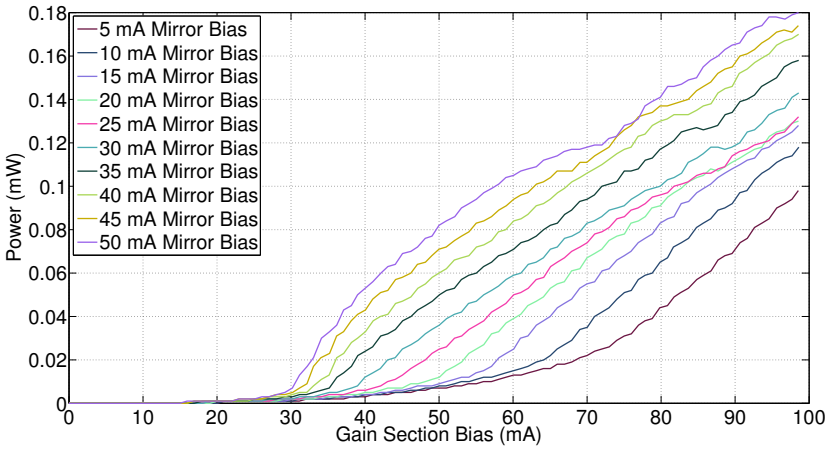

Figure 3.14: LI Curves of the SFP for various mirror section biases.

A typical optical spectrum from the SFP laser with a mirror section bias of 40 mA and a gain section bias of 50 mA is shown in Figure 3.15.

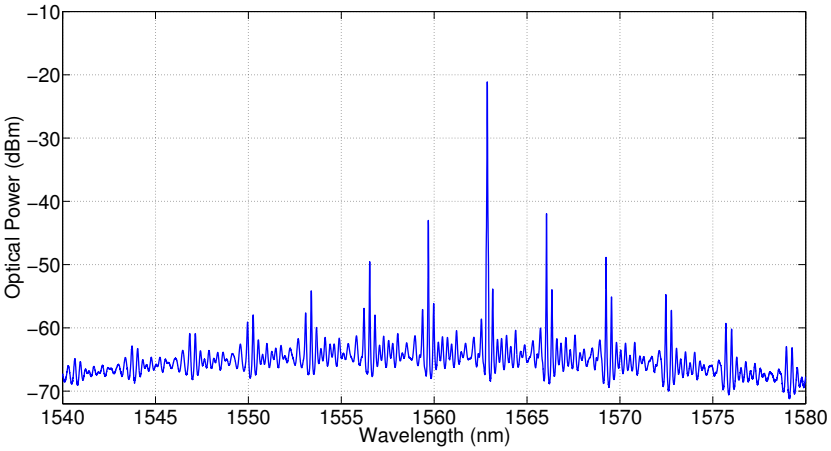

Figure 3.15: Free-running optical spectrum of the SFP laser.

The main lasing mode of the laser occurs at 1562.86 nm, with a side mode suppression ratio (SMSR) of > 20 dB. The wavelength separation between the super modes of the SFP spectrum, $\Delta\lambda$, was found to be 3.14 nm. This wavelength separation can be related to a physical cavity length, L, by Equation (3.1). Taking the group index to be approximately 3.5, a wavelength separation of 3.14 nm can be related to a physical cavity length of 111.53 μm, which matches the interslot distance of the slotted mirror section which defines its transmission spectrum. (The designed interslot distance of this laser was 108 μm.) The average spacing between the FP modes of the spectrum was calculated to be 0.301 nm, which corresponds to a physical length of 1163.52 μm, representing the effective cavity length of the SFP laser, which was formed between the

gain section cleaved facet and the effective mirror penetration depth.

3.3.1 Tuning Maps of SFP Lasers

For a fixed mirror section bias of 40 mA, the gain section current was swept from 0 mA to 100 mA while recording the optical spectra on an OSA. The resulting plots were concatenated in Matlab to investigate how the spectrum varied with gain section bias. Figure 3.16 shows a tuning map for the laser. For low gain section biases, < 30 mA, the SFP was still below its threshold current and no signal was recorded on the OSA. Once the gain section bias was increased above 30 mA, the SFP started to lase and distinct lasing modes were observed on the OSA. The spectrum has one dominant lasing mode, which varied in wavelength as the bias current was increased. Between 32 mA and 65 mA, the wavelength remained at 1563 nm with some tuning observed. For biases outside of this range, the main lasing mode of the laser was seen to hop quickly between different wavelengths with no large stable region obtained.

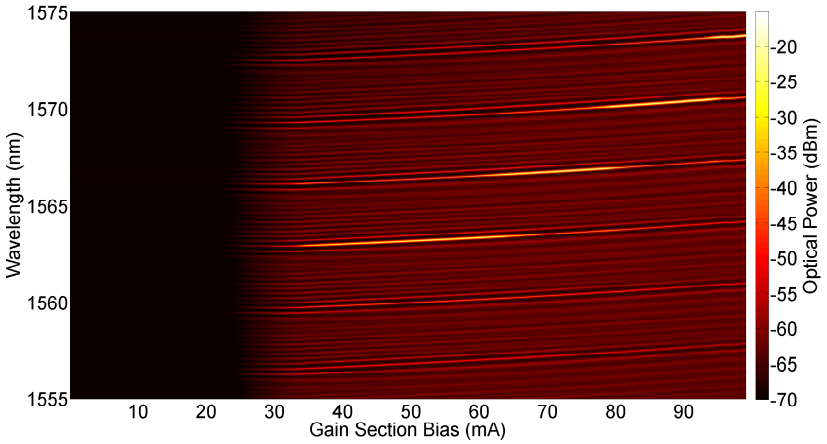

Figure 3.16: Variation of SFP optical spectra with the mirror section bias fixed at 40 mA while the gain section current was swept from 0 mA to 100 mA.

The SFP spectrum for gain section biases between 30 mA and 65 mA is shown in Figure 3.17, where the tuning of the lasing mode near 1563 mA can be seen. The wavelength of the mode varies from 1562.95 nm to 1563.50 nm within this range, which results in a wavelength shift of 0.018 nm/mA of the laser.

The optical spectra of the SFP were recorded on the OSA as the mirror and gain section biases were varied from 20 to 60 mA and 20 to 120 mA, respectively. The SMSR of the main lasing mode to the next highest mode was determined from this data. The SMSR indicated the degree of the single mode nature of the laser output. A high SMSR means highly single mode. The variation of the SMSR across this range is shown in Figure 3.18.

At mirror/gain section biases of 20 mA/100 mA, 35 mA/120 mA and 60 mA/70 mA the SFP operated with a large SMSR, indicating good single mode performance. At

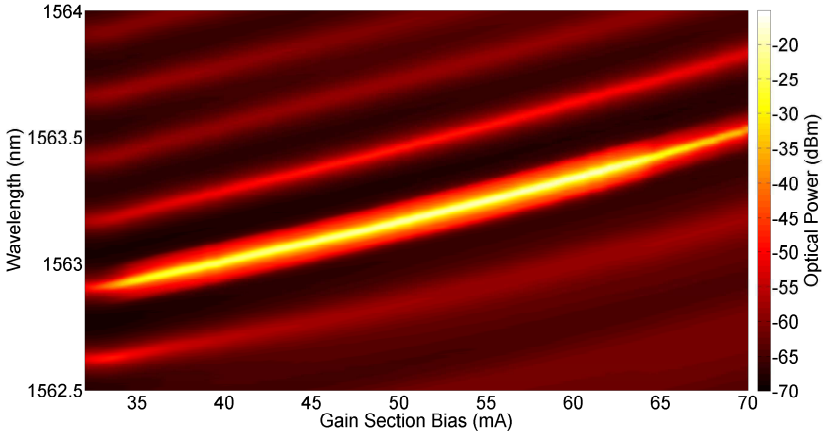

Figure 3.17: Close up view of SFP spectral output with the gain section bias swept between 32 mA to 65 mA. The output was found to be tunable over this range.

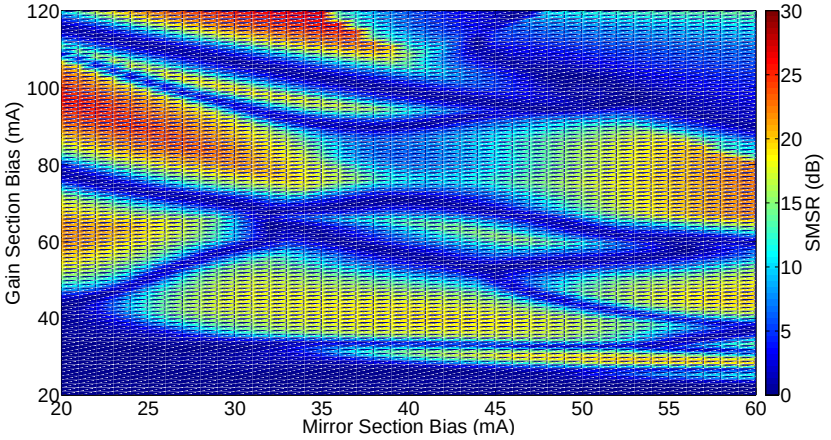

Figure 3.18: SMSR of the SFP optical spectra as a function of the mirror and gain section biases.

mirror/gain section biases of 40 mA/70 mA and 60 mA/110 mA the SMSR was very low. Therefore, at these biases the output of the SFP is multimode.

The preferential lasing mode of the SFP was also extracted from these spectra. Figure 3.19a shows the variation of the lasing wavelength versus gain section bias, where the z-axis (or colour) represents the peak wavelength of the optical output of the SFP laser.

As the total current applied to the SFP increased, the output was shifted to longer wavelengths. At mirror/gain section biases of 35 mA/35 mA the main lasing mode was at 1559.3 nm whereas, at 60 mA/120 mA the main lasing mode was at 1576.6 nm. Abrupt shifts in the wavelength can be seen. Comparing Figure 3.19a with Figure 3.18, shows that these shifts coincide to regions of very low SMSR. Therefore, at these biases the SFP operated multimodally. In the areas of high SMSR seen in Figure 3.18, and hence highly single mode operation, the wavelength of the main lasing mode did not have any rapid changes. In these regions, tuning effects similar to those shown in Figure 3.17 were observed.

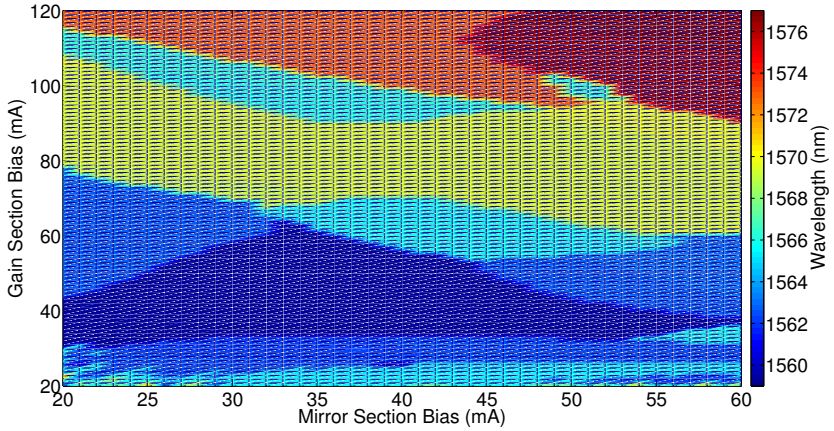

(a) Peak wavelength of the SFP optical spectra as a function of the mirror and gain section biases.

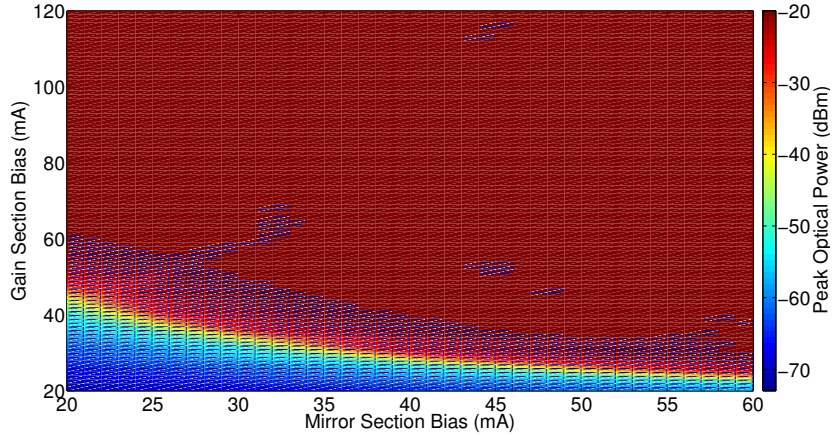

(b) Peak power of the SFP optical spectra as a function of the mirror and gain section biases.

Figure 3.19: Wavelength and power of the main mode in the SFP optical spectra as a function of the mirror and gain section biases.

Figure 3.19b shows the power of the preferential lasing mode of the SFP. As the total current applied to the SFP increased, the power of the main mode increased. At mirror/gain section biases of 35 mA/35 mA the power of the main lasing mode was -25.4 dBm whereas, at 60 mA/120 mA the power of the main lasing mode was -16.1 dBm. The power is low due to the loss introduced by coupling to a lensed fibre.

The same data was further analysed and the relationship between the highest order lasing modes of the laser was investigated. At each bias, the modes of the laser were sorted in descending order. The number of modes within 10 dB of the peak mode and greater than 10 dB from the noise floor were extracted. This determined the number of *main* lasing modes at each bias. The results of this analysis are shown in Figure 3.20, where the modal behaviour of the SFP was examined up to a cut off of three main lasing modes.

The number of modes at each bias which satisfy the 10 dB cut off condition are given on the z-axis of the plot. A modal behaviour of zero (shown in light blue) indicated

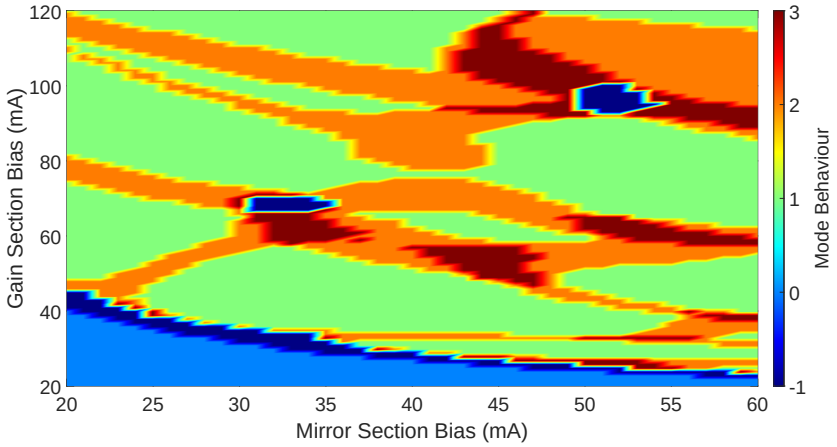

Figure 3.20: Modal behaviour of the SFP optical spectra as a function of the mirror and gain section biases. The z-axis represents the multimode nature of the waveguide at particular biases.

that the optical spectra from the SFP had low power peaks, which was expected for biases around threshold. A negative modal behaviour (shown in dark blue) indicated a breakdown of the 10 dB cut off condition and the spectra contained greater than three main lasing modes within 10 dB of each other. The regions where the output of the SFP was single mode (shown in green) are clearly seen in Figure 3.20 at mirror/gain section biases of 20 mA/100 mA, 35 mA/120 mA and 60 mA/70 mA. At these biases the SFP operated with a large SMSR, indicating good single mode performance. This agrees with the result shown in Figure 3.18, where the laser output had a large SMSR at these biases. At mirror/gain section biases of 40 mA/70 mA and 60 mA/110 mA the output spectra of the SFP is dual multimode. Figure 3.21 shows the output spectra of the SFP at mirror and gain section biases of 40 mA and 70 mA, respectively, where two modes of almost equal power are seen.

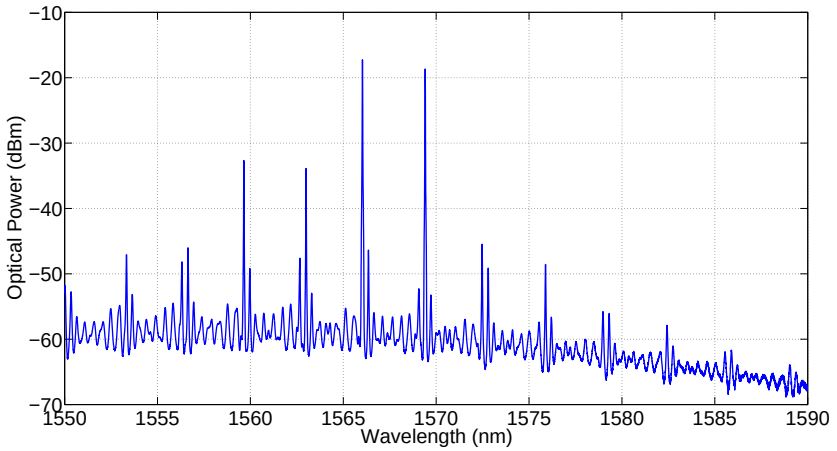

Figure 3.21: Multimode output of the SFP at mirror and gain section biases of 40 mA and 70 mA, respectively.

The same data was used to examine the change in wavelength and power of each mode in the laser output as the bias varied. At each bias, the wavelength and power of each

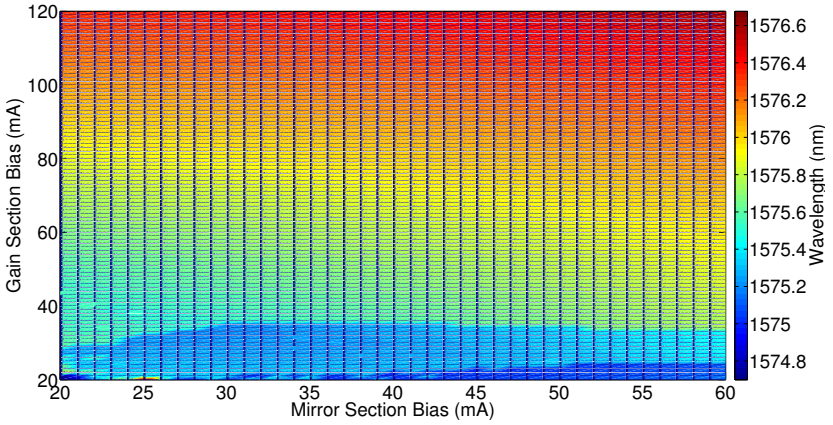

(a) The wavelength of one of the modes in the laser output as a function of the mirror and gain section biases.

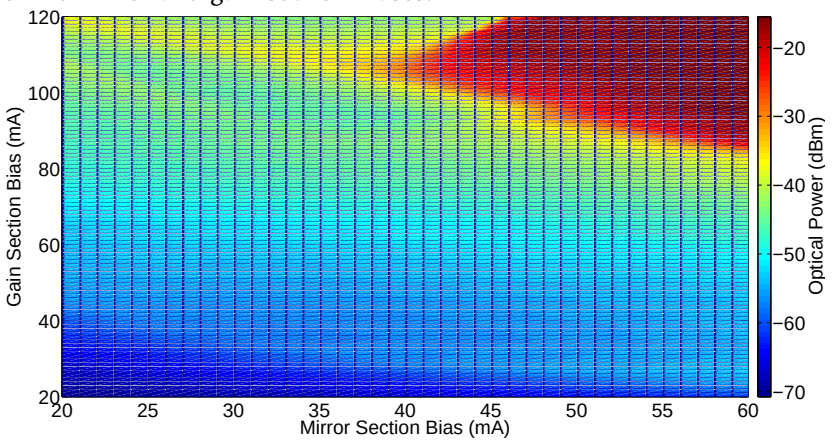

(b) The power of this mode as a function of the mirror and gain section biases.

Figure 3.22: Tracking the wavelength and power of one of the modes in the laser output with the mirror and gain section biases. The sudden increase in power at the top right indicates that at these biases this mode was the main lasing mode of the laser.

mode in the optical spectrum was extracted. As the total current applied to the SFP increased, the wavelength of each mode was shifted to longer wavelengths. Figure 3.22a shows how the wavelength of one of the modes varied with bias. At mirror/gain section biases of 25 mA/35 mA the wavelength of this mode was 1575.528 nm whereas, at 60 mA/120 mA the wavelength was 1576.564 nm. Figure 3.22b shows how the power of the mode varied with bias. At mirror/gain section biases of 25 mA/35 mA the power of this mode was -60.3 dBm whereas, at 60 mA/120 mA the power was -16.1 dBm. The sudden increase in power at the top right of Figure 3.22b indicated that at these biases this mode was the main lasing mode in the output spectra of the SFP.

The output of the SFP laser was coupled into a lensed fibre and the optical power was measured using an optical power meter as the bias varied. Figure 3.23 shows the results. The measured power depended on how accurately the lensed fibre was

coupled. Therefore, very little of the emitted light was coupled into the fibre, hence the power output measured on the PM was much less than the actual power output of the laser. As expected, the output power of the laser increased with bias current. At mirror/gain section biases of 25 mA/35 mA the output power of this laser was -24.5 dBm whereas, at 60 mA/120 mA the power was -0.7 dBm.

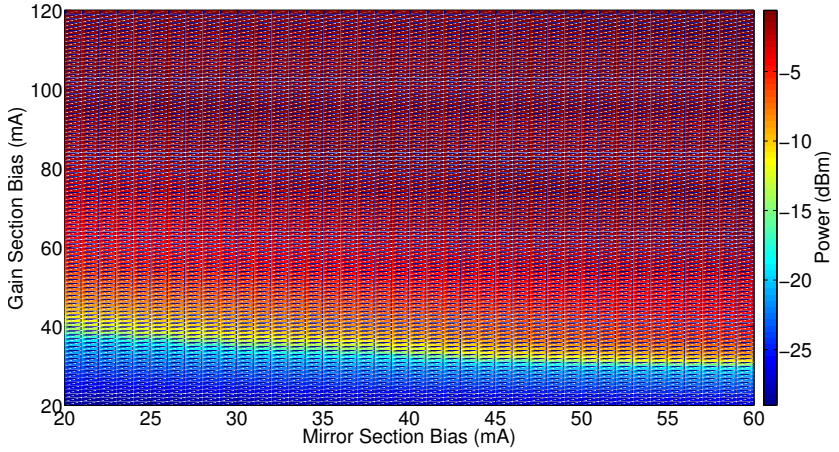

Figure 3.23: Optical power output of the SFP laser as a function of the mirror and gain section biases coupled into a lensed fibre and measured using an optical power meter.

A reverse bias of -2 V was applied to the SOA section next to the SFP laser and the photocurrent generated by the light being emitted from the SFP was recorded as the bias current varied. It was assumed that each measured electron equalled one photon emitted by the laser. The photocurrent was converted to optical power using the following equation;

$$Power(dBm) = 10\log_{10}\frac{h\,c\,I_{ph}(mA)}{e\,\lambda} \tag{3.2}$$

where I_{ph} is the photocurrent, h is Planck's constant, c is the speed of light and e is the electron charge. The results can be seen in Figure 3.24. While this is still only an approximation of the power output of the laser, it is much more accurate than the previous measurement. More light will also be transmitted to the SOA section, since the reflection of the slotted mirror is much less than the cleaved facet, causing some asymmetry in the power measurements. As expected the output power of the laser increased with bias. At mirror/gain section biases of 25 mA/35 mA the output power of this laser was 2.0 dBm whereas, at 60 mA/120 mA the power was 8.4 dBm.

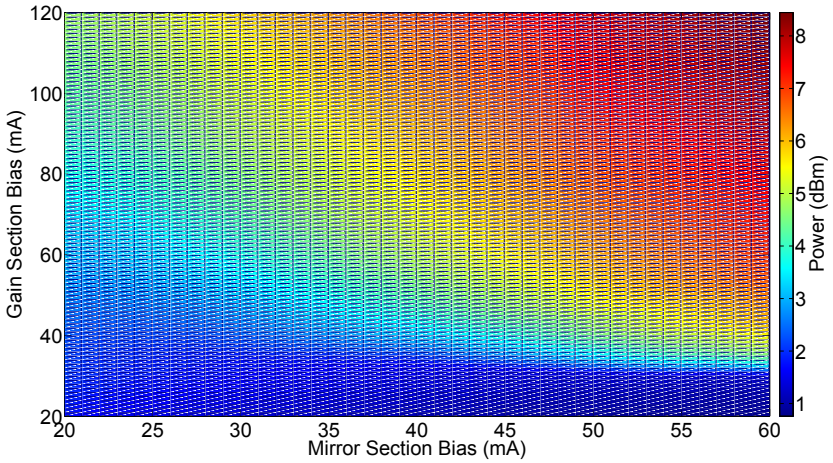

Figure 3.24: Total optical power output of the SFP laser as a function of mirror and gain section biases obtained by measuring the photocurrent generated by the light being emitted from the SFP.

3.3.2 Relaxation Oscillations

When a laser is subjected to changes in its bias, it exhibits damped oscillations known as *relaxation oscillations* (ROs). ROs are a result of the interaction between injected carriers and emitted photons of the laser. The frequency of the oscillations is largely dependent on the output power of the laser [74]. ROs for the SFP under test were investigated by analysing the SFP output on an ESA. The electrical spectrum of the SFP was recorded as the bias across the gain section of the SFP was swept from 0 mA to 100 mA. The results are shown in Figure 3.25.

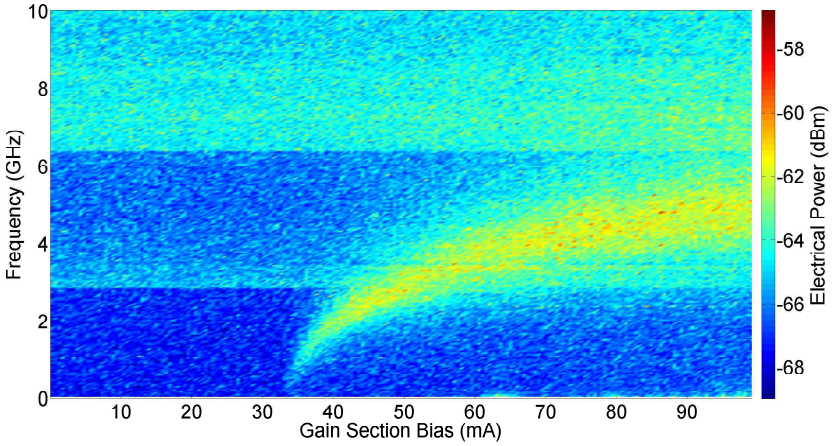

Figure 3.25: Power spectrum of SFP laser output as the gain section bias was varied with the mirror section bias held fixed at 40 mA. Relaxation oscillations are observed.

The ROs of the laser can be seen with increasing bias. The ROs start to appear at the threshold current of this particular laser, which was 30 mA. As the bias was increased, the ROs approached a peak value of $\sim$6 GHz.

This section described the characterisation of a SFP laser. The SFP played a key role

in the Photonic Integrated Circuits (PICs) analysed as part of this thesis work. The SFP was optically examined under various bias conditions across the mirror and gain sections while its optical and electrical spectra were recorded. From these, the optical characteristics and the RO's of the SFP were examined in detail. It was ensured that tuning regions existed where the laser had single mode operation. The power output of the laser as a function of bias was also analysed.

3.4 Injection Locking of SFP Laser to a Tuneable Laser Source

The next step was to investigate the viability of stable optical injection locking of SFP lasers by examining the optical injection locking of a SFP laser to the TLS. A High Speed Oscilloscope (HSO) was added to the setup used to investigate injection locking between a FP laser and the TLS (see Figure. 3.4) for this experiment, in order to investigate the time traces of the light output of the SFP.

Based on the results from the previous section, the SFP mirror and gain sections were biased at 40 mA and 50 mA, respectively, so that the SFP operated in a single mode. The TLS wavelength was set close to that of one of the side modes of the SFP laser and injected into the SFP cavity via the ciculator. A side mode was chosen rather than the main lasing mode so that the suppression of the modes could be clearly seen. Figure 3.26 shows the output from port 3 of the circulator where the detuned TLS signal can clearly be seen on the OSA trace.

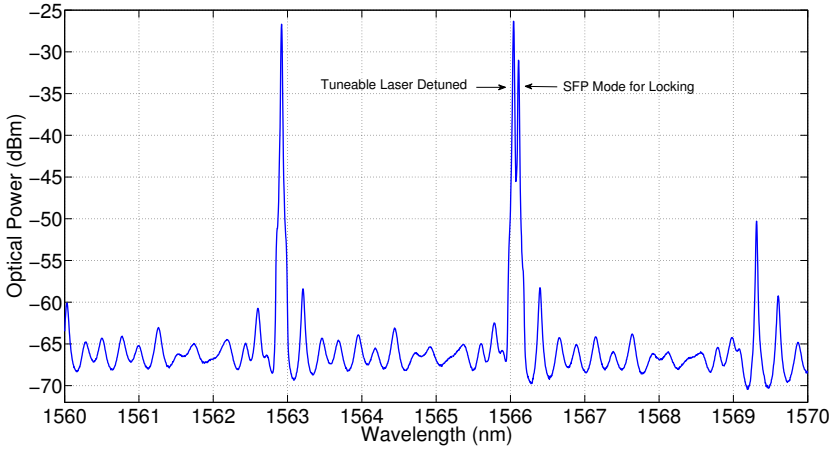

Figure 3.26: Spectral output of the SFP with injected signal from the TLS. The mode chosen to be injected to is at 1566.1 nm where the detuned TLS input can also be seen.

The chosen free-running mode of the SFP laser is clearly seen at ∼1566.1 nm, with the TLS peak occurring at a slightly shorter wavelength. The power of the TLS was set to -3 dBm and its wavelength was then swept across resonance with the chosen mode of the SFP while OSA, ESA and HSO traces were recorded at each swept wavelength. The experiment was then repeated with the TLS power decreased to -6 dBm. Figure 3.27

shows colour intensity plots of the optical spectrum of the SFP as the wavelength of the master laser was detuned across the SFP for each of the master laser powers chosen.

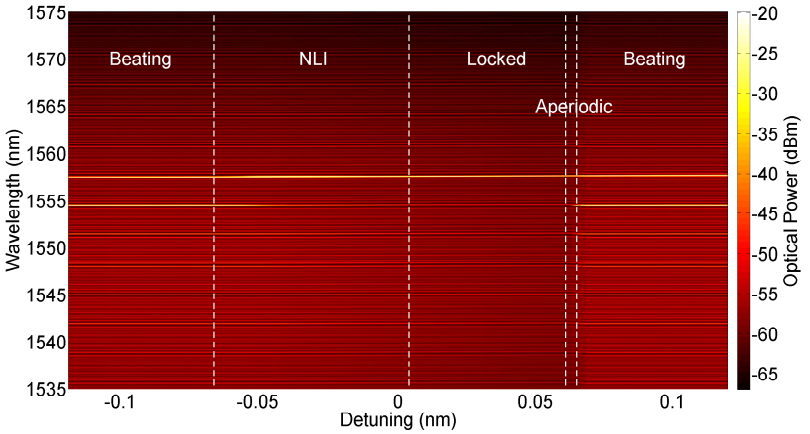

(a) Injected TLS power at -3 dBm.

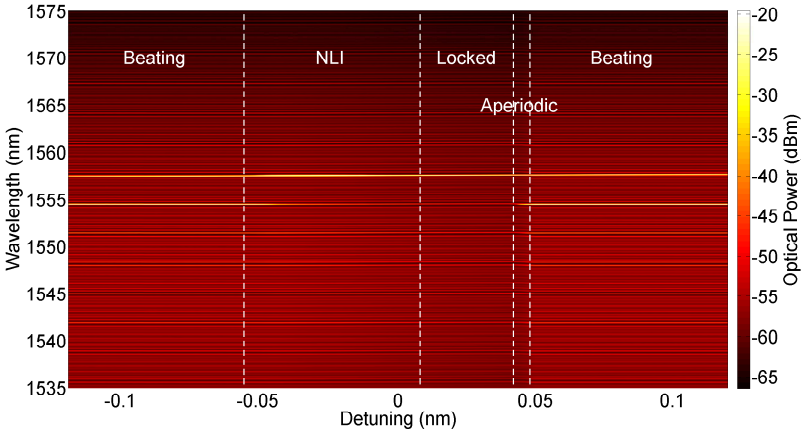

(b) Injected TLS power at -6 dBm.

Figure 3.27: OSA traces from the SFP laser as the TLS wavelength was swept across resonance with a chosen mode of the SFP. Two different TLS powers are shown where the effect of higher injected power can be seen. For close to zero detuning in both cases, significant suppression of the side modes of the SFP was observed and the SFP lased strongly at the injected wavelength.

As when injection locking was obtained between the TLS and the FP, as the detuning between the master and slave laser becomes smaller, suppression of the modes occurs and the SFP laser operates with a single lasing mode at the injected master laser wavelength of 1557.5 nm. Figure 3.27 clearly shows that the width of the region where the suppression of the main lasing mode occurs, increases with higher injected powers. The detuning can extend to almost 0.06 nm before the output returns to that of a free running SFP, for an injected power of -3 dBm (Figure 3.27a), whereas for an injected power of -6 dBm (Figure 3.27b) the detuning only extends to $\sim$0.03 nm.

The power spectra of the SFP are shown in Figure 3.28. The four regions of distinct behaviour observed for the FP laser in Figure 3.6 are also seen in Figure 3.28a for the SFP: (i) a quiet region close to zero detuning where the SFP was shown to be injection

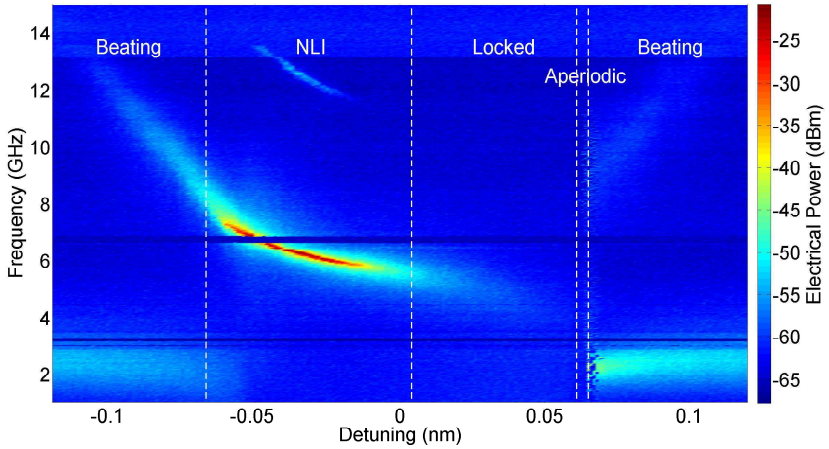

(a) Injected TLS power at -3 dBm.

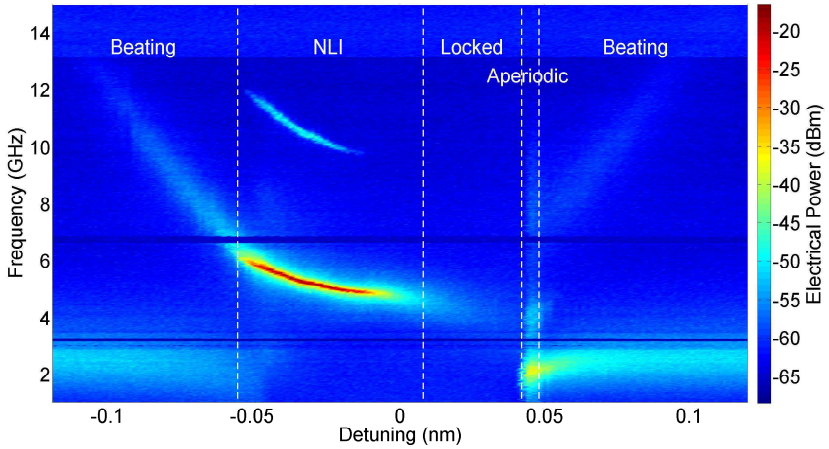

(b) Injected TLS power at -6 dBm.

Figure 3.28: ESA traces from the SFP laser as the TLS wavelength was swept across resonance with a chosen mode of the SFP. The beat note between the two signals is observed and a quiet region close to zero detuning.

locked to the external master laser; (ii) an unlocked region for both large negative and positive detuning where the ESA displayed a beat note corresponding to the frequency difference between the lasers; (iii) a region of non-linear interaction (NLI) between the lasers at small negative detuning; and (iv) a region of aperiodic behaviour close to the positive detuning boundary (i.e. higher external master laser wavelength). Similar regions are observed in Figure 3.28b for the lower master laser injected power, but the quiet region close to zero detuning is much smaller and a narrower stable injection locking region is present. Suppression of the lasing modes of the SFP is observed at the same wavelength detunings in the optical spectra in Figure 3.27.

Figure 3.29 shows colour intensity plots of the HSO traces. Four regions of distinct behaviour are also observed in Figure 3.29a: (i) a low voltage region close to zero detuning where the SFP is shown to be injection locked to the external master laser; (ii) an unlocked region for both large negative and positive detuning where the HSO displays a noisy signal; (iii) a region of non-linear interaction (NLI) between the lasers at small

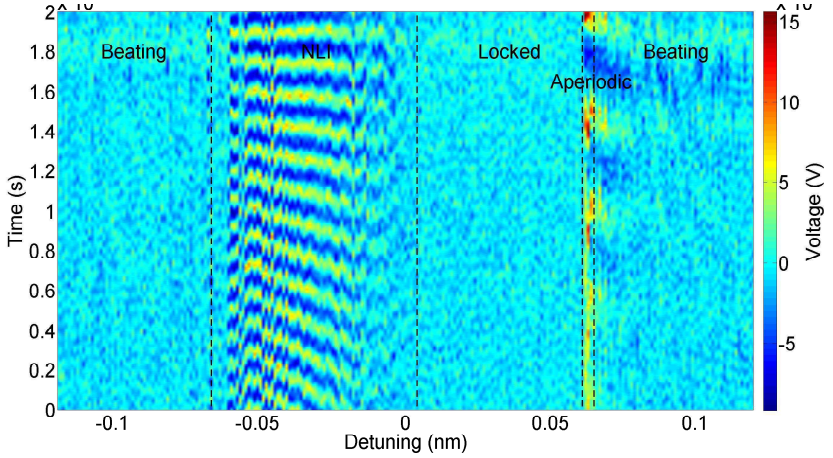

(a) Injected TLS power at -3 dBm.

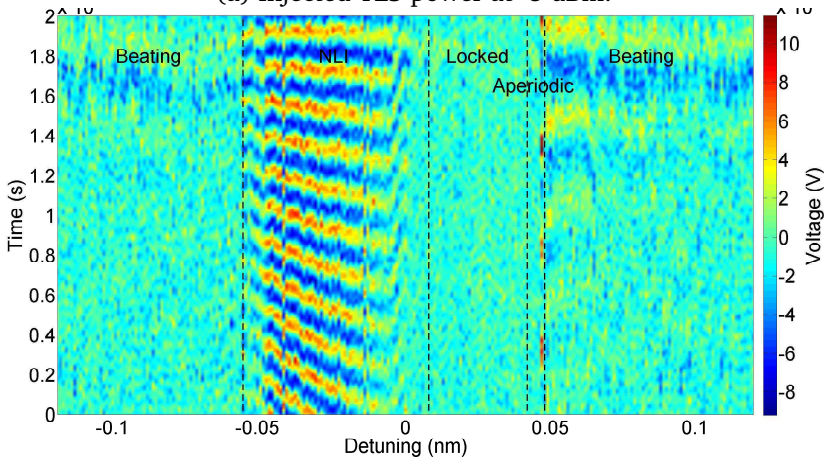

(b) Injected TLS power at -6 dBm.

Figure 3.29: HSO traces from the SFP laser as the TLS wavelength was swept across resonance with a chosen mode of the SFP. The beating between the two signals is observed and a quiet region close to zero detuning.

negative detuning where the HSO displays a sinusoidal voltage which decreases in frequency as the detuning gets closer to zero; and (iv) a region of aperiodic behaviour close to the positive detuning boundary (i.e. higher external master laser wavelength). Similar regions are observed in Figure 3.29b for the lower master laser injected power, but the low voltage region close to zero detuning is much smaller and a narrower injection locking region is present. Suppression of the lasing modes of the SFP in the optical spectra in Figure 3.27 and beat notes in the electrical spectra in Figure 3.28 are observed at the same wavelength detunings.

The Fast Fourier Transform (FFT) of the HSO data shown in Figure 3.29 was performed and the resulting power spectrum data can be seen in Figure 3.30. These colour plots match up well with the colour plots of the ESA data shown in Figure 3.28. The resolution of the FFT is not as high as the resolution of the ESA, therefore the second beat note seen at negative detunings in Figure 3.28 is barely visible in Figure 3.30. However, the four regions of behaviour discussed previously can clearly been observed in

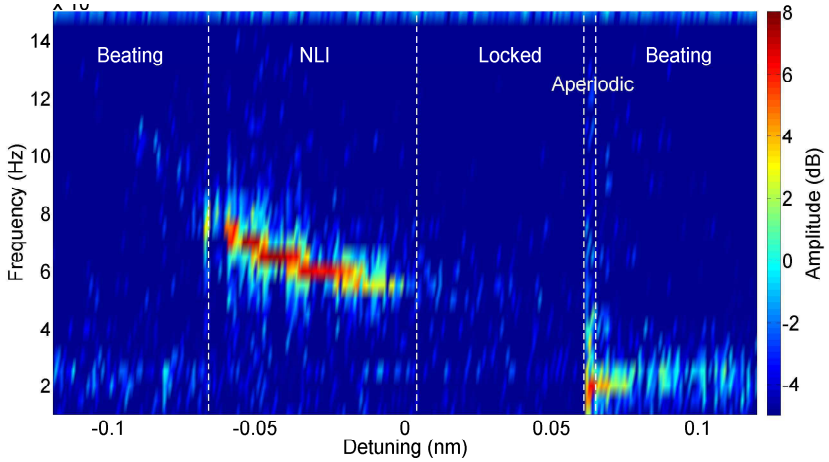

(a) Injected TLS power at -3 dBm.

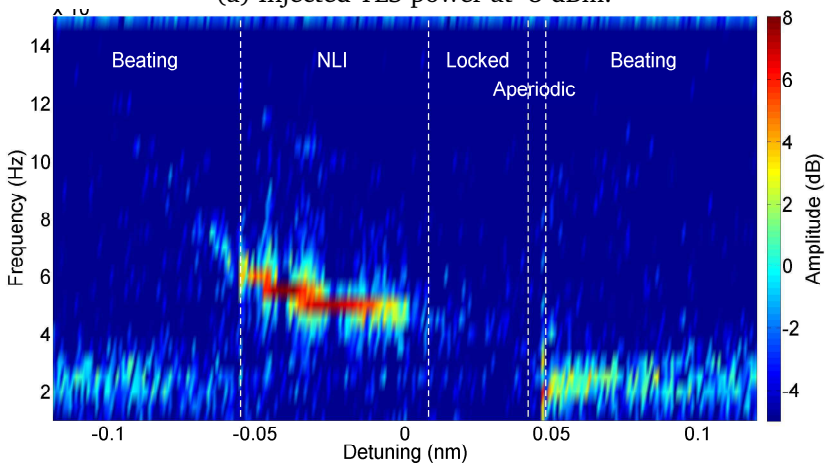

(b) Injected TLS power at -6 dBm.

Figure 3.30: FFT of the HSO traces shown in Figure 3.29. The beat note between the two signals is observed and a quiet region close to zero detuning.

the FFT.

Figure 3.31 shows cross sections of Figures 3.27a, 3.28a and 3.29a, from each of the four behavioural regimes. The main mode of the free-running S-SFP had a wavelength of approximately 1554.5 nm and the side mode chosen for locking was at approximately 1557.5 nm, both shown in red in Figure 3.27a. The optical spectrum of the S-SFP for a detuning of -0.090 nm is shown in Figure 3.31a. The TLS can be seen $\sim$0.090 nm to the left of the S-SFP side mode. A corresponding weak beat note is seen in the electrical spectrum, Figure 3.31b, at $\sim$11 GHz. The time trace shows a noisy signal Figure 3.31c.

As the wavelength of the TLS gets close to that of the S-SFP the lasers begin to interact non-linearly and the main mode of the SFP begins to be suppressed while the side mode chosen for locking is amplified, Figure 3.31d. The interaction between the lasers creates a strong beat note seen on the ESA, represented in red in Figure 3.28. As the wavelength difference between the lasers decreased the frequency of the beat note also

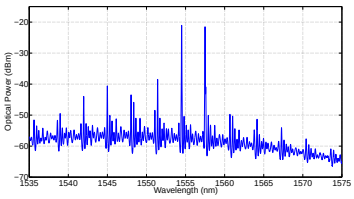

(a) Optical spectrum of the SFP for -0.090 nm detuning.

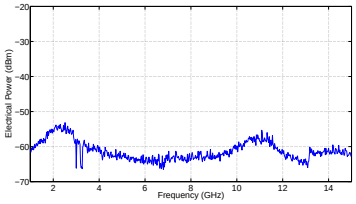

(b) Electrical spectrum of the SFP for -0.090 nm detuning.

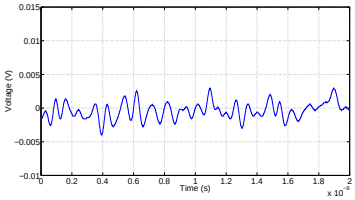

(c) Time trace of the SFP for -0.090 nm detuning.

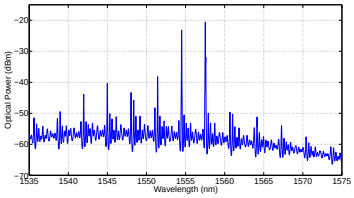

(d) Optical spectrum of the SFP for -0.058 nm detuning.

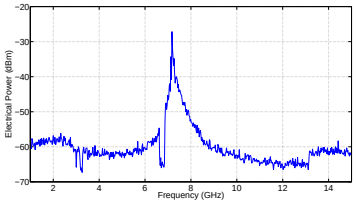

(e) Electrical spectrum of the SFP for -0.058 nm detuning.

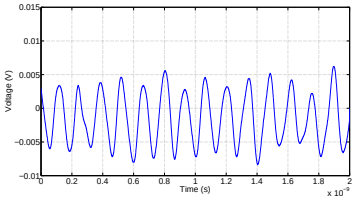

(f) Time trace of the SFP for -0.058 nm detuning.

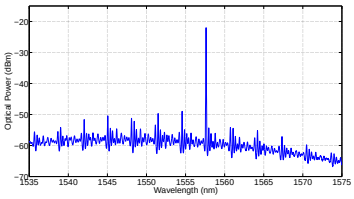

(g) Optical spectrum of the SFP for 0.040 nm detuning.

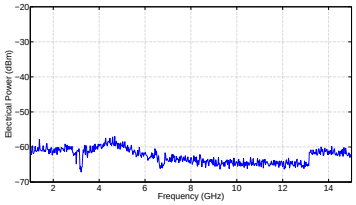

(h) Electrical spectrum of the SFP for 0.040 nm detuning.

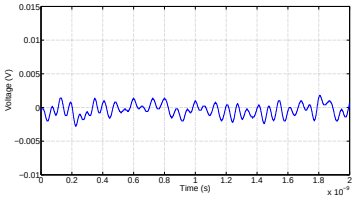

(i) Time trace of the SFP for 0.040 nm detuning.

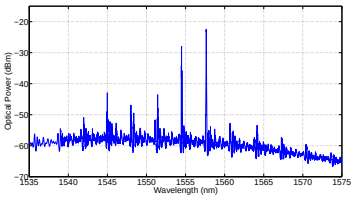

(j) Optical spectrum of the SFP for 0.064 nm detuning.

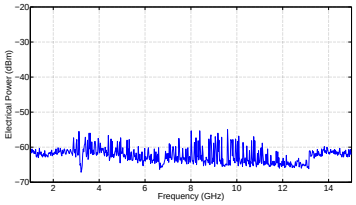

(k) Electrical spectrum of the SFP for 0.064 nm detuning.

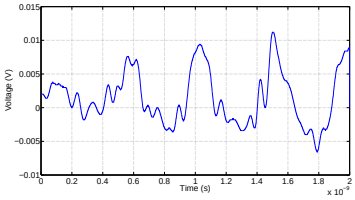

(l) Time trace of the SFP for 0.064 nm detuning.

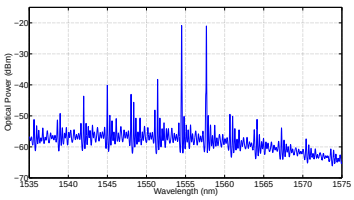

(m) Optical spectrum of the SFP for 0.080 nm detuning.

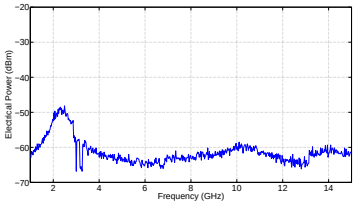

(n) Electrical spectrum of the SFP for 0.080 nm detuning.

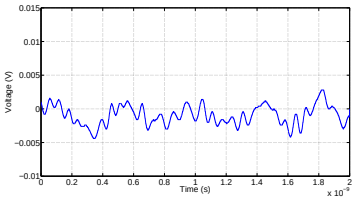

(o) Time trace of the SFP for 0.080 nm detuning.

Figure 3.31: Cross sections of Figures 3.27a, 3.28a and 3.29a, from each of the four behavioural regimes: (i) beating at large negative detunings; (a), (b) and (c) and at large positive detunings; (m), (n) and (o), (ii) NLI at small negative detunings; (d), (e) and (f), (iii) locked at close to zero detuning; (g), (h) and (i), and (iv) aperiodic behaviour close to the positive detuning boundary; (j), (k) and (l).

decreased. This can clearly be seen in Figure 3.28a for master-slave detunings between -0.06 nm and -0.02 nm. The beat note at approximately 2.5 GHz is the relaxation oscillations of the S-SFP. The additional lower amplitude beat notes are harmonics of

the main beat note. Figure 3.31e is a cross section of Figure 3.28a for a detuning of -0.058 nm, showing a strong beat note at approximately 7 GHz. As the lasers beat together a sinusoidal signal was observed on the HSO. The peaks of the signal are represented by red and the troughs by blue in Figure 3.29a. One such trace for a detuning of -0.058 nm is shown in Figure 3.31f, showing a sinusoidal signal with a frequency of $\sim$7 GHz.

When the wavelength of the TLS was close to the wavelength of the S-SFP, the S-SFP locked to the TLS and the S-SFP lased at the injected wavelength of the TLS and all other modes were suppressed. Suppression of the modes of the S-SFP can clearly be seen in Figure 3.27a for detunings between 0.004 nm and 0.06 nm. In Figure 3.31g (detuning = 0.04 nm) the main mode of the S-SFP had been suppressed by more than 25 dB compared to Figure 3.31a and the laser was lasing at the injected wavelength of approximately 1554.5 nm. When injection locked, both lasers lased at the same wavelength therefore there was no beating between them. Hence there was a quiet region visible on the ESA (Figure 3.28a) and HSO (Figure 3.29a) for detunings between 0.004 nm and 0.06 nm. The relaxation oscillations are also suppressed. Figures 3.31h and 3.31i are examples of the quiet region on the ESA and HSO, respectively for a detuning = 0.04 nm. The signals shown in these two graphs represent the noise floor of the equipment used.

When the wavelength of the TLS passed that of the S-SFP there was a narrow region of aperiodic behaviour (detunings between 0.061 nm and 0.065 nm) where the lasers beat together before the S-SFP returned to its free-running state. Figure 3.31j (detuning = 0.064 nm) shows the S-SFP beginning to lase at its free running wavelength of approximately 1557.5 nm again. The TLS can also be seen close the side mode of the S-SFP. At this detuning an aperiodic signal was observed on the HSO, Figure 3.31l, and on the ESA, Figure 3.31k. For detunings larger than 0.065 nm, the SFP has returned to is free-running state, Figure 3.31m for a detuning of 0.08 nm. The TLS can be seen at $\sim$0.08 nm to the right of the side mode of the SFP. A corresponding weak beat note at $\sim$10 GHz is observed in the electrical spectrum, Figure 3.31n and a noisy signal in the time trace, Figure 3.31o.

3.5 Conclusion

This chapter discussed the characterisation of a basic FP laser. The injection locking of the FP laser to an external TLS was demonstrated and four regions of distinct behaviour are observed: (i) a quiet region close to zero detuning where the FP was shown to be injection locked to the external master laser; (ii) an unlocked region for both large negative and positive detuning where the ESA displayed a beat note corresponding to the frequency difference between the lasers; (iii) a region of non-linear interaction

(NLI) between the lasers at small detunings; and (iv) a region of aperiodic dynamics close to the positive detuning boundary (i.e. higher external master laser wavelength).

FP lasers are not suitable for integration since their operation depends on the feedback from both cleaved facets. Their multimode output also makes FP lasers unsuitable for mutual laser interactions where single mode lasers are required. Therefore, the SFP laser, where one of the cleaved facets of the FP laser is replaced by a slotted mirror, was investigated. The optical and electrical characteristics of the SFP were examined in detail under various bias conditions across the mirror and gain sections. The injection locking of the SFP laser to an external TLS was demonstrated and the same four regions of distinct behaviour are observed. Each of these behaviours was discussed and an optical and electrical spectrum and a time trace representing each was presented.

The aim of this thesis work is to investigate integrated lasers in a Photonic Integrated Circuit, therefore the next chapter will discuss injection locking between two identical SFP lasers coupled together through a waveguide interconnect.

Chapter 4

Comparison of Off & On-Chip Injection Locking

After demonstrating that stable injection locking of an SFP laser to an external master laser was achievable, the next step was to examine injection locking between two identical SFP lasers coupled together through a waveguide interconnect. The waveguide interconnect between the lasers was referred to as the variable optical attenuator/amplifier (VOA). Since it was fabricated on an active substrate, it required a positive electrical bias to overcome the loss due to the high absorption of the material at 1550 nm. Left unbiased the VOA was designed to be long enough to attenuate most of any optical signal that passed through it. Applying a reverse bias to the VOA further attenuated the signal. A schematic of the full device, with each variable parameter labelled, is shown in Figure 4.1.

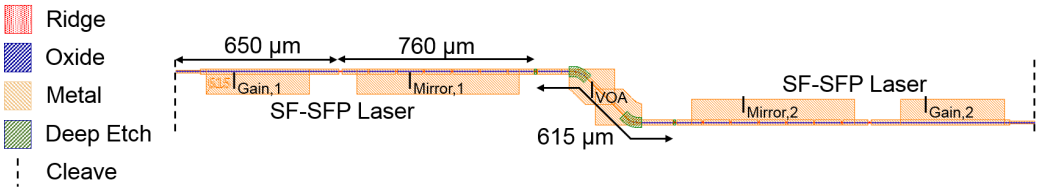

Figure 4.1: Schematic of the PIC with all variable parameters labelled. Two SF-SFP lasers are integrated together through a 615 µm VOA section. Laser 1, referred to as the master laser in this experiment, was tuned by varying the currents $I_{Mirror,1}$ and $I_{Gain,1}$. Laser 2, referred to as the slave laser in this experiment, was tuned by varying the currents $I_{Mirror,2}$ and $I_{Gain,2}$. The VOA section was made absorbing by applying a negative bias or transparent by applying a positive bias.

SFP 1 was controlled by independently biasing the mirror, $I_{Mirror,1}$, and gain, $I_{Gain,1}$, sections of the laser. SFP 2 was similarly controlled by independently biasing its mirror, $I_{Mirror,2}$, and gain, $I_{Gain,2}$, sections. The two SFP lasers were connected via a 615 µm VOA. Forward or reverse biasing this section controlled the amplification or attenuation of the optical signal and hence varied the power coupled between the lasers. This

section acted as a large photodiode when reversed biased, which could be used to measure the power output of each SFP laser on-chip, without the need for external fibre coupling.

The mirror section biases of both SFPs, $I_{Mirror,1}$, and $I_{Mirror,2}$, were set at 42 mA. At this mirror section bias, the gain section threshold current, $I_{threshold}$, of the lasers was found to be 20 mA. The gain section of SFP-2 $I_{Gain,2}$, was set at 24 mA, just above $I_{threshold}$. The gain section of SFP-1 was operated between 35 mA and 50 mA, giving it a higher output power than SFP-2. In this bias range the wavelength of SFP-1 varied linearly with applied bias. Tuning SFP-1 in this way, allowed it to be swept across the optical resonance of the fixed SFP-2 to obtain injection locking. For convenience in the following descriptions, the higher power laser will be referred to as the master SFP (M-SFP) and the lower power laser referred to as the slave SFP (S-SFP) therefore, $I_{Gain,1}$ will be referred to as M-GS and $I_{Gain,2}$ as S-GS. Injection locking was investigated for two types of coupling between the M-SFP and the S-SFP. These were:

Off-Chip Coupling: The waveguide interconnect (VOA) section between the SFPs was reverse biased to -1 V making it completely absorbing. The SFPs were coupled externally using an optical circulator.

On-Chip Coupling: The waveguide interconnect (VOA) section between the SFPs was forward biased to transparency. The SFPs were coupled on the PIC through the waveguide interconnect, without the need for a circulator.

In the following sections, the injection locking performance of the SFPs is discussed for both coupling mechanisms.

4.1 Injection Locking of two Single Facet Slotted Fabry Pérot Lasers - Off-Chip Coupling

The off-chip coupling scheme was investigated first. A schematic of the experimental setup is shown in Figure 4.2 [44, 75, 76]. The output of each SFP was fibre coupled using lensed fibre. The output of the M-SFP, was guided through single mode fibre and a polarisation controller to port 1 of an optical circulator, which provided a greater than 40 dB isolation between its ports. Port 2 of the circulator was coupled to the output of the S-SFP. The signal from port 3 of the circulator was split in three and fed to an optical spectrum analyser (OSA), an electrical spectrum analyser (ESA) and a high speed oscilloscope (HSO), in order to investigate the optical and electrical characteristics of the signal. The signal was amplified using an erbium doped fibre amplifier (EDFA) before going to the photodetectors (PD) to obtain a strong signal on the ESA and HSO. The VOA was reverse biased to -1 V, thus removing any on-chip coupling between the lasers on-chip. Setting one laser lasing, reverse biasing the other laser and recording

photocurrent confirmed that the VOA absorbed all of the light, such that there was no on-chip coupling between the two lasers.

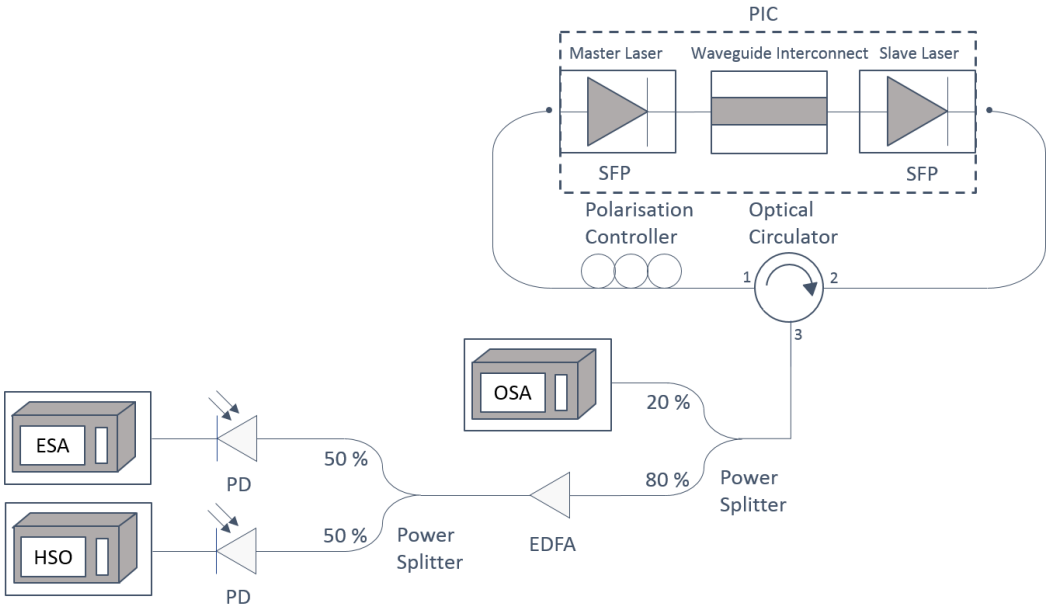

Figure 4.2: Experimental setup showing the off-chip coupling scheme between two lasers on the same integrated device. The waveguide interconnect linking both lasers was reverse biased to -1 V which removed any coupling between the lasers on-chip. Instead, light from the master laser was coupled into the slave laser via a polarisation controller and optical circulator.

4.1.1 S-GS bias = 24 mA

The M-SFP was swept across resonance with one of the side modes of the S-SFP by varying its gain section bias, M-GS between 35 mA and 50 mA. At each bias step the output of the S-SFP was recorded on the OSA, ESA and HSO. The OSA traces were concatenated to create the colour intensity plot in Figure 4.3a with master gain section (M-GS) bias on the x-axis, wavelength on the y-axis and the colour bar represents optical power. Similarly, the colour intensity plot of the ESA traces is shown in Figure 4.3b and the colour intensity plot of the HSO traces in Figure 4.3c. The FFT of the HSO traces in Figure 4.3c was performed in Matlab and the result is seen in Figure 4.3d.

The main mode of the free-running S-SFP had a wavelength of approximately 1557 nm and the side mode chosen for locking was at approximately 1563 nm, both visible in red in Figures 4.3a and 4.4. The M-GS bias was swept from 35 mA to 50 mA, thus sweeping the M-SFP across resonance with the S-SFP, see Figure 4.4a. The total sweep was approximately 0.285 nm. At a M-GS bias of 35 mA the M-SFP is detuned from the slave by approximately -0.13 nm. The detuning between the lasers decreases linearly as the M-GS increases, until M-GS = 38.8 mA, when the modes of the S-SFP are pulled towards the M-SFP by approximately 0.02 nm. The wavelength detuning, Δ is defined

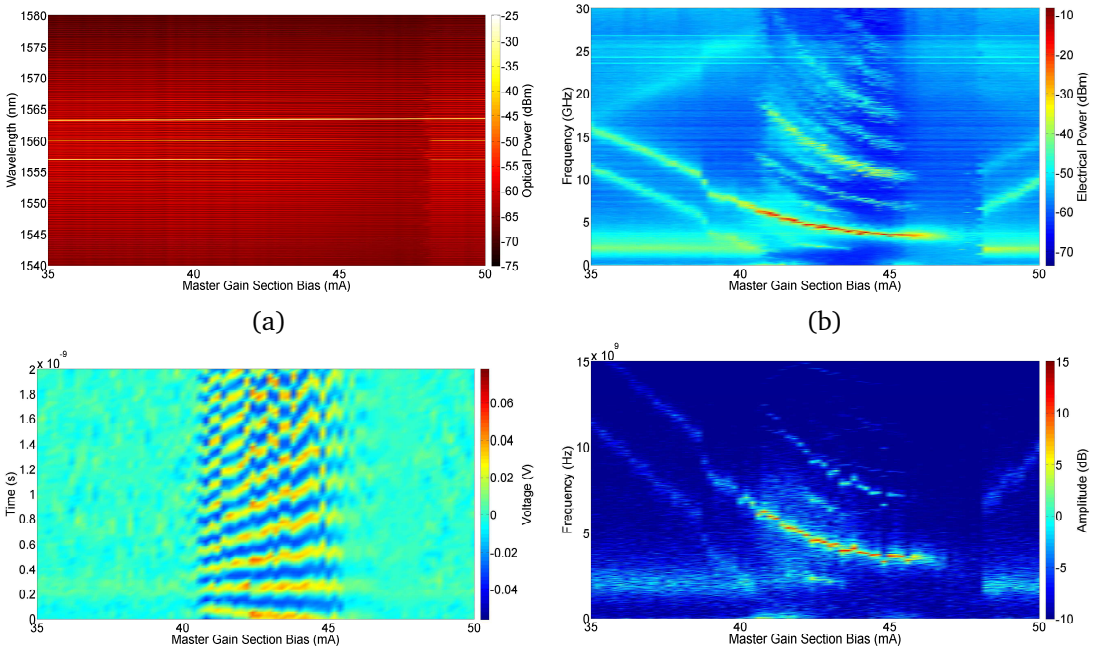

Figure 4.3: Colour intensity plots of (a) the optical spectra, (b) the electrical spectra, (c) the time traces and (d) the FFT of the time traces from the S-SFP for a S-GS of 24 mA and for the off-chip coupling scheme.

as the wavelength of the master laser minus the wavelength of the slave. The beat note corresponding to the detuning between the lasers is clearly visible in the colour plot of the ESA traces in Figure 4.3b. The frequency shift of ∼2.5 GHz in the beat note caused by the mode pulling is also observed. At M-GS = 41 mA, the side mode of the slave is amplified to almost the same power as the main mode of the master. The two lasers then beat together strongly, before injection locking. When injection locked the slave lases at the wavelength of the master and all other modes of the slave are suppressed.

The optical spectra in Figure 4.4b shows how the main mode of the S-SFP is suppressed during injection locking. Once the wavelength of the M-SFP becomes longer than the slave, the lasers unlock and the S-SFP returns to its free running state.

For each M-GS bias, the data from all equipment was analysed to determine the characteristics of the interactions taking place. The main regions that are expected in injection locked systems were identified, namely (i) beating; where the lasers are coupled together and the detuning between the lasers can be seen on the ESA but the lasers do not interact, (ii) non-linear interactions; where the detuning between the lasers is small enough that strong beating is observed between the master and slave lasers, and (iii) injection locking; where the S-SFP is injection locked to the M-SFP and hence lases at the wavelength of the M-SFP.

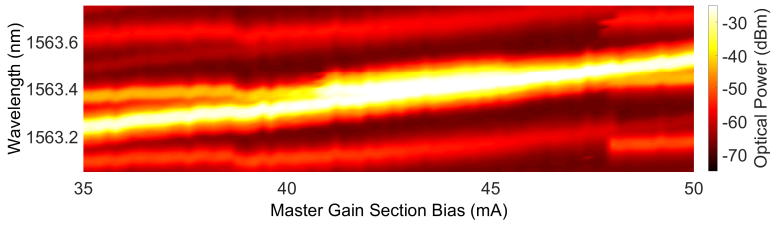

(a)

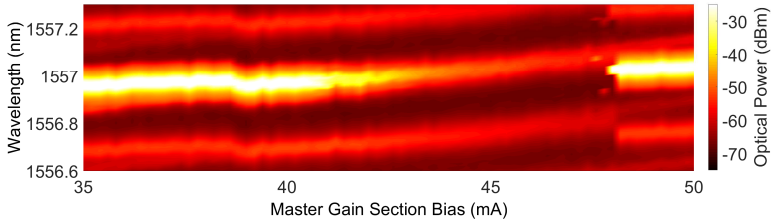

(b)

Figure 4.4: Colour intensity plots of the optical spectra from the S-SFP for the off-chip coupling scheme, showing (a) the main mode of the M-SFP being swept across resonance with a side mode of the S-SFP and (b) the main mode of the S-SFP.

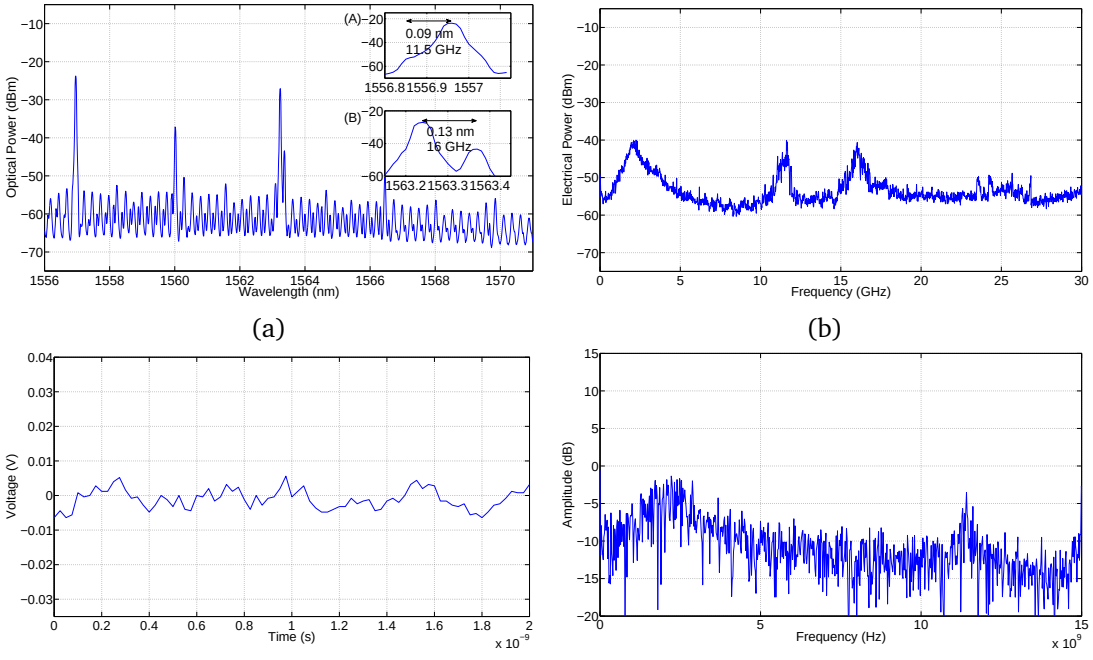

(a) (b)

(c) (d)

Figure 4.5: (a) The optical spectrum, (b) the electrical spectrum, (c) the time trace and (d) the FFT of the time trace of the S-SFP for the off-chip coupling scheme, for a M-GS = 35 mA. The lasers beat together and are ∼16 GHz apart.

For a M-GS bias below 40.6 mA (for example: Figure 4.5; M-GS = 35 mA) the lasers beat together and low frequency ESA peaks are associated with relaxation oscillations, while higher frequency ESA peaks are caused by the beating of the lasing modes of both lasers. These ESA peaks correspond to the detuning between the two lasers. The electrical spectrum in Figure 4.5b shows two peaks/beat notes, one at ∼16 GHz corresponding to a detuning of approximately -0.13 nm between the main mode of the

M-SFP and the side mode of the S-SFP, and a second beat note at ∼11.5 GHz, which corresponds to the beating of the main peak of the S-SFP with the closest side mode of the M-SFP. In the expanded graph of the OSA trace (Figure 4.5a, insert (A)), the main mode of the M-SFP can be seen detuned from the S-SFP side mode by approximately -0.13 nm. Figure 4.5a, insert (B) shows the detuning of 0.09 nm between the main peak of the S-SFP with the closest side mode of the M-SFP. The HSO trace in Figure 4.5c appears noisy but both the 2 GHz and the ∼11.5 GHz beat notes seen on the ESA are found in the FFT of the HSO trace, Figure 4.5d. (The ∼16 GHz beat note corresponding to the frequency detuning between the lasers is outside the bandwidth of the HSO.)

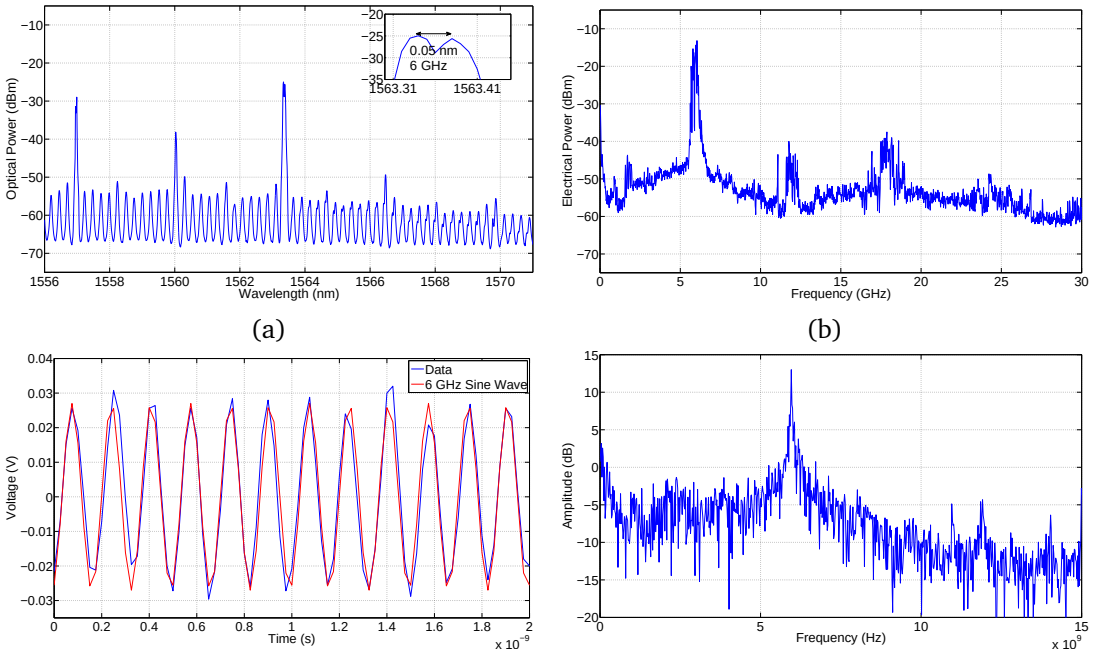

Figure 4.6: (a) The optical spectrum, (b) the electrical spectrum, (c) the time trace and (d) the FFT of the time trace of the S-SFP for the off-chip coupling scheme, for a M-GS = 41 mA. The lasers interact non-linearly and are ∼6 GHz apart.

Between 40.6 and 46.4 mA, strong beating is observed between the master and slave lasers as they interact non-linearly, represented in red in Figure 4.3b. Figure 4.6b is a cross section of Figure 4.3b for a M-GS bias of 41 mA, showing a strong beat note at approximately 6 GHz, corresponding to approximately -0.05 nm detuning between the lasers. The optical spectrum in Figure 4.6a shows, in comparison to that of Figure 4.5a, that the suppression of the main mode of the S-SFP has begun. The expanded spectrum shows that the side mode of the S-SFP has been amplified to approximately the same power as the main mode of the M-SFP. As the lasers beat together a sinusoidal signal is observed on the HSO. The peaks of the signal are represented by red and the troughs by blue in Figure 4.3c. One such trace for a M-GS bias of 41 mA is shown in Figure 4.6c. A 6 GHz sine wave was fitted to the data and excellent agreement within approximately

5% experimental error was obtained. The 6 GHz beat note is also clearly seen in Figure 4.6d, the FFT of the HSO trace.

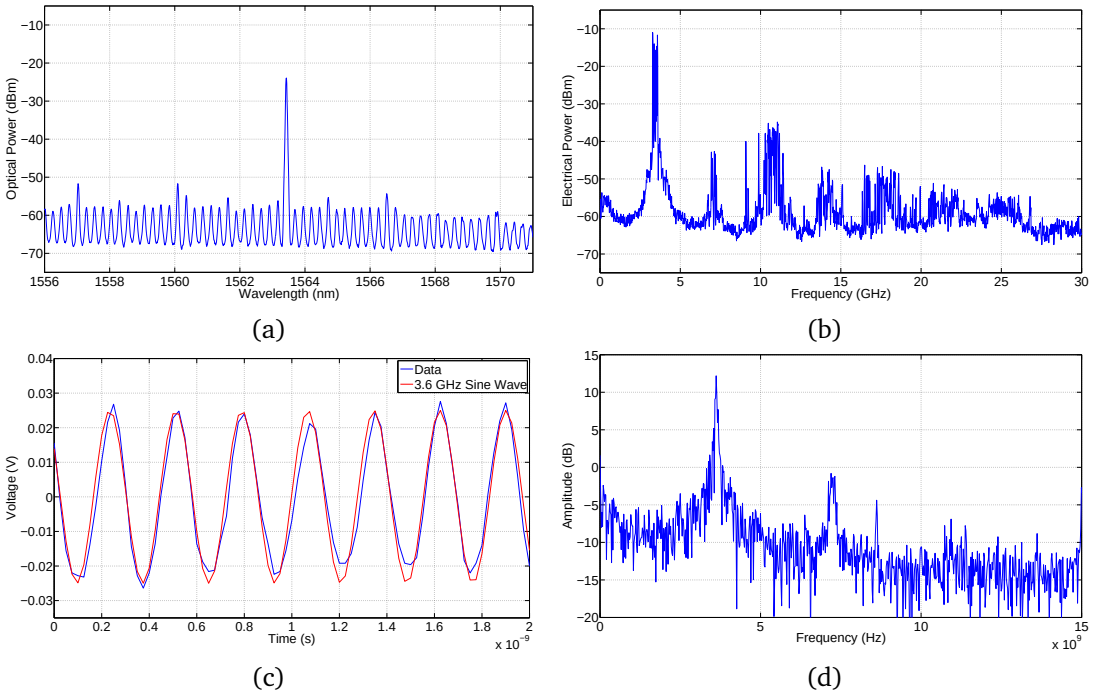

Figure 4.7: (a) The optical spectrum, (b) the electrical spectrum, (c) the time trace and (d) the FFT of the time trace of the S-SFP for the off-chip coupling scheme, for a M-GS = 45 mA. The lasers interact non-linearly and are ∼3.6 GHz apart.

Continuing to increase the M-GS to 45 mA, thus decreasing the detuning between the lasers to 3.6 GHz (-0.03 nm), further suppresses the main mode of the S-SFP, see Figure 4.7a. The ESA trace and FFT of the HSO trace in Figures 4.7b and 4.7d show the 3.6 GHz beat note and its harmonics, and the HSO trace in Figure 4.7c shows a 3.6 GHz sinusoidal signal. At this detuning, it is no longer possible to see the frequency/wavelength difference on the OSA because it is less than the resolution of the OSA.

The S-SFP is injection locked for M-GS biases between 46.4 and 48 mA and lases at the injected wavelength of the M-SFP with all other modes suppressed. In Figure 4.8a (M-GS bias = 47.8 mA) the main mode of the S-SFP has been suppressed by more than 30 dB and the S-SFP is lasing at the injected wavelength of approximately 1563.5 nm.

When injection locked, both lasers lased at the same wavelength and therefore there was no beating between them. Hence, there is a quiet region visible on the ESA (Figure 4.3b) and HSO (Figure 4.3c) (resulting in a quiet region in the FFT of the HSO (Figure 4.3d)) for M-GS biases between 46.4 mA and 48 mA (Δ between 0.030 nm and 0.052 nm). The relaxation oscillations are also suppressed. Figures 4.8b and 4.8c are examples of the quiet region measured by the ESA and HSO, respectively for a M-GS bias = 47.8 mA (Δ = 0.049 nm). The signals shown in these two graphs represent the

noise floor of the equipment used. Figure 4.8d shows the quiet region in the FFT of the HSO.

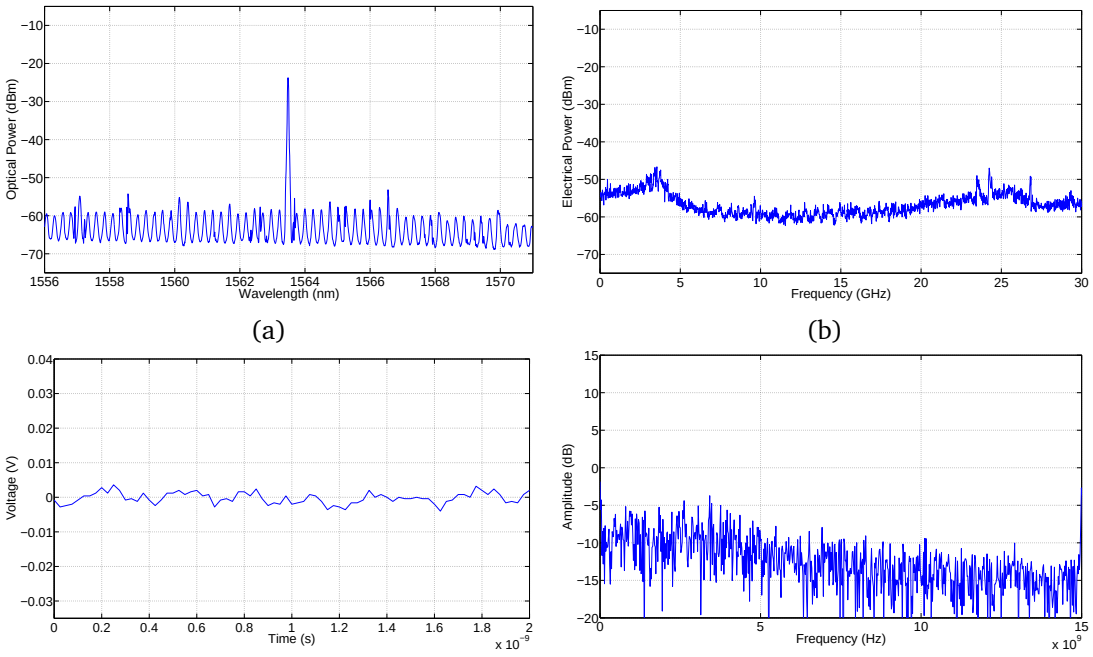

Figure 4.8: (a) The optical spectrum, (b) the electrical spectrum, (c) the time trace and (d) the FFT of the time trace of the S-SFP for the off-chip coupling scheme, for a M-GS = 47.8 mA. The lasers are injection locked.

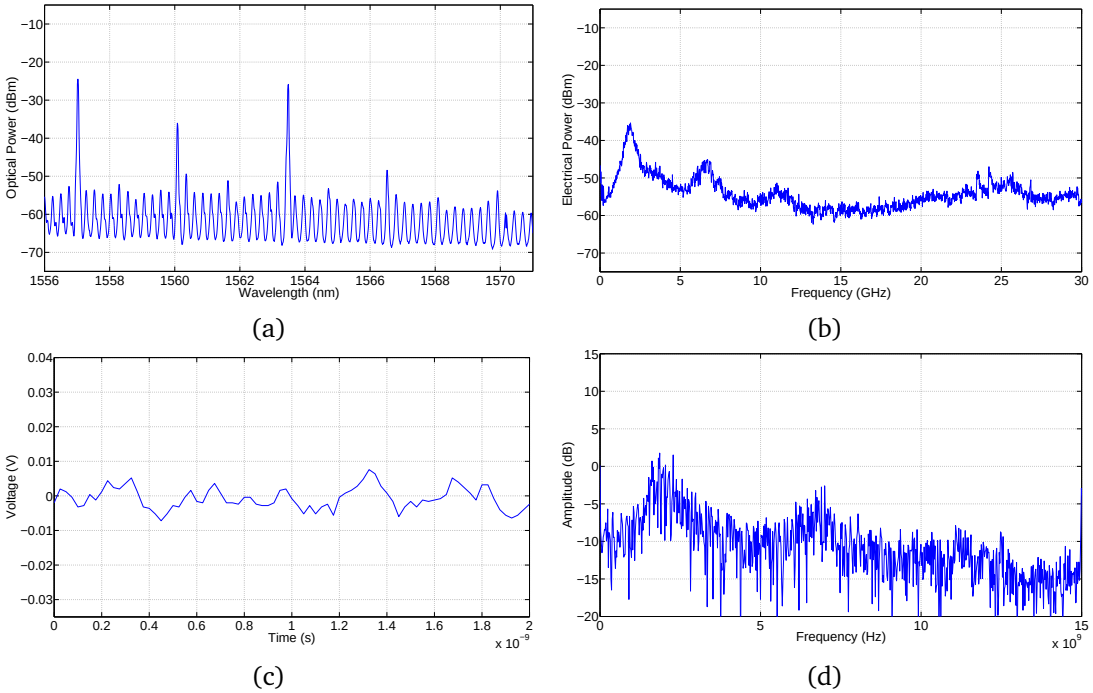

Figure 4.9: (a) The optical spectrum, (b) the electrical spectrum, (c) the time trace and (d) the FFT of the time trace of the S-SFP for the off-chip coupling scheme, for a M-GS = 48.2 mA. The lasers beat together and are ∼6.6 GHz apart.

Then for higher biases the S-SFP goes out of locking and beating can again be seen from the ESA and HSO data. As the peak wavelength of the M-SFP becomes longer than that of the free-running S-SFP the lasers unlock and the S-SFP returns to its free-running state. Figure 4.9a (M-GS bias = 48.2 mA, $\Delta \approx 0.054$ nm) shows the S-SFP beginning to lase at its free running wavelength of approximately 1557 nm again. At this M-GS bias a noisy signal is observed on the HSO, Figure 4.9c, and a beat note at approximately 6.6 GHz in the FFT of the HSO trace and in the ESA trace, Figures 4.9d and 4.9b, respectively. Continuing to increase the M-GS to 50 mA, thus increasing the detuning between the lasers to 10 GHz (0.08 nm), the main mode of the M-SFP can be seen to the right of the side mode of the S-SFP in the optical spectrum shown in Figure 4.10a. A noisy signal is seen on the HSO in Figure 4.10c and a 10 GHz beat note is seen in the electrical spectrum in Figure 4.10b and in the FFT of the HSO trace in Figure 4.10d.

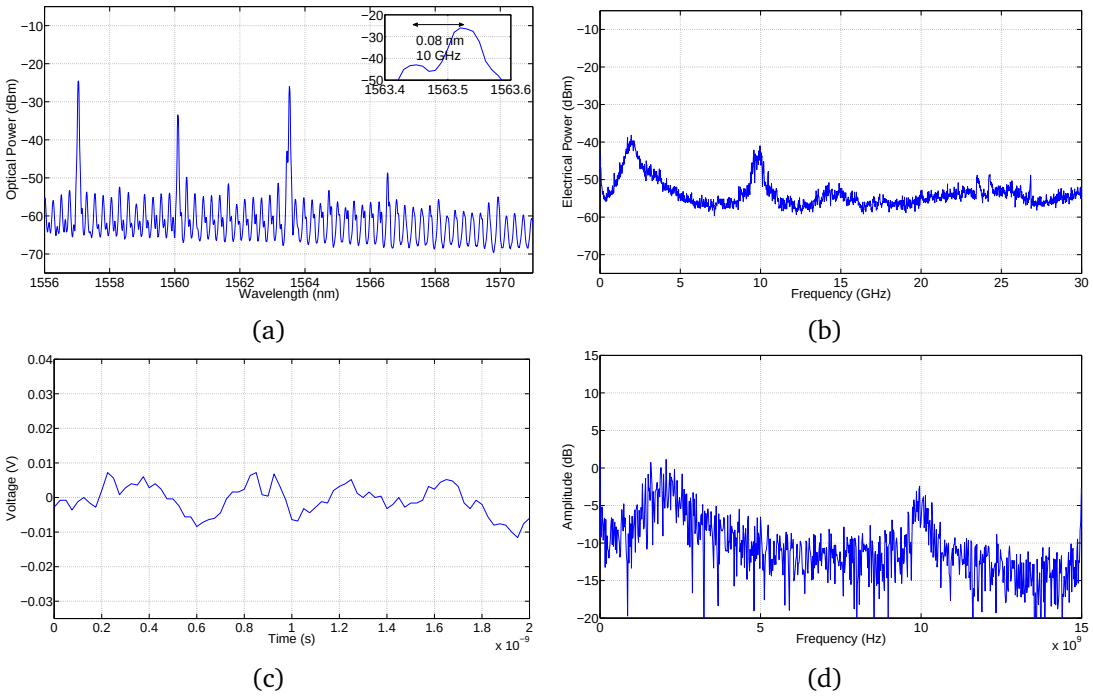

Figure 4.10: (a) The optical spectrum, (b) the electrical spectrum, (c) the time trace and (d) the FFT of the time trace of the S-SFP for the off-chip coupling scheme, for a M-GS = 50 mA. The lasers beat together and are ∼10 GHz apart.

Figure 4.11 is a summary of the types of behaviour obtained during injection locking as a function of M-GS bias. These types of behaviour; (i) beating, (ii) non-linear interactions (NLI) and (iii) locked, are similar to those presented in [44]. The figures above, provide examples of the OSA, ESA and HSO data demonstrating these types of behaviours; Figures 4.5, 4.9 and 4.10 are examples of beating, where the lasers beat together and the detuning between the lasers can be seen on the ESA but the lasers do not interact, Figures 4.6 and 4.7 of NLI, where the detuning between the lasers is small enough that they beat strongly together, and Figure 4.8 of injection locking, where the

S-SFP is injection locked to the M-SFP and hence lases at the wavelength of the M-SFP.

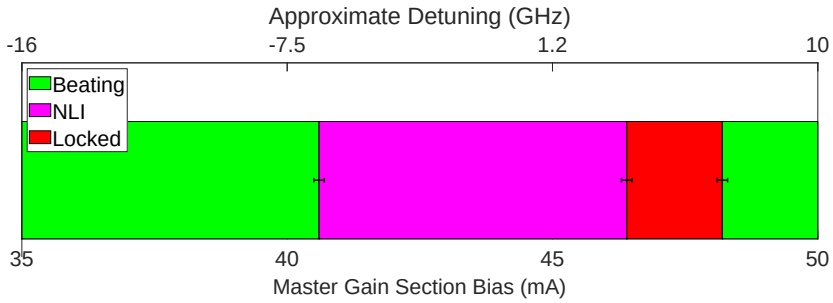

Figure 4.11: Summary of the types of behaviour obtained during injection locking as a function of M-GS bias, for a S-GS of 24 mA and for the off-chip coupling regime.

The dependence of the various types of behaviour on the M-GS and S-GS biases can be replaced by the detuning between the lasers. The wavelength detuning, Δ was defined previously as the wavelength of the master laser minus the wavelength of the slave. During the injection locking experiment, the S-GS bias was kept fixed, thus fixing its wavelength and the M-GS bias was swept from 35 - 50 mA. Over this bias range the wavelength of the M-SFP varied linearly. Therefore, it could be assumed that the detuning between the lasers varies linearly with M-GS bias. This is true when the lasers are beating together but not interacting and the beat note observed on the ESA is equal to the frequency detuning between the lasers. However once the lasers begin to interact, the detuning is no longer linear because the master pulls the modes of the slave, see Figure 4.4a. As the lasers interact non-linearly the detuning levels out to approximately 0.03 nm (3.5 GHz), before the lasers injection lock and the detuning drops to zero. When the wavelength of the M-SFP becomes approximately 0.05 nm (6 GHz) longer than the free-running wavelength of the S-SFP the lasers snap out of locking and the detuning varies linearly with M-GS bias again.

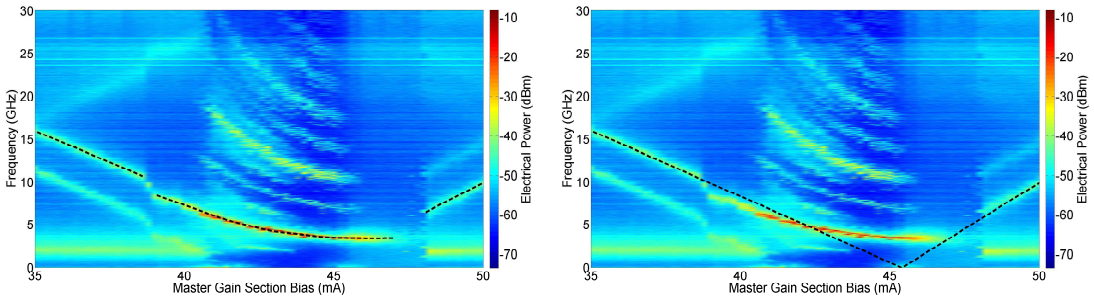

(a) (b)

Figure 4.12: Colour intensity plots of the electrical spectra from the S-SFP for a S-GS of 24 mA and for the off-chip coupling scheme showing (a) the actual and (b) the linear detuning between the lasers.

The black dashed lines on the ESA colour plot in Figure 4.12a is the actual detuning between the lasers during the injection locking experiment. In Figure 4.12b the linear detuning between the lasers has been extrapolated for all M-GS biases. This detuning

assumes that the lasers are not interacting and can be defined as the wavelength of the M-SFP minus the free-running wavelength of the S-SFP. This is the detuning that is used in figures. The top x-axis in Figure 4.11 is the detuning between the lasers.

The FFT of the optical spectra of the lasers was performed to determine the cavities present, Figure 4.13a. Figure 4.13b is the FFT of the optical spectrum from the S-SFP for a M-GS of 35 mA. The large peak at ∼1330 μm corresponds to the effective length of the SFP. Two lower amplitude peaks equal to twice and three times this length are also obtained. The small peaks at the left of the figure, at multiples of 108 μm, correspond to the interslot distance. These peaks are also observed as bright lines across the colour intensity plot, Figure 4.13a.

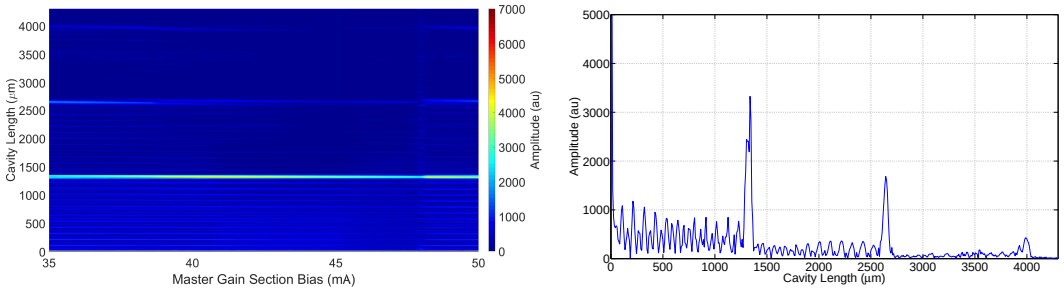

(a) (b)

Figure 4.13: (a) Colour intensity plot of the FFT of the optical spectra from the S-SFP for a S-GS of 24 mA and for the off-chip coupling scheme. (b) The FFT of the optical spectrum from the S-SFP for a M-GS of 35 mA and a S-GS of 24 mA and for the off-chip coupling scheme showing the cavities present in the system.

4.1.2 S-GS bias = 27 mA

The experiment was repeated for S-GS biases between 23 and 27 mA. Figure 4.14 shows the colour plots of the OSA, ESA and HSO data and the FFT of the HSO data from the S-SFP for a S-GS bias of 27 mA. The same three types of behaviour are observed; (i) coupled, (ii) beating and (iii) locked. Increasing the S-GS bias and hence its wavelength, results in a higher M-GS bias being required to obtain injection locking. The M-GS bias was swept over the same range (35 - 50 mA), therefore the locking region has shifted to the right of the plots and 50 mA was not high enough for the lasers to unlock. Figure 4.15 is a summary of the three types of behaviour as a function of M-GS bias. Again, the top x-axis is the detuning between the lasers.

Comparing Figures 4.11 and 4.15 shows, that even though the beating between the lasers begins at a similar M-GS biases in both cases (40.6 mA for S-GS = 24 mA and 41 mA for S-GS = 27 mA) and therefore much higher negative detuning for S-GS = 27 mA (-6.4 GHz for S-GS = 24 mA and -10.4 GHz for S-GS = 27 mA), that the injection locking begins at almost the same detuning in both cases (3.7 GHz for S-GS = 24 mA and 3.1 GHz for S-GS = 27 mA).

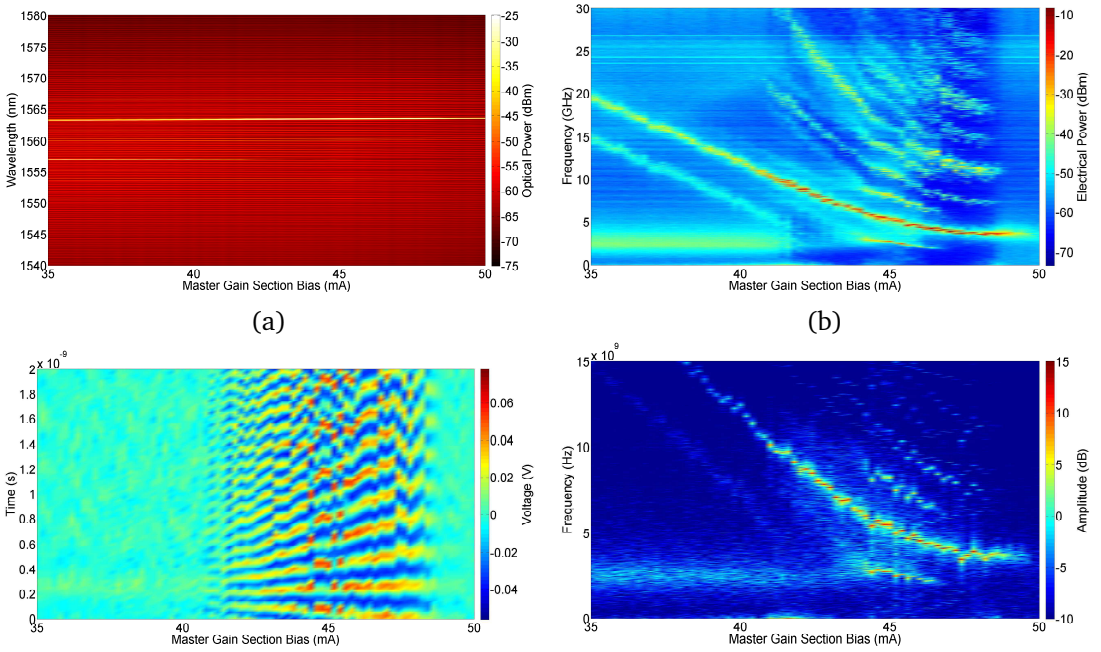

Figure 4.14: Colour intensity plots of (a) the optical spectra, (b) the electrical spectra, (c) the time traces and (d) the FFT of the time traces from the S-SFP for a S-GS of 27 mA and for the off-chip coupling scheme.

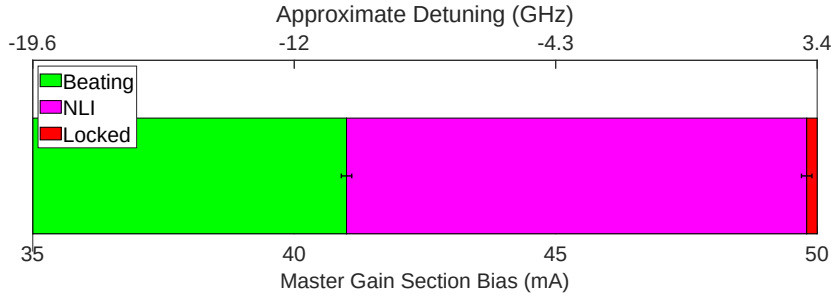

Figure 4.15: Summary of the types of behaviour obtained during injection locking as a function of M-GS bias, for a S-GS of 27 mA and for the off-chip coupling regime.

4.1.3 Summary of Off-Chip Results

All the data obtained from the injection locking experiments for S-GS biases between 23 and 27 mA was collated and is plotted as a function of M-GS and detuning in Figure 4.16. The same three types of behaviour are observed for each S-GS bias; (i) coupled, (ii) beating and (iii) locked.

The lasers begin to beat together at approximately the same M-GS bias for each S-GS bias and therefore at a higher negative detuning for higher S-GS biases. Increasing the S-GS bias increases the output power of the S-SFP and hence the power of each of its lasing modes. Therefore for higher S-GS biases the S-SFP is higher powered and hence it begins to beat with the M-SFP when there is a larger detuning between them. Injection locking occurs at approximately the same detuning for each S-GS bias. The

(a)

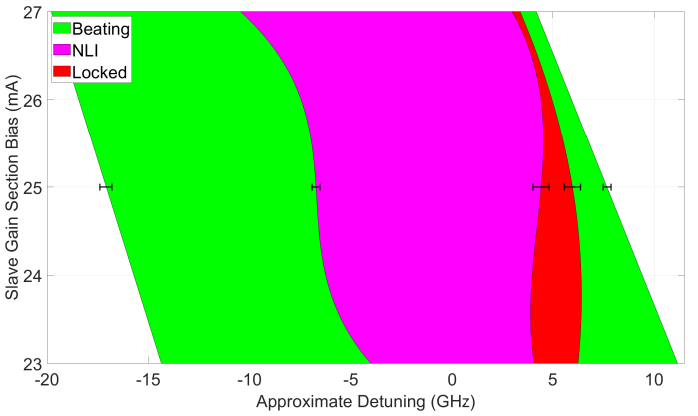

(b)

Figure 4.16: Summary of the types of behaviour obtained during injection locking as a function of (a) M-GS bias and (b) detuning between the lasers, for the off-chip coupling regime. The errors associated with the data fitting is shown on each line.

locking width decreases as the S-GS bias increases, since increasing the S-GS, increases its output power, hence making it more difficult to injection lock.

Having clearly demonstrated that it was possible to stably injection lock the S-SFP using the M-SFP in the “off-chip” case, the viability of obtaining stable injection locking in the “on-chip” case, where the circulator was removed and the SFPs were coupled through the VOA on the chip itself was investigated.

4.2 Injection Locking of two Single Facet Slotted Fabry Pérot Lasers - On Chip Locking

A schematic of the experimental setup for the on-chip coupling regime is shown in Figure 4.17 [44]. The circulator was removed and the VOA was forward biased to overcome the inherent losses of the material at 1550 nm. Biasing this section made it transparent, allowing the lasers to interact on-chip. An optical switch enabled the output of both lasers to be examined on the ESA, OSA and HSO, as described previously.

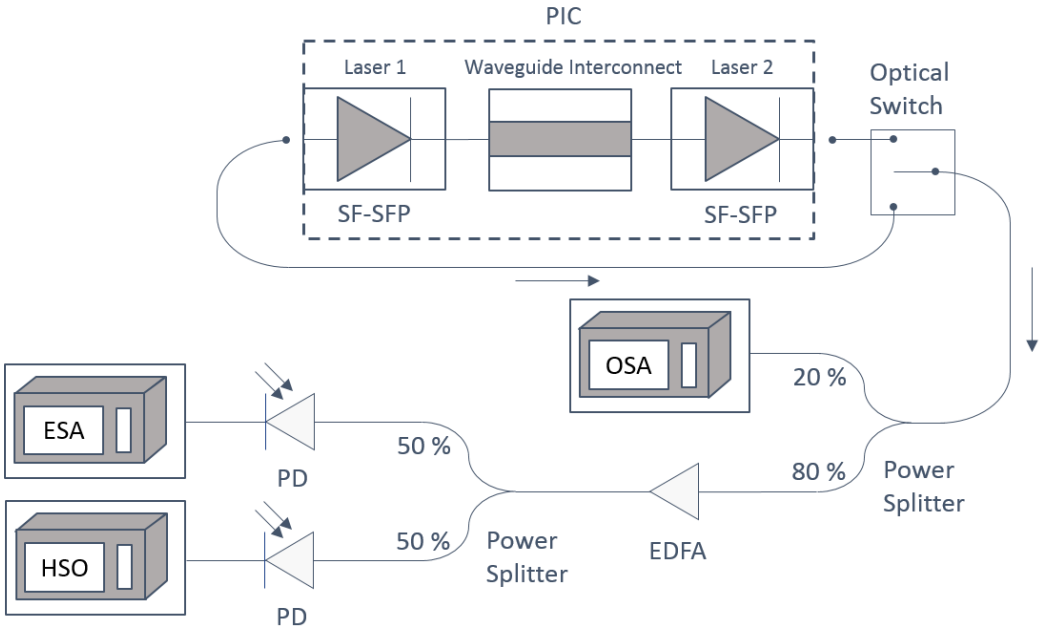

Figure 4.17: Experimental setup showing the on-chip coupling scheme between two lasers on the same integrated device. The waveguide interconnect linking both lasers was forward biased to allow the lasers to interact on-chip. An optical switch enabled the output of both lasers to be examined.

4.2.1 S-GS = 24 mA

The bias of the VOA section controls the coupling between the lasers, adding another variable and also introduces optical feedback into the system. Colour plots of the ESA and OSA traces from the M-SFP and S-SFP are shown in Figures 4.18 and 4.19, for a S-SFP gain section of 24 mA and various VOA biases between 1.051 V and 1.141 V.

At 1.051 V the VOA was still absorbing resulting in very little interaction between the lasers. At a VOA bias of 1.081 V there was enough light coupling between the lasers to allow them to beat together but not lock. Increasing the VOA bias above 1.081 V, the coupling between the lasers was strong enough that the lasers locked together. At high biases, the VOA became fully transparent and the whole PIC behaved as a

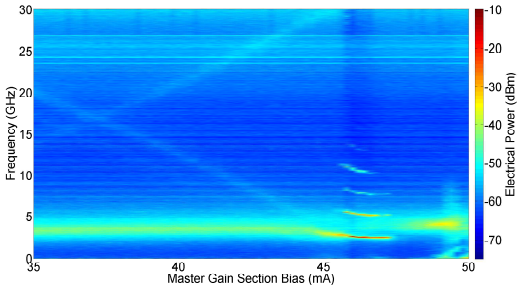

(a) ESA traces from the master laser for a VOA bias = 1.051 V.

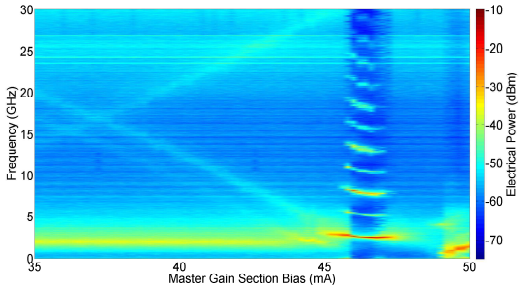

(b) ESA traces from the slave laser for a VOA bias = 1.051 V.

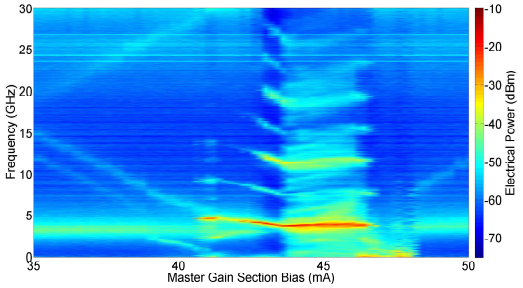

(c) ESA traces from the master laser for a VOA bias = 1.081 V.

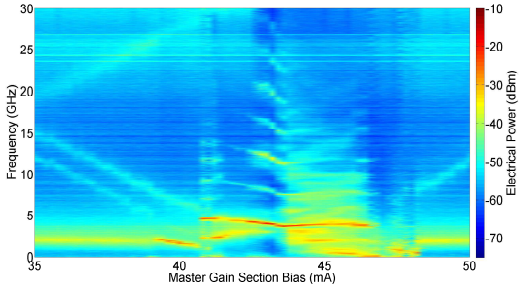

(d) ESA traces from the slave laser for a VOA bias = 1.081 V.

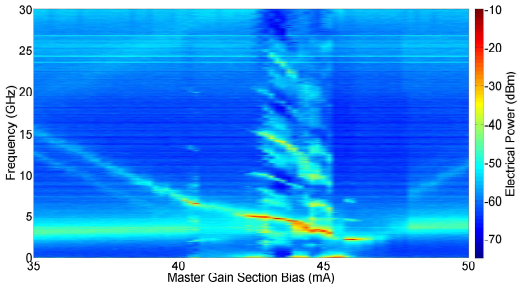

(e) ESA traces from the master laser for a VOA bias = 1.111 V.

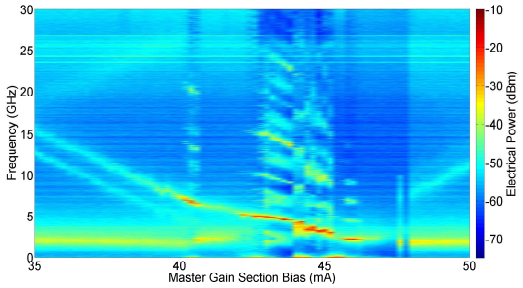

(f) ESA traces from the slave laser for a VOA bias = 1.111 V.

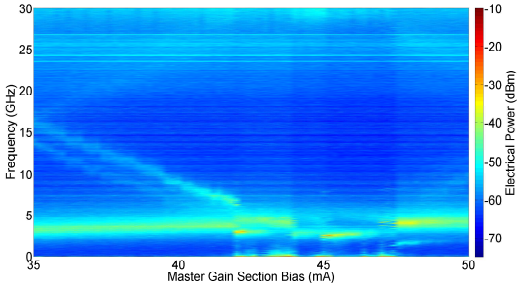

(g) ESA traces from the master laser for a VOA bias = 1.141 V.

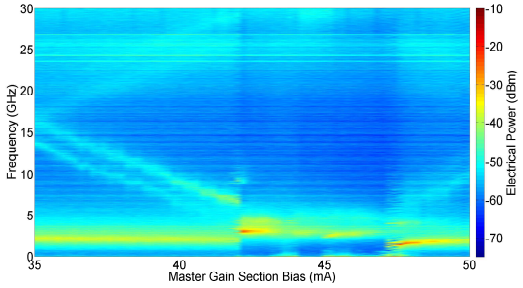

(h) ESA traces from the slave laser for a VOA bias = 1.141 V.

Figure 4.18: Colour plots of the ESA traces from the master and slave lasers for the on-chip coupling scheme, a slave gain section bias of 24 mA and various VOA biases.

compound laser rather than two separate SFP lasers. Comparing these colour plots with those obtained for the off-chip coupling regime (Figure 4.3), the results for VOA biases between 1.081 V and 1.111 V are most similar, suggesting that the VOA becomes

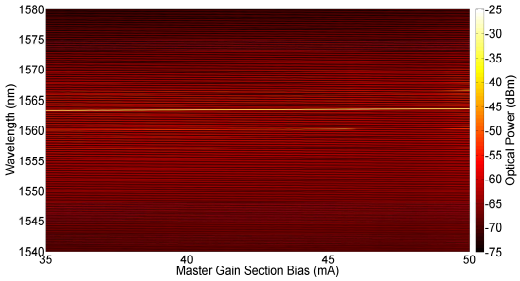

(a) OSA traces from the master laser for a VOA bias = 1.051 V.

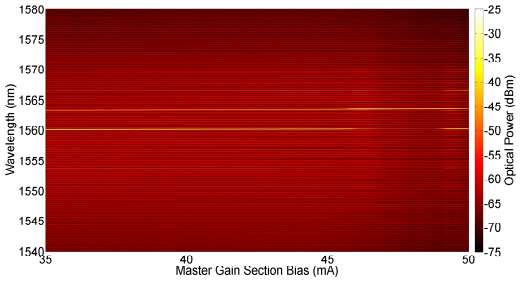

(b) OSA traces from the slave laser for a VOA bias = 1.051 V.

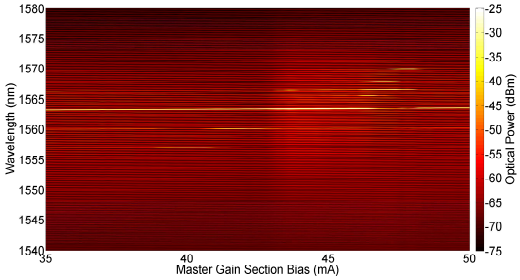

(c) OSA traces from the master laser for a VOA bias = 1.081 V.

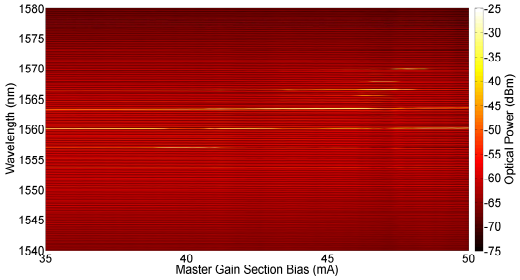

(d) OSA traces from the slave laser for a VOA bias = 1.081 V.

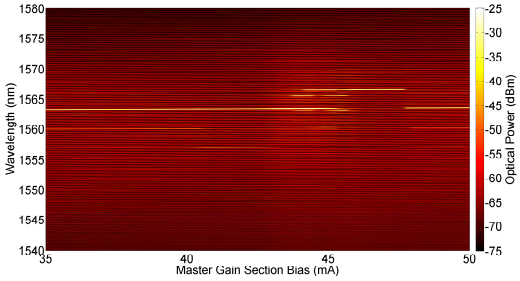

(e) OSA traces from the master laser for a VOA bias = 1.111 V.

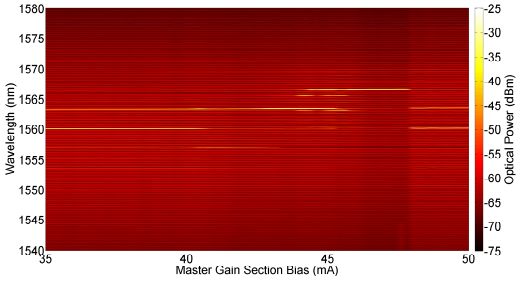

(f) OSA traces from the slave laser for a VOA bias = 1.111 V.

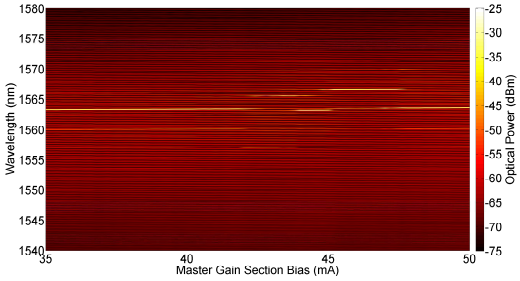

(g) OSA traces from the master laser for a VOA bias = 1.141 V.

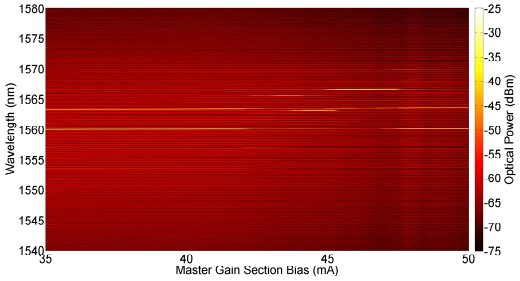

(h) OSA traces from the slave laser for a VOA bias = 1.141 V.

Figure 4.19: Colour plots of the OSA traces from the master and slave lasers for the on-chip coupling scheme, a slave gain section bias of 24 mA and various VOA biases.

transparent between these biases.

The colour intensity plots of the OSA, ESA and HSO traces from the M-SFP and S-SFP for a VOA bias of 1.091 V are shown in Figure 4.20. The types of behaviour observed are similar to the off-chip coupling regime, Figure 4.3, however some new types of

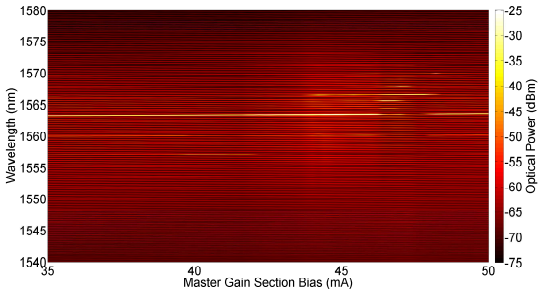

(a) OSA traces from the master laser.

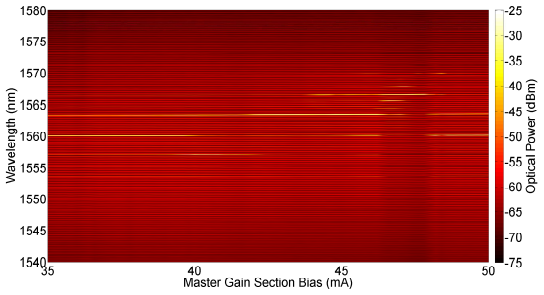

(b) OSA traces from the slave laser.

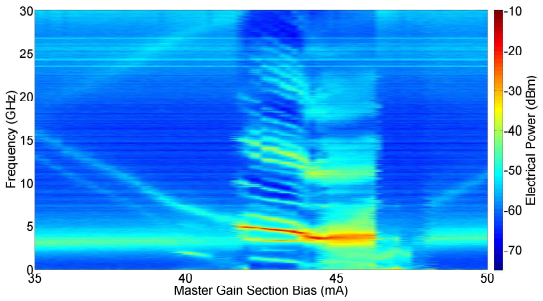

(c) ESA traces from the master laser.

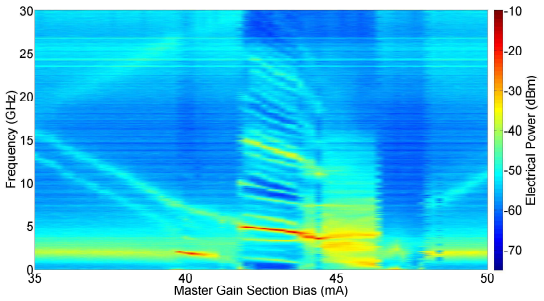

(d) ESA traces from the slave laser.

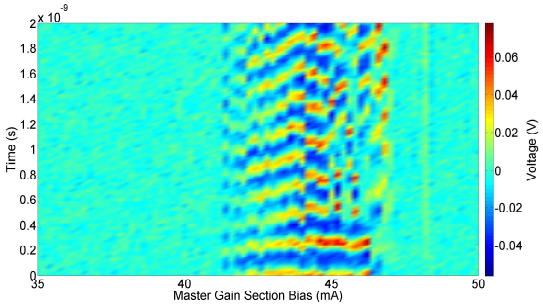

(e) HSO traces from the master laser.

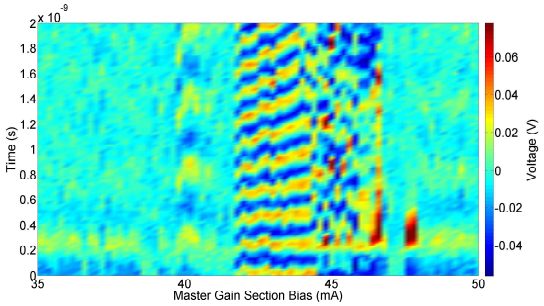

(f) HSO traces from the slave laser.

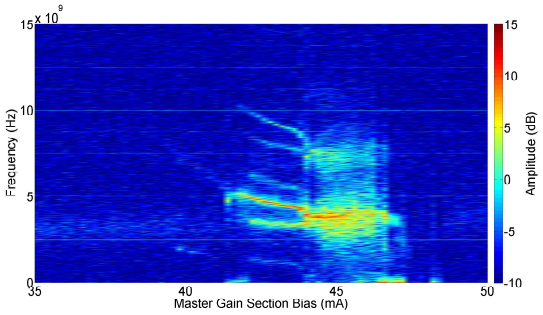

(g) FFT of the HSO traces from the master laser.

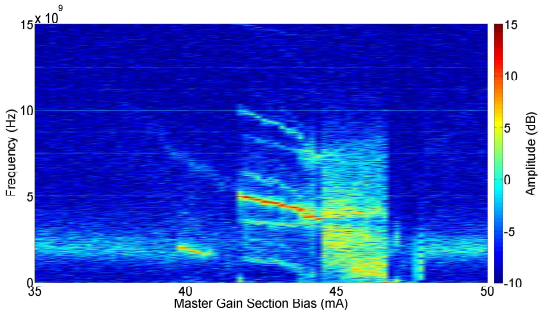

(h) FFT of the HSO traces from the slave laser.

Figure 4.20: Output of the master and slave lasers for a VOA bias of 1.091 V and a S-GS bias of 24 mA (on-chip coupling scheme).

behaviour generated by the feedback between the lasers are also observed.

When the M-GS bias is below 40 mA, the lasers are coupled and the expected beating between the different lasing modes are seen with the relaxation oscillation peak. Figure 4.21a is the optical spectrum of the M-SFP, showing its main lasing mode at approximately 1563 nm. The forward biasing of the VOA and the interaction between the two lasers results in the main lasing mode of the S-SFP shifting from approximately 1557 nm (in the off-chip case) to approximately 1560 nm, Figure 4.21b.

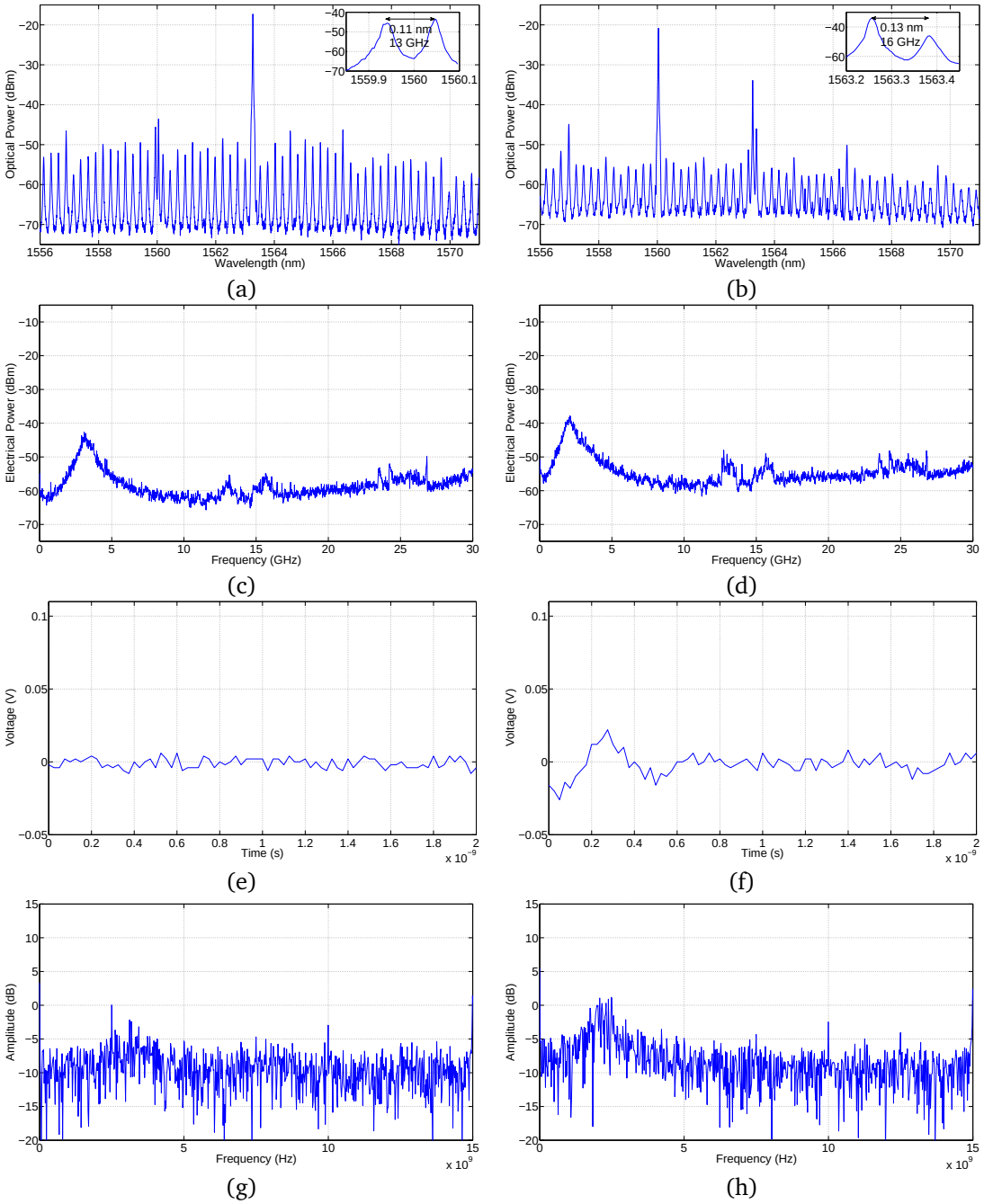

Figure 4.21: (a) and (b) The optical spectra, (c) and (d) the electrical spectra, (e) and (f) the time traces and (g) and (h) the FFTs of the time traces of the M-SFP and S-SFP, respectively, for the on-chip coupling scheme, for a VOA bias = 1.091 V and a M-GS = 35 mA. The lasers beat together and are ∼16 GHz apart.

The main mode of the M-SFP can be seen detuned from the side mode of the slave by ∼0.13 nm (16 GHz). A beat note of this frequency is seen in both the electrical spectra of the M-SFP and S-SFP, Figures 4.21c and 4.21d, respectively. At second beat note at ∼13 GHz, corresponding to the beating of the main mode of the S-SFP with the closest side mode of the M-SFP is also observed in both spectra. The beat notes at 3 GHz, for the M-SFP, and 2 GHz for the S-SFP correspond to the relaxation oscillations of the lasers. The time traces, Figures 4.21e and 4.21f appear noisy but the beat notes corresponding to the relaxation oscillations can be seen in the FFTs of the HSO traces, Figures 4.21g and 4.21h. (The beat notes at ∼13 GHz and ∼16 GHz observed in the ESA traces are too low powered to be seen in the FFTs.)

Increasing the M-GS bias to 40 mA, thus decreasing the detuning between the lasers to -0.057 nm (∼7 GHz), shifts the main mode of the S-SFP from approximately 1560 nm to approximately 1557 nm, Figure 4.22b. The main mode of the S-SFP can now be seen in the spectrum of the M-SFP, Figure 4.22a. A low power beat note at ∼7 GHz, corresponding to the detuning of ∼0.057 nm between the lasers (Figure 4.22b, insert (B)), is observed in both electrical spectra, Figures 4.22c and 4.22d.

There is also significant beating between a suppressed mode of the master and a dominant mode of the slave, at ∼1560 nm (Figure 4.22b, insert (A)), at 1.9 GHz, Figure 4.22. The corresponding ESA signal is much stronger (∼27.5 dBm) in the slave than the master, and can only be seen in the HSO trace of the slave, Figure 4.22f. This behaviour will be referred to as asymmetric beating.

For M-GS bias between 41 and 45 mA, the expected beating occurs between the unlocked lasers as they interact non-linearly. The HSO signal from both lasers forms a clear sinusoidal trace. At a M-GS bias of 43.8 mA, the detuning between the lasers has reduced to ∼0.035 nm (∼4.3 GHz). The mode at 1556 nm in the S-SFP spectra (Figure 4.23b) has been suppressed compared to Figure 4.22b. The mode at 1563 nm (main lasing mode of the M-SFP) has been amplified in the S-SFP spectrum. A higher wavelength mode, approximately 1567 nm, has been amplified in both spectra. (This behaviour was not seen in the off-chip coupling regime.) The ∼4.3 GHz beat note and its harmonics are seen in both electrical spectra (Figures 4.23c and 4.23d) and in the FFTs of the time traces (Figures 4.23g and 4.23h), since a ∼4.3 GHz sinusoidal signal was obtained for both time traces (Figures 4.23e and 4.23f). A 4.3 GHz sine wave was fitted to the data and a good agreement within approximately 10% experimental error was obtained.

These longer wavelength modes are not due to a temperature increase in the laser; high resolution OSA data showed that there was no change in the gain peak of the laser from 1563 nm. These modes are most likely due to lower losses in the VOA at longer wavelengths.

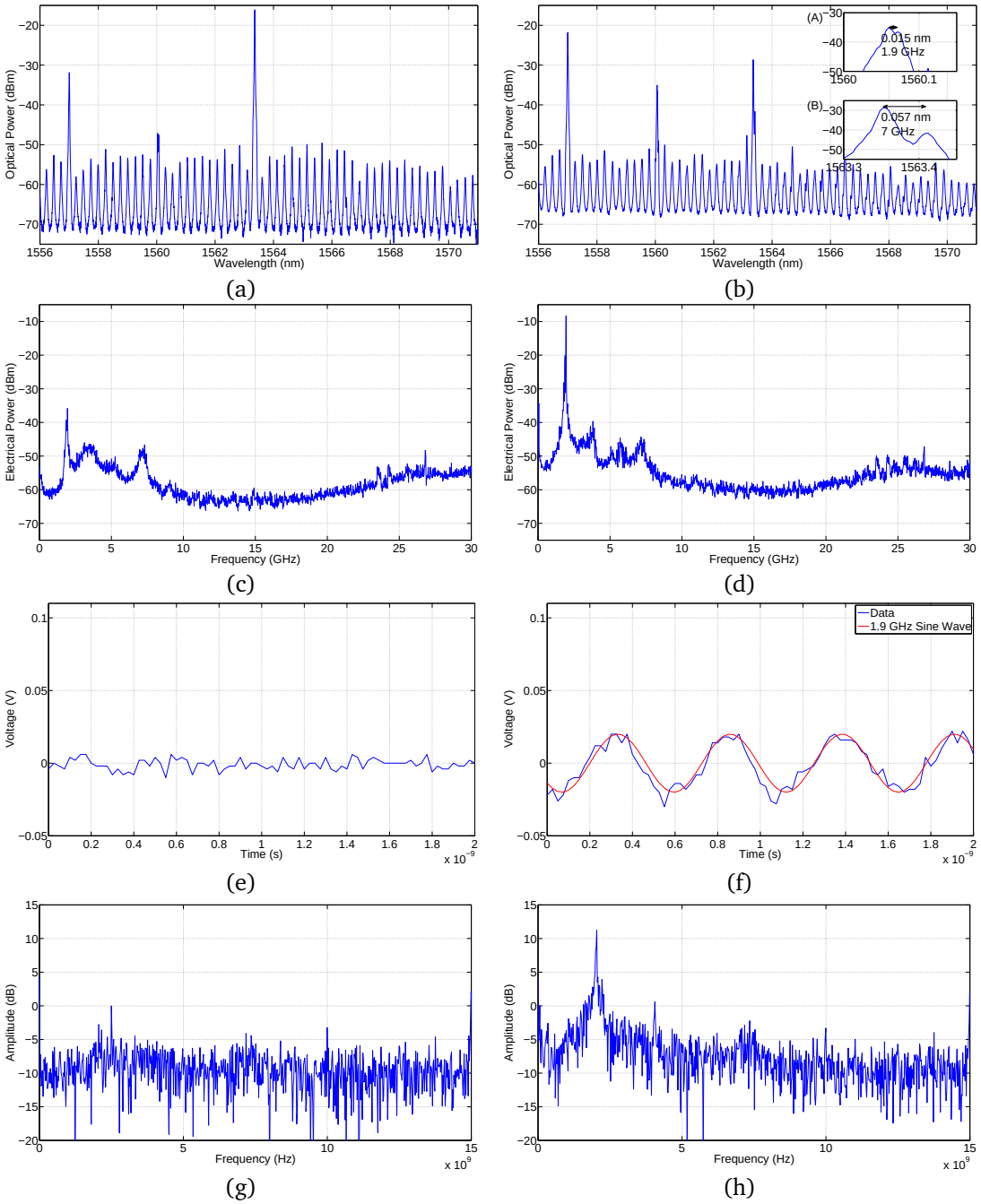

Figure 4.22: (a) and (b) The optical spectra, (c) and (d) the electrical spectra, (e) and (f) the time traces and (g) and (h) the FFTs of the time traces of the M-SFP and S-SFP, respectively, for the on-chip coupling scheme, for a VOA bias = 1.091 V and a M-GS = 40 mA. The lasers beat together asymmetrically and are ∼7 GHz apart.

Increasing the M-GS bias further to 45 mA reduces the detuning between the lasers to ∼3.8 GHz (0.03 nm) and the lasers are still unlocked and beating. The optical spectra (Figures 4.24a and 4.24b) are similar to Figures 4.23a and 4.23b. The HSO traces (Figures 4.24e and 4.24f) show irregular dynamics with a frequency of ∼3.8 GHz and large changes in the amplitude of the signal. Therefore the ∼3.8 GHz beat note seen

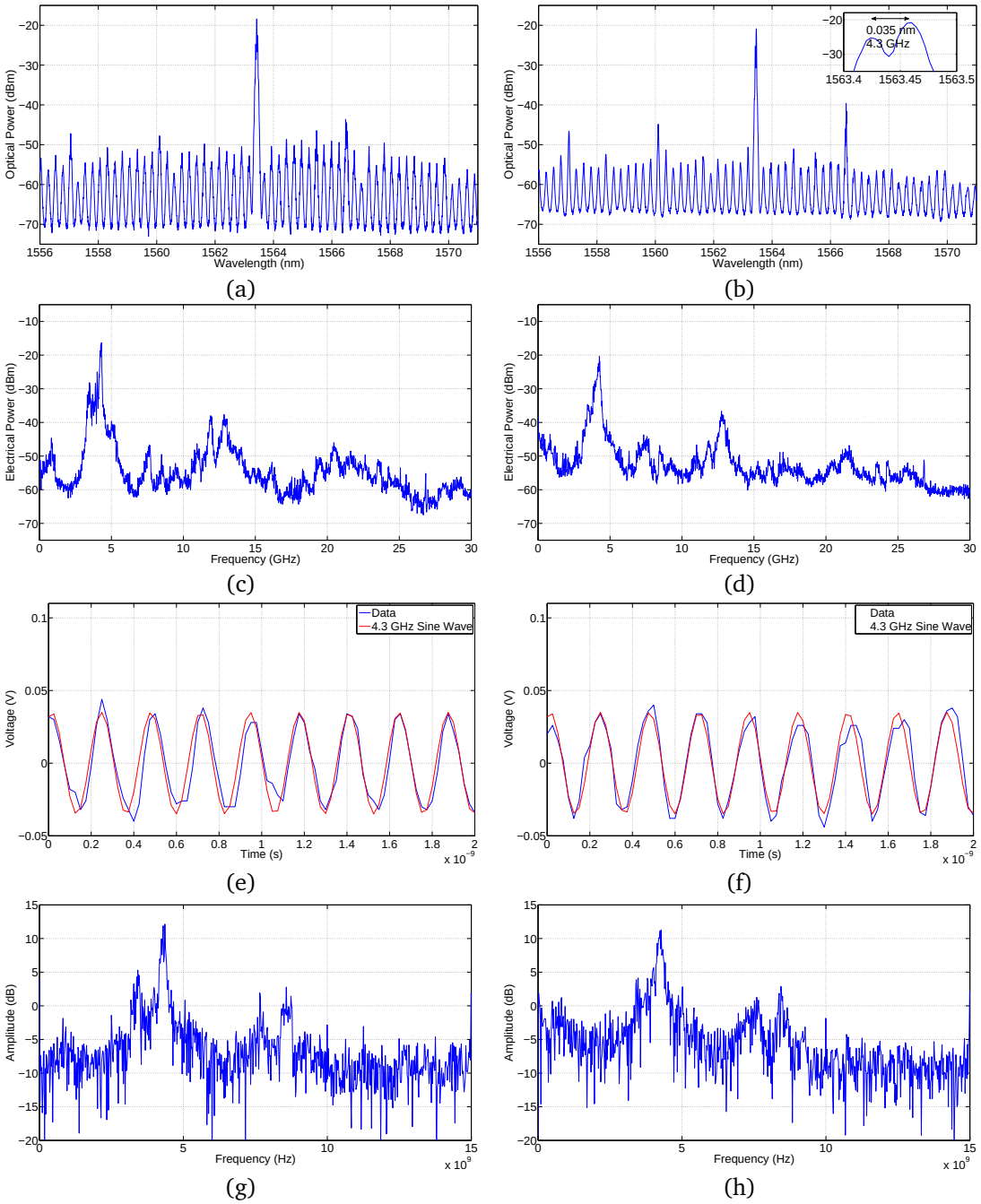

Figure 4.23: (a) and (b) The optical spectra, (c) and (d) the electrical spectra, (e) and (f) the time traces and (g) and (h) the FFTs of the time traces of the M-SFP and S-SFP, respectively, for the on-chip coupling scheme, for a VOA bias = 1.091 V and a M-GS = 43.8 mA. The lasers interact non-linearly and are ∼4.3 GHz apart.

in both electrical spectra (Figures 4.24c and 4.24d) and in the FFTs of the HSO traces (Figures 4.24g and 4.24h) is much broader and has fewer harmonics.

At a M-GS bias of 46.6 mA the interaction changes, Figure 4.25. Both lasers are now operating highly multi-mode, Figures 4.25a and 4.25b. Very little beating is observed in the electrical spectra (Figures 4.25c and 4.25d) or in the FFTs of the HSO traces (Fig-

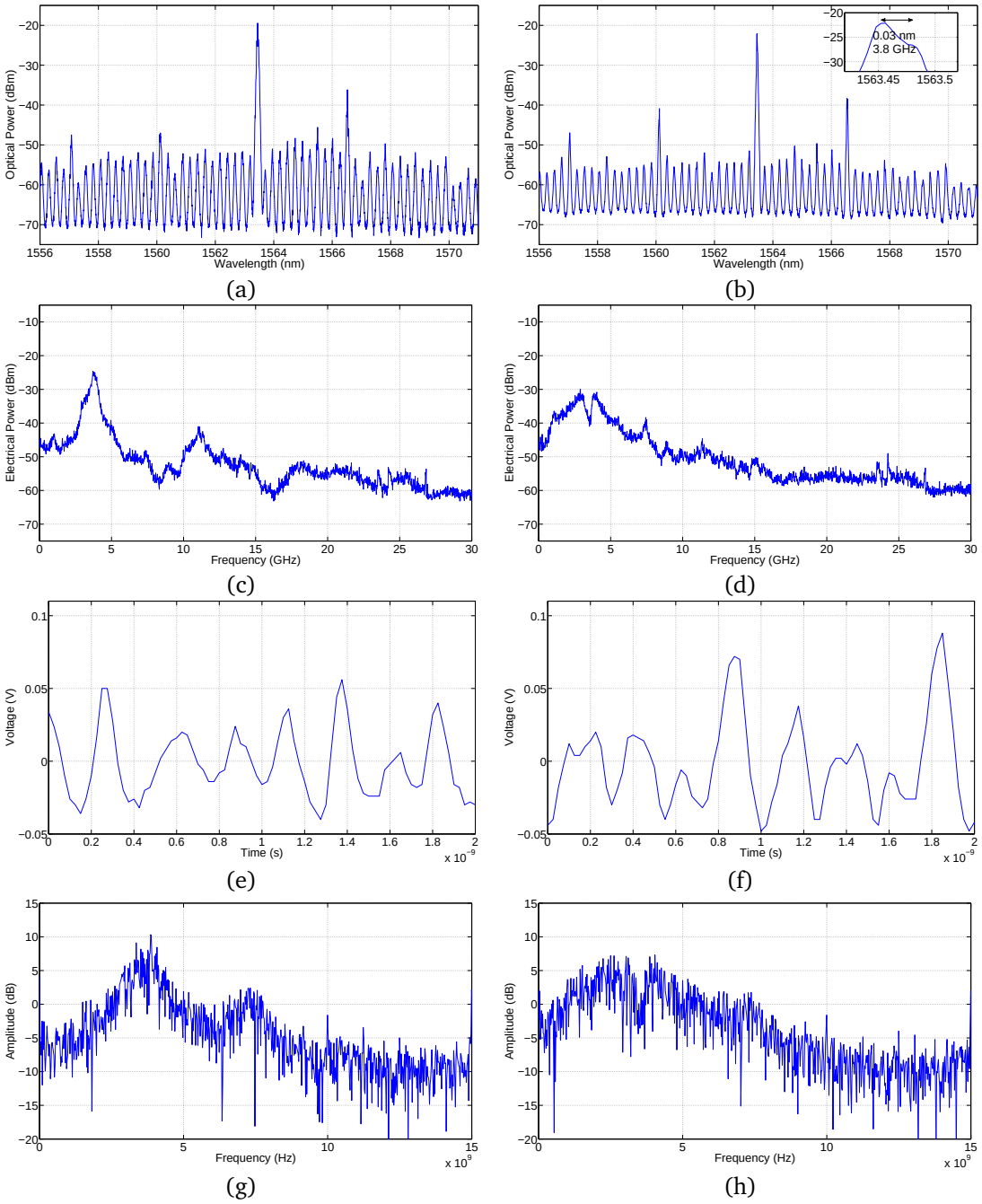

Figure 4.24: (a) and (b) The optical spectra, (c) and (d) the electrical spectra, (e) and (f) the time traces and (g) and (h) the FFTs of the time traces of the M-SFP and S-SFP, respectively, for the on-chip coupling scheme, for a VOA bias = 1.091 V and a M-GS = 45 mA. The lasers beat together and are ∼3.8 GHz apart. The beating between the lasers is not uniform but irregular.

ures 4.25g and 4.25h), but the HSO traces of the master and slave appear completely patternless, Figures 4.25e and 4.25f, a behaviour that will be referred to as aperiodic.

At a M-GS bias of 47.4 mA the lasers are locked. However, unlike the off-chip case where the S-SFP locks to the M-SFP and they both lase at the wavelength of the M-SFP,

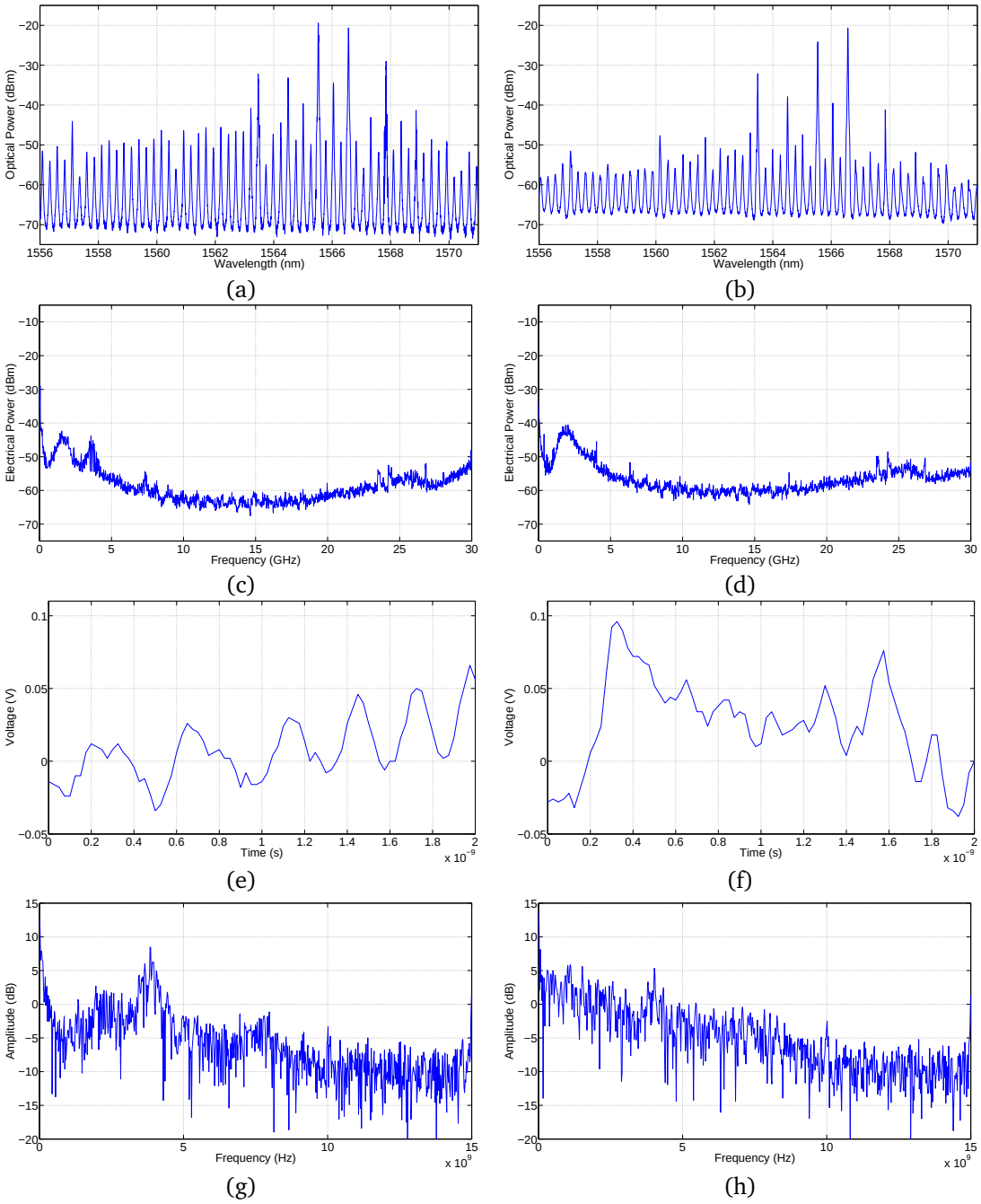

Figure 4.25: (a) and (b) The optical spectra, (c) and (d) the electrical spectra, (e) and (f) the time traces and (g) and (h) the FFTs of the time traces of the M-SFP and S-SFP, respectively, for the on-chip coupling scheme, for a VOA bias = 1.091 V and a M-GS = 46.6 mA. The lasers beat together aperiodically and are ∼1.6 GHz apart.

in the on-chip case when the lasers lock together both of their lasing wavelengths jump to a longer wavelength mode, approximately 1566.5 nm, see Figures 4.26a and 4.26b. This shift toward longer wavelength is unexpected, since this mode is past the gain peak of the material. All other modes were suppressed. There is no beating observed on the ESA or HSO, just the ROs (Figures 4.26c - h).

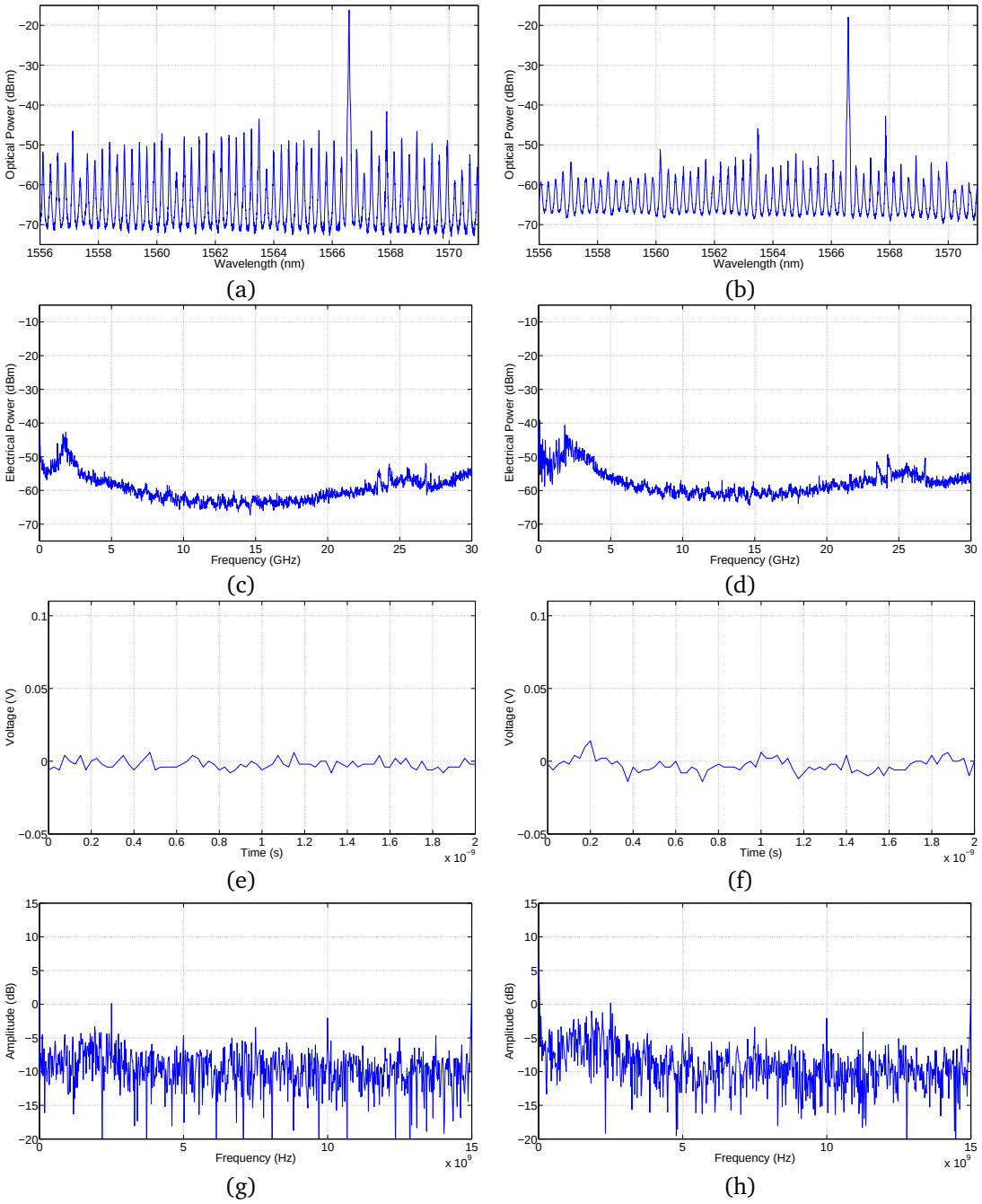

Figure 4.26: (a) and (b) The optical spectra, (c) and (d) the electrical spectra, (e) and (f) the time traces and (g) and (h) the FFTs of the time traces of the M-SFP and S-SFP, respectively, for the on-chip coupling scheme, for a VOA bias = 1.091 V and a M-GS = 47.4 mA. The lasers are mutually injection locked. Both lasers have mode hopped and now lase at ∼1566.5 nm.

At the final M-GS bias of 50 mA, the S-SFP has returned to its free-running state, with the main lasing mode at approximately 1560 nm and the M-SFP can be seen detuned from the side mode of the S-SFP by ∼0.089 nm (∼11 GHz), Figure 4.27b. The higher modes that were amplified in both spectra have now been suppressed again, Figures 4.27a and 4.27b. The ROs and the 11 GHz beat note are visible in both electrical

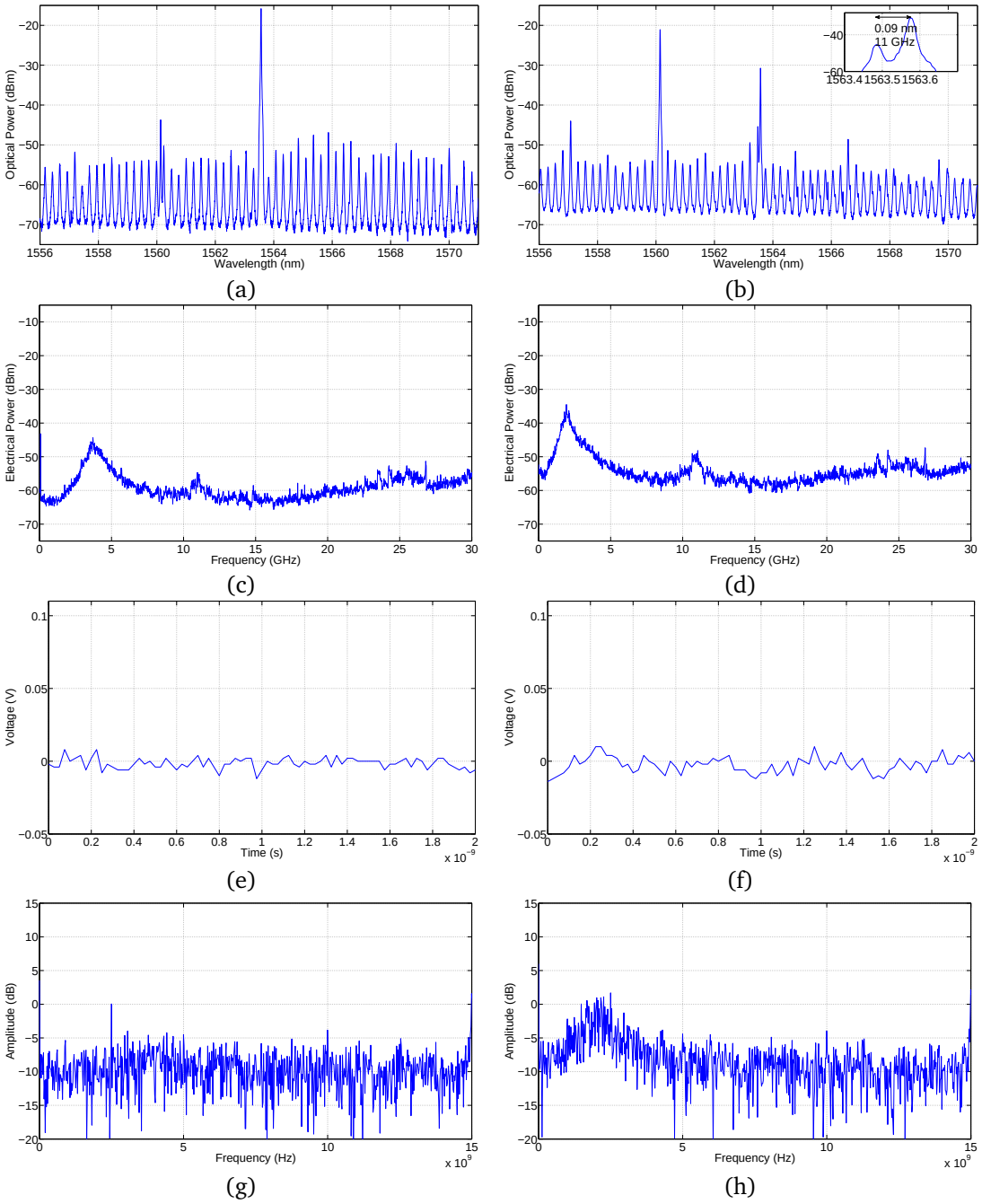

Figure 4.27: (a) and (b) The optical spectra, (c) and (d) the electrical spectra, (e) and (f) the time traces and (g) and (h) the FFTs of the time traces of the M-SFP and S-SFP, respectively, for the on-chip coupling scheme, for a VOA bias = 1.091 V and a M-GS = 50 mA. The lasers beat together and are ∼11 GHz apart.

spectra, Figures 4.27c and 4.27d. The time traces are noisy (Figures 4.27e and 4.27f) and the ROs are observed in the FFTs of the time traces, Figures 4.27g and 4.27h.

This study was repeated for multiple VOA biases between 1.08 and 1.13 V. Figure 4.28 provides a summary of the types of behaviour obtained from the M-SFP and the S-SFP during injection locking as a function of M-GS bias and VOA bias. The dashed line

across the graphs represents the data set discussed above for a VOA bias of 1.091 V. The three types of behaviour identified for the off-chip coupling regime; (i) beating, (ii) non-linear interactions (NLI) and (iii) locked, are also present for the on-chip coupling regime and new types of behaviour have been generated due to the feedback between the lasers. Irregular dynamics, asymmetric beating and aperiodic behaviour are exhibited by both the M-SFP and S-SFP, while pulsing was exhibited by the S-SFP alone.

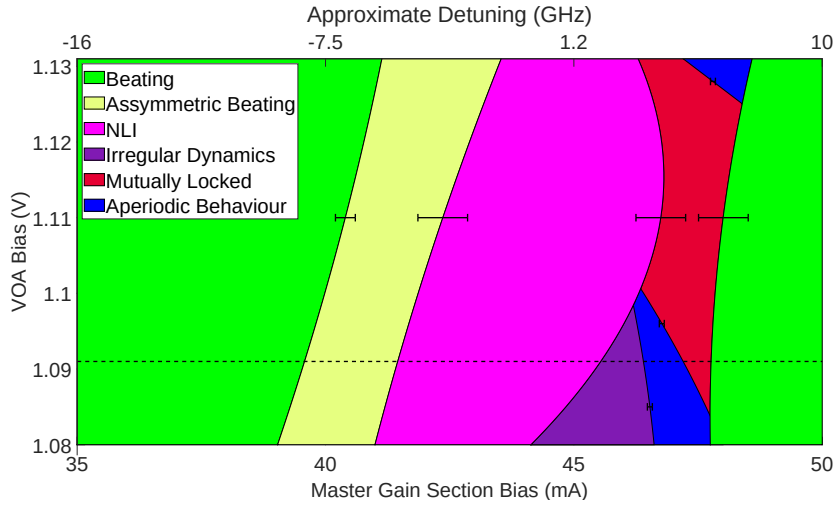

(a)

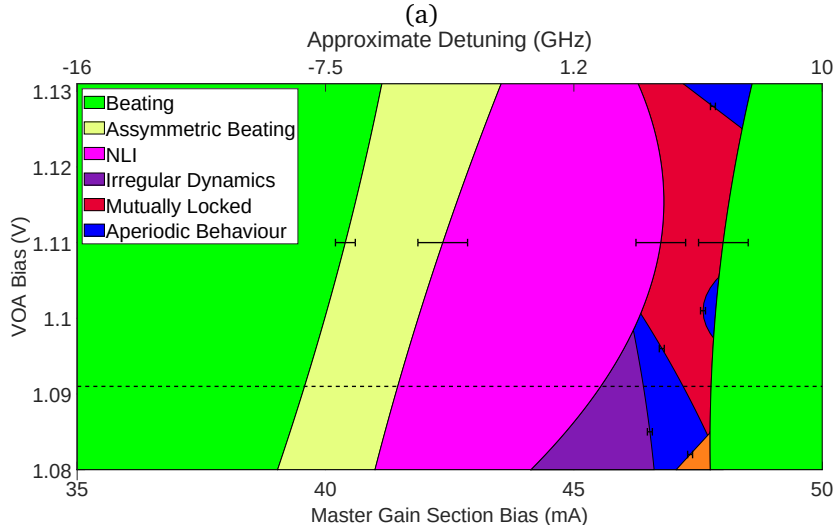

(b)

Figure 4.28: Summary of the types of behaviour obtained from (a) the M-SFP and (b) the S-SFP during injection locking as a function of M-GS bias, for a S-GS bias of 24 mA and the on-chip coupling regime. The errors associated with the data fitting is shown on each line.

The biggest difference between the off and on-chip coupling regimes is that for the off-chip coupling regime when the lasers injection lock the S-SFP locks to the M-SFP and both lasers then lase at the wavelength of the M-SFP. However, for the on-chip coupling regime when the lasers mutually injection lock, both lasers lock to a higher mode. The

locking width is also narrower for the on-chip coupling regime due to the regions of irregular beating and aperiodic behaviour before the locking region. However, it can be increased by increasing the VOA bias. The approximate detuning between the free-running lasers is shown on the top x-axis of the summaries in Figure 4.28.

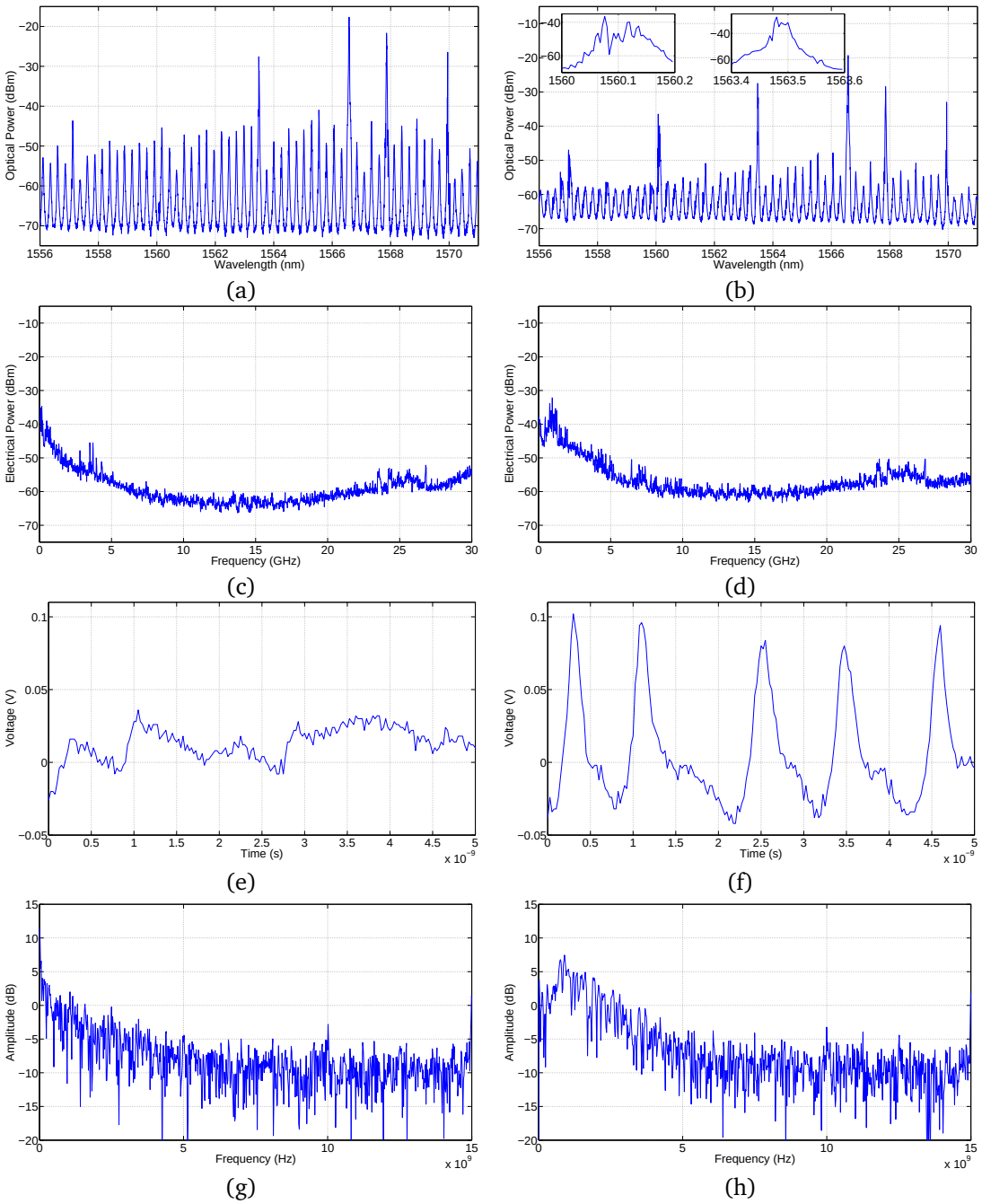

Figure 4.29: (a) and (b) The optical spectra, (c) and (d) the electrical spectra, (e) and (f) the time traces and (g) and (h) the FFTs of the time traces of the M-SFP and S-SFP, respectively, for the on-chip coupling scheme, for a VOA bias = 1.081 V and a M-GS = 47.2 mA. The lasers beat together aperiodically and are ∼1 GHz apart. The S-SFP exhibits pulsing behaviour.

Reducing the VOA bias to 1.081 V, reduces the coupling between the lasers therefore

preventing the lasers from injection locking. At the M-GS biases where injection locking would be expected the lasers behave aperiodically. However, there is a small region (M-GS = 47.2 - 48 mA) where the time traces of the S-SFP show pulsing behaviour, Figure 4.29. The time trace of the S-SFP, Figure 4.29e, shows pulsing at ∼0.94 GHz and a corresponding beat note is observed in the electrical spectrum, Figure 4.29d, and the FFT of the HSO trace, Figure 4.29g. The signal obtained on the HSO (Figure 4.29e) has a frequency of 0.94 GHz but it is not a sinusoidal signal. Without the HSO data it may have been assumed that the beating between the lasers was sinusoidal. This illustrates how important the time traces are to fully understand the interaction between the lasers. When this pulsing occurs, the modes in the optical spectrum of the S-SFP are not smooth, but have many little peaks close together, as is shown in the inserts of Figure 4.29b.

The FFT of the optical spectra of the lasers was again performed to determine the cavities present, Figure 4.30. Peaks at multiples of the effective length of the SFP, ∼1330 μm and the interslot distance, 108 μm are again obtained. A very small peak at ∼3230 μm is observed for a VOA bias of 1.091 V, Figures 4.30a and b. This length corresponds to the full PIC from facet-to-facet, confirming that a VOA bias of 1.091 V is sufficient to allow light to couple between the lasers. Increasing the VOA bias to 1.141 V, Figures 4.30c and d, increases the amplitude of this peak, suggesting that the VOA is almost transparent and the PIC is no longer behaving as two coupled lasers but is becoming a compound laser from facet-to-facet. Continuing to increase the VOA bias makes the VOA transparent and causes the PIC to become a compound laser.

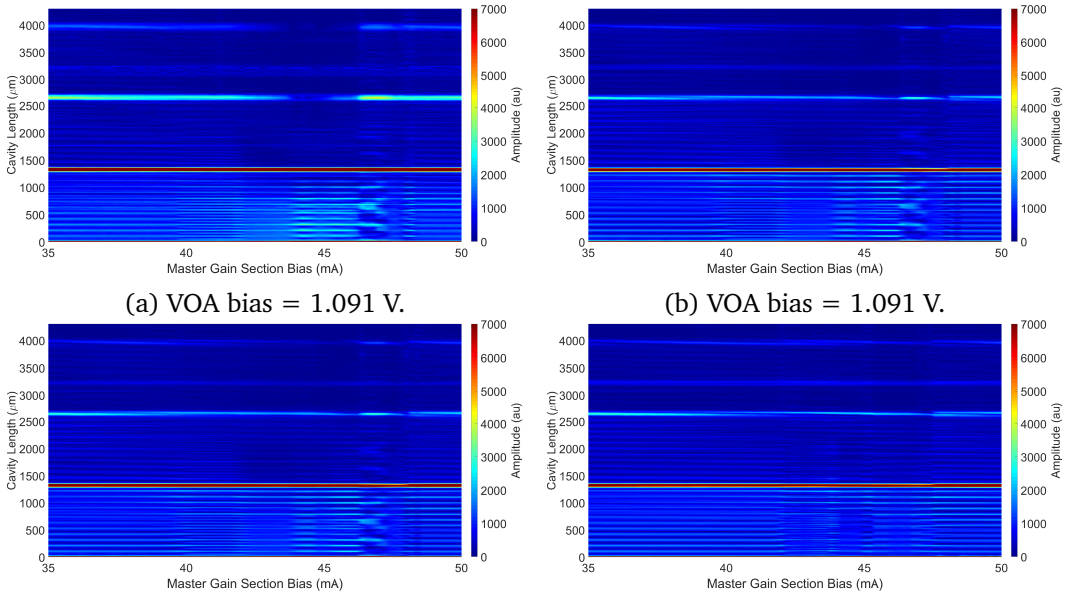

(a) VOA bias = 1.091 V.

(b) VOA bias = 1.091 V.

(c) VOA bias = 1.141 V.

(d) VOA bias = 1.141 V.

Figure 4.30: Colour plots of the FFT of the OSA traces from the master, (a) and (c), and slave, (b) and (d), lasers for the on-chip coupling scheme, a slave gain section bias of 24 mA and various VOA biases.

4.2.2 S-GS = 27 mA

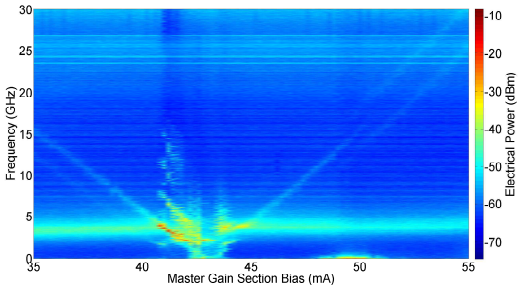

(a) ESA traces from the master laser for a VOA bias = 1.051 V.

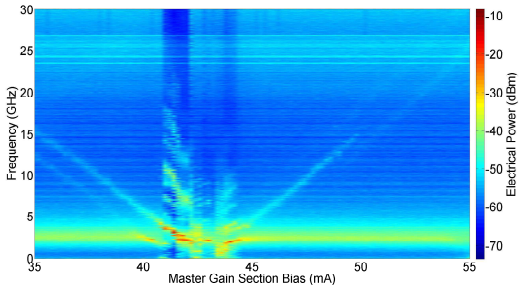

(b) ESA traces from the slave laser for a VOA bias = 1.051 V.

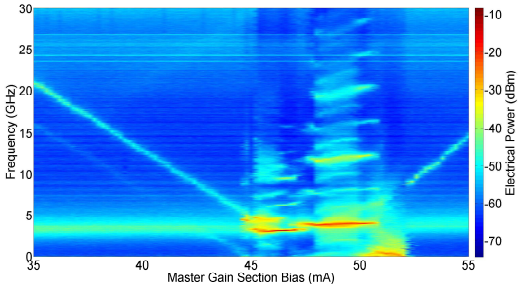

(c) ESA traces from the master laser for a VOA bias = 1.081 V.

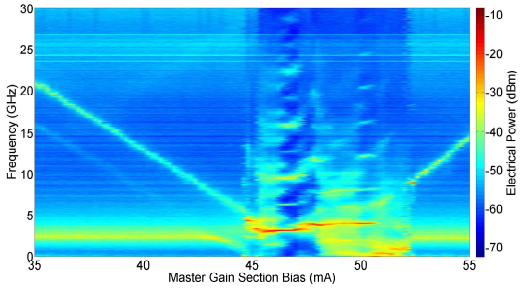

(d) ESA traces from the slave laser for a VOA bias = 1.081 V.

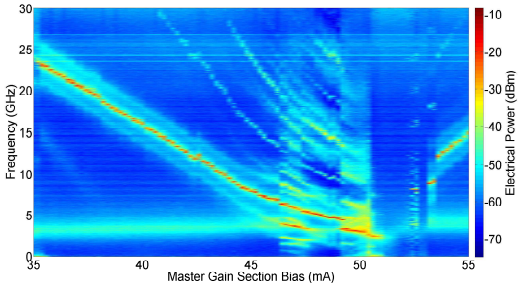

(e) ESA traces from the master laser for a VOA bias = 1.111 V.

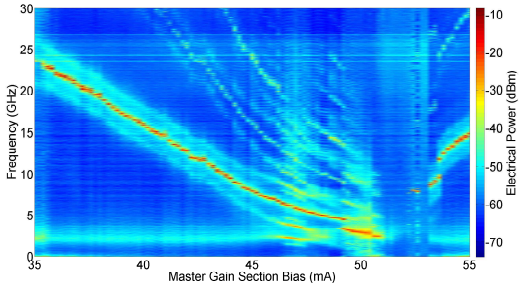

(f) ESA traces from the slave laser for a VOA bias = 1.111 V.

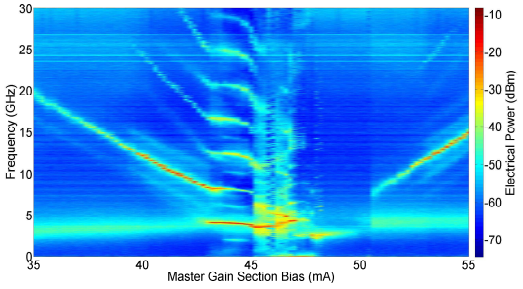

(g) ESA traces from the master laser for a VOA bias = 1.141 V.

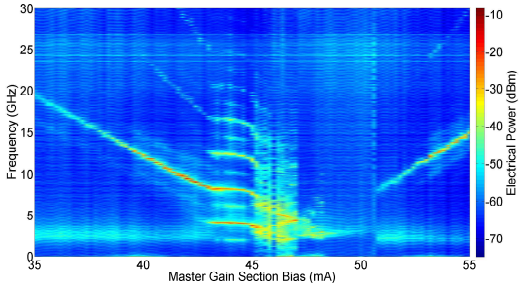

(h) ESA traces from the slave laser for a VOA bias = 1.141 V.

Figure 4.31: Colour plots of the ESA traces from the master and slave lasers for the on-chip coupling scheme, a slave gain section bias of 27 mA and various VOA biases.

Similar to the off-chip coupling regime, the experiment was repeated for a S-GS bias of 27 mA. Colour plots of the ESA and OSA traces from the M-SFP and S-SFP are shown

in Figures 4.31 and 4.32, respectively for a S-SFP gain section of 27 mA and various VOA biases between 1.051 V and 1.141 V.

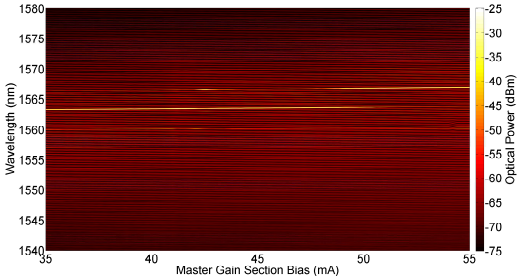

(a) OSA traces from the master laser for a VOA bias = 1.051 V.

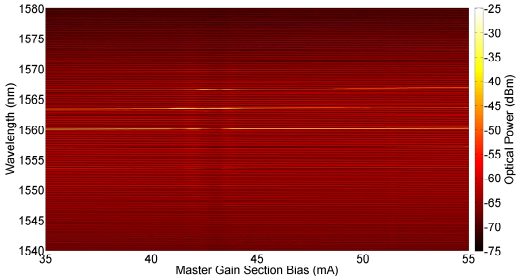

(b) OSA traces from the slave laser for a VOA bias = 1.051 V.

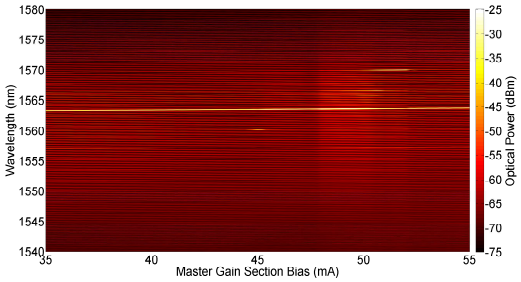

(c) OSA traces from the master laser for a VOA bias = 1.081 V.

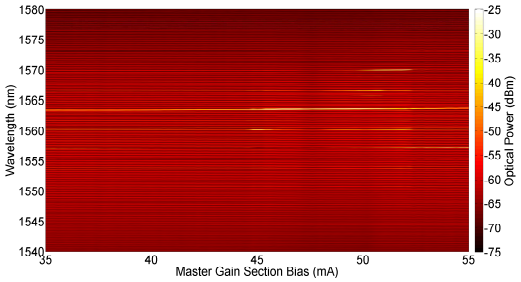

(d) OSA traces from the slave laser for a VOA bias = 1.081 V.

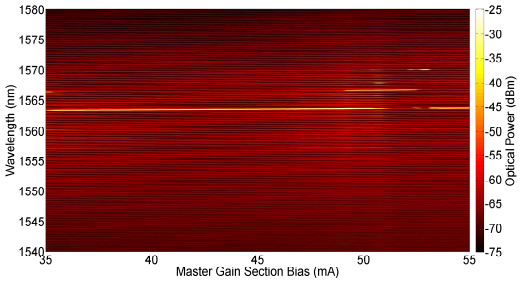

(e) OSA traces from the master laser for a VOA bias = 1.111 V.

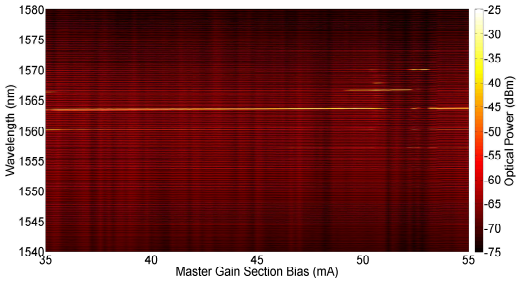

(f) OSA traces from the slave laser for a VOA bias = 1.111 V.

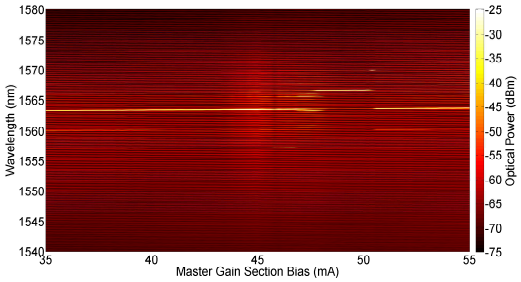

(g) OSA traces from the master laser for a VOA bias = 1.141 V.

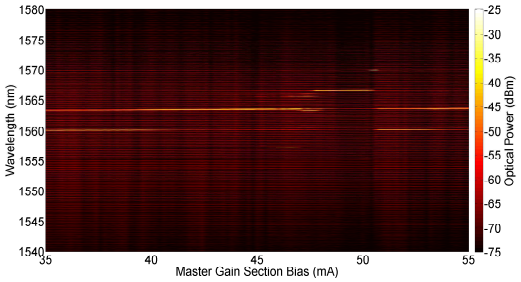

(h) OSA traces from the slave laser for a VOA bias = 1.141 V.

Figure 4.32: Colour plots of the OSA traces from the master and slave lasers for the on-chip coupling scheme, a slave gain section bias of 27 mA and various VOA biases.

Again the VOA was still absorbing at 1.051 V, resulting in very little interaction between the lasers. At VOA biases of 1.081 V and above, the coupling between the lasers was

strong enough that the lasers could interact and lock together. At high biases, the VOA became fully transparent and the whole PIC behaved as a compound laser rather than two separate SFP lasers. Comparing these colour plots with those obtained for the off-chip coupling regime (Figure 4.14), the results for a VOA bias of 1.111 V is most similar, suggesting that the VOA becomes transparent at this bias.

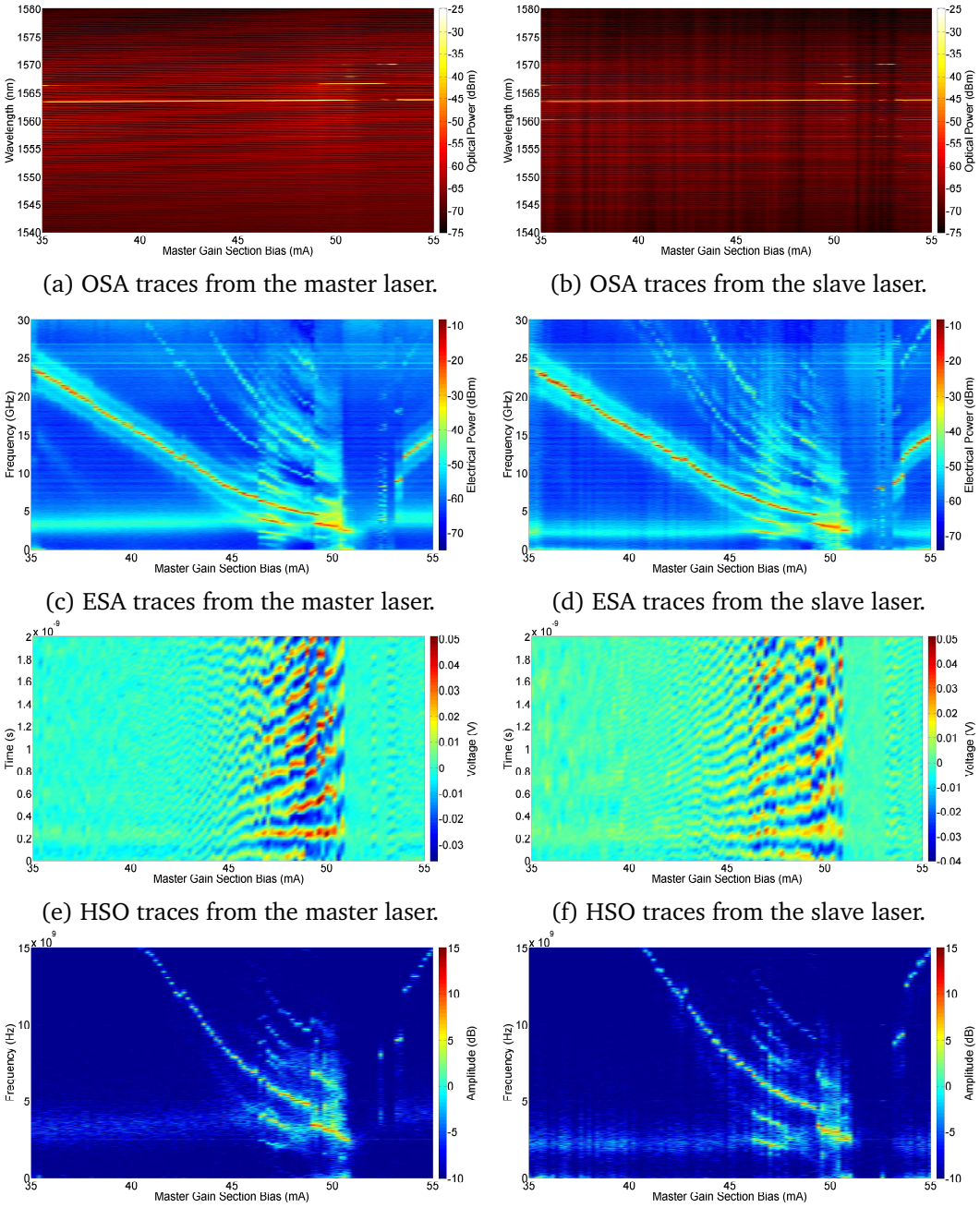

(a) OSA traces from the master laser.

(b) OSA traces from the slave laser.

(c) ESA traces from the master laser.

(d) ESA traces from the slave laser.

(e) HSO traces from the master laser.

(f) HSO traces from the slave laser.

(g) FFT of the HSO traces from the master laser.

(h) FFT of the HSO traces from the slave laser.

Figure 4.33: Output of the master and slave lasers for a VOA bias of 1.111 V and a S-GS bias of 27 mA (on-chip coupling scheme).

The colour intensity plots of the OSA, ESA and HSO traces from the M-SFP and S-SFP

for a VOA bias of 1.111 V are shown in Figure 4.33. The types of behaviour observed are similar to the off-chip coupling regime, Figure 4.14, however some of the new types of behaviour seen for a S-GS bias of 24 mA and the on-chip coupling regime (Figure 4.20) generated by the feedback between the lasers are also observed. Figure 4.34 provides a summary of the types of behaviour obtained from the M-SFP and the S-SFP during injection locking as a function of M-GS bias and VOA bias. The dashed line across the graphs represents the colour plots above for a VOA bias of 1.111 V. The three types of behaviour identified for the off-chip coupling regime; (i) beating, (ii) non-linear interactions (NLI) and (iii) locked, are also present for the on-chip coupling regime and new types of behaviour have been generated due to the feedback between the lasers. Irregular dynamics and aperiodic behaviour are exhibited by both the M-SFP and S-SFP.

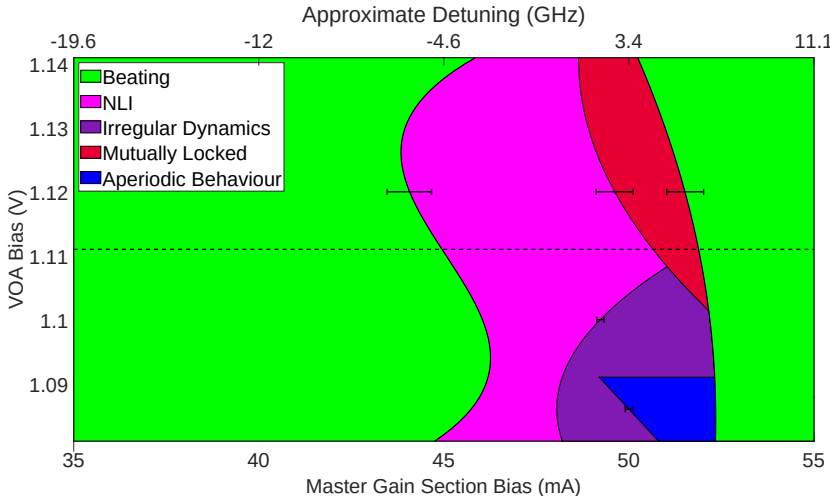

(a)

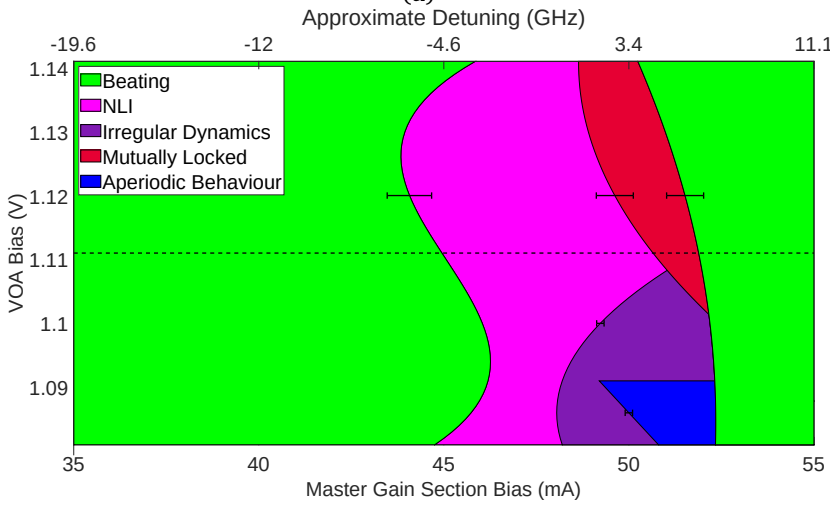

(b)

Figure 4.34: Summary of the types of behaviour obtained from (a) the M-SFP and (b) the S-SFP during injection locking as a function of M-GS bias, for a S-GS bias of 27 mA and the on-chip coupling regime. The errors associated with the data fitting is shown on each line.

Again, the lasers mutually injection lock to a higher mode. The locking width is also narrower due to the regions of irregular beating and aperiodic behaviour before the locking region. The regions of asymmetric beating and pulsing seen in Figure 4.28 for a S-GS bias of 24 mA are not seen for a S-GS bias of 27 mA. The approximate detuning between the free-running lasers is shown on the top x-axis of the summaries in Figure 4.34.

4.2.3 Comparison with Theoretical Results

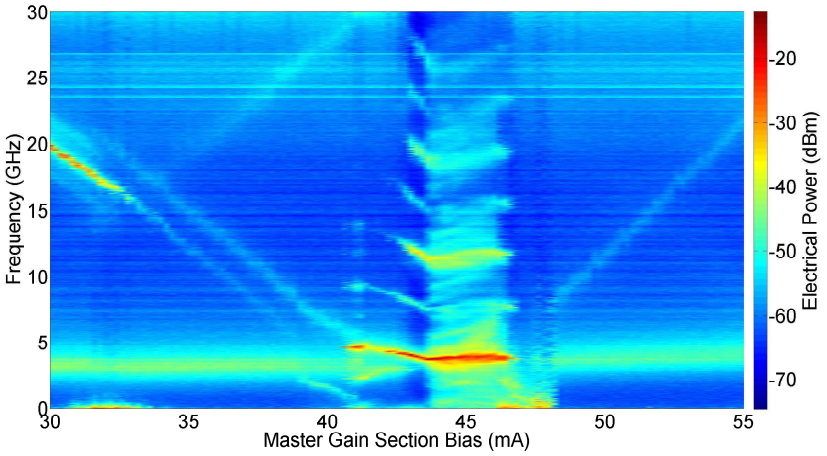

(a)

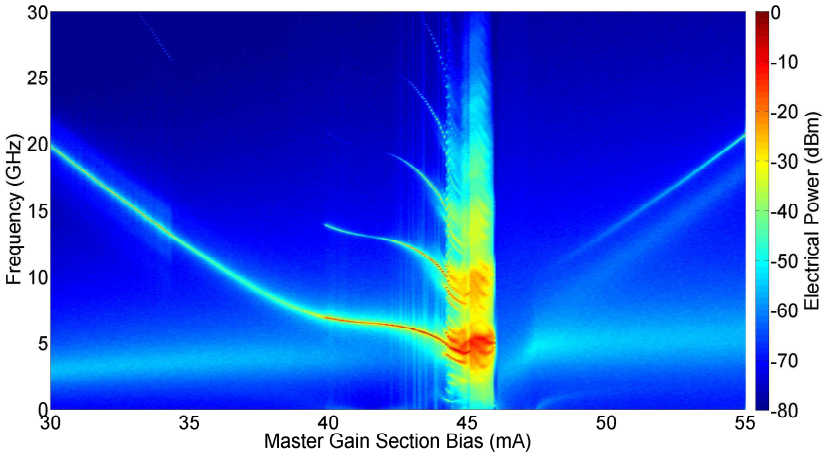

(b)

Figure 4.35: Colour plots of (a) the ESA traces from the master laser for the on-chip coupling scheme, a slave gain section bias of 24 mA and a VOA bias of 1.081 V on the 615 μm VOA PIC and (b) the simulated data reproducing the experiment [77].

Presenting these results opened up a collaboration with laser dynamics colleagues. A theoretical model was formulated which considered the dynamics of the two main laser modes in Figures 4.19c and d [77]. (This model was different to the model described in Equations 2.1 - 2.4.) It was found that by modelling the VOA as a saturable absorber,

the laser model accurately reproduced the qualitative dynamics of the asymmetric coupling setup. Figure 4.35 shows the comparison between the experimental and simulated data. (Figure 4.35a is a plot of the same data as Figure 4.18c.) The exact position and extent of the dynamical regions differ between simulation and experiment since the dynamics of only two laser modes were considered in the model. However, overall a very good agreement was obtained. This work indicates that the left-hand boundary of the mutually locked region in Figure 4.28 is saddle-node bifurcations and the right-hand boundary is either saddle-node bifurcations or a Hopf bifurcation. Since the coupling strength and phase cannot be tuned independently in the experiment and the coupling phase is unknown experimentally, exactly replicating the dynamics theoretically is challenging.

4.3 Conclusion

This chapter described the initial testing of laser interactions on photonic integrated circuits (PICs). The first PIC investigated consisted of two SF-SFP lasers integrated together through a 615 μm waveguide interconnect referred to as a VOA. One SFP, the slave, was biased at threshold and the bias (wavelength) of the other SFP, the master, was swept to obtain injection locking. Two types of coupling were investigated; off-chip coupling - where the VOA was reverse biased to make it absorbing and the SFPs were coupled externally via an optical circulator and on-chip coupling - where the VOA was forward biased to transparency so that the SFPs were coupled on the PIC without the need for a circulator.

For the off-chip coupling regime, the injection locking experiment was repeated for various S-GS biases. The three types of behaviour discussed in the previous chapter for injection locking the SFP to an external TLS were observed for each S-GS bias: (i) beating, where the lasers beat together and the detuning between the lasers can be seen on the ESA but the lasers do not interact, (ii) non-linear interactions (NLI), where the detuning between the lasers is small enough that they beat strongly together and (iii) injection locking, where the S-SFP is injection locked to the M-SFP and hence lases at the wavelength of the M-SFP.

The experiment was repeated for the on-chip coupling regime. The bias of the VOA section controls the coupling between the lasers, adding another variable and also introduces optical feedback into the system. The effect of the VOA bias on the interactions between the lasers was discussed. At low biases the VOA was absorbing, resulting in very little interaction between the lasers. Increasing the VOA bias allowed the lasers to interact and lock together. At high biases, the VOA became sufficiently transparent so that the whole PIC behaved as a compound laser rather than two separate SFP lasers. The three types of behaviour identified for the off-chip coupling regime were

also present for the on-chip coupling regime and new types of behaviour were generated by the feedback between the lasers. Irregular dynamics, asymmetric beating and aperiodic behaviour were exhibited by both the M-SFP and S-SFP, while pulsing was exhibited by the S-SFP alone. The biggest difference between the off and on-chip coupling regimes was that for the off-chip coupling regime when the lasers injection lock, the S-SFP locks to the M-SFP and both lasers then lase at the wavelength of the M-SFP. However, for the on-chip coupling regime when the lasers mutually injection lock, both lasers lock to a longer wavelength.

In all of the injection locking experiments discussed in this chapter, the lasers operated in a master-slave regime where the master was much higher powered than the slave. The next chapter will investigate if injection locking can be achieved when both lasers are equally powered and hence no longer operating in a master-slave regime.

Chapter 5

Mutually Coupled Lasers

In this chapter, the variable optical attenuator/amplifier (VOA) section is further investigated. The IV characteristics and absorption of the VOA is examined along with the effect of VOA bias on the free-running and coupled lasers. Mutual coupling between two equally powered lasers will then be demonstrated. A schematic of the PIC used is shown in Figure 5.1. Two identical SFP lasers were integrated together through a 1.1 mm VOA section. Again, SFP-1 was controlled by independently biasing the mirror, $I_{Mirror,1}$, and gain, $I_{Gain,1}$, sections of the laser. SFP-2 was similarly controlled by independently biasing its mirror, $I_{Mirror,2}$, and gain, $I_{Gain,2}$, sections. Forward or reverse biasing the VOA section controlled the amplification or attenuation of the optical signal and hence varied the power coupled between the lasers.

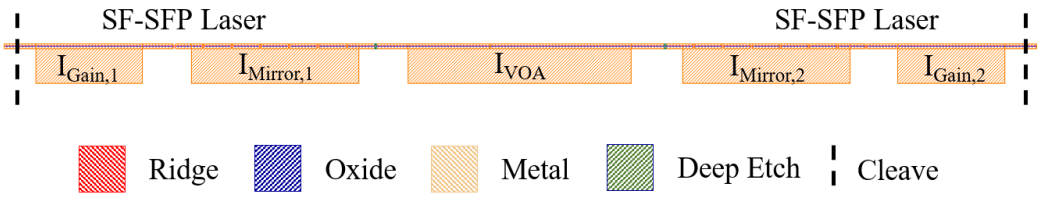

Figure 5.1: Schematic of the PIC. Two SF-SFP lasers are integrated together through a 1.1 mm VOA section. Laser 1 was tuned by varying the currents $I_{Mirror,1}$ and $I_{Gain,1}$. Laser 2 was tuned by varying the currents $I_{Mirror,2}$ and $I_{Gain,2}$. The VOA section was made absorbing by applying a negative bias or transparent by applying a positive bias.

5.1 The Variable Optical Attenuator/Amplifier Section

The IV characteristics of the VOA section were investigated by sweeping the voltage applied to the VOA between -4 V and 1 V while recording current. (All other sections on the device were left unbiased during this experiment.) The IV curve for the VOA is shown in Figure 5.2.

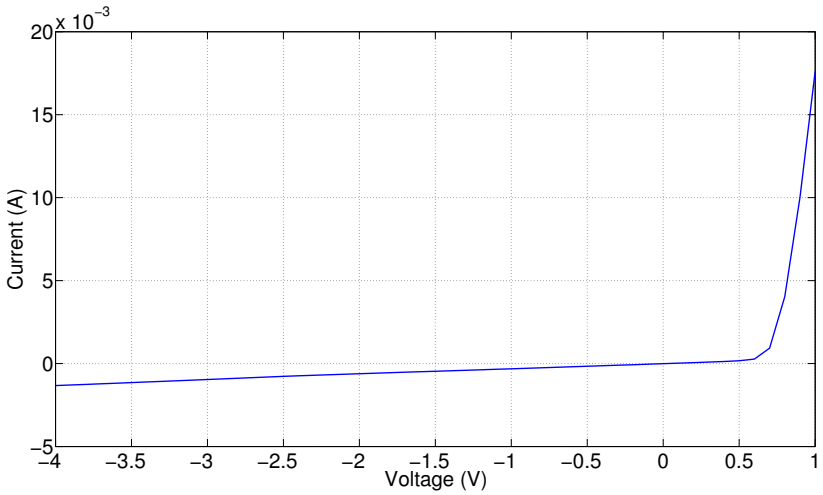

Figure 5.2: The IV characteristics of the VOA section.

The IV matches that of a diode with a turn-on voltage of approximately 0.7 V, which suggests that if biased high enough, the VOA could in fact lase or if the lasers are lasing that the full device would behave as a compound laser from facet-to-facet. The current was negative up to a voltage of ∼0 V, indicating that below this bias the VOA was absorbing and very little light could pass between the lasers. Above 0 V the VOA begins to become transparent and light begins to couple between the lasers, before increasing rapidly above the turn-on voltage.

The next step was to determine if the VOA section was long enough to absorb all of the light emitted by the lasers when reverse biased. SFP-1 was biased so that it lased strongly and the voltage applied to the VOA was swept between 1 V and -4 V while recording the current. In order to determine if the VOA was actually absorbing all of the light being emitted by the laser, the experiment was repeated, applying the voltage to the VOA section and SFP-2 while recording the current, see Figure 5.3 for a schematic of the setup.

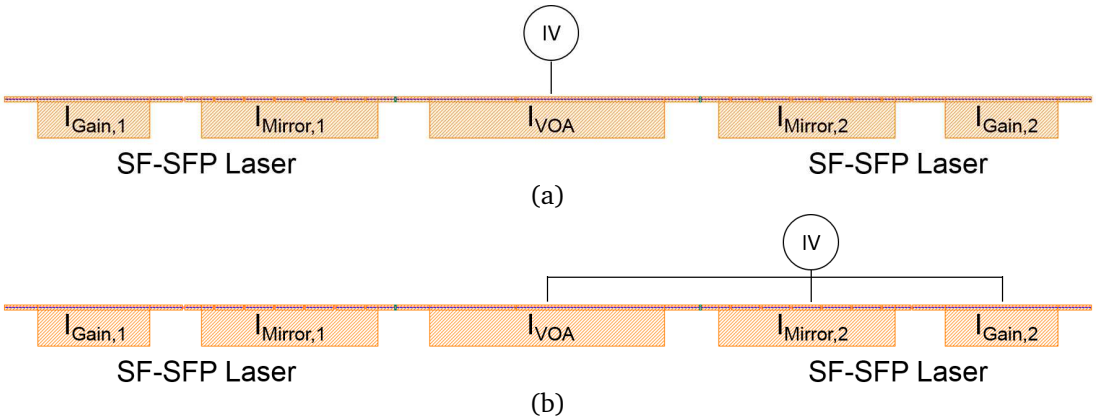

Figure 5.3: To determine if the VOA was long to absorb all of the light emitted by the lasers when reverse biased, SFP-1 was biased so that it lased strongly and an IV was carried out on (a) the VOA section and (b) the VOA section and SFP-2.

This experiment was repeated for SFP-2 and the results are plotted in Figure 5.4a. The current saturates at approximately -1 V, therefore either the VOA has absorbed all of the light emitted by the laser at this voltage or the VOA has saturated and cannot absorb any more light. The current recorded when the voltage was applied to the three sections (VOA section, SFP-2 mirror and gain sections) was very similar, hence applying a reverse bias of -1 V to the VOA is sufficient to absorb all of the light emitted by SFP-1. The results for SFP-2 were very similar, therefore the VOA is long enough to absorb all of the light emitted by one SFP. Next it was examined if the VOA was long enough to absorb the light emitted by both lasers simultaneously.

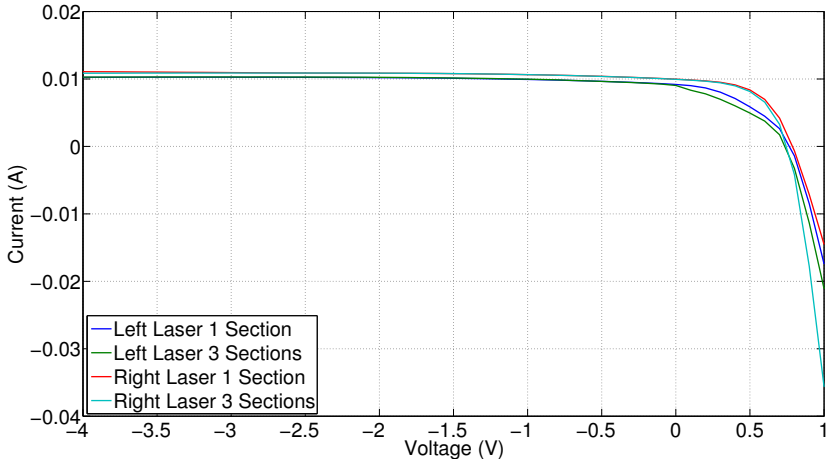

(a) Plot of current in the VOA section (1 section) and the VOA section and the second laser (3 sections) versus applied voltage when the lasers were biased separately.

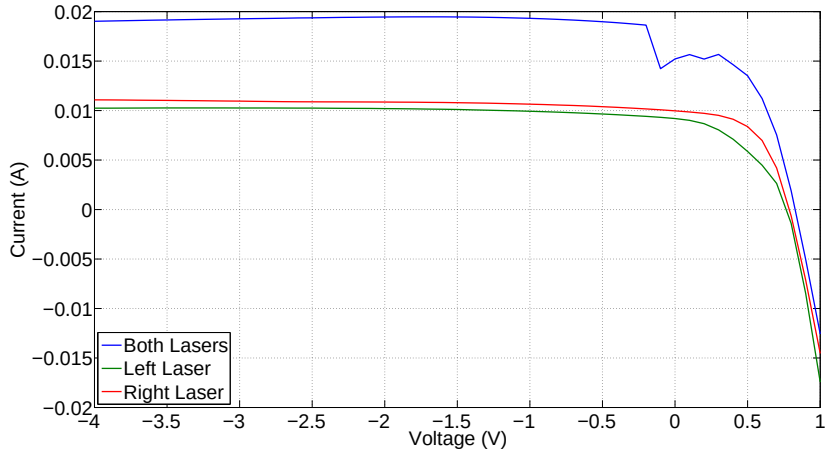

(b) Plot of current in the VOA section versus applied voltage for both lasers lasing separately and together.

Figure 5.4: IV curves to determine if the VOA section was long enough to absorb all of the light emitted by the lasers when reverse biased.

Both lasers were biased so that they lased strongly and an IV was performed on the VOA section. However, since both lasers were lasing, it was not possible to repeat the experiment for three sections. Figure 5.4 is a plot of current versus voltage for both lasers lasing separately and together. The current at -1 V when both lasers are lasing

together is almost equal to the sum of the currents when both lasers were lasing separately. During these experiments the light output at the facets was also monitored on a PM and the power output decreased slightly when both lasers were biased together, most likely due to heating effects. Therefore, it was concluded that the VOA was long enough to absorb all of the light from the lasers when reverse biased.

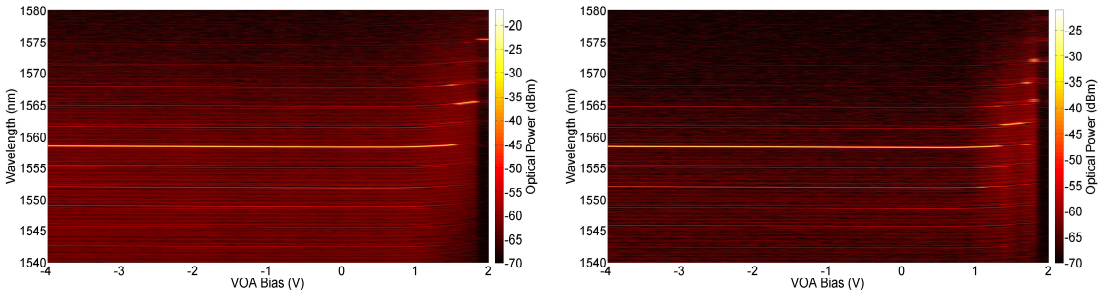

(a) (b)

Figure 5.5: Colour intensity plots of the optical spectra of (a) SFP-1 and (b) SFP-2 as the voltage applied to the VOA was varied.

SFP-1 was biased at mirror and gain section biases of 40 mA and 65 mA, respectively and the optical spectra of the laser were recorded while the VOA bias was varied between -4 V and 1 V to determine if the applied VOA voltage effected the optical output of the lasers. The experiment was repeated for SFP-2 and the results are plotted in Figure 5.5. The optical spectra of the lasers were not effected up to a VOA bias of approximately 1.4 V when the lasing mode shifted to a higher wavelength and the full device began to act as a compound laser. The bias of the VOA did not alter the optical spectra of the lasers in this device, however a deep etched area between the lasers and the VOA section was added to all future PIC designs to reduce the possibility of electrical cross-talk between the sections. After characterising the VOA section, the next step was to investigate the effect of the VOA bias on 'on-chip' locking.

5.2 Effect of VOA bias on 'On-Chip' Locking

Section 4.2 discussed the on-chip injection locking of two SFP lasers in detail. It was shown that a small change in VOA bias (0.01 V) had a large effect on the dynamical behaviour of the lasers. The VOA bias was therefore varied over a 0.1 V range. The 'on-chip' injection locking experiment was repeated using the PIC described in Figure 5.1 for various VOA biases between -1.5 and +1.5 V. The mirror sections of both lasers were biased at 40 mA. The gain section of SFP-2 was biased at 65 mA and the bias of the gain section of SFP-1 was swept between 20 mA and 120 mA. SFP-1 will be referred to as the master laser and SFP-2 as the slave in the following. Colour intensity plots of the ESA and OSA traces are shown in Figure 5.6.

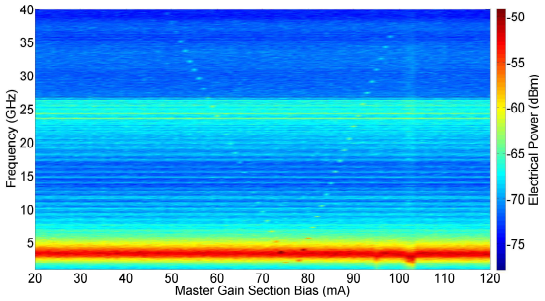

(a) ESA traces from the S-SFP as the wavelength of the M-SFP was swept across resonance with its modes, for a VOA bias of -0.5 V.

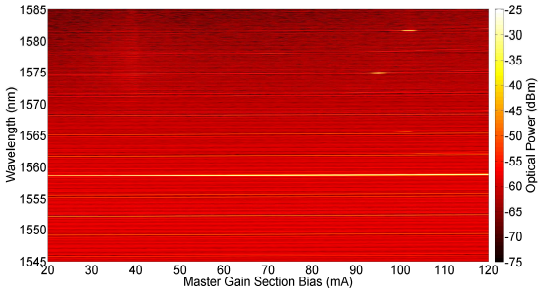

(b) OSA traces from the S-SFP as the wavelength of the M-SFP was swept across resonance with its modes, for a VOA bias of -0.5 V.

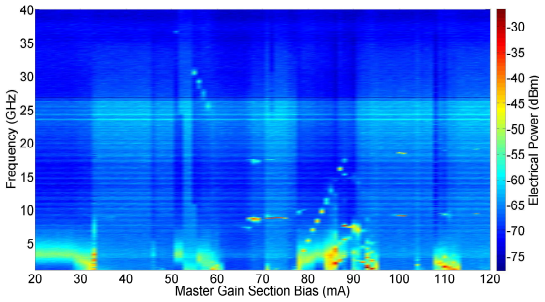

(c) ESA traces from the S-SFP as the wavelength of the M-SFP was swept across resonance with its modes, for a VOA bias of 0.0 V.

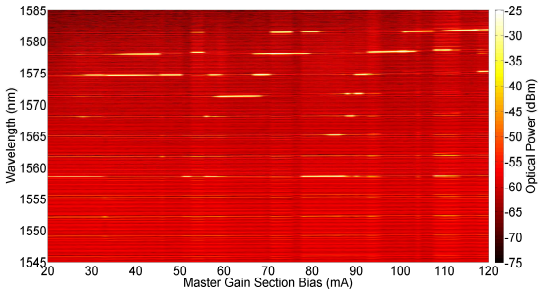

(d) OSA traces from the S-SFP as the wavelength of the M-SFP was swept across resonance with its modes, for a VOA bias of 0.0 V.

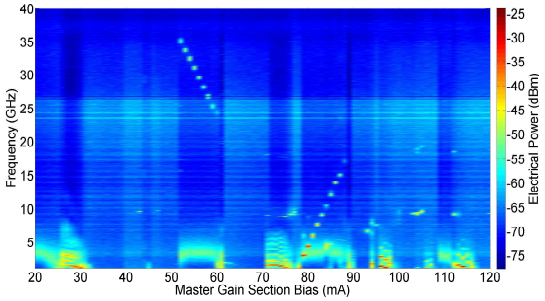

(e) ESA traces from the S-SFP as the wavelength of the M-SFP was swept across resonance with its modes, for a VOA bias of 0.5 V.

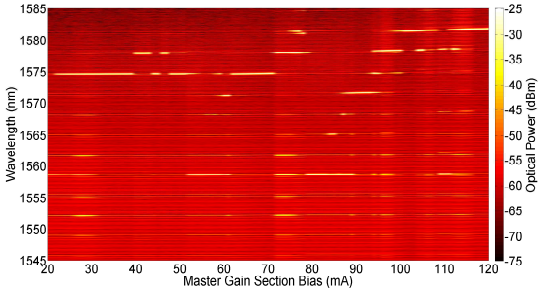

(f) OSA traces from the S-SFP as the wavelength of the M-SFP was swept across resonance with its modes, for a VOA bias of 0.5 V.

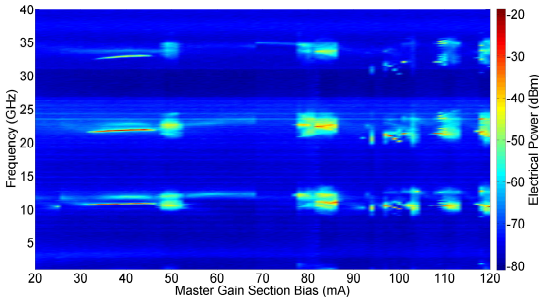

(g) ESA traces from the S-SFP as the wavelength of the M-SFP was swept across resonance with its modes, for a VOA bias of 1.0 V.

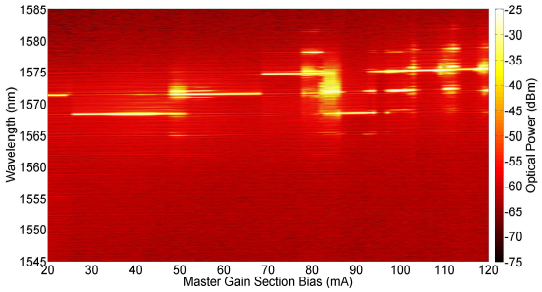

(h) OSA traces from the S-SFP as the wavelength of the M-SFP was swept across resonance with its modes, for a VOA bias of 1.0 V.

Figure 5.6: ESA and OSA traces from the slave SFP as the wavelength of the master SFP was swept across resonance with its modes, for various VOA biases.

For a VOA bias of -0.5 V (and higher negative biases), a faint beat note can be seen in the electrical spectra, Figure 5.6a. The amplitude of the beat note is less that the RO's, therefore it was concluded that the VOA was still absorbing at this bias and the lasers were isolated from each other. At this VOA bias, the optical spectra, Figure 5.6b, as expected, remained unchanged, since the lasers did not interact.

The results obtained for VOA biases of 0.0 V and 0.5 V (Figures 5.6c-f) were what was expected for the 'on-chip' injection locking experiment described in Section 4.2. The VOA was semi-transparent at these biases and light coupled between the lasers allowing them to interact. Various beat notes were observed in the electrical spectra and the lasing wavelength of the slave jumps between various modes. At a VOA bias of 0.5 V, regions of injection locking were obtained for master gain section biases between 45 mA - 50 mA, 61 mA - 66 mA and 95 mA - 99 mA.

Biasing the VOA at 1.0 V (or higher) completely changed the behaviour of the lasers (Figures 5.6g-h). The only beat notes observed in the electrical spectra were around 11 GHz (the beat notes at ∼22 GHz and ∼33 GHz are harmonics of the beat notes at ∼11 GHz). Converting Equation 3.1 to frequency using $\Delta\lambda = \lambda^2\Delta\nu/c$ gives

$$\Delta\nu = \frac{c}{2n_{gr}L}. \tag{5.1}$$

where n_{gr} is the group index and L is the cavity length. Therefore, a frequency of approximately 11 GHz corresponds to a cavity length of ∼3.9 mm which is equal to the FP length of the device, from facet to facet.

Broadening of the optical modes also occurred. The FFT of the optical spectra of the lasers was performed to determine the cavities present. Figure 5.7a shows the cavities present for a VOA bias of -0.5 V. The highest peak is at 579.7 μm, which corresponds to the gain section of the SFP laser. The six peaks to the right of this peaks, each separated by ∼108 μm (the separation between the slots in the mirror section), are the gain section + the cavities created by the slots in the mirror section.

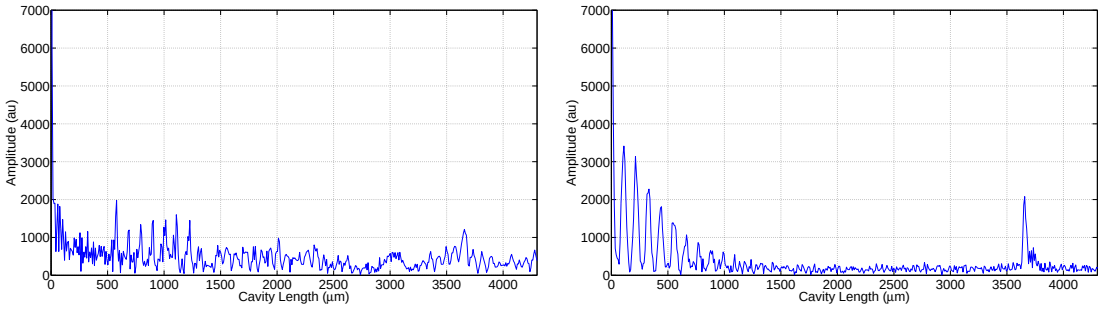

(a) (b)

Figure 5.7: FFT of the optical spectra for a VOA bias of (a) -0.5 V and (b) 1.0 V.

For VOA bias = 1.0 V, Figure 5.7b, the highest peak is at 110.8 μm (the approximate distance between the slots) and the peaks to its right are multiples of this. There is also

a significant peak at 3657 μm which corresponds to the length of the full device from facet-to-facet. (Using equation 5.1, a cavity of 3.66 mm equals a frequency of 11.7 GHz, which corresponds to the pale blue lines across the colour plot of the electrical spectra, Figure 5.6g.) Therefore it was concluded that at this bias, the VOA was sufficiently transparent so that the full device behaved as a compound laser.

The VOA bias has a large effect on the injection locking properties of the system; if the VOA bias is too low, the VOA is absorbing; isolating the lasers from each other and injection locking cannot be obtain, if the VOA bias is too high, the VOA is fully transparent and the full device behaves as a compound laser. Biasing the VOA to semi-transparency allows the lasers to interact and mutual locking can then be obtained.

Figure 5.5 shows that for mirror and gain section biases of 40 mA and 65 mA both lasers have very similar optical spectra. All previous injection locking experiments were based on a master-slave system where one laser, the master, was much higher power than the other laser, the slave. Applying the same bias to both lasers and obtaining similar optical spectra results in both lasers being equally powered. Therefore, having verified the work presented in [44, 45], the next experiment carried out investigated, for the first time, the dynamics that occur when the coupling, VOA bias, between two equally powered SFP lasers is varied.

5.3 Mutually Coupled Lasers

Both lasers in Figure 5.1 were biased at, mirror/gain section, 40 mA/65 mA. Both lasers were equally powered and had very similar spectra, see Figure 5.8, and were therefore no longer operating in a master-slave system.

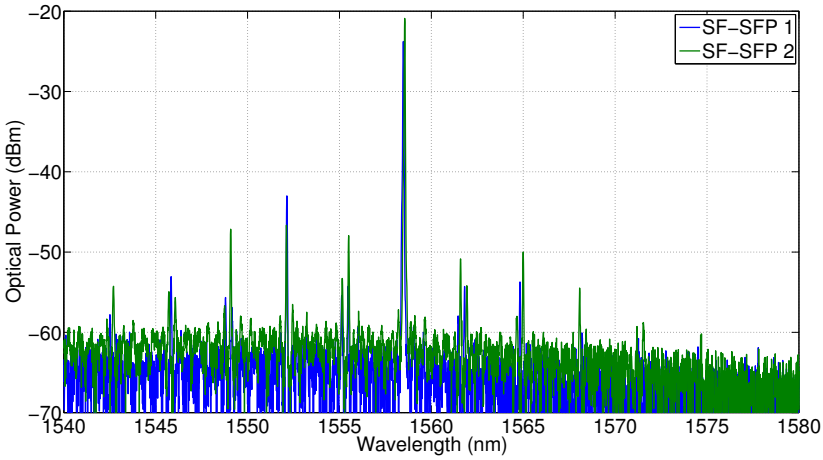

Figure 5.8: Optical spectra of SFP-1 and SFP-2 for mirror and gain section biases of 40 mA and 65 mA, respectively.

Fixing the biases of both lasers, meant that both lasers were fixed at the same wavelength and power. The VOA bias was swept from +1 V to -1 V, thus varying the coupling

between the lasers. The output of both lasers was recorded on the ESA, OSA and HSO and are plotted in Figure 5.9.

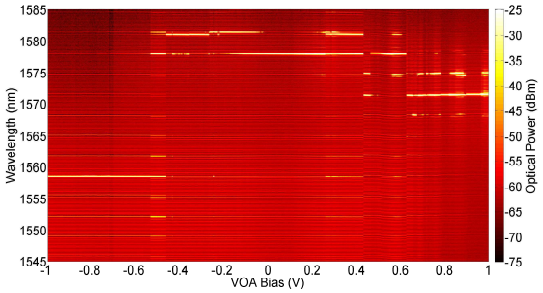

(a) Colour plot of the OSA traces from SFP-1.

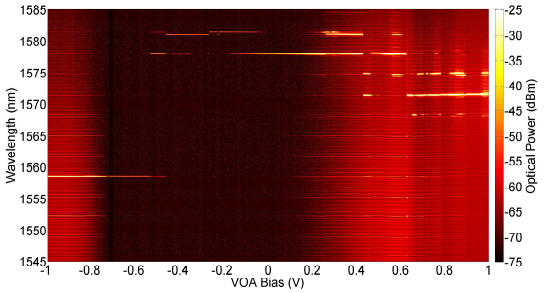

(b) Colour plot of the OSA traces from SFP-2.

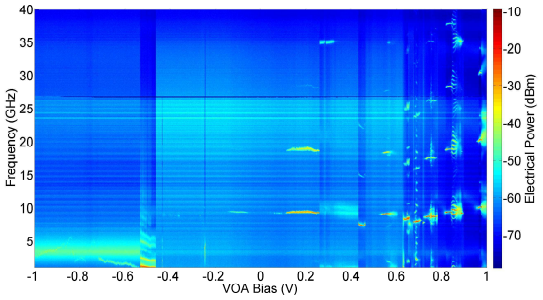

(c) Colour plot of the ESA traces from SFP-1.

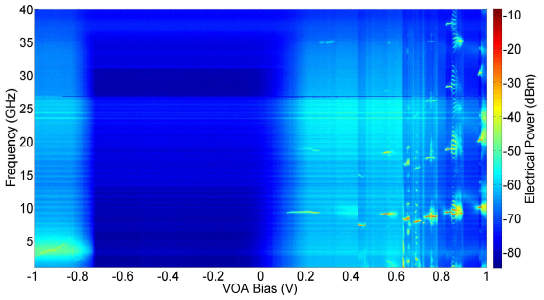

(d) Colour plot of the ESA traces from SFP-2.

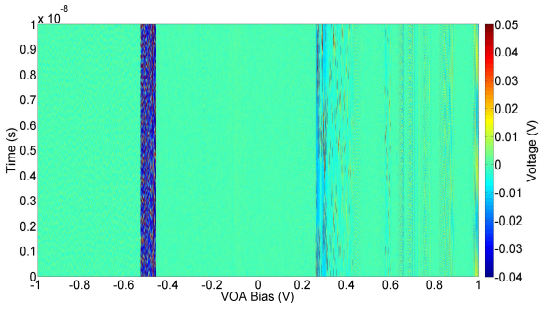

(e) Colour plot of the HSO traces from SFP-1.

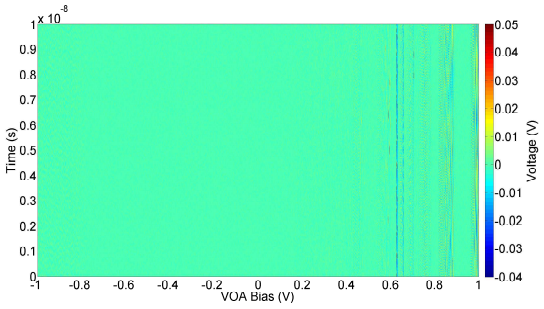

(f) Colour plot of the HSO traces from SFP-2.

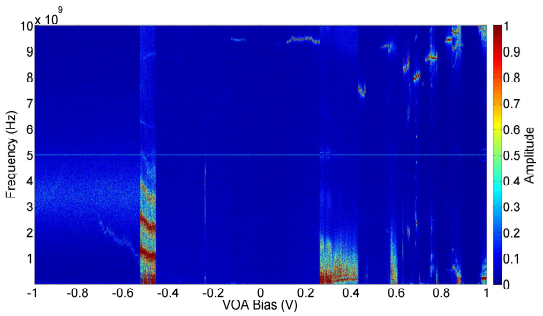

(g) Colour plot of the FFT of the HSO traces from SFP-1.

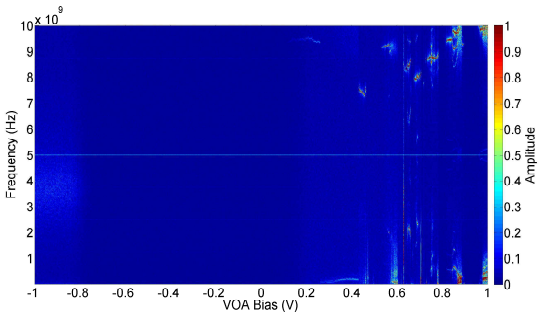

(h) Colour plot of the FFT of the HSO traces from SFP-2.

Figure 5.9: Output of SFP-1 and SFP-2 as a function of VOA bias for mirror/gain section biases of 40 mA/65 mA.

A step size of 1 mV was used for the VOA bias sweep between +1 V to -1 V, therefore the sweep took approximately 17 hrs. The NanoTrak on the lensed fibre used to couple light from SFP-1 was able to maintain coupling over this time but the lensed fibre

coupled to SFP-2 drifted away from the laser facet at a VOA bias of approximately 0.1 V and drifted back at approximately -0.7 V due to changes in the air-conditioning in the lab. Between these biases very little light was coupled into the fibre and nothing was observed in the measurements.

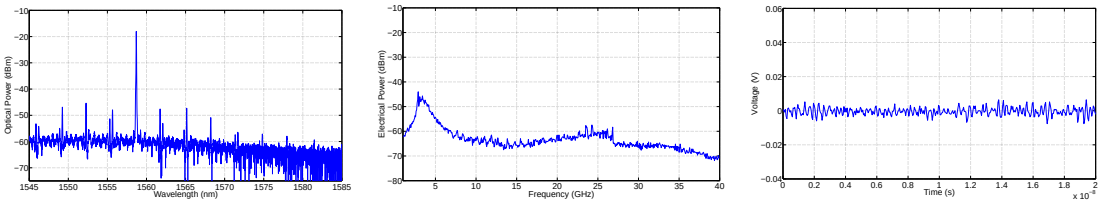

(a) (b) (c)

Figure 5.10: (a) OSA, (b) ESA and (c) HSO traces from SFP-1 for a VOA bias of -1.000 V (Cross-sections of Figure 5.9).

The VOA was absorbing for VOA biases below -0.532 V, thus isolating the lasers. They were free-running and their optical spectra are shown in Figure 5.8. The optical and electrical spectra and the time trace from SFP-1 for a VOA bias of -1 V are shown in Figure 5.10. The RO's can be clearly seen at 2.5 GHz and noise is observed on the HSO.

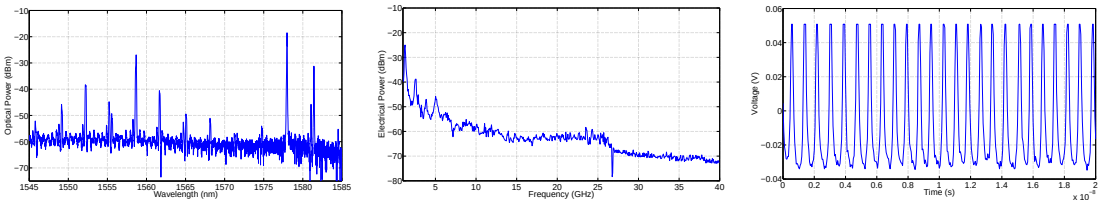

(a) (b) (c)

Figure 5.11: (a) OSA, (b) ESA and (c) HSO traces from SFP-1 for a VOA bias of -0.532 V (Cross-sections of Figure 5.9).

Increasing the VOA bias, the VOA began to become transparent and the lasers began to interact. For VOA biases between -0.532 V and -0.462 V the lasers underwent multimode behaviour and higher wavelengths appeared in the optical spectra, see Figure 5.11a. Strong beating, with a frequency of 1.25 GHz, between the lasers was also observed on the ESA and HSO, see Figures 5.11b and c.

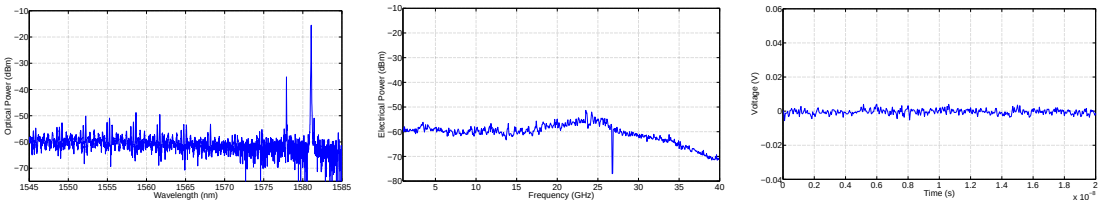

(a) (b) (c)

Figure 5.12: (a) OSA, (b) ESA and (c) HSO traces from SFP-1 for a VOA bias of -0.463 V (Cross-sections of Figure 5.9).

At biases above -0.462 V, the RO's have been suppressed and between VOA biases of -0.463 V and -0.247 V, there is no beating observed on the ESA or HSO, Figures 5.12b

and c. The natural lasing modes of the lasers (between 1545 nm and 1565 nm) have been suppressed and the lasers now lase at approximately 1577.9 nm and 1581.1 nm, Figure 5.12a. This shift to longer wavelengths is unexpected as the lasers now lase beyond the gain peak of the material.

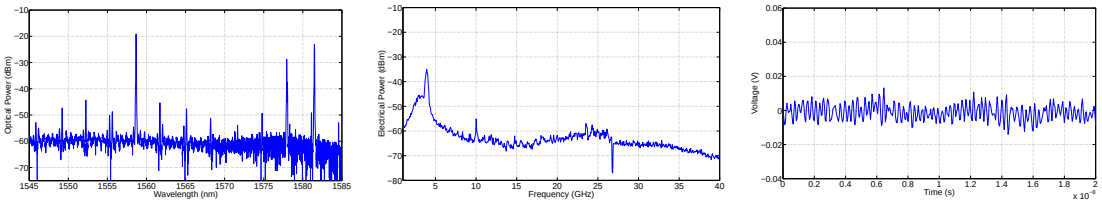

(a) (b) (c)

Figure 5.13: (a) OSA, (b) ESA and (c) HSO traces from SFP-1 for a VOA bias of -0.247 V (Cross-sections of Figure 5.9).

There is a narrow region of VOA biases between -0.247 V and -0.243 V where both the natural lasing modes of the lasers and the higher wavelength modes are present in the optical spectra, Figure 5.13a. There is a beat note at 3.9 GHz in the electrical spectrum and some irregular beating on the HSO, Figures 5.13b and c. Behaviour similar to Figure 5.12 is observed up to a VOA bias of 0.115 V, where only the higher wavelength modes are observed in the optical spectra. No beating is seen in the time trace or the electrical spectra, except for a narrow, low amplitude beat note at approximately 9.5 GHz for VOA biases between -0.134 V and 0.055 V and between 0.060 V and 0.094 V.

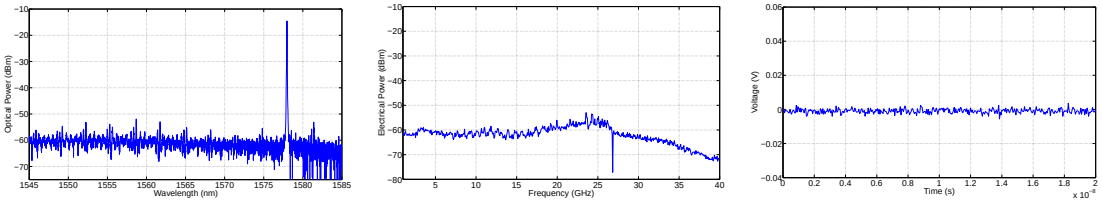

(a) (b) (c)

Figure 5.14: (a) OSA, (b) ESA and (c) HSO traces from SFP-1 for a VOA bias of -0.016 V (Cross-sections of Figure 5.9).

The lasers lock to the mode at 1578 nm for VOA biases between -0.016 V and 0.059 V, Figure 5.14a. No beating between the laser was observed on the ESA and HSO, Figures 5.14b and c, confirming that the lasers were indeed mutually injection locked.

As the VOA bias increases past 0.115 V, the lasers continue to lase at 1578 nm and no beating is observed on the HSO. However, two narrow beat notes at approximately 9.3 GHz and 18.6 GHz appear in the electrical spectra, Figure 5.15. 9.3 GHz corresponds to a wavelength detuning of approximately 0.077 nm. Zooming in on the mode at 1578 nm, shows a lower amplitude side-mode approximately 0.077 nm away from the main mode. The same output was obtained from SFP-2.

At a VOA bias of 0.262 V, the beat notes at 9.3 GHz and 18.6 GHz in the electrical

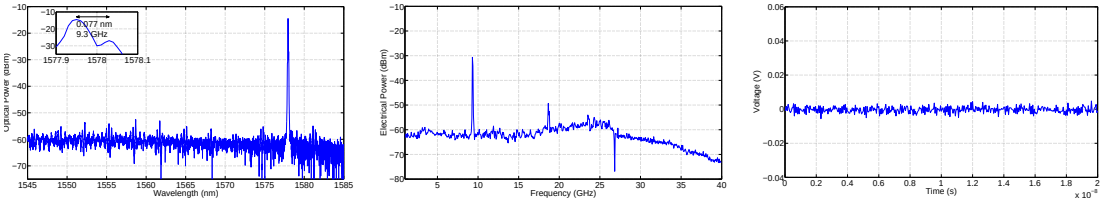

(a) (b) (c)

Figure 5.15: (a) OSA, (b) ESA and (c) HSO traces from SFP-1 for a VOA bias of 0.115 V (Cross-sections of Figure 5.9).

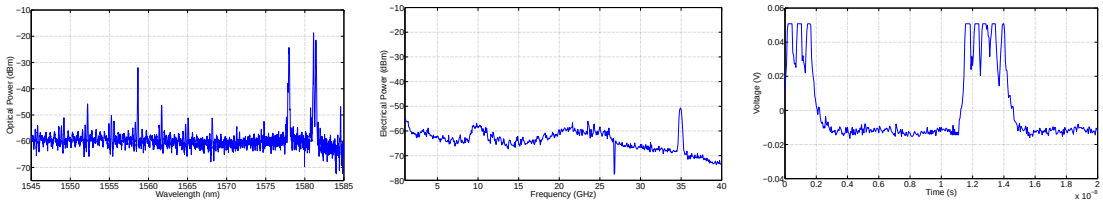

(a) (b) (c)

Figure 5.16: (a) OSA, (b) ESA and (c) HSO traces from SFP-1 for a VOA bias of 0.262 V (Cross-sections of Figure 5.9).

spectra disappear and a peak at approximately 35 GHz appears, Figure 5.16b. The lasers begin to lase again at their natural lasing wavelengths as well as the higher wavelength modes, Figure 5.16a. The time trace show pulsing behaviour at 0.085 GHz, Figure 5.16c.

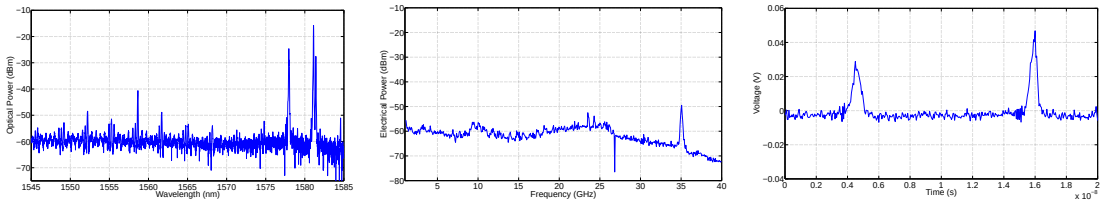

(a) (b) (c)

Figure 5.17: (a) OSA, (b) ESA and (c) HSO traces from SFP-1 for a VOA bias of 0.319 V (Cross-sections of Figure 5.9).

The time traces change to a more regular pulsing behaviour, Figure 5.17c, at a VOA bias of 0.319 V, while the optical and electrical spectra remain the same, Figures 5.17a and b.

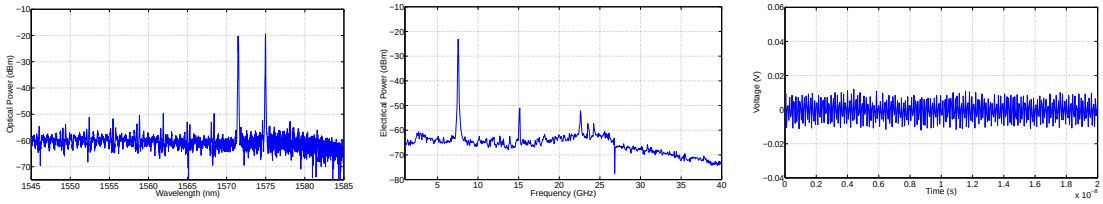

(a) (b) (c)

Figure 5.18: (a) OSA, (b) ESA and (c) HSO traces from SFP-1 for a VOA bias of 0.432 V (Cross-sections of Figure 5.9).

The pulsing behaviour continues till a VOA bias of 0.432 V where the time trace changes to irregular beating with a frequency of approximately 7.5 GHz, Figure 5.18c. The natural lasing modes of the lasers, between 1545 nm and 1565 nm, along with the higher wavelength modes at 1578 nm and 1581 nm have been suppressed and the lasers now lase at 1571.5 nm and 1575nm, Figure 5.18a. The 7.5 GHz beat note and its harmonics at 15 GHz and 22.5 GHz can be seen in the electrical spectrum, Figure 5.18b. At a VOA bias of 0.464 V, the behaviour becomes similar to that shown in Figure 5.12 but the lasing modes are now at 1571.5 nm and 1578 nm. There are two narrow regions of mutual injection locking for VOA biases between 0.485 V - 0.492 V and 0.505 V - 0.524 V, where the lasers lock to the mode at 1578 nm, similar to Figure 5.14. The behaviour becomes similar to Figure 5.15 again at a VOA bias of 0.528 V. The pulsing behaviour returns at a VOA bias of 0.574 V and at a VOA bias of 0.602 V, the behaviour becomes similar to that shown in Figure 5.12 again but the lasing modes are now at 1574.8 nm, 1578 nm and 1581. The behaviour then becomes similar to Figure 5.18 at a VOA bias of 0.635 V.

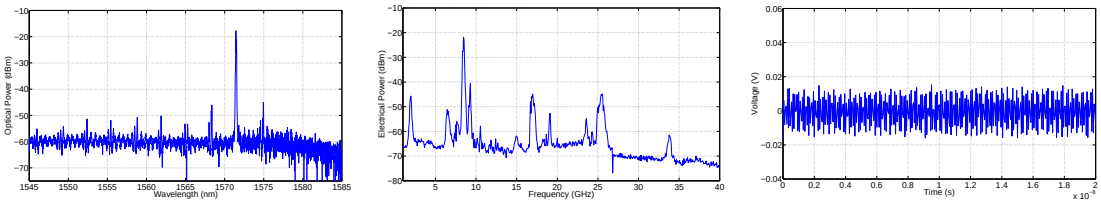

(a) (b) (c)

Figure 5.19: (a) OSA, (b) ESA and (c) HSO traces from SFP-1 for a VOA bias of 0.646 V (Cross-sections of Figure 5.9).

The lasers continue to lase at approximately 1571.5 nm as the VOA bias increases to 0.646 V, Figure 5.19a. Irregular beating is observed in the time traces, Figure 5.19c. However, the beat notes in the electrical spectra broaden and many more appear, Figure 5.19b. At a VOA bias of 0.658 V the behaviour of the lasers becomes similar to Figure 5.12 again and the mode at 1568.4 nm is amplified.

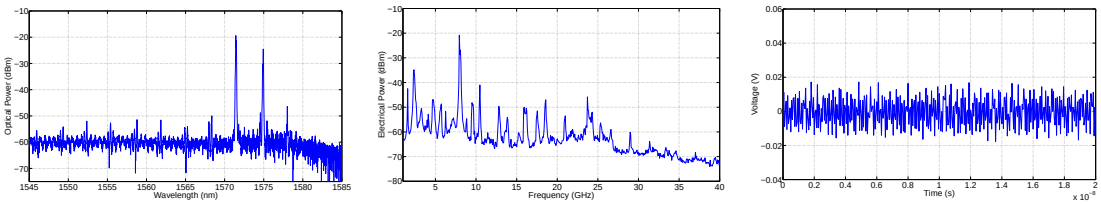

(a) (b) (c)

Figure 5.20: (a) OSA, (b) ESA and (c) HSO traces from SFP-1 for a VOA bias of 0.687 V (Cross-sections of Figure 5.9).

Continuing increasing the VOA bias to 0.687 V suppresses the mode at 1572 nm and amplifies the mode at 1575 nm, Figure 5.20a and more beat notes are observed in the ESA trace, Figure 5.20b, while the time traces remain similar irregular beating, Figure 5.20c. At a VOA bias of 0.702 V, the behaviour becomes similar to Figure 5.15 again

with the lasers lasing at 1568.4 nm, 1571.5 nm and 1574.9 nm.

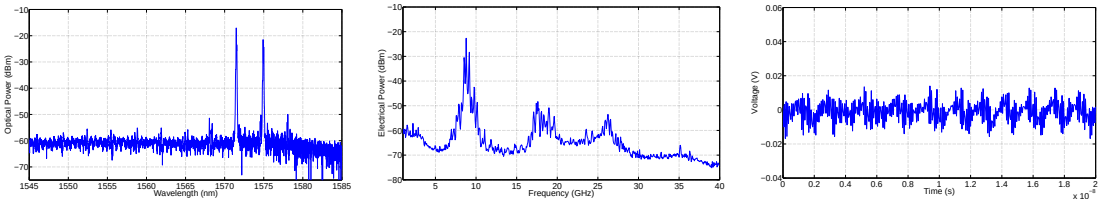

(a) (b) (c)

Figure 5.21: (a) OSA, (b) ESA and (c) HSO traces from SFP-1 for a VOA bias of 0.751 V (Cross-sections of Figure 5.9).

The behaviour changes again at a VOA bias of 0.751 V. The lasers lase at 1571.5 nm and 1575 nm, Figure 5.21a. There are broad peaks in the electrical spectrum at 8.8 GHz and its harmonics, Figure 5.21b. The time trace, Figure 5.21c, shows irregular beating with a 0.55 GHz pattern. At a VOA bias of 0.759 V, the behaviour of the lasers becomes similar to Figure 5.18 again and at a VOA bias of 0.787 V, the behaviour becomes similar to Figure 5.15 again with the lasers lasing at 1571.6 nm.

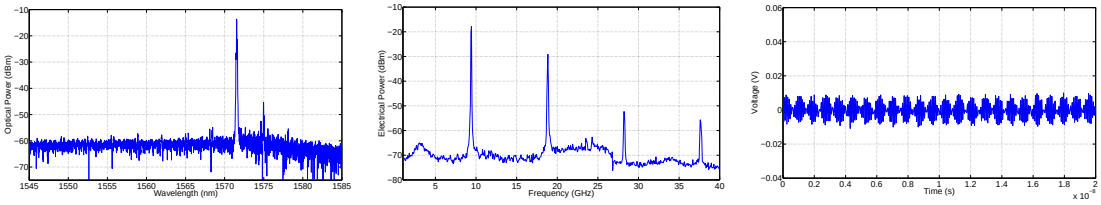

(a) (b) (c)

Figure 5.22: (a) OSA, (b) ESA and (c) HSO traces from SFP-1 for a VOA bias of 0.820 V (Cross-sections of Figure 5.9).

Further increasing the VOA bias to 0.820 V, the lasers continue to lase at 1571.6 nm, Figure 5.22a and a 9.4 GHz beat note and its harmonics are observed in the ESA trace, Figure 5.22b. The time trace, Figure 5.22c, shows irregular beating with a 1.2 GHz envelope.

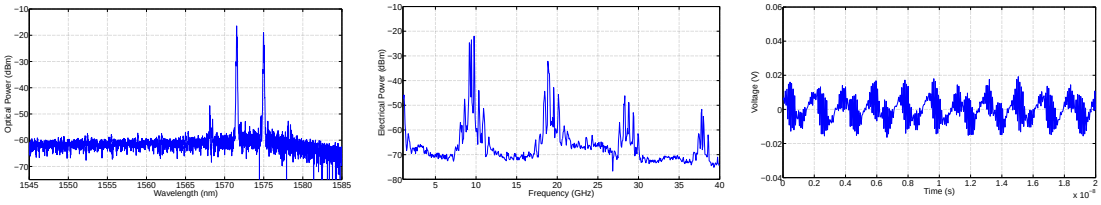

(a) (b) (c)

Figure 5.23: (a) OSA, (b) ESA and (c) HSO traces from SFP-1 for a VOA bias of 0.845 V (Cross-sections of Figure 5.9).

As the VOA bias increases the lasing mode at 1575 nm is amplified, Figure 5.23a. The beat notes in the electrical spectra broaden and small peaks appear at both sides of the main beat notes, Figure 5.23b. The signal on the HSO, Figure 5.23c, has also changed.

Increasing the VOA bias to 0.868 V, results in the amplification and broadening of the

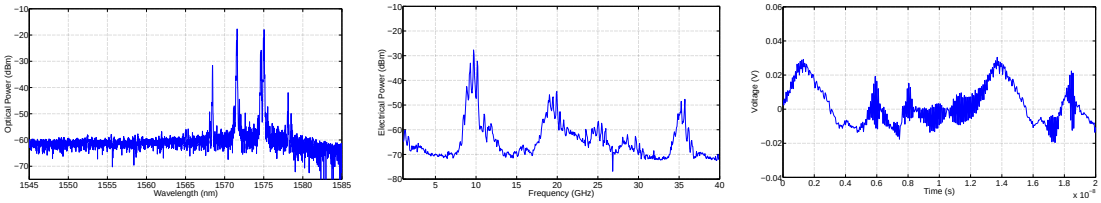

(a) (b) (c)

Figure 5.24: (a) OSA, (b) ESA and (c) HSO traces from SFP-1 for a VOA bias of 0.868 V (Cross-sections of Figure 5.9).

higher wavelength lasing modes, Figure 5.24a. The beat notes in the electrical spectra, Figure 5.24b, have also broadened. The time traces, Figure 5.24c have become more aperiodic. At a VOA bias of 0.894 V, the behaviour becomes similar to Figure 5.15 again with the lasers lasing at 1571.6 nm and 1575 nm. The behaviour then, becomes similar to Figure 5.22 with an envelope of approximately 0.083 GHz at a VOA bias of 0.962 V.

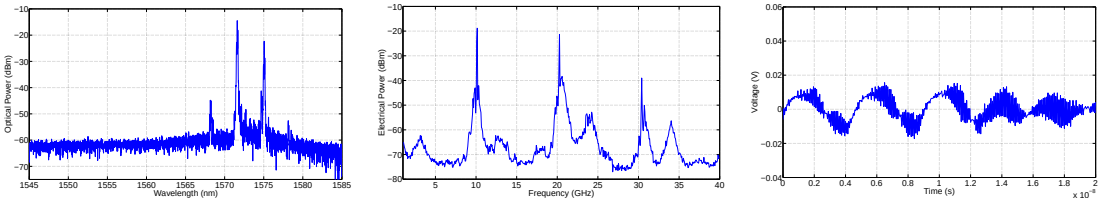

(a) (b) (c)

Figure 5.25: (a) OSA, (b) ESA and (c) HSO traces from SFP-1 for a VOA bias of 0.976 V (Cross-sections of Figure 5.9).

The frequency of the envelope increases with increasing VOA bias until 0.976 V where the behaviour changes to Figure 5.25c. The higher wavelength modes have broadened again, Figure 5.25a, and the 10 GHz beat note and its harmonics in the electrical spectra, Figure 5.25b are also broadened.

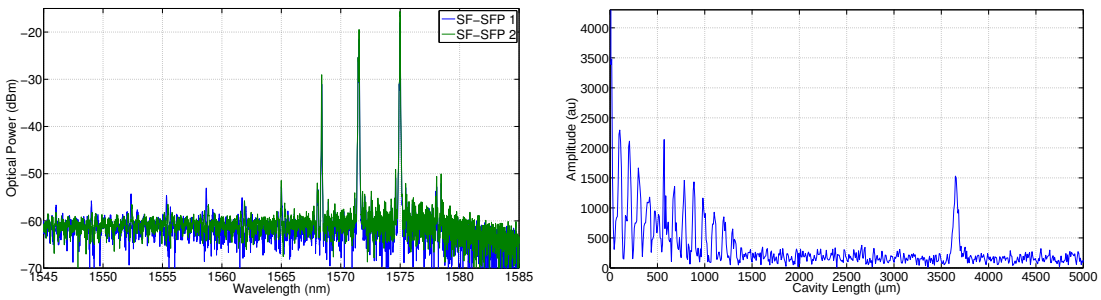

(a) (b)

Figure 5.26: (a) OSA traces and (b) FFT of the OSA trace for a VOA bias of 0.779 V.

The VOA was fully transparent for biases above ∼0.635 V. Above this bias, the full device behaved as a compound laser from facet-to-facet with a main lasing mode at 1571.5 nm. The optical spectra from both facets are exactly the same, see Figure 5.26a, confirming that both lasers and the VOA section were lasing together. The FFT of the

optical spectra was performed to identify the cavity lengths present in the system. The result is plotted in Figure 5.26b. The large peak at 570 nm corresponds to the length of the gain section of the SFP. The seven peaks to the right of this peak correspond to the cavities created by the gain section and the slots. The peaks to the left are the cavities created by the slots. The peak at 3650 nm corresponds to the full cavity from facet-to-facet, again confirming that the full device is lasing.

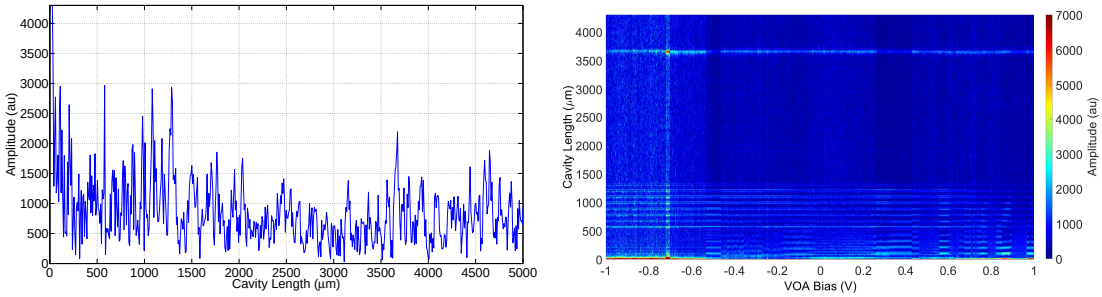

(a) (b)

Figure 5.27: (a) FFT of the OSA trace for a VOA bias of -1 V and (b) Colour plot of the FFT of the OSA traces from SFP-1.

The FFT of the optical spectrum obtained from SFP-1 at a VOA bias of -1 V (Figure 5.10a) was performed so that the cavity lengths present in the system when the lasers were isolated could be compared with the cavity lengths identified for the compound laser, Figure 5.27a. However, the FFT is very noisy but the peak at 3650 nm is still present. The colour plot of the FFT of the OSA traces from SFP-1 in Figure 5.27b shows that the peak at 3650 nm is present at nearly all VOA biases from -1 V to 1 V.

An attempt was then made to measure the coupling between the lasers by recording the photocurrent generated in the lasers at each VOA bias. The results are plotted in Figure 5.28. Figures 5.28c and b show that the VOA bias has very little effect on the LI characteristics of the lasers. It was expected that at a VOA bias of -1 V, there would be no light coupling between the lasers therefore, very little photocurrent would be measured in the lasers and that the photocurrent would increase with increasing VOA bias. Figures 5.28c and d show that this is true for low gain section biases, but at high gain section biases the VOA bias had very little effect on the photocurrent measured. It was realised that the light from each laser was going down into the substrate and coupling into the other laser, rather than only coupling into the other laser via the waveguide interconnect between the lasers. Therefore reverse biasing the VOA could not fully isolate the lasers. This explains why the cavity length corresponding to the full device from facet-to-facet was present at all VOA biases in Figure 5.27b. This substrate coupling cannot be completely eliminated but changing the design of the PIC can greatly reduce its effect. The next chapter will examine new PIC designs where the VOA will be curved and the lasers will not be in a straight line, which will reduce the effect of substrate coupling.

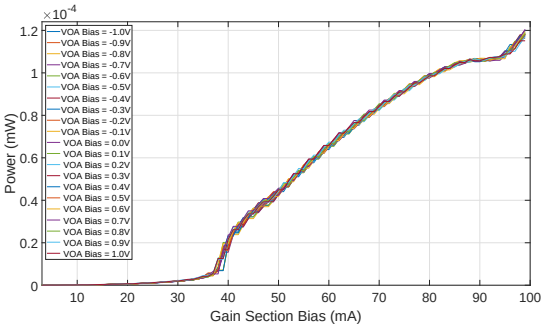

(a) LI curves from SFP-1 for various VOA biases.

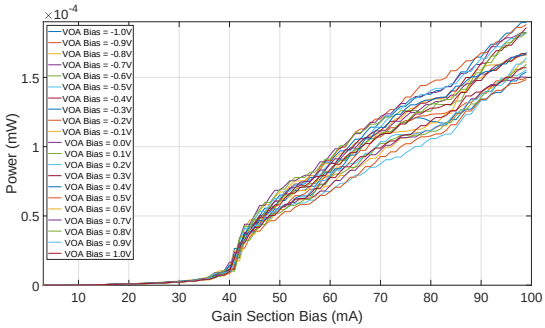

(b) LI curves from SFP-2 for various VOA biases.

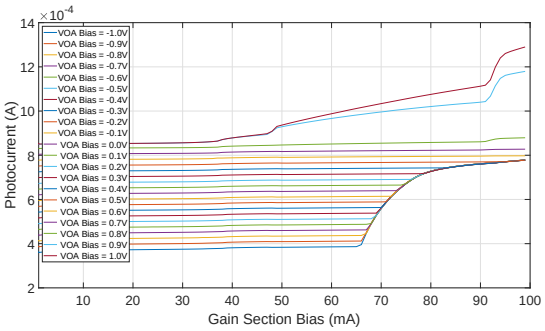

(c) Photocurrent generated in SFP-2 from SFP-1 for various VOA biases.

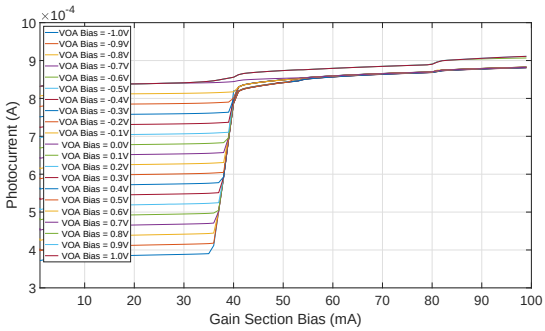

(d) Photocurrent generated in SFP-1 from SFP-2 for various VOA biases.

Figure 5.28: Measuring the coupling between the lasers as a function of VOA bias.

5.4 Conclusion

In this chapter, the effect of the VOA bias on the injection locking properties of the system was investigated. It was demonstrated that the VOA section was long enough to absorb all the light from both lasers, when reverse biased. The VOA bias did not alter the optical spectra of the lasers in this particular device, however a deep etch region between the VOA section and the lasers was added to all future designs to reduce the possibility of electrical cross-talk between the sections. As expected, the coupling between the lasers (VOA bias) had a large effect on the injection locking properties of the system. For low VOA biases, the VOA was absorbing thus partially isolating the lasers. However, even at low VOA biases, the full cavity length is observed in the FFT of the optical spectra. This suggests that light is coupling into the substrate, creating the full cavity length, but not enough light is coupling between the lasers for them to interact and create any dynamical behaviour. At high VOA biases, the VOA was fully transparent and the system behaved as a compound laser. It was demonstrated that the wavelength (mirror and gain section biases) of the lasers could be fixed, and the coupling between the lasers varied to obtain injection locking. In this regime the lasers were equally powered and their free running spectra were almost identical, but when mutually locked, they lased at a higher wavelength than their natural lasing modes.

This shift was unexpected and requires further investigation. An attempt was made to measure the coupling between the lasers but it was discovered that substrate coupling was effecting the results. The next chapter examines new PIC designs that try to reduce the effect of substrate coupling.

Chapter 6

The U-Bend VOA PIC

In the previous chapter, the issue of substrate coupling was introduced. It was discovered that some of the light emitted by the lasers was going down into the substrate and coupling into the other laser, rather than being coupled through the VOA. Substrate coupling had a particularly large effect in the PIC discussed in the last chapter because both lasers were in a straight line. Substrate coupling cannot be fully eliminated but offsetting the lasers can significantly reduce its effect.

6.1 Next Generation of PICs

Figure 6.1 is a schematic of the next generation of PICs designed and tested. Three different designs with various VOA lengths were investigated; (i) Curved VOA, (ii) S-bend in the VOA and (iii) U-bend in the VOA.

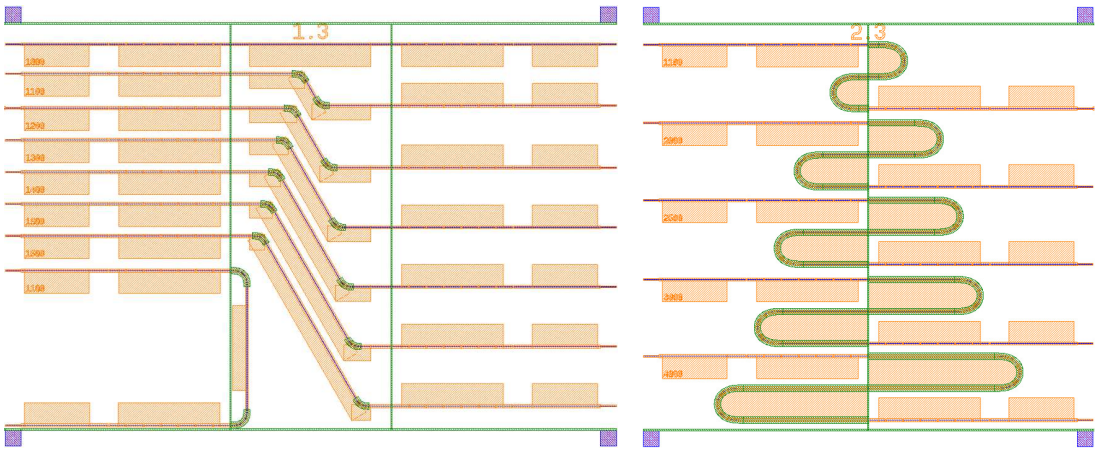

(a) (b)

Figure 6.1: The next generation of PICs, with various VOA length and shape designed to reduce the effect of substrate coupling.

The curved VOA design did not reduce the effect of substrate coupling sufficiently for the short VOA lengths. None of the longer VOA length PICs worked; the VOA sections may have been too long. The high loss due to the bends and deep etches on the S-bend VOA design meant that too little light coupled between the lasers to obtain any dynamical behaviour. In comparison, the U-bend VOA design worked well and the results obtained will be discussed in the following sections. Thus, the U-Bend VOAs were adopted for further experiments.

6.2 The U-Bend 1100 μm VOA PIC

A schematic of the PIC with all variable parameters labelled is shown in Figure 6.2. The U-bend in the VOA section resulted in the lasers being one beside the other which almost completely eliminated the effect of substrate coupling. It was possible to tune both of these lasers over a 0.5 nm range while maintaining a SMSR > 27 dB, therefore the effect of the detuning between the lasers on the injection locking properties of the system was also investigated.

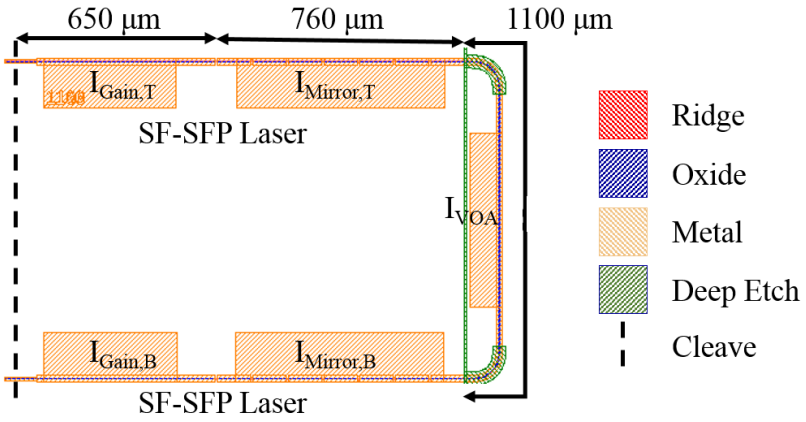

Figure 6.2: Schematic of the PIC with all variable parameters labelled. Two SF-SFP lasers are integrated together through a 1100 μm U-Bend VOA section.

The mirror and gain section biases of each laser were chosen to set the wavelength of each laser and hence the detuning, Δ between them, see Figure 6.3a. Figure 6.3b is a colour intensity plot of the detuning between the lasers as a function of their gain section biases, for $I_{Mirror,T} = 26$ mA and $I_{Mirror,B} = 15$ mA.

Once the detuning, and hence the mirror and gain section biases, had been chosen they remained fixed while the coupling between the lasers (VOA bias) was varied. For this device, the VOA section was completely absorbing below 0.75 V, therefore the VOA bias was swept from 0.75 V to 2.00 V and the output of the lasers was recorded on an ESA, OSA and HSO. The results for $\Delta = 1.3$ GHz, -2.2 GHz, -4.6 GHz and -7.4 GHz are plotted in Figures 6.4 - 6.6. (Since both lasers are on the same facet it was only

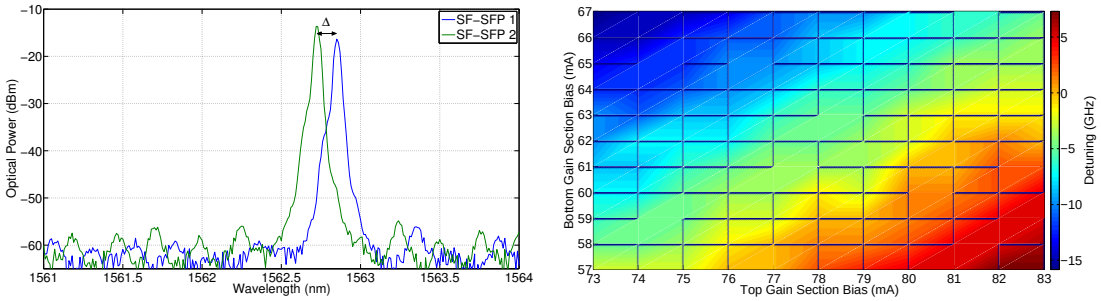

(a) (b)

Figure 6.3: (a) The biases of the lasers were chosen to give a particular wavelength detuning, Δ between the lasers. (b) Colour intensity plot of the frequency detuning between the lasers as a function of their gain section biases, for $I_{Mirror,T} = 26$ mA and $I_{Mirror,B} = 15$ mA.

possible to record the output of one laser during a sweep.)

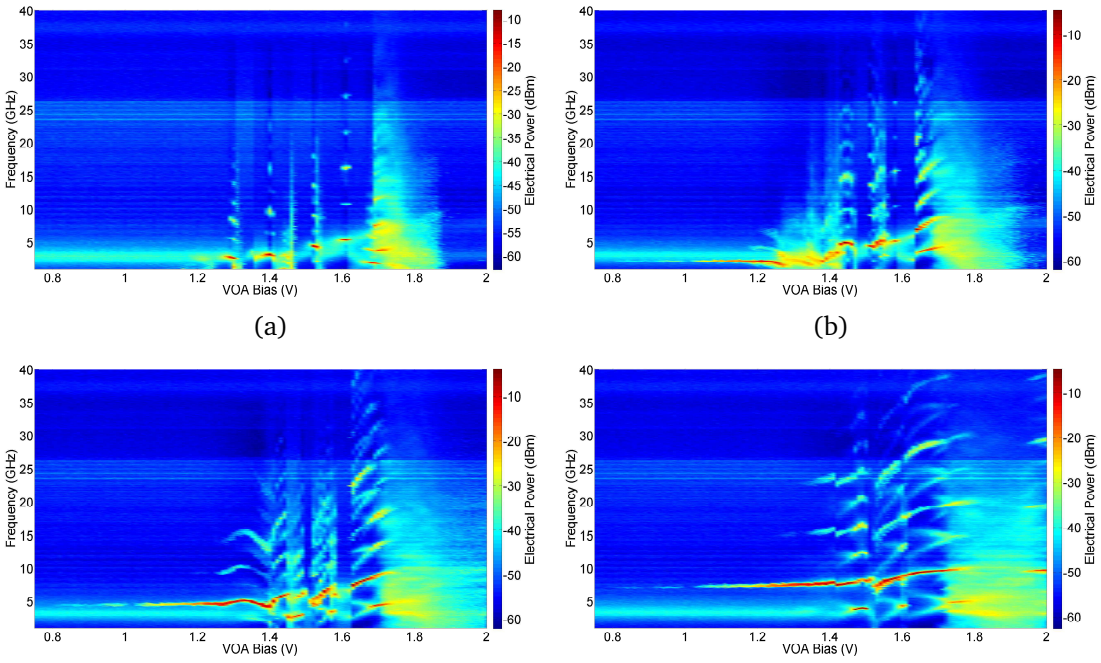

(a) (b)

(c) (d)

Figure 6.4: ESA traces from the bottom SFP as function of VOA bias for (a) 1.3 GHz, (b) -2.2 GHz, (c) -4.6 GHz and (d) -7.4 GHz detuning between the lasers.

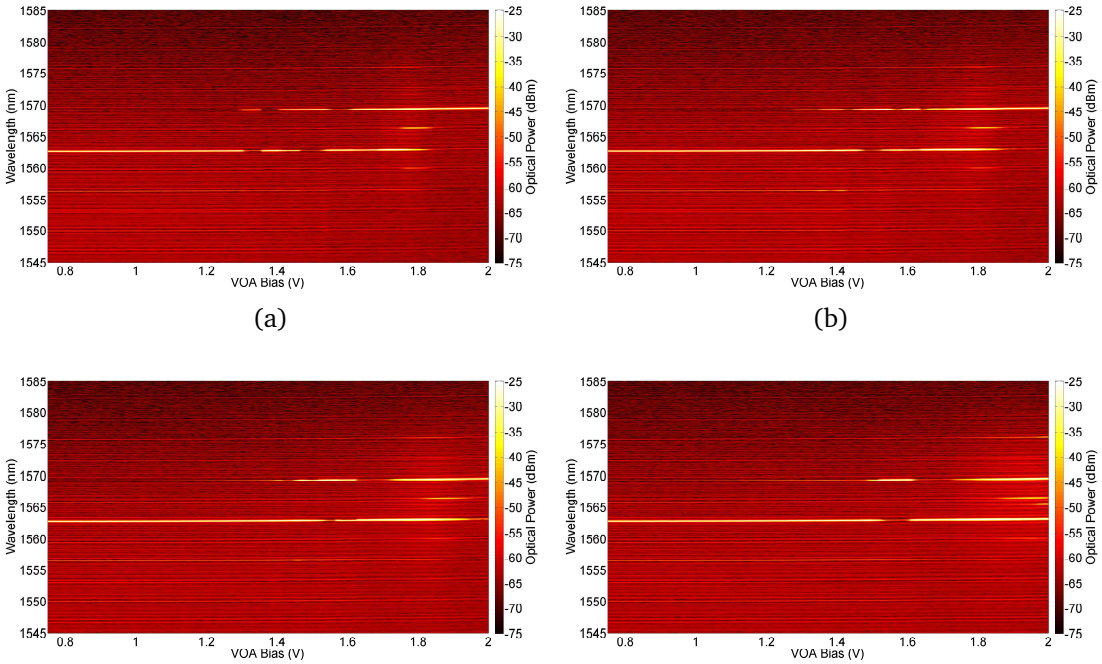

Figure 6.5: OSA traces from the bottom SFP as function of VOA bias for (a) 1.3 GHz, (b) -2.2 GHz, (c) -4.6 GHz and (d) -7.4 GHz detuning between the lasers.

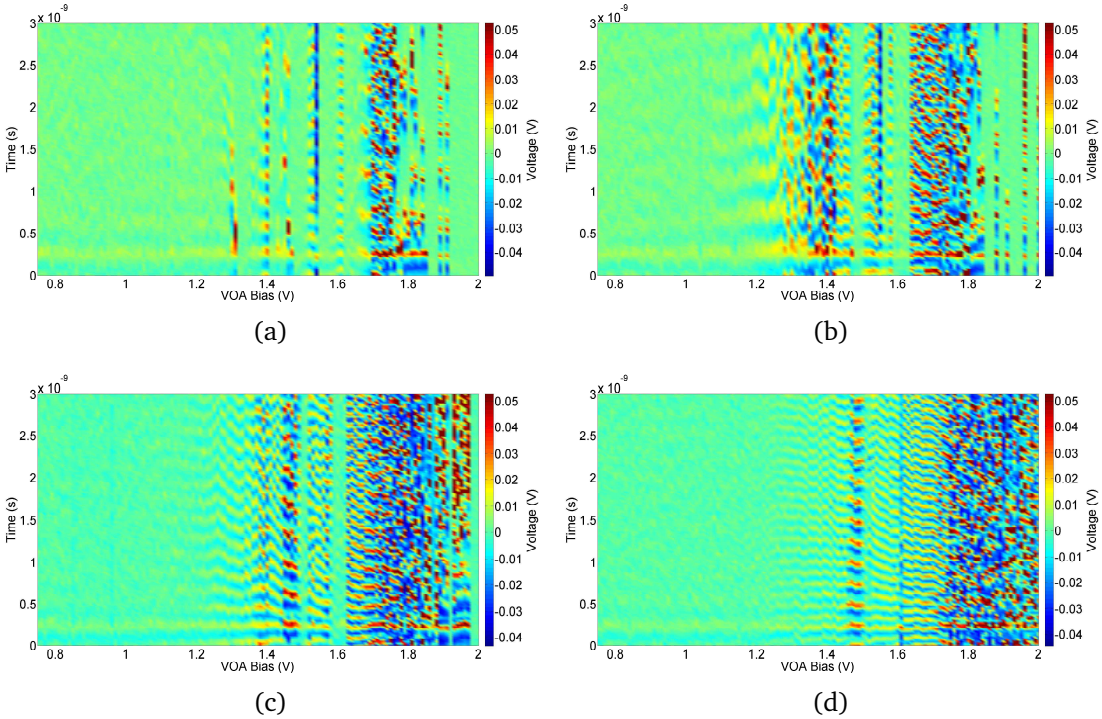

Figure 6.6: HSO traces from the bottom SFP as function of VOA bias for (a) 1.3 GHz, (b) -2.2 GHz, (c) -4.6 GHz and (d) -7.4 GHz detuning between the lasers.

The plots in Figures 6.4 - 6.6 are only a small example of the full data set obtained ranging from -16 GHz to 8 GHz detuning. Therefore a method of summarising the results needed to be developed for ease of interpretation. Various patterns and regions of dynamical behaviour can be seen in the colour intensity plots. Below is a description of the types of behaviour that have been identified.

Uncoupled - at low VOA biases, there was very little light coupling between the lasers, hence they were almost isolated and did not interact. When the lasers were uncoupled, only the RO's of the laser were observed on the ESA, the laser's natural lasing spectrum was seen on the OSA and no signal was found on the HSO, just noise, see Figure 6.7.

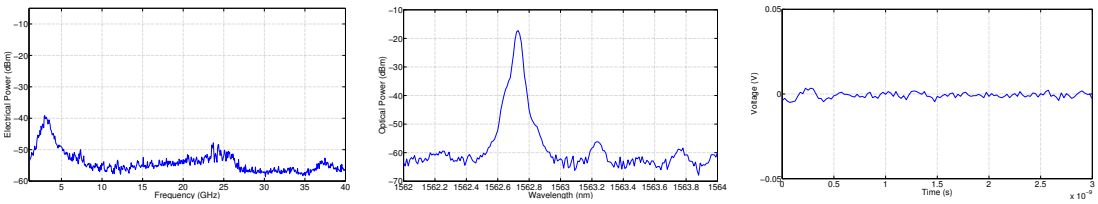

(a) (b) (c)

Figure 6.7: (a) ESA, (b) OSA and (c) HSO traces for $\Delta = -7.55$ GHz and a VOA bias of 0.90 V – the lasers were uncoupled.

Beating - as the VOA bias increased the VOA began to become transparent and sufficient light coupled between the lasers so that they began to interact, causing a beat note corresponding to the detuning (Δ) between the lasers to appear in the electrical spectra, as seen in Figure 6.8a. If a very high resolution OSA was used, a second peak Δ away from the original lasing mode would be visible in the optical spectrum, Figure 6.8b. A sine wave of frequency Δ is observed on the HSO. Figure 6.8c shows the HSO trace for Δ = -7.55 GHz and I_{VOA}= 1.15 V, with a 7.7 GHz sine wave fitted to the data. A good agreement was obtained within approximately 10% experimental error.

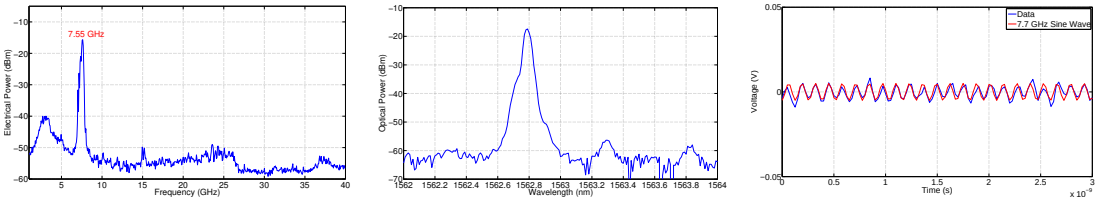

(a) (b) (c)

Figure 6.8: (a) ESA, (b) OSA and (c) HSO traces for $\Delta = -7.55$ GHz and a VOA bias of 1.15 V – the lasers beat together.

Frequency Locked - for small detunings (-5 GHz $< \Delta <$ 5 GHz) regions of frequency locking were observed where only the RO's were visible on the ESA, Figures 6.9a and 6.10a, and noise on the HSO, Figures 6.9c and 6.10c. The natural lasing wavelength for these lasers over this bias range was approximately 1563 nm, see Figure 6.7b. When frequency locked the lasers either remained at their natural lasing wavelengths, $\sim$1563 nm, Figure 6.9b, or jumped to a higher lasing mode at $\sim$1569 nm, Figure 6.10b.

Since the RO's are not suppressed, the lasers are not phase locked but both lasers are lasing at the same wavelength.

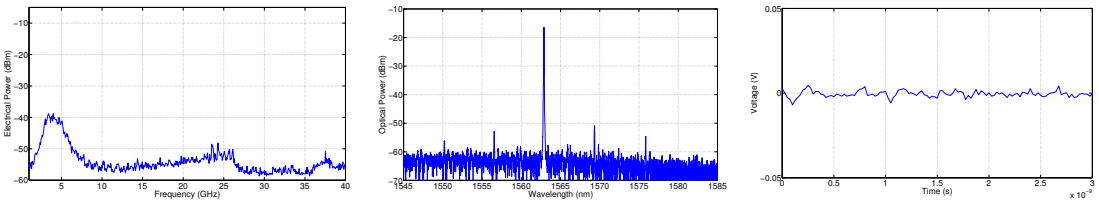

(a) (b) (c)

Figure 6.9: (a) ESA, (b) OSA and (c) HSO traces for Δ = 1.26 GHz and a VOA bias of 1.56 V – the lasers are both frequency locked to their natural lasing mode, ∼1563 nm.

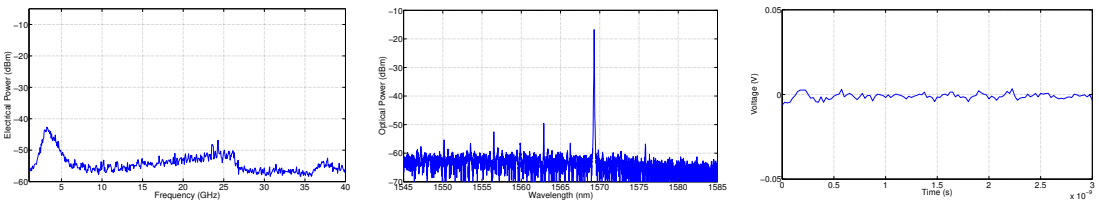

(a) (b) (c)

Figure 6.10: (a) ESA, (b) OSA and (c) HSO traces for Δ = 1.26 GHz and a VOA bias of 1.49 V – the lasers are both frequency locked to a higher lasing mode, ∼1569 nm.

Aperiodic - regions of multimode behaviour, where two or more lasing modes appeared in the optical spectra, were observed, Figure 6.11b. In these regions a patternless signal was obtained on the HSO, Figure 6.11c and the electrical spectra were aperiodic, Figure 6.11a.

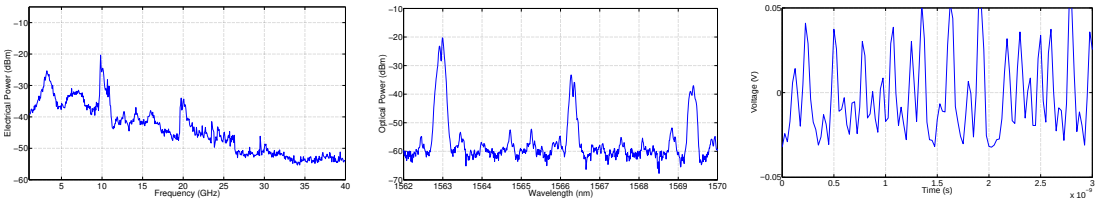

(a) (b) (c)

Figure 6.11: (a) ESA, (b) OSA and (c) HSO traces for Δ = -7.55 GHz and a VOA bias of 1.52 V – the lasers are behaving aperiodically.

Period Doubling - regions where peaks at Δ and 0.5Δ and their harmonics are seen in the electrical spectra, were also identified. Figure 6.12a is a plot of the ESA trace for Δ = -7.55 GHz and VOA bias = 1.28 V. Peaks are observed at 4.4 GHz ($\sim 0.5\Delta$) and 8.8 GHz ($\sim \Delta$). Peaks corresponding to their harmonics are also obtained. The signal on the HSO also contains both frequencies. The HSO trace for Δ = -7.55 GHz and VOA bias = 1.28 V, Figure 6.12c, was fitted with the sum of a 4.4 GHz and a 8.8 GHz sine wave. Good agreement was obtained. Another example of period doubling is shown in Figure 6.13, Δ = -5.02 GHz and VOA bias = 1.17 V. The ESA trace contains

peaks at 2.6 GHz and 5.2 GHz and the HSO traces was a sine wave of the sum of these frequencies.

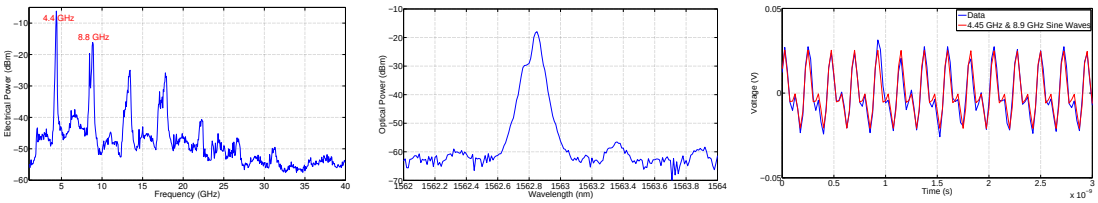

(a) (b) (c)

Figure 6.12: (a) ESA, (b) OSA and (c) HSO traces for Δ = -7.55 GHz and a VOA bias of 1.28 V – the lasers have undergone period doubling.

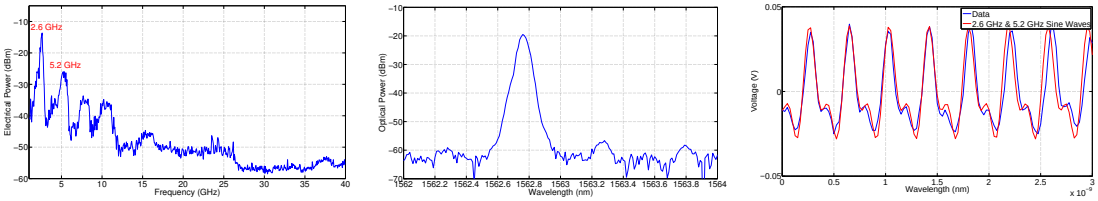

(a) (b) (c)

Figure 6.13: (a) ESA, (b) OSA and (c) HSO traces for Δ = -5.02 GHz and a VOA bias of 1.17 V – the lasers have undergone period doubling.

Code was written in Matlab to identify these five types of behaviour as a function of detuning and VOA bias. The results are plotted in Figure 6.14.

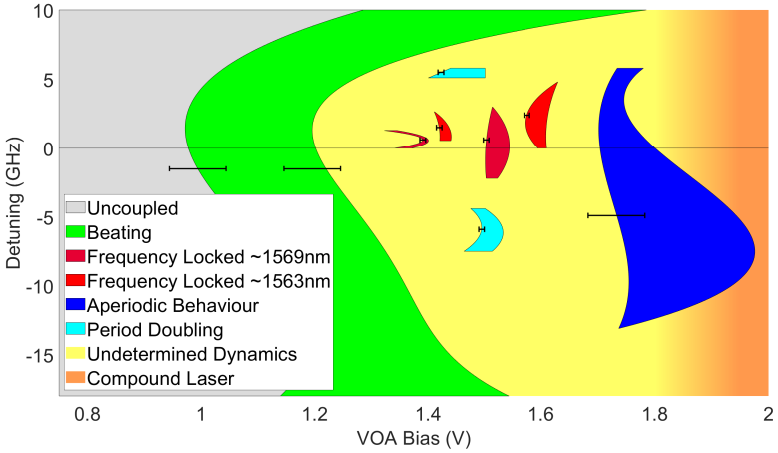

Figure 6.14: Summary of the types of behaviour obtained from the bottom laser as a function of VOA bias and detuning while both lasers were lasing at approximately 1563 nm. The errors associated with the data fitting is shown on each line.

These five types of behaviour are only a subset of the full data set. There is a large section of the summary plot (Figure 6.14), where the dynamics are as yet undetermined. Figures 6.15 to 6.18 are examples of these undetermined dynamics. The time trace shown in Figure 6.15c is a sinusoidal signal but the ESA trace in Figure 6.15a shows very wide, noisy beat notes. The ESA and OSA traces in Figures 6.16 and 6.17 are

very similar; the beat notes at ∼9.8 GHz and its harmonics are much narrower and the optical spectra have become multimode. However the time traces, Figures 6.16c and 6.17c, are very different. Figure 6.16c is a sinusoidal signal with an envelope and some sort of pulsing in between, while Figures 6.17c shows pulsing at ∼1.01 GHz. The ESA trace in Figure 6.18 has a noisy beat note at multiples of 10 GHz and the OSA trace is still multimode but the time trace now shows a ∼1.54 GHz irregular sinusoidal signal.

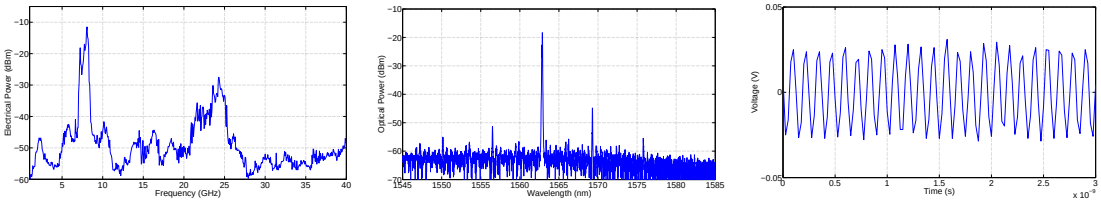

(a) (b) (c)

Figure 6.15: (a) ESA, (b) OSA and (c) HSO traces for Δ = -5.02 GHz and a VOA bias of 1.35 V – an example of undetermined dynamics between the lasers.

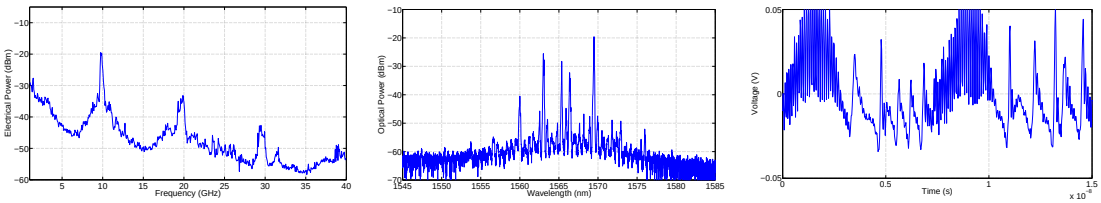

(a) (b) (c)

Figure 6.16: (a) ESA, (b) OSA and (c) HSO traces for Δ = -5.02 GHz and a VOA bias of 1.65 V – an example of undetermined dynamics between the lasers.

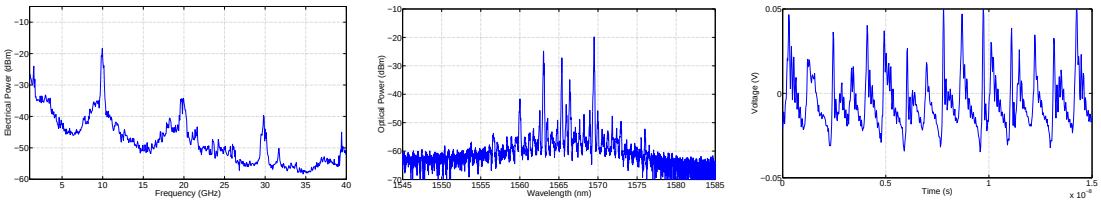

(a) (b) (c)

Figure 6.17: (a) ESA, (b) OSA and (c) HSO traces for Δ = -5.02 GHz and a VOA bias of 1.67 V – an example of undetermined dynamics between the lasers.

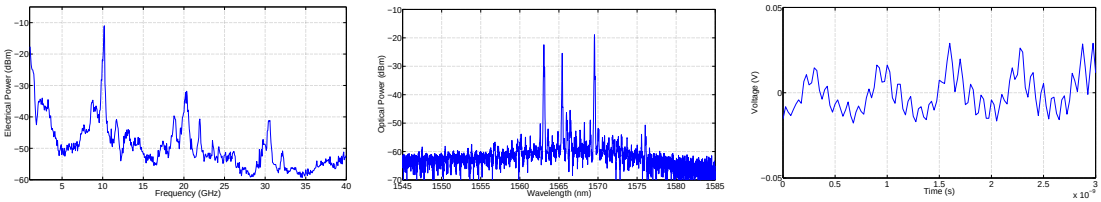

(a) (b) (c)

Figure 6.18: (a) ESA, (b) OSA and (c) HSO traces for Δ = -5.02 GHz and a VOA bias of 1.72 V – an example of undetermined dynamics between the lasers.

At high VOA biases the VOA is fully transparent and the full PIC, from facet-to-facet,

behaves as a compound laser. The ESA trace shown in Figure 6.19a has some broad, low amplitude beating and the time trace, Figure 6.19c shows the noise floor of the HSO. The optical spectrum in Figure 6.19b shows that the lasing wavelength has shifted to approximately 1570 nm. Figure 6.19d is the FFT of the optical spectrum in Figure 6.19b and shows the cavity lengths present in the system. There is a peak at 571 μm which corresponds to the length of the gain section. The small peak at 1679 μm is the effective length of the SFP laser. There is also a small peak at 3674 μm which is the length of the full PIC. (If a higher resolution OSA had been used, these peaks would be clearer.) The PIC is now behaving as a compound laser. The shift to a compound laser is gradual which is indicated in the shaded region in Figure 6.14.

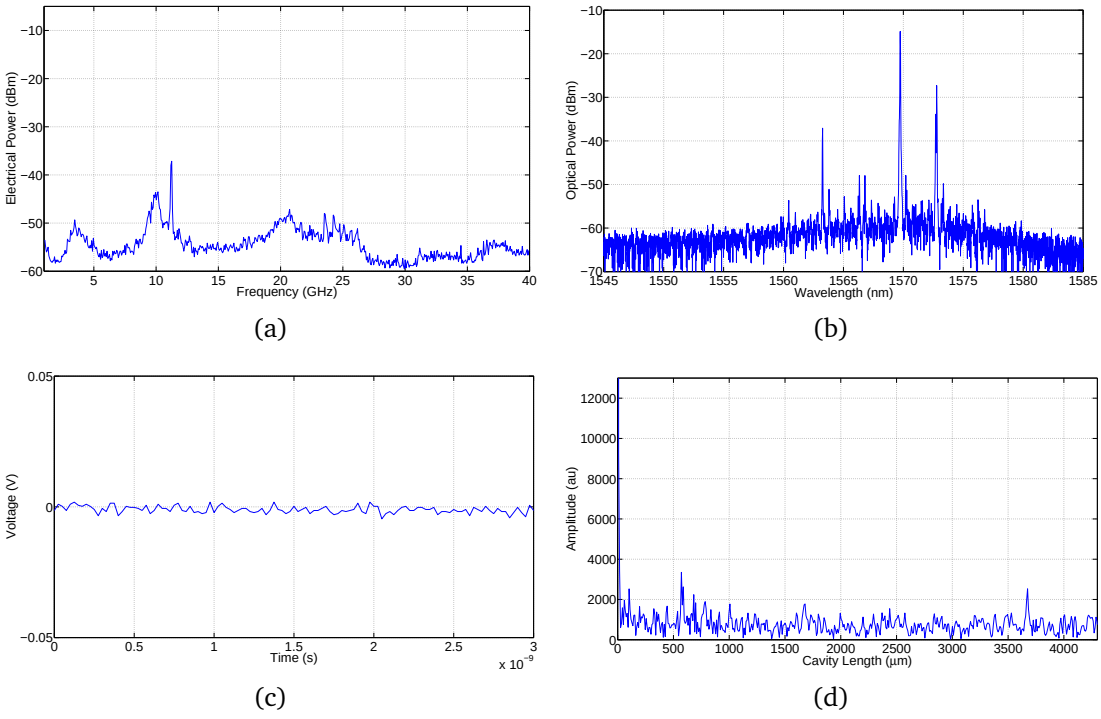

Figure 6.19: (a) ESA, (b) OSA, (c) HSO traces and (d) FFT of the OSA trace for Δ = -5.02 GHz and a VOA bias of 1.94 V – the PIC is behaving as a compound laser.

Figure 6.14 shows that as the detuning between the lasers increases the coupling between the lasers required for the lasers to begin beating together also increases. The detuning between the lasers must be less than |5| GHz in order for locking to be obtained. Two regions of period doubling were observed, between |4| and |7.5| GHz. There is a large region of aperiodic behaviour at high VOA biases. The experiment was repeated and the output of the top lasers was recorded, changing the sign of the detuning and a summary of the types of behaviour obtained is plotted in Figure 6.20. The dynamics have shifted to lower VOA bias but occur at similar detunings.

The biases of the lasers was increased so that their free running lasing wavelength was at approximately 1569 nm. The experiment was repeated twice, recording the output of the top laser both times and the summaries of the results are plotted in Figures 6.21

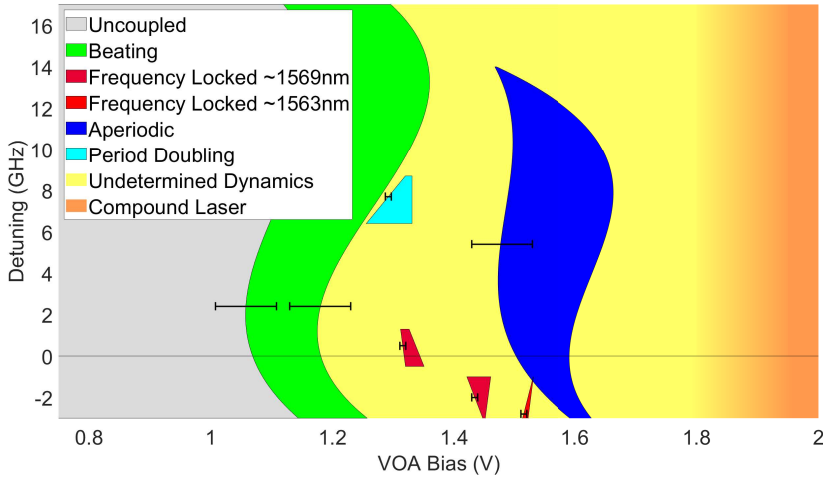

Figure 6.20: Summary of the types of behaviour obtained from the top laser as a function of VOA bias and detuning while both lasers were lasing at approximately 1563 nm. The errors associated with the data fitting is shown on each line.

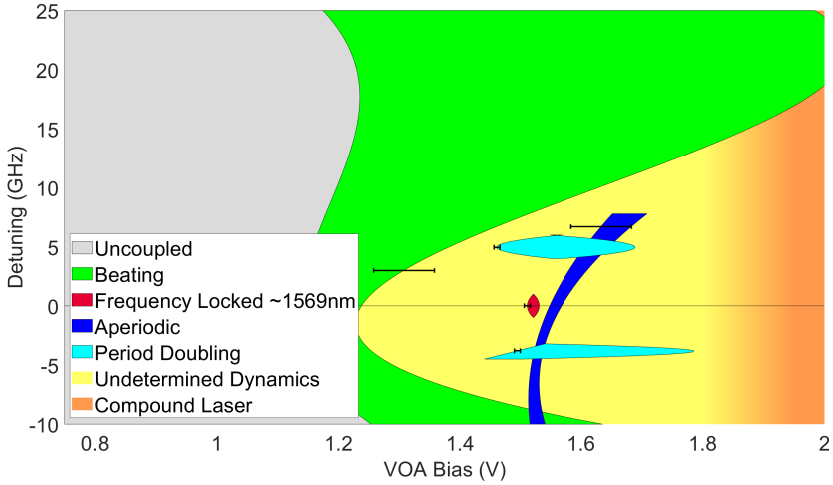

Figure 6.21: Summary of the types of behaviour obtained from the top laser as a function of VOA bias and detuning while both lasers were lasing at approximately 1569 nm. The errors associated with the data fitting is shown on each line.

and 6.22. The VOA bias required for the lasers to begin beating together has increased. A narrow region of aperiodic behaviour is observed. Two regions of period doubling were obtained in the first experiment (Figure 6.21) and none in the second (Figure 6.22). Very small regions of locking to approximately 1569 nm were also observed.

The results from the repeated experiments are not identical even when recording from the same laser each time. It was found that due to environmental changes e.g. temperature, humidity, etc. due to the air conditioning cycles in the lab, the output of each laser differed from sweep to sweep. The settings of the air conditioning were fixed and controlled by central services, and therefore could not be adjusted to improve the experiment. Hence, repeating the experiment did not yield the same results making it difficult to compare results from multiple sweeps.

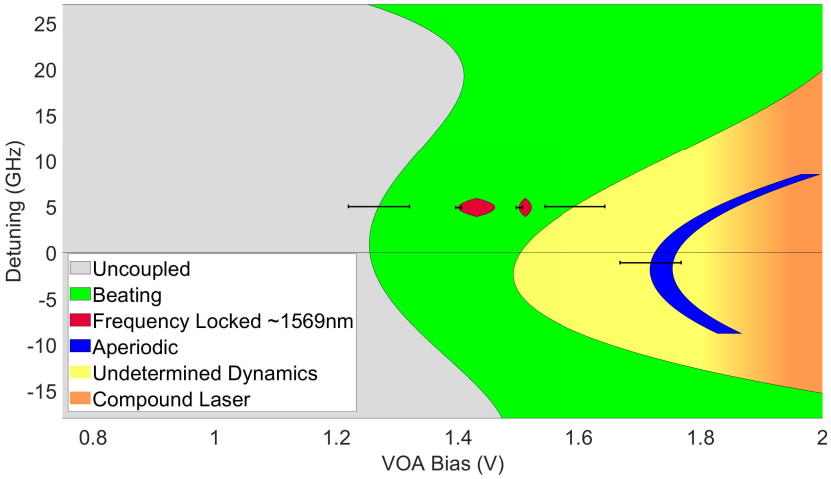

Figure 6.22: Summary of the types of behaviour obtained from the top laser as a function of VOA bias and detuning while both lasers were lasing at approximately 1569 nm. The errors associated with the data fitting is shown on each line.

6.2.1 Coupling Ratio, κ

The next step was to measure the coupling ratio (the percentage of the light emitted by one laser that couples into the other) between the lasers as a function of VOA bias. The bottom laser was biased at mirror/gain section biases of 35 mA / 65 mA. The VOA was reverse biased to -2 V and the photocurrent was recorded. Equation 3.2 was used to convert the photocurrent to power and this was assumed to be the total power, P_{Tot} emitted by the laser. The top laser was then reverse biased to -2 V and the photocurrent was recorded while the VOA bias was swept between -1 V and 2 V. Converting to power, this was assumed to be the power emitted by the bottom laser that couples into the top laser, $P_{B\rightarrow T}$. The coupling ratio from the bottom laser to the top, $\kappa_{B\rightarrow T}$ was defined as

$$\kappa_{B\rightarrow T} = \frac{P_{B\rightarrow T}}{P_{Tot}} \tag{6.1}$$

and repeating for the top laser gave $\kappa_{T\rightarrow B}$. The results are plotted in Figure 6.23.

It was expected that the coupling in both directions would be the same, however this was not the case. For this experiment both lasers were biased the same but they did not lase at the same wavelengths. Therefore, it was assumed that due to the absorption of the material $\kappa_{B\rightarrow T} \neq \kappa_{T\rightarrow B}$. It was hoped that if both lasers were at the same wavelength that the coupling ratios would be equal. The experiment was repeated with the top and bottom lasers biased at 26 mA/73 mA and 15 mA/57 mA, respectively. These biases corresponded to 5.02 GHz detuning between the lasers, therefore the absorption of the material should have been the same for the light emitted by both lasers. However, Figure 6.24 shows that there is an even bigger difference between $\kappa_{B\rightarrow T}$ and $\kappa_{T\rightarrow B}$ now that the wavelengths are almost the same than when they were

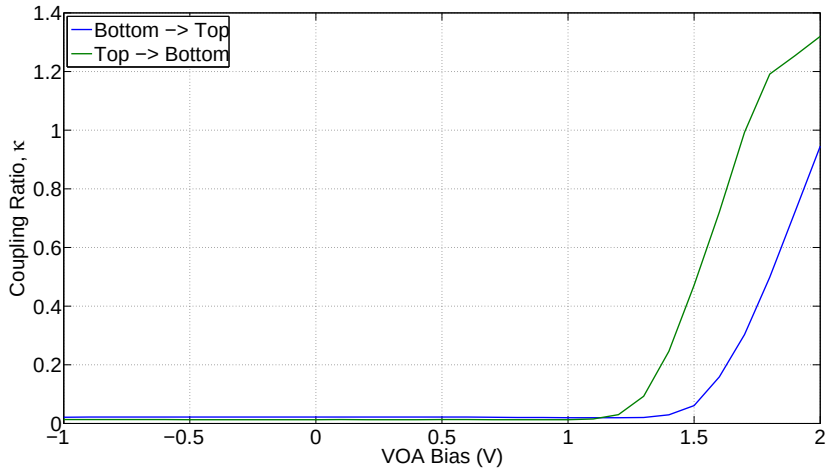

Figure 6.23: The coupling ratio, κ between the lasers as a function of VOA bias. Both lasers biased at 35 mA/65 mA.

very different, Figure 6.23. Although, when the wavelengths are nominally the same, the turn on of the coupling ratio occurs at the same VOA bias, ∼1.3 V. To obtain a similar wavelength output from both lasers, they were biased differently. Therefore, the output power was not the same resulting in $\kappa_{B\to T} \neq \kappa_{T\to B}$. The coupling ratio exceeds one due to the amplification of the VOA at high biases.

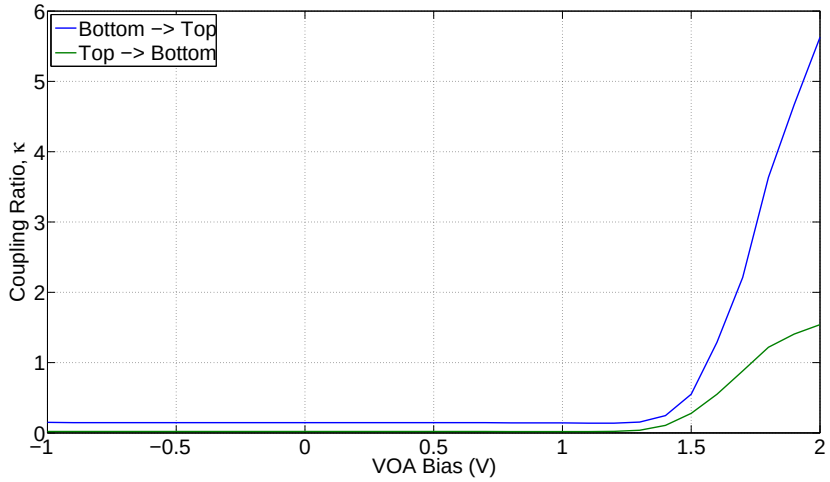

Figure 6.24: The coupling ratio, κ between the lasers as a function of VOA bias. The top and bottom lasers were biased at 26 mA/73 mA and 15 mA/57 mA, respectively.

6.2.2 Comparison with Theoretical Results

As mentioned in Chapter 2, this experimental work was carried out in tandem with theoretical studies of the system. Figure 6.25 shows some of the colour plots of the FFT of $|E|^2$ that were generated using Equations 2.1 - 2.4 [69]. The FFT of $|E|^2$ is the data given by the ESA, therefore these figures were compared with the colour plots of the ESA traces shown in Figure 6.4.

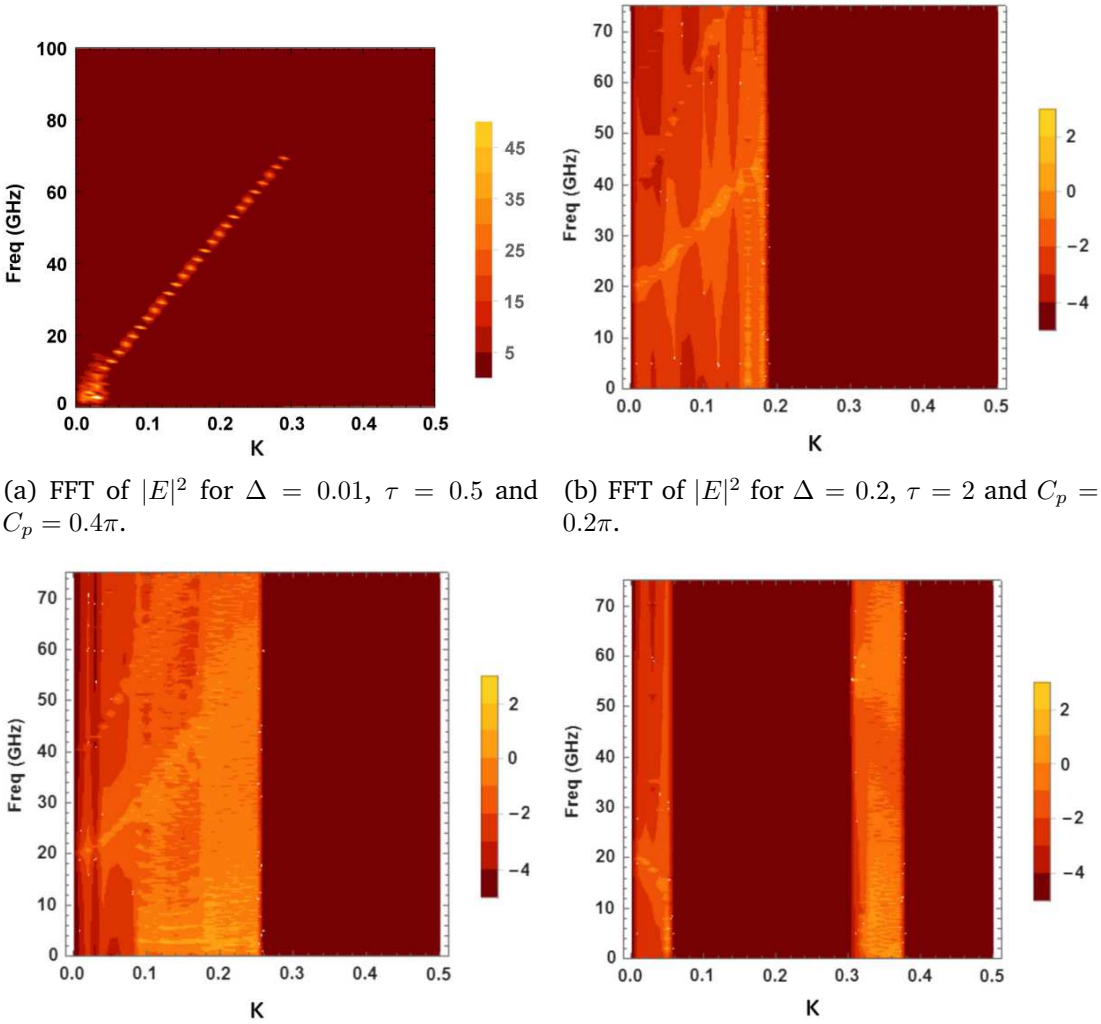

(a) FFT of $|E|^2$ for $\Delta = 0.01$, $\tau = 0.5$ and $C_p = 0.4\pi$.

(b) FFT of $|E|^2$ for $\Delta = 0.2$, $\tau = 2$ and $C_p = 0.2\pi$.

(c) FFT of $|E|^2$ for $\Delta = 0.2$, $\tau = 2$ and $C_p = 0.4\pi$.

(d) FFT of $|E|^2$ for $\Delta = 0.2$, $\tau = 2$ and $C_p = 0.7\pi$.

Figure 6.25: FFT of $|E|^2$ for various Δ, τ and C_p values in the theoretical model [69].

Figure 6.24 shows that for VOA biases less than 1.3 V, the coupling ratio κ between the lasers was less than 0.1. Hence only the regions of $\kappa < 0.1$ of the theoretical results (Figure 6.25) can be used for comparison. A VOA of length 1100 μm corresponds to $\tau \approx 0.3$ and a detuning of 10 GHz corresponds to $\Delta = 0.1$.

The beat note seen at low VOA biases in Figure 6.4, corresponding to the detuning between the lasers (the region referred to as *Beating* in Figure 6.14) corresponds to the theoretical results in Figure 6.25, where the two-colour states (strong beat note) have a frequency difference equal to the detuning for low κ. The aperiodic regions obtained at high VOA biases can be compared to the aperiodic behaviour between $\kappa = 0.16$ and $\kappa = 0.18$ in Figure 6.25b. The series of equally spaced beat notes, whose frequencies increase with VOA bias, observed at a VOA bias of approximately 0.7 V in Figure 6.4d have been identified as at least a period-four self-pulsation, as higher frequency beat notes are beyond the bandwidth of the the ESA [69].

It was realised that this single mode model could not successfully recreate the experimental results, since despite being tuned to be single mode, a side mode of the SFP laser was excited during coupling to the second SFP laser. This prompted the development of a multi-mode model to try and re-create the experiment. More details on this model can be found in Chapter 6 [78]. This initial multi-mode model gave positive results and indicated that a multi-mode model is what is required to recreate the dynamics seen experimentally.

However, the collaboration with laser dynamic colleagues discussed in Section 4.2.3 reproduced the qualitative dynamics of the asymmetric coupling setup much more accurately because the VOA was modelled as a saturable absorber. This suggests that the dynamics observed experimentally are generated by the interaction of the lasers with each other and with a saturable absorber, the VOA. Hence, while fabricating the VOA on the same active material as the lasers makes the fabrication and integration process much simpler, it makes the resulting dynamical behaviour more complex.

Out of the three VOA designs investigated the U-Bend VOA worked best, as the curved VOA design did not sufficiently reduce the effect of substrate coupling for the short VOA lengths. The PICs with longer VOAs did not work. Too little light coupled between the lasers in the S-Bend VOA PICs to obtain any dynamical behaviour. In comparison, it was possible to tune both lasers on the 1100 μm U-bend VOA PIC over a 0.5 nm range while maintaining a SMSR > 27 dB. Thus, the U-Bend design was retained for further experiments.

6.3 Third Generation of PICs

Since the U-Bend VOA PIC design was the most successful in eliminating the effect of substrate coupling, the next generation of PICs was based on this design and included 4 different VOA lengths; 385 μm, 835 μm, 1285 μm and 1735 μm, see Figure 6.26, to allow an investigation of the effect of the delay between the lasers (length of the VOA section) as well as the coupling and detuning on the injection locking properties of the system.

The fabricated bar of devices consisted of two sets of the U-Bend VOA PICs. The IV characteristics of each VOA were measured before investigating the injection locking properties of the devices and the results are plotted in Figure 6.27a. The applied voltage was the same for each VOA. As the length of the VOA increased so did the measured current. Therefore, from the well known equation; $V = IR$ (V = Voltage, I = Current and R = Resistance), it can be deduced that the length of the VOA is inversely proportional to the resistance.

This is expected since the voltage is being applied to a larger area as the length of the

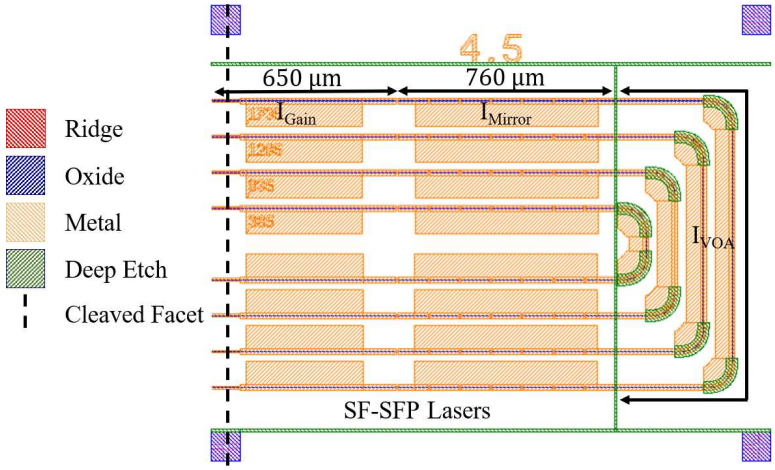

Figure 6.26: The next generation of PICs with U-Bend VOAs, designed to allow an investigation of the effect of the delay between the lasers (length of the VOA section) on the injection locking properties of the system.

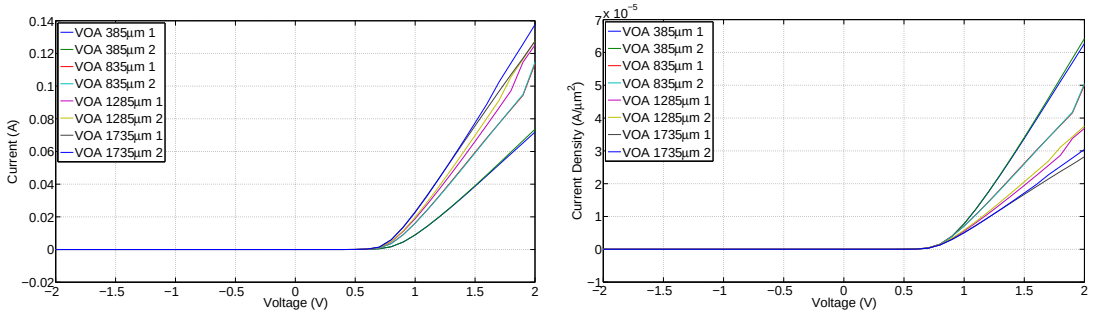

(a) (b)

Figure 6.27: (a) IV and (b) JV characteristics of each of the VOAs on a bar.

VOA increases (the size of the contact pad for the VOA also increases) thus reducing the resistance and hence the measured current. Dividing the measured current by the area of the VOA ridge to get current density (Figure 6.27b) shows that the current density decreased with increasing VOA length. It was expected that the current density would be the same for each VOA, independent of length, but this assumes that the current density is constant along the entire ridge, which in practice is inaccurate due to variations in the resistance of the metal along the ridge.

6.3.1 The 1285 µm VOA PIC

Similar to the 1100 µm U-bend VOA PIC discussed in Section 6.2, the 1285 µm U-bend VOA PIC was tunable while maintaining a high SMSR. The VOA bias was swept from 0.5 V to 2.5 V and the output of the lasers were recorded on an ESA, OSA and HSO. The experimental setup was improved and a higher resolution (0.045 nm) OSA was used. Therefore, it was possible to resolve peaks that were ∼3 GHz apart. This gave further insight into the behaviour of the lasers during interaction. High resolution

optical spectra from each of the behavioural regimes, discussed in Section 6.2, will be investigated in the following to see clearer how the lasing modes of the lasers are affected by their interaction.

Uncoupled - at low VOA biases there was too little light coupling between the lasers for them to interact, therefore only the RO's were observed on the ESA and noise was found on the HSO. The single clean peak of the laser's natural lasing spectrum with an SMSR >30 dB was seen on the OSA, see Figure 6.28.

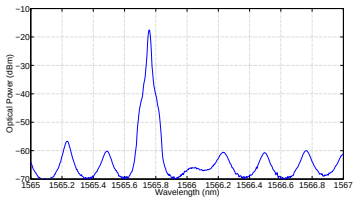

Figure 6.28: OSA trace for $\Delta \approx 6.3$ GHz; VOA bias = 0.50 V – lasers uncoupled.

Beating - as the lasers began to interact a beat note corresponding to Δ (∼6.3 GHz in this example) was seen on the ESA and a sine wave of frequency Δ on the HSO. On the OSA, satellite peaks occurred on either side of the main peak, Figure 6.29. The satellites were approximately 0.05 nm from the main peak which corresponds to a frequency separation of ∼6.1 GHz.

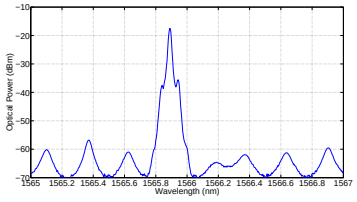

Figure 6.29: OSA trace for $\Delta \approx 6.3$ GHz; VOA bias = 1.39 V – lasers beat together.

Frequency Locked - regions of frequency locking were observed where only the RO's were visible on the ESA and noise on the HSO. A single clean peak was seen on the OSA, Figure 6.30. In this example, the lasers were both locked to their natural wavelength of ∼1566 nm with a SMSR of 34 dB.

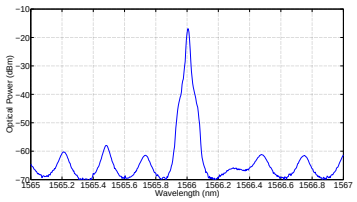

Figure 6.30: OSA trace for $\Delta \approx 4.3$ GHz; VOA bias = 1.40 V – the lasers were both frequency locked at ∼1566 nm.

Aperiodic - in the regions of aperiodic behaviour seen on the ESA and the HSO, two or more modes lase in the optical spectrum and many satellite peaks of varying separations were observed on every mode, Figure 6.31.

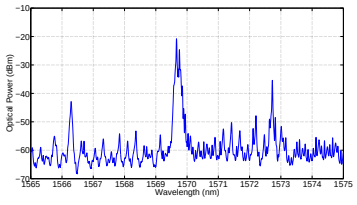

Figure 6.31: OSA trace for $\Delta \approx 6.3$ GHz; VOA bias = 2.23 V – lasers behaving aperiodically.

Period Doubling - when peaks at Δ and 0.5Δ ($\sim$6.3 GHz and $\sim$3.15 GHz in this example) and their harmonics were visible in the electrical spectrum and the signal on the HSO consisted of sine waves of frequency 0.5Δ and Δ, the main mode in the optical spectrum showed four peaks each separated by approximately 0.028 nm, which corresponds to a frequency separation of $\sim$3.4 GHz, Figure 6.32.

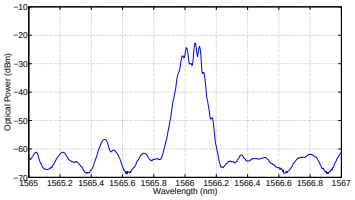

Figure 6.32: OSA trace for $\Delta \approx 6.3$ GHz; VOA bias = 1.73 V – lasers undergo period doubling.

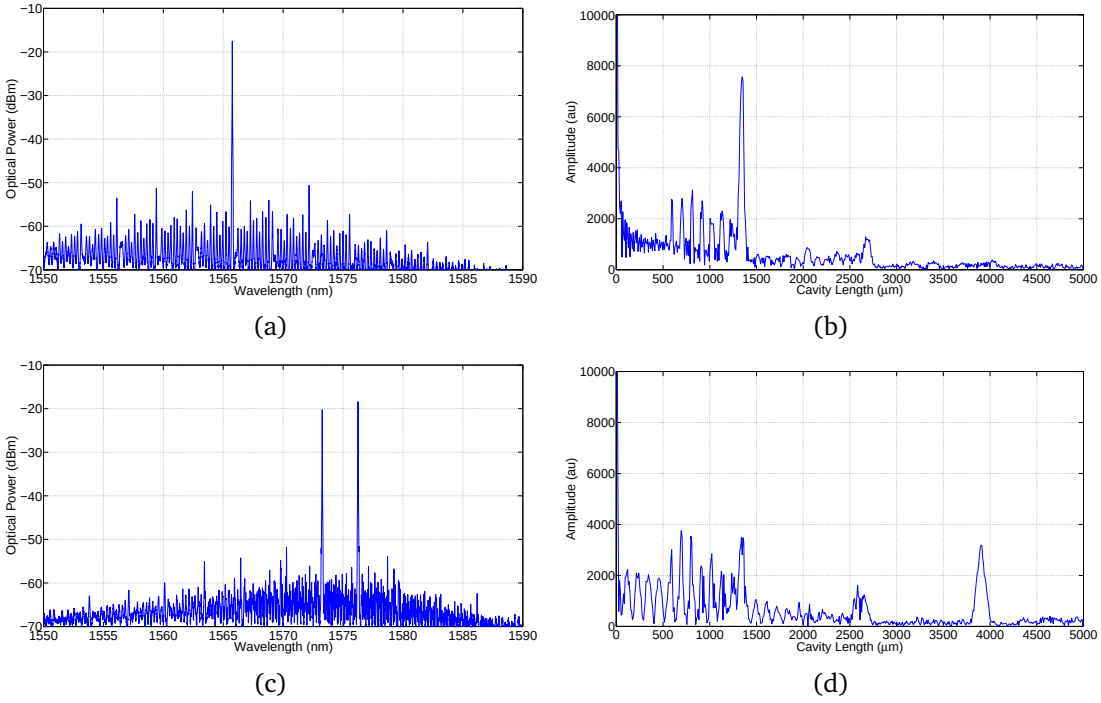

Figure 6.33: (a) The optical spectrum and (b) FFT of (a) at a VOA bias of 0.5 V – the lasers are uncoupled. (c) The optical spectrum and (d) FFT of (c) at a VOA bias of 2.4 V – the full PIC was behaving as a compound laser. All for $\Delta \approx 6.3$ GHz.

Compound Laser - the FFT of the high resolution OSA data showed clearly defined peaks corresponding to the cavity lengths within the laser. Figure 6.33a is the optical spectrum of the bottom laser at a VOA bias of 0.5 V. The lasers were uncoupled, therefore this is the free running-spectrum of the laser. Figure 6.33b is the FFT of this spectrum. The peak at $\sim$600 μm is the gain section. The next six peaks are the gain section plus $n\times$(the interslot distance) ($\sim$100 μm). The strong peak at $\sim$1350 μm corresponds to the effective length of the laser. A small peak at twice this length is also visible. The optical spectrum of the laser for a VOA bias of 2.4 V is plotted in Figure 6.33c. The laser was multimode and was redshifted. The FFT of the spectrum, Figure 6.33d, shows the gain section and the interslot distances. The peak corresponding to the effective length of the laser is suppressed and a strong peak at $\sim$3900 μm has ap-

peared. This is the full length of the PIC from facet-to-facet, indicating that the device was now behaving as a compound laser.

6.3.2 The 385 μm U-Bend VOA PIC

The straight, curved and S-bend VOA PICs had a laser on each facet, therefore using two lensed fibres, one on each side, and an optical switch, the output of both lasers could be recorded during a sweep. This allowed for a direct comparison between both laser outputs. The U-bend VOA PICs had both lasers on the same facet, therefore the output of only one laser could be recorded during a sweep. As mentioned previously, the output from the same laser would differ slightly from sweep to sweep due to environmental changes e.g. temperature, humidity, etc. of the lab. Therefore even if the sweep was repeated, recording the output of the second laser, it was unknown if the results could be accurately compared.

To solve this problem, the experiment was updated, such that one of the lensed fibres on the probe station was controlled via motors and nanotrak piezo controllers. These controllers were LabView programmable. It is described in Appendix A, how LabView code was written to automate the coupling to one laser and move the fibre and couple to the second laser during a sweep. Hence, for the first time the output of both lasers on a U-bend VOA PIC could be recorded during a sweep.

Figure 6.34 shows colour plots of the ESA (a and b), OSA (c and d), FFT of the OSA (e and f) and HSO (g and h) for both the top (a,c,e and g) and the bottom (b,d,f and h) lasers for a detuning of $\sim$15 GHz between the lasers. The outputs of both lasers are very similar. The same beating patterns were observed in the electrical spectra of both lasers, Figures 6.34a and b. The lasers were always coupled, even at 0.5 V, since the VOA is shorter than those previously examined it was not as absorbing, allowing the lasers to interact more. There were also much fewer dynamics observed and no regions of quiet or period doubling, since the lasers were $\sim$15 GHz apart.

The optical spectra of both lasers are very similar, they both mode-hop and become multimode at the same VOA biases, Figures 6.34c and d. The FFT of the optical spectra, Figures 6.34e and f, show the gain section and the interslot distances. A strong peak at 1330 μm corresponding to the effective length of the laser and twice this length are observed. A peak at 3050 μm, corresponding to length of the full PIC appears at a VOA bias of 1.3 V. As expected the PIC becomes a compound laser at a lower VOA bias than previous PICs. The HSO used has a bandwidth of 15 GHz, therefore since most of the beating occurs at 15 GHz or above, very little is observed on the HSO, Figures 6.34g and h.

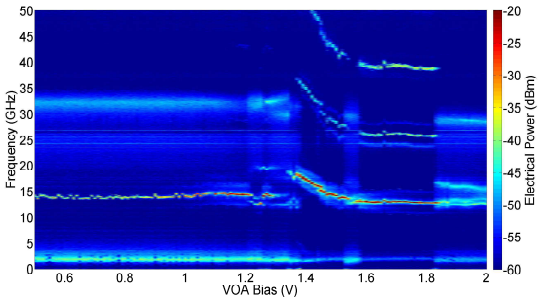

(a) Colour plot of the ESA traces from the top laser.

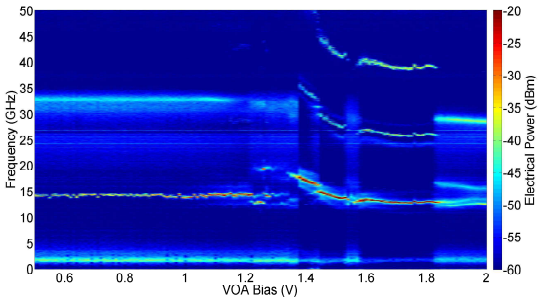

(b) Colour plot of the ESA traces from the bottom laser.

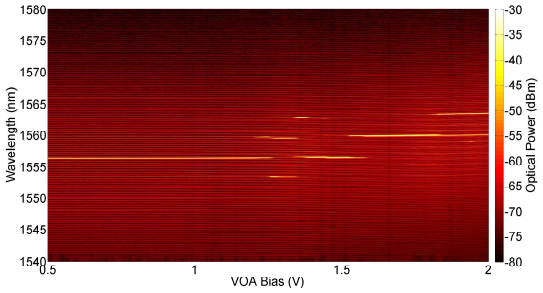

(c) Colour plot of the OSA traces from the top laser.

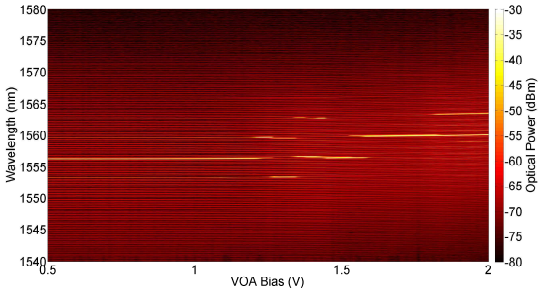

(d) Colour plot of the OSA traces from the bottom laser.

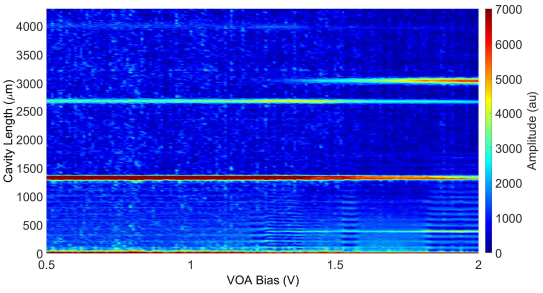

(e) Colour plot of the FFT of the OSA traces from the top laser.

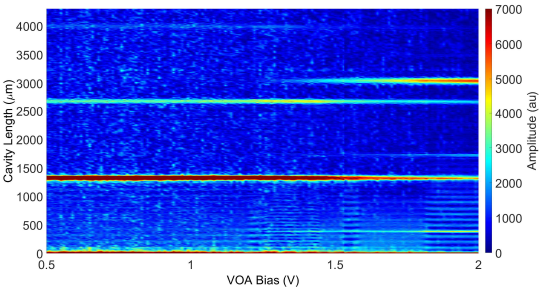

(f) Colour plot of the FFT of the OSA traces from the bottom laser.

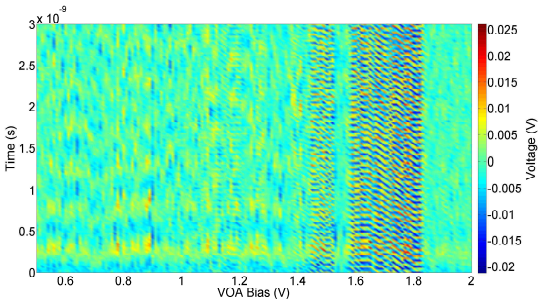

(g) Colour plot of the HSO traces from the top laser.

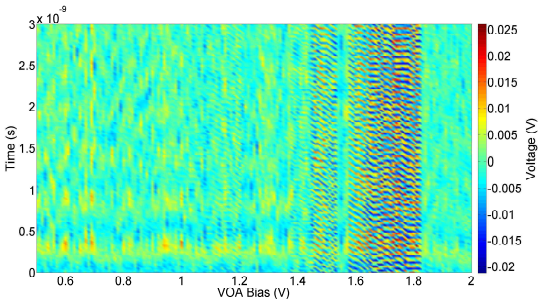

(h) Colour plot of the HSO traces from the bottom laser.

Figure 6.34: Colour plots of the output of both lasers of the 385 μm VOA PIC as a function of VOA bias for $\Delta \approx 15$ GHz.

6.3.2.1 Investigation of Beating using a Tuneable Optical Filter

A tunable optical filter (bandwidth at -3 dB = 0.4 ± 0.1 nm) was added to the setup (immediately after the lensed fibre). The filter was used to investigate the source of the beating seen on the ESA.

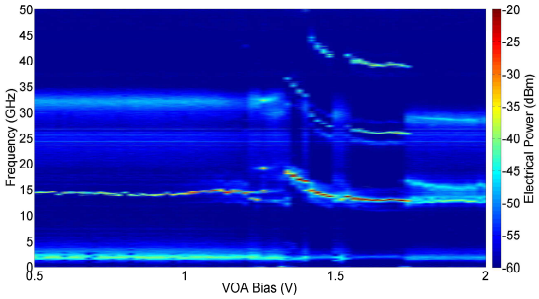

(a) Colour plot of the ESA traces from the top laser - unfiltered.

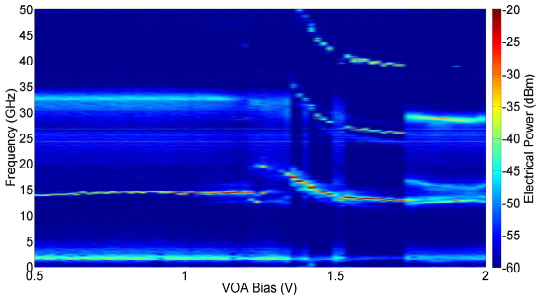

(b) Colour plot of the ESA traces from the bottom laser - unfiltered.

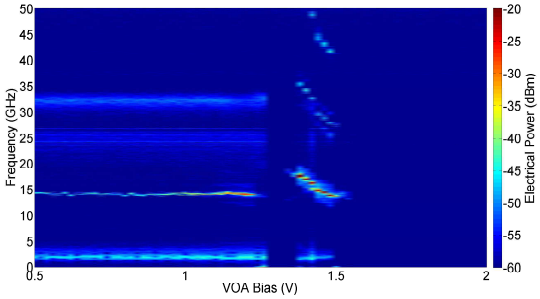

(c) Colour plot of the ESA traces from the top laser - filter at ∼1556 nm.

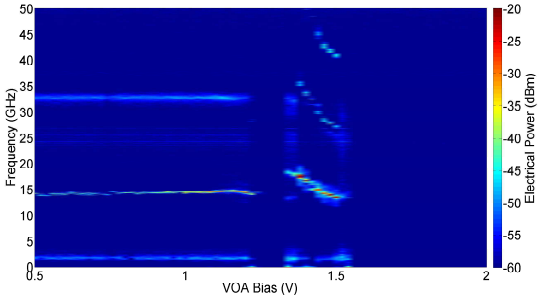

(d) Colour plot of the ESA traces from the bottom laser - filter at ∼1556 nm.

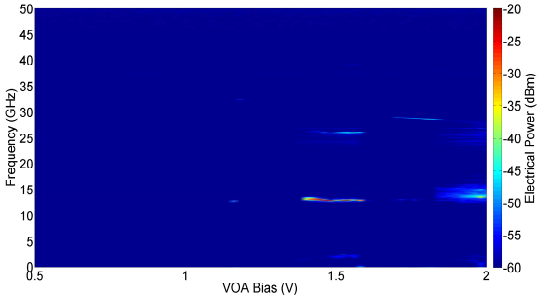

(e) Colour plot of the ESA traces from the top laser - filter at ∼1560 nm.

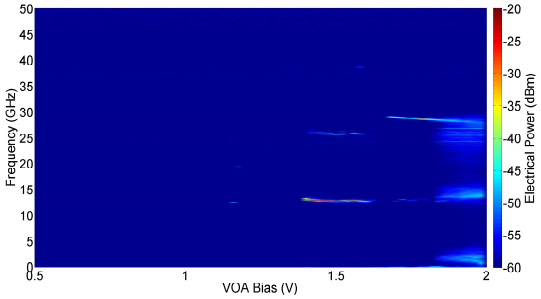

(f) Colour plot of the ESA traces from the bottom laser - filter at ∼1560 nm.

Figure 6.35: Colour plots of ESA traces as a function of VOA bias from the unfiltered and filtered output of both lasers of the 385 μm VOA PIC for $\Delta \approx 15$ GHz.

Figures 6.35a and b are the unfiltered ESA data and Figures 6.36a and b are the unfiltered OSA data. The filter was first placed at ∼1556 nm, around the lasers' natural lasing mode. The results are plotted in Figures 6.35 and 6.36 (c and d). As expected a beat note equal to the detuning between the lasers was clearly seen in the filtered data. This beat note was formed by the beating between the main modes of each laser. The beat note and its harmonics seen between 1.32 and 1.52 V in the unfiltered data was

also generated by the main modes. The filter was also placed at ∼1560 nm, around the mode that the lasers hopped to at high VOA biases. The beat note and its harmonics seen between 1.40 and 1.62 V in the unfiltered data was generated by this mode. Hence the beating between 1.40 and 1.52 V is partially created by both modes (at 1556 and 1560 nm).

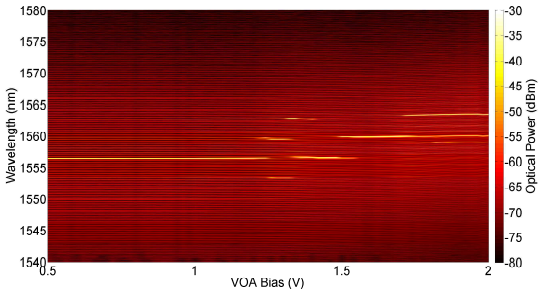

(a) Colour plot of the OSA traces from the top laser - unfiltered.

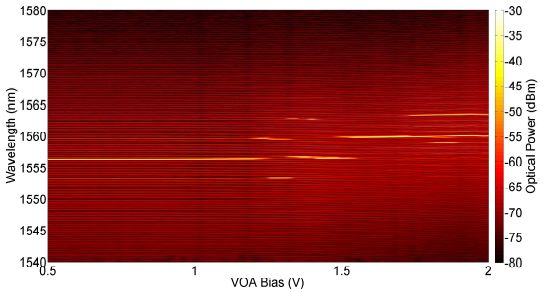

(b) Colour plot of the OSA traces from the bottom laser - unfiltered.

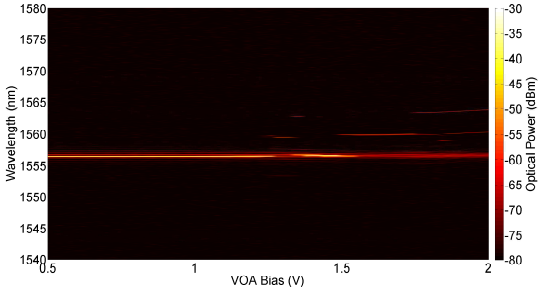

(c) Colour plot of the OSA traces from the top laser - filter at ∼1556 nm.

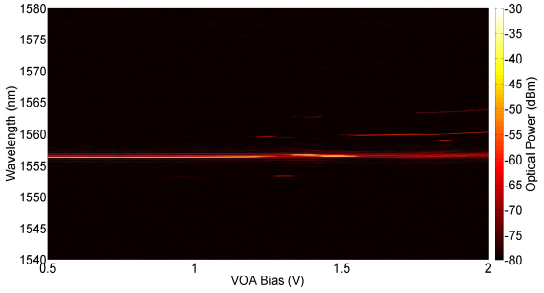

(d) Colour plot of the OSA traces from the bottom laser - filter at ∼1556 nm.

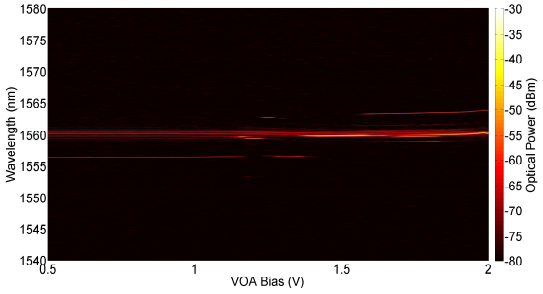

(e) Colour plot of the OSA traces from the top laser - filter at ∼1560 nm.

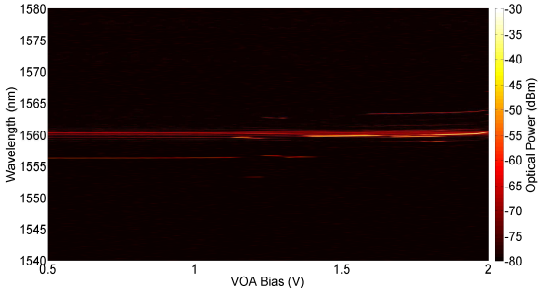

(f) Colour plot of the OSA traces from the bottom laser - filter at ∼1560 nm.

Figure 6.36: Colour plots of OSA traces as a function of VOA bias from the unfiltered and filtered output of both lasers of the 385 μm VOA PIC for $\Delta \approx 15$ GHz.

No beating was observed on the ESA above 1.52 V in the data filtered at ∼1556 nm. There was some beating at high VOA biases in the data filtered at ∼1560 nm but not as much as in the unfiltered data. Therefore, the beating at high VOA biases must be generated by other wavelengths. At high VOA biases the lasers became multimode, therefore filtering the data around one mode did not give all the information. In the unfiltered optical spectra, there is a second higher wavelength mode, at ∼1563 nm, excited at high VOA biases, which also contributes to this beating. There was also a

region of multimode behaviour between 1.22 and 1.32 V in the unfiltered data which did not appear in either of the filtered data. Therefore, there was a quiet region in the ESA data between these voltages in both filtered cases. In order to better understand this data, a detailed analysis of the optical spectra was performed.

6.3.2.2 Analysis of the Optical Spectra

A peak finder was used to pick out the main peaks in the optical spectra of both lasers. The results overlaid on the colour plots are shown in Figure 6.37. If both lasers did not have peaks within 0.4 nm of each other at the same VOA bias, the data was removed and the resulting peaks are plotted in Figure 6.38a. The separation between the peaks of each laser, at the same VOA bias, was calculated and converted to frequency. The frequency separation between the peaks is plotted in Figure 6.38b.

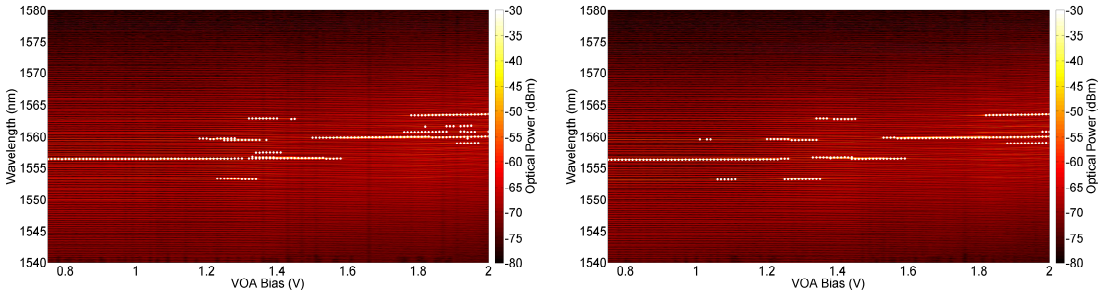

(a) Colour plot of the OSA traces from the top laser.

(b) Colour plot of the OSA traces from the bottom laser.

Figure 6.37: Colour plots of OSA traces as a function of VOA bias from the output of both lasers of the 385 μm VOA PIC for $\Delta \approx 15$ GHz with the main peaks highlighted.

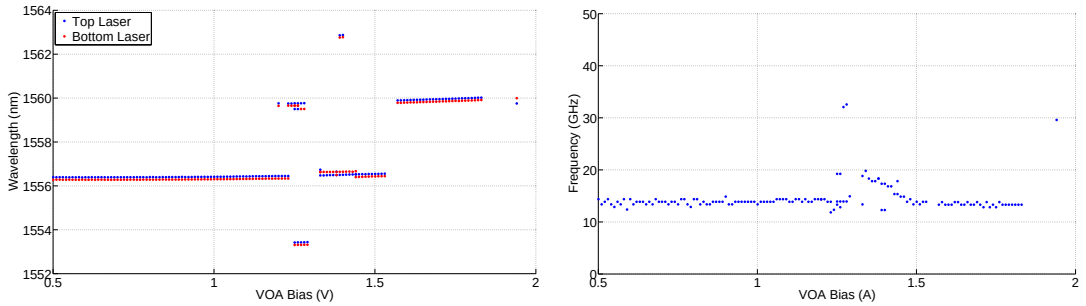

(a) Main lasing modes of the lasers.

(b) Frequency separation between the main lasing modes of the lasers.

Figure 6.38: Main lasing modes of the lasers as a function of VOA bias.

It can be clearly seen in Figure 6.38b, that the frequency separation between the main lasing modes has the same shape as the ESA data. The harmonics of the beat notes at VOA biases between 1.32 and 1.62 V are not observed since they were generated by the separation between the satellite peaks on the main modes. The frequency separation was overlaid on the colour plots of the ESA traces and plotted in Figure 6.39. The data

match within experimental error, confirming how the behaviour of the main lasing modes of the lasers formed the spectra observed on the ESA.

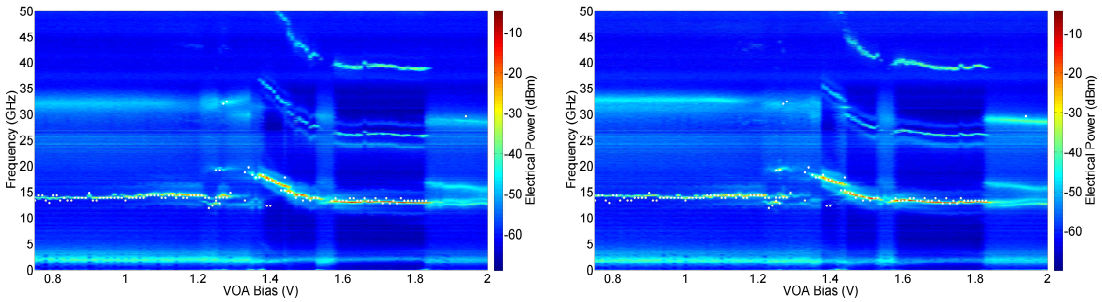

(a) Colour plot of the ESA traces from the top laser.

(b) Colour plot of the ESA traces from the bottom laser.

Figure 6.39: Colour plots of ESA traces from the output of both lasers of the 385 μm VOA PIC for $\Delta \approx 15$ GHz overlaid with the frequency separation between the main lasing modes of the lasers.

The optical output of both lasers has been used to replicate the beating between the lasers seen on the ESA. The electrical spectra can be formed by the output of each laser separately because the optical spectra of each laser contains its own lasing modes plus the main lasing modes of the second laser but at a lower power. (The lasing modes of the second laser were not picked up in the peak search since they were below the threshold used.) Figures 6.40a to c show how the main lasing modes of both lasers were seen in the optical spectra of each laser with the modes of the second laser at a much lower power.

The beating between these modes was then observed on the ESA. In Figure 6.40d the separation between the main modes of the two lasers was approximately 3.4 nm, much larger than 50 GHz, therefore this method of generating the electrical spectra from the optical breaks down at high VOA biases. The coupling ratio was also measured for this device and the results are discussed in the next section.

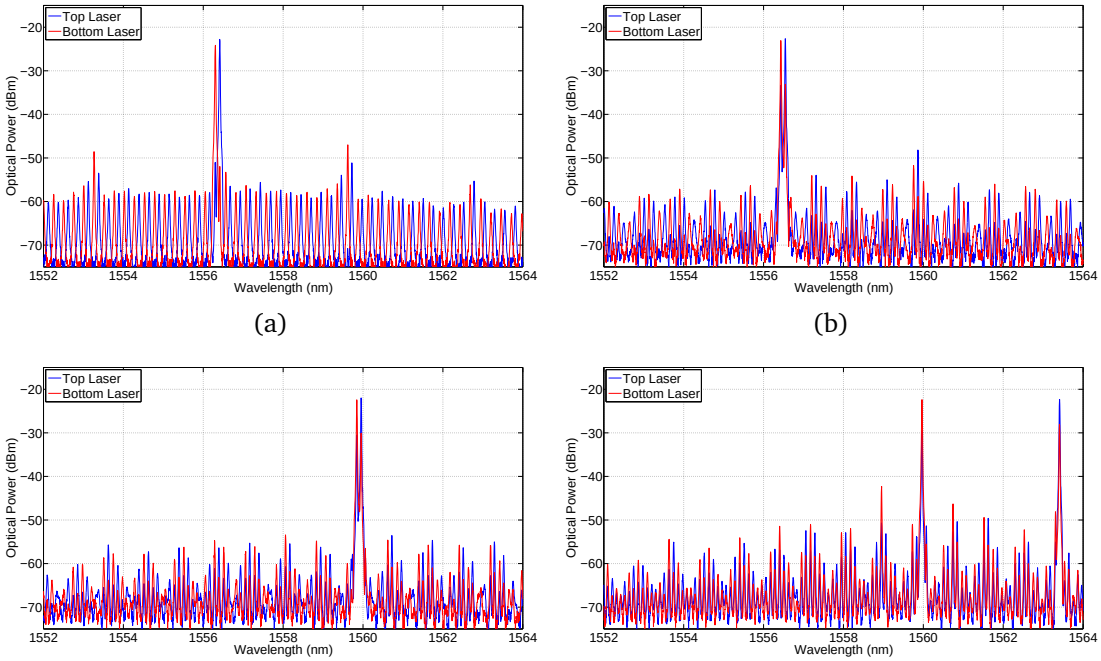

Figure 6.40: Optical spectra of both lasers at VOA biases of (a) 1.0 V (b) 1.5 V, (c) 1.7 V and (d) 1.9 V.

6.3.3 Coupling Ratio, κ

Section 6.2.1 described how the coupling ratio, κ between the lasers was measured. As discussed earlier when κ was measured it was found that $\kappa_{T\rightarrow B} \neq \kappa_{B\rightarrow T}$ and $\kappa > 1$. The same experiment was repeated for these new devices and $\kappa_{T\rightarrow B}$ and $\kappa_{B\rightarrow T}$ were measured as a function of the VOA bias and the laser biases.

Figure 6.41 is surface plots of $\kappa_{T\rightarrow B}$ and $\kappa_{B\rightarrow T}$ for a fixed mirror section bias of 45 mA, for the 1285 μm VOA PIC. Figure 6.42 is the results for the 385 μm VOA PIC. Again, $\kappa_{T\rightarrow B} \neq \kappa_{B\rightarrow T}$. The maximum obtained for $\kappa_{B\rightarrow T}$ for the 1285 μm VOA PIC was 0.035 which is much larger than the maximum for $\kappa_{T\rightarrow B}$ of 0.023. Conversely, for the 385 μm VOA PIC, the maximum for $\kappa_{B\rightarrow T}$ was 0.479 as opposed to 0.962 for $\kappa_{T\rightarrow B}$. It is currently unclear why there is such a significant difference between $\kappa_{T\rightarrow B}$ and $\kappa_{B\rightarrow T}$. However, the turn-on of the coupling ratio occurs at approximately the same VOA bias for both $\kappa_{T\rightarrow B}$ and $\kappa_{B\rightarrow T}$, ∼1.8 V for the 1285 μm VOA PIC and ∼1.2 V for the 385 μm VOA PIC.

The shorter VOA absorbed much less light therefore for the 385 μm VOA PIC, the values obtained for κ were more than twenty times bigger than for the 1285 μm VOA PIC. To overcome the absorption of the longer VOA, a higher bias could have been applied. However, applying a bias greater than 2 V risks damaging the device, and 2 V applied to the VOA was sufficient to cause the full PIC to behave as a compound laser. The minimum κ obtained for the 1285 μm VOA PIC was 0.008 and for the 385 μm VOA PIC

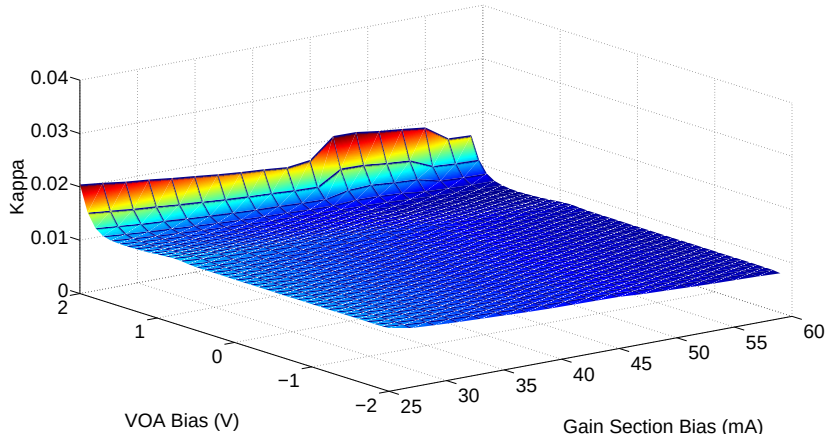

(a) $\kappa_{T\rightarrow B}$

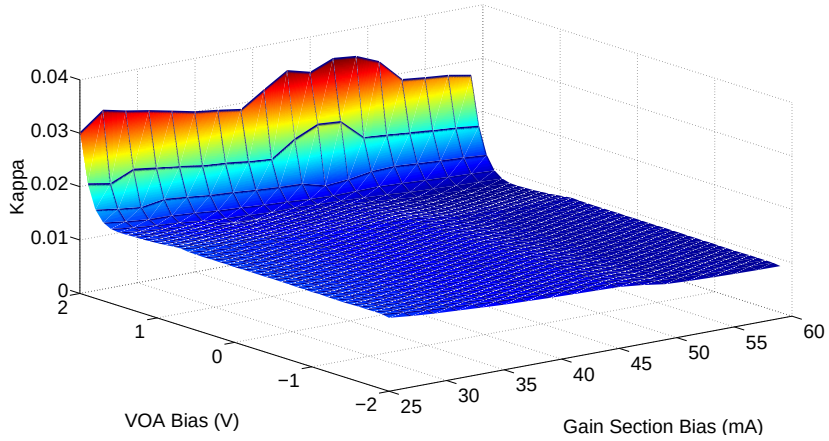

(b) $\kappa_{B\rightarrow T}$

Figure 6.41: Surface plots of the coupling ratio, κ between the lasers on the 1285 μm VOA PIC, as a function of the VOA bias and the laser gain section bias for a fixed mirror section bias of 45 mA.

was 0.015.

Surprisingly, κ for low GS biases was larger than for high GS biases. It was expected that κ would increase with increasing GS bias i.e. increasing power emitted by the laser. The photocurrent measured in the bottom laser for a top GS bias of 25 mA and 60 mA is plotted in Figure 6.43a, along with the dark current measured in the bottom laser, for a top MS bias of 45 mA (385 μm VOA PIC). As expected the photocurrent increases with increasing GS bias. The dark current was subtracted from the measured photocurrent and the result is plotted in Figure 6.43b. The result for GS = 60 mA is still larger than for GS = 25 mA.

These results are plotted again in Figure 6.43c along with the photocurrent measured in the VOA, which corresponds to the total output power of the laser. I_{tot} for GS = 60mA is much larger than for GS = 25 mA, therefore when the photocurrent measured in the bottom laser is divided by the total photocurrent, to get κ, the result for GS = 60 mA is now smaller than for GS = 25 mA, see Figure 6.43d.

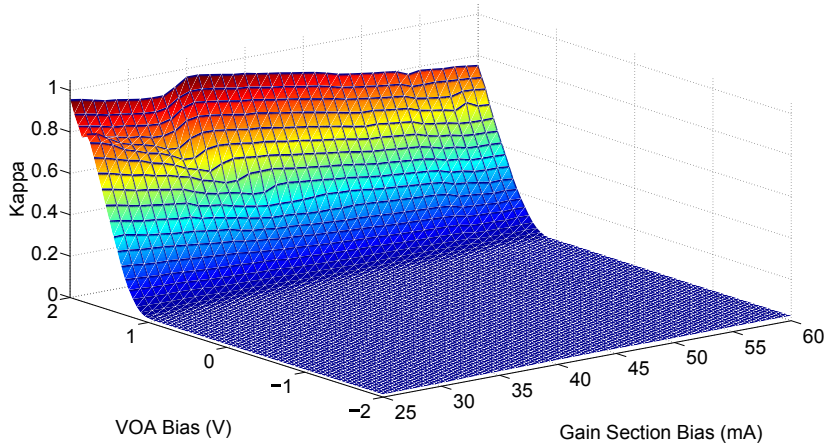

(a) $\kappa_{T\rightarrow B}$

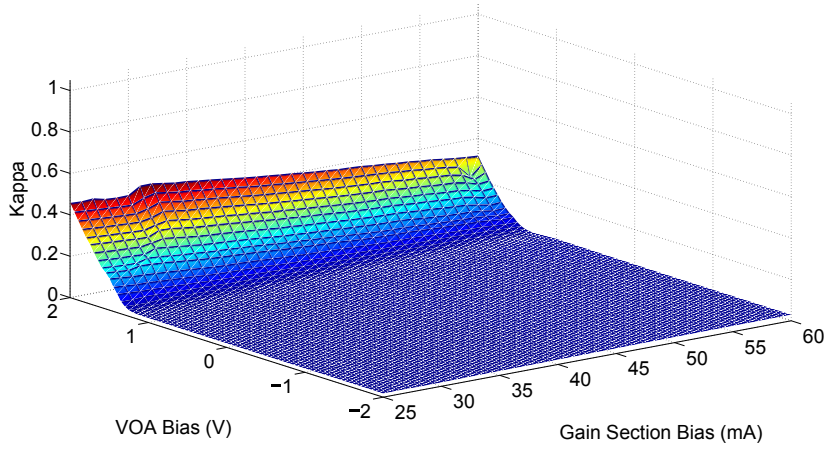

(b) $\kappa_{B\rightarrow T}$

Figure 6.42: Surface plots of the coupling ratio, κ between the lasers on the 385 μm VOA PIC, as a function of the VOA bias and the laser gain section bias for a fixed mirror section bias of 45 mA.

Since $\kappa_{T\rightarrow B} \neq \kappa_{B\rightarrow T}$, κ was assumed to best be given as the average of the two. Therefore, the average coupling, κ between the lasers as a function of VOA bias for a MS bias of 35 mA and various GS biases (for the 385 μm VOA PIC) is plotted in Figure 6.44. As before κ decreased with increasing GS bias. Over the range of VOA bias used, the maximum κ obtained was 0.97.

The VOA bias on the x-axis in Figures 6.34 was converted to κ and the resulting plots are shown in Figures 6.45. The positions of the dynamics has moved, and the PIC becomes a compound laser at $\kappa = 0.75$.

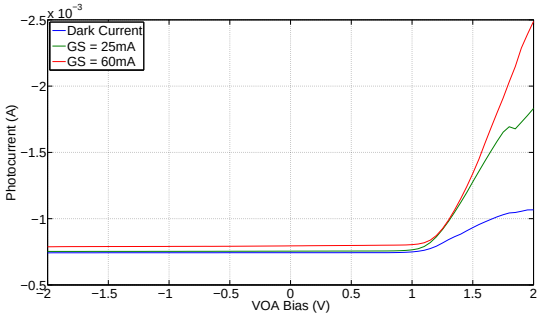

(a) The photocurrent measured in the bottom laser for a top GS bias of 25 mA and 60 mA, and the dark current measured in the bottom laser.

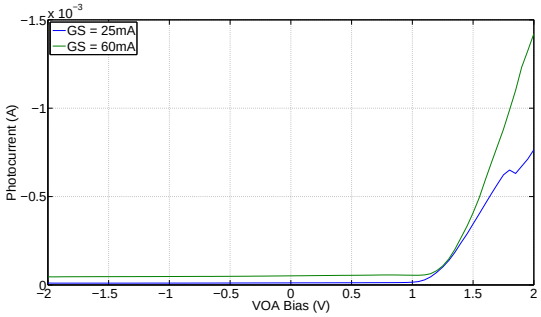

(b) The photocurrent measured in the bottom laser minus the dark current.

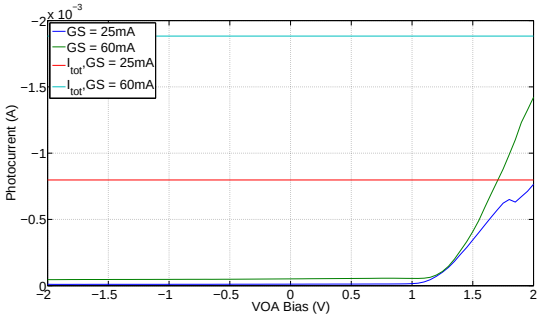

(c) The photocurrent measured in the bottom laser minus the dark current and the photocurrent measured in the VOA, which corresponds to the total output power of the laser.

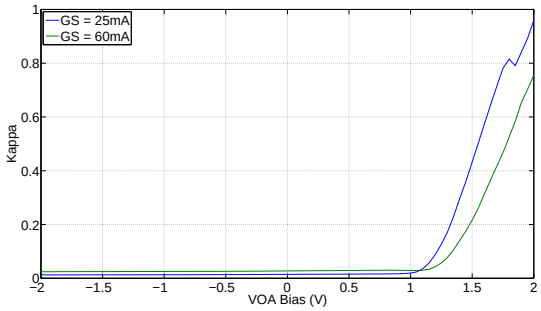

(d) The photocurrent measured in the bottom laser divided by the total photocurrent giving κ.

Figure 6.43: Photocurrent & $\kappa_{T\rightarrow B}$ measurements for a top MS bias of 45 mA for the 385 μm VOA PIC.

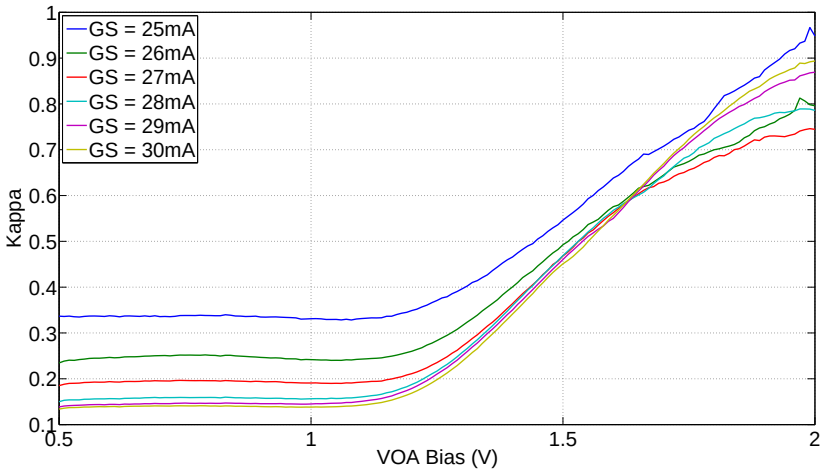

Figure 6.44: Average of $\kappa_{T\rightarrow B}$ and $\kappa_{B\rightarrow T}$ as a function of VOA bias for various GS biases for the 385 μm VOA PIC, for a MS bias of 35 mA.

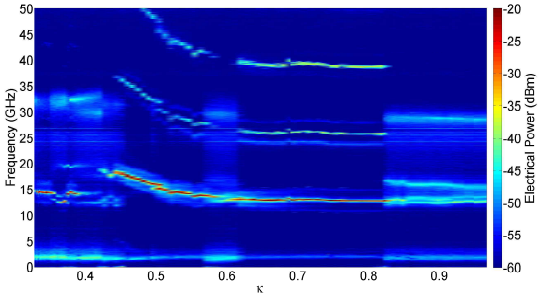

(a) Colour plot of the ESA traces from the top laser.

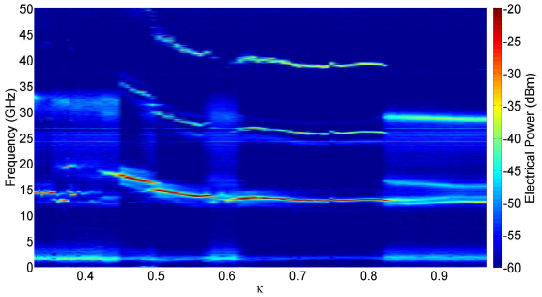

(b) Colour plot of the ESA traces from the bottom laser.

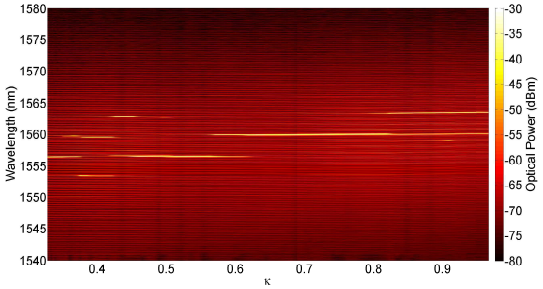

(c) Colour plot of the OSA traces from the top laser.

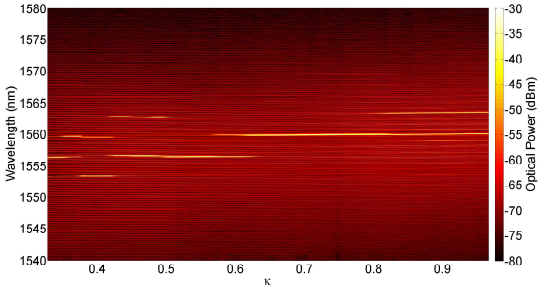

(d) Colour plot of the OSA traces from the bottom laser.

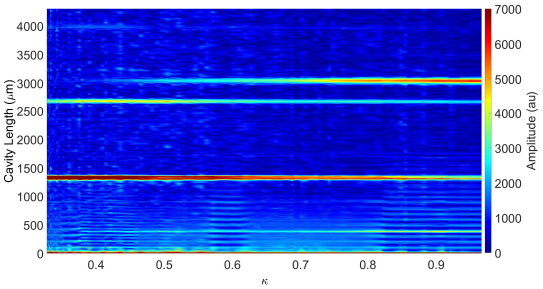

(e) Colour plot of the FFT of the OSA traces from the top laser.

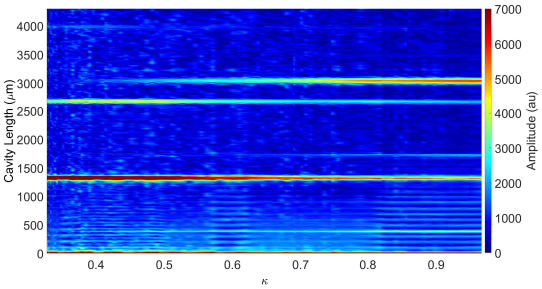

(f) Colour plot of the FFT of the OSA traces from the bottom laser.

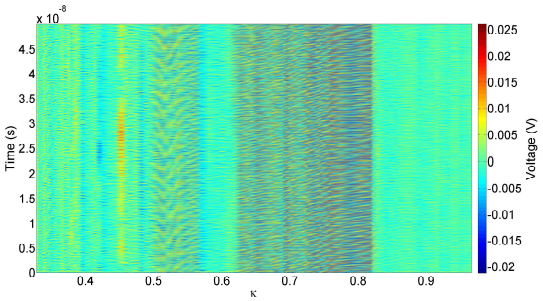

(g) Colour plot of the HSO traces from the top laser.

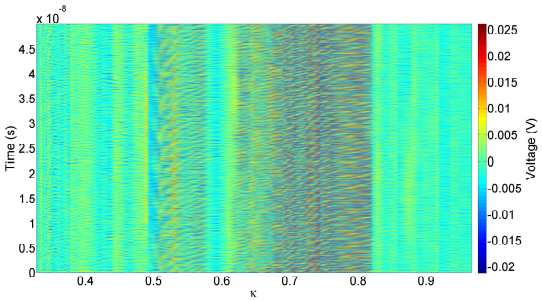

(h) Colour plot of the HSO traces from the bottom laser.

Figure 6.45: Colour plots of the output of both lasers as a function of κ for the 385 μm VOA PIC for $\Delta \approx 15$ GHz.

6.4 Conclusion

In this chapter, the U-Bend VOA design was found to be the most effective in eliminating the effect of substrate coupling. The results for three different VOA lengths were presented; 385 μm, 1100 μm and 1285 μm. The dynamical behaviour of the lasers as a function of the coupling and detuning between the lasers was investigated. In order to summarise the results, five types of dynamical behaviour were identified; uncoupled, beating, frequency locked, aperiodic and period doubling. These behavioural types were used to create a summary plot as a function of the VOA bias and the detuning between the lasers for the 1100 μm VOA PIC. Further work is required to identify more of the types of dynamical behaviour and interactions.

The experiment was repeated for the 1285 μm VOA PIC and a higher resolution OSA was used to obtain these results which gave further insight into the optical behaviour of the lasers that created the beating observed on the ESA and HSO.

A LabView programme was written to automate the fibre coupling to the lasers and enable moving the fibre between the lasers during a sweep. Therefore, for the first time, the output of both lasers was recorded during a sweep. The only detuning obtained for the 385 μm VOA PIC was approximately 15 GHz. The separation between the main modes of the optical spectra of the lasers was investigated in order to recreate the beating between the lasers seen in the electrical spectra. A tunable optical filter was added to the setup to confirm which lasing modes were beating together to form the spectra observed on the ESA.

Mutual injection locking was not obtained on the PIC with a 385 μm VOA, since the lasers were always coupled at a detuning of approximately 15 GHz. The VOAs that were longer than 1285 μm were too absorptive to achieve sufficient coupling between the lasers to observe any dynamics. Similar dynamics were obtained from the PICs with 1100 μm and 1285 μm VOAs.

The coupling ratio, κ between the lasers was measured for all three PICs. It was found that $\kappa_{T\rightarrow B} \neq \kappa_{B\rightarrow T}$ and κ decreased with increasing gain section bias. At a VOA bias of 2 V, κ was more than twenty times greater for the 385 μm VOA PIC (0.962) than for the 1285 μm VOA PIC (0.035) since it is shorter, therefore much less absorbing.

Chapter 7

Conclusions & Future Work

7.1 Summary

The work presented in this thesis has focused on designing and testing photonic integrated circuits consisting of two single facet slotted Fabry Pérot lasers integrated together through a waveguide interconnect. Photonic integration offers excellent potential for combining otherwise discrete system components together on a single device providing a robust, power efficient and cost effective solution. Injection locking has been proposed as a method for de-multiplexing a comb so that the signal from each laser can be modulated individually before recombining the signal again to a coherent comb for CoWDM. It has been shown that photonic integration is necessary for all coherent super-channel implementations. An introduction to photonic integration and an overview of past experimental studies of mutually coupled semiconductor lasers was given in chapters 1 and 2.

In chapter 3 of this thesis, a Fabry Pérot and a slotted Fabry Pérot laser were characterised and injection locked to an external tunable laser source. Four regions of distinct behaviour were observed: (i) a quiet region close to zero detuning where the laser was shown to be injection locked to the external master laser; (ii) an unlocked region for both large negative and positive detuning where the ESA displayed a beat note corresponding to the frequency difference between the lasers; (iii) a region of non-linear interaction (NLI) between the lasers at small detunings; and (iv) a region of aperiodic dynamics close to the positive detuning boundary (i.e. higher external master laser wavelength).

Having demonstrated the injection locking of a semiconductor laser to an external master laser, the injection and mutual locking of two integrated SFP lasers both off and on-chip were compared in chapter 4. The biases of the lasers were chosen so that they operated in a master-slave regime where the master was much higher powered

than the slave. These experiments allowed for the development of the measurement technique using an OSA, ESA and HSO used to investigate mutual coupling. A baseline was also established for future experiments. Various types of dynamical behaviour were detected; including beating, NLI, injection locking, irregular dynamics, asymmetric beating, pulsing and aperiodic behaviour. It was found that for the on-chip coupling regime when the lasers mutually injection lock, both lasers lock to a wavelength longer than either of their natural lasing wavelengths. The effect of the VOA bias and hence the coupling strength on the mutual coupling properties of the system were also observed for the first time; at low VOA biases the VOA was absorbing, therefore the lasers did not interact. Biasing the VOA to semi-transparency allowed the lasers to interact and injection lock, while high VOA biases made the VOA sufficiently transparent to cause the full PIC to behave as a compound laser.

In chapter 5, the wavelength (using the mirror and gain section biases) of the two integrated SFP lasers was fixed and the VOA bias/coupling was varied to obtain injection locking. In this regime the lasers were equally powered and their free running spectra were almost identical, but when mutually locked, they lased at a higher wavelength than their natural lasing modes. This shift was unexpected and requires further investigation. An attempt was made to measure the coupling between the lasers but it was discovered that substrate coupling was affecting the results.

New VOA designs were proposed and tested in chapter 6 to combat substrate coupling. The U-Bend VOA design was found to be the most effective at eliminating the effect of substrate coupling. The results for three different VOA lengths were presented; 385 μm, 1100 μm and 1285 μm. The dynamical behaviour of the lasers as a function of the coupling and detuning between the lasers was investigated. In order to summarise the results, five types of dynamical behaviour were identified; uncoupled, beating, frequency locked, aperiodic and period doubling. A LabView programme was written to automate the fibre coupling to the lasers and enable moving the fibre between the lasers during a sweep. Therefore, for the first time, the output of both lasers on a U-Bend VOA PIC was recorded during a sweep. The coupling ratio, κ between the lasers was measured for all three PICs. It was found that $\kappa_{T\rightarrow B} \neq \kappa_{B\rightarrow T}$.

The primary goal of this work was to experimentally investigate mutual injection locking between different lasers on a PIC and to provide a set of experimental results to aid theoretical work. Multiple PICs, with various length and shape VOAs, were designed and tested from six fabrication runs. The U-shaped VOAs were found to work the best out of the VOA designs investigated. Mutual injection locking was obtained between two integrated SFP lasers on multiple PICs with VOA lengths ranging from 615 μm to 1285 μm. Mutual injection locking was not obtained on the PIC with a 385 μm VOA, since the lasers were always coupled at a detuning of approximately 15 GHz. The VOAs that were longer than 1285 μm were too absorptive to obtain sufficient coupling

between the lasers to observe any dynamics. It was demonstrated that the detuning between the lasers must be less than 10 GHz, if mutual injection locking is to be achieved. The coupling between the lasers is also critical for injection locking.

7.2 Future Work

It was unexpected that when mutually injection locked, the lasers would lase at a higher wavelength than their natural lasing mode. However, these longer wavelength modes are most likely due to lower losses in the VOA at longer wavelengths, but this requires further investigation. Further work is also required to identify more of the types of dynamical behaviour between the mutually coupled lasers.

A full set of operational U-Bend VOA PICs was not obtained due to fabrication issues. Future work would include testing PICs with various VOA lengths in order to better understand how the mutual injection properties depend on the length of the delay between the lasers. Testing these devices using the automated coupling LabView would record the output of both lasers, which would aid in identifying the behaviour of the lasers.

In the current PIC design, the VOA is fabricated on the same active material as the lasers. Therefore, the maximum coupling obtained between the lasers is controlled by the length of the VOA. The VOA is absorbing at 1550 nm, hence the absorption increases with increasing VOA length and a larger electrical bias is required to overcome the absorption. However, it was found that even for the longest VOA tested (1285 μm) that a bias of 2 V was sufficient for the full PIC to behave as a compound laser and the maximum coupling ratio obtained was less than 0.04. The maximum coupling ratio obtained for the shortest VOA length (385 μm) was almost 1, but the full PIC began to behave as a compound laser at $\kappa = 0.75$. Investigating how to increase the coupling achieved without the PIC becoming a compound laser would allow for further study of the behaviour.

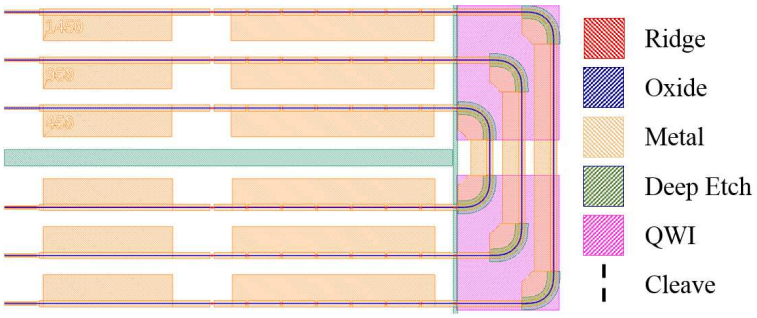

Figure 7.1: Proposed next generation of PICs with U-Bend VOAs, designed with quantum well intermixing on the bends to reduce the absorption of the VOAs and have a constant coupling for various length delays between the lasers.

Figure 7.1 is a proposed set of U-Bend VOA PICs designed with quantum well intermixing (QWI) on the bends. The length of the VOA section that is not intermixed is 110 μm, which is less than half the length of the shortest VOA tested and should therefore increase the coupling achievable. Since the non-intermixed section is the same length for each device, the coupling should be similar across the full set of PICs and no longer directly linked to the length of the VOA. The deep etched region between the lasers has been added to reduce the risk of thermal crosstalk between the lasers.

The work presented in this thesis has begun to generate some interest among laser dynamics colleagues and some work has been done to create a model that matches the experimental data [77]. It has been concluded that the presence of the saturable VOA greatly increases the complexity of the bifurcation structure. A passive coupling waveguide would reproduce the bifurcation scenario known from optically injected lasers. Both for reproducibility and simplicity of the design a passive optical waveguide was found to be preferable. Therefore, future PIC designs would include a passive waveguide interconnect between the lasers. Figure 7.2 shows another proposed set of U-Bend VOA PICs, where the full waveguide interconnect is quantum well intermixed, thus simplifying the system. However, fully intermixing the VOA is likely to greatly reduce the variability of the coupling.

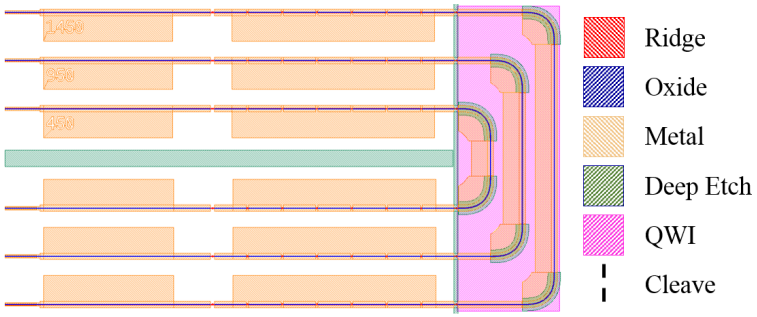

Figure 7.2: Proposed next generation of PICs with U-Bend VOAs, designed with quantum well intermixing on the entire VOA to form a passive interconnect between the lasers, thus reducing the complexity of the system.

Another possible avenue for future work is examining the mutual injection locking characteristics of a system of alternative semiconductor lasers, especially with higher SMSR and tuning range. For example the slotted mirror of the SFP lasers could be replaced with pits in the waveguide [79]. These lasers have been shown to have a larger tuning range and SMSR than SFP lasers, which would also simplify the dynamics since there should be less mode-hopping. Alternatively, if this work were to be continued in a different fab that had access to an epitaxial regrowth process, DFB lasers could be used in the PICs. Also, having access to an epitaxial regrowth process, would allow for a truly passive interconnect between the lasers that would have no dependence on wavelength.

7.3 Conclusion

The main results presented in this thesis focused on the experimental investigation of mutual injection locking of two slotted Fabry Pérot lasers integrated together through various length variable optical attenuators/amplifiers. The U-bend VOA design was found to be the most effective at eliminating substrate coupling. The testing of such a PIC required significant work on automating the test set-up to enable the output of both lasers to be recorded during a sweep. A measurement technique using an OSA, ESA and HSO for investigating mutual coupling was developed, establishing a baseline for future experiments. For the first time, it has been demonstrated that different lasers can coexist on a PIC without an isolator and without operating in a highly asymmetric, master-slave system.

References

[1] "Internet World Statistics." `http://www.internetworldstats.com`.

[2] "Cisco." `http://www.cisco.com`.

[3] E. B. Desurvire, "Capacity demand and technology challenges for lightwave systems in the next two decades," *Journal of Lightwave Technology*, vol. 24, pp. 4697–4710, dec 2006.

[4] G. E. Keiser, "Tutorial Paper A Review of WDM Technology and Applications," *Optical Fiber Technology*, vol. 5, pp. 3–39, jan 1999.

[5] N. S. Bergano, "Wavelength division multiplexing in long-haul transoceanic transmission systems," *Journal of Lightwave Technology*, vol. 23, pp. 4125–4139, dec 2005.

[6] R. Nagarajan, M. Kato, D. Lambert, P. Evans, S. Corzine, V. Lal, J. Rahn, A. Nilsson, M. Fisher, M. Kuntz, J. Pleumeekers, A. Dentai, H.-S. Tsai, D. Krause, H. Sun, K.-T. Wu, M. Ziari, T. Butrie, M. Reffle, M. Mitchell, F. Kish, and D. Welch, "Terabit/s class InP photonic integrated circuits," *Semiconductor Science and Technology*, vol. 27, p. 094003, sep 2012.

[7] A. Ellis and F. Gunning, "Spectral density enhancement using coherent WDM," *IEEE Photonics Technology Letters*, vol. 17, pp. 504–506, feb 2005.

[8] X. Yi, W. Shieh, and Y. Tang, "Phase estimation for coherent optical OFDM transmission," in *2007 Joint International Conference on Optical Internet and Australian Conference on Optical Fibre Technology, COIN-ACOFT 2007*, 2007.

[9] Q. Zou, A. Tarighat, and A. H. Sayed, "Compensation of phase noise in OFDM wireless systems," *IEEE Transactions on Signal Processing*, vol. 55, pp. 5407–5424, nov 2007.

[10] J. H. Baek, F. M. Soares, S. W. Seo, W. Jiang, N. K. Fontaine, R. G. Broeke, J. Cao, F. Olsson, S. Lourdudoss, and S. J. Yoo, "10-GHz and 20-GHz channel spacing high-resolution AWGs on InP," *IEEE Photonics Technology Letters*, vol. 21, pp. 298–300, mar 2009.

[11] K. Takada, M. Abe, M. Shibata, M. Ishii, and K. Okamoto, "Low-crosstalk 10-GHz-spaced 512-channel arrayed-waveguide grating multi/demultiplexer fabricated on a 4-in wafer," *IEEE Photonics Technology Letters*, vol. 13, pp. 1182–1184, nov 2001.

[12] H. Takahashi, S. Suzuki, K. Kato, and I. Nishi, "Arrayed-Waveguide Grating for Wavelength Division Multi/Demultiplexer with Nanometre Resolution," *Electronics Letters*, vol. 26, no. 2, pp. 87–88, 1990.

[13] D. Feng, W. Qian, H. Liang, C. C. Kung, J. Fong, B. J. Luff, and M. Asghari, "Fabrication insensitive echelle grating in silicon-on-insulator platform," *IEEE Photonics Technology Letters*, vol. 23, no. 5, pp. 284–286, 2011.

[14] S. Janz, A. Balakrishnan, S. Charbonneau, P. Cheben, M. Cloutier, A. Delâge, K. Dossou, L. Erickson, M. Gao, P. A. Krug, B. Lamontagne, M. Packirisamy, M. Pearson, and D. X. Xu, "Planar Waveguide Echelle Gratings in Silica-On-Silicon," *IEEE Photonics Technology Letters*, vol. 16, pp. 503–505, feb 2004.

[15] S. Pathak, P. Dumon, D. Van Thourhout, and W. Bogaerts, "Comparison of AWGs and Echelle Gratings for Wavelength Division Multiplexing on Silicon-on-Insulator," *IEEE Photonics Journal*, vol. 6, oct 2014.

[16] W. Cotter, D. Goulding, B. Roycroft, J. O'Callaghan, B. Corbett, F. H. Peters, J. O'Callaghan, B. Corbett, and F. H. Peters, "Investigation of active filter using injection-locked slotted Fabry-Perot semiconductor laser.," *Applied optics*, vol. 51, pp. 7357–61, oct 2012.

[17] S. Jansen, "Multi-Carrier Approaches for Next-Generation Transmission: Why, Where and How?," in *Proc. Optical Fiber Communication (OFC) Conference*, 2012.

[18] N. Sarmah, J. Grzyb, K. Statnikov, S. Malz, P. Rodriguez Vazquez, W. Föerster, B. Heinemann, and U. R. Pfeiffer, "A fully integrated 240-GHz direct-conversion quadrature transmitter and receiver chipset in SiGe technology," *IEEE Transactions on Microwave Theory and Techniques*, vol. 64, pp. 562–574, feb 2016.

[19] A. Poustie, "Hybrid Integration for Advanced Photonic Devices," *Proceedings of SPIE*, vol. 7135, nov 2008.

[20] M. Wale, "Self aligned, flip chip assembly of photonic devices with electrical and optical connections," *40th Conference Proceedings on Electronic Components and Technology*, pp. 34–41, 1990.

[21] L. A. Coldren, S. C. Nicholes, L. Johansson, S. Ristic, R. S. Guzzon, E. J. Norberg, and U. Krishnamachari, "High Performance InP-Based Photonic ICs—A Tutorial," *Journal of Lightwave Technology*, vol. 29, pp. 554–570, feb 2011.

[22] E. J. Skogen, J. W. Raring, G. B. Morrison, C. S. Wang, V. Lai, M. L. Mašanović, and L. A. Coldren, "Monolithically integrated active components: A quantum-well intermixing approach," *IEEE Journal on Selected Topics in Quantum Electronics*, vol. 11, pp. 343–355, mar 2005.

[23] M. Aoki, M. Suzuki, H. Sano, T. Kawano, T. Ido, T. Taniwatari, K. Uomi, and A. Takai, "InGaAs/InGaAsP MQW Electroabsorption Modulator Integrated with a DFB Laser Fabricated by Band-Gap Energy Control Selective Area MOCVD," *IEEE Journal of Quantum Electronics*, vol. 29, no. 6, pp. 2088–2096, 1993.

[24] L. Hou and J. H. Marsh, "Photonic Integrated Circuits Based on Quantum Well Intermixing Techniques," in *Procedia Engineering*, vol. 140, pp. 107–114, Elsevier Ltd, 2016.

[25] J. H. Marsh, P. Cusumano, A. C. Bryce, B. S. Ooi, and S. G. Ayling, "GaAs/AlGaAs photonic integrated circuits fabricated using impurity-free vacancy disordering," in *Functional Photonic Integrated Circuits* (M. N. Armenise and K.-K. Wong, eds.), vol. 2401, pp. 74–85, mar 1995.

[26] R. G. Gould *et al.*, "The laser, light amplification by stimulated emission of radiation," in *The Ann Arbor conference on optical pumping, the University of Michigan*, vol. 15, p. 92, 1959.

[27] R. N. Hall, G. E. Fenner, J. D. Kingsley, T. J. Soltys, and R. O. Carlson, "Coherent light emission from GaAs junctions," *Physical Review Letters*, vol. 9, no. 9, pp. 366–368, 1962.

[28] M. I. Nathan, W. P. Dumke, G. Burns, F. H. Dill, and G. Lasher, "Stimulated emission of radiation from GaAs p-n junctions," *Applied Physics Letters*, vol. 1, no. 3, pp. 62–64, 1962.

[29] T. M. Quist, R. H. Rediker, R. J. Keyes, W. E. Krag, B. Lax, A. L. McWhorter, and H. J. Zeigler, "Semiconductor maser of GaAs," *Applied Physics Letters*, vol. 1, no. 4, pp. 91–92, 1962.

[30] N. Holonyak Jr and S. Bevacqua, "Coherent (visible) light emission from ga (asp) junctions," in *Applied Physics Letters*, vol. 1, p. 82, 1962.

[31] H. Kroemer, "A Proposed Class of Hetero-junction Injection Lasers," *Proceedings of the IEEE*, vol. 51, no. 12, pp. 1782–1783, 1963.

[32] H. Kressel and H. Nelson, "Close-Confinement Gallium Arsenide Pn Junction Lasers with Reduced Optical Loss at Room Temperature," *RCA Review*, vol. 30, p. 106, 1969.

[33] Z. I. Alferov, V. M. Andreyev, V. I. Korolkov, E. L. Portnoi, and D. Tretiakov, "Coherent radiation of epitaxial heterojunction structures in the AlAs-GaAs system

(Coherent emission in epitaxial structures with heterojunctions in AlAs-GaAs system)," *Soviet Physics-Semiconductors*, vol. 2, pp. 1289–1291, 1969.

[34] D. Goulding, *Non-Linear Dynamics of Optically Injected Quantum Dot Lasers, PhD Thesis*. Cork, Ireland: University College Cork, 2010.

[35] L. A. Coldren, S. W. Corzine, and M. L. Mašanović, *Diode Lasers and Photonic Integrated Circuits*. USA: John Wiley & Sons, Inc., 2^{nd} ed., 2012.

[36] T. Ihn, *Semiconductor Nanostructure Quantum States and Electronic Transport*. USA: Oxford University Press, 2010.

[37] R. Lang, "Injection locking properties of a semiconductor laser," *IEEE Journal of Quantum Electronics*, vol. 18, no. 6, pp. 976–983, 1982.

[38] G. H. M. van Tartwijk and D. Lenstra, "Semiconductor lasers with optical injection and feedback," *Quantum and Semiclassical Optics: Journal of the European Optical Society Part B*, vol. 7, pp. 87–143, apr 1995.

[39] S. Wieczorek, B. Krauskopf, and D. Lenstra, "Unifying view of bifurcations in a semiconductor laser subject to optical injection," *Optics Communications*, vol. 172, pp. 279–295, dec 1999.

[40] S. P. Hegarty, D. Goulding, B. Kelleher, G. Huyet, M.-T. Todaro, A. Salhi, A. Passaseo, and M. De Vittorio, "Phase-locked mutually coupled 1.3 μm quantum-dot lasers," *Optics Letters*, vol. 32, pp. 3245–3247, nov 2007.

[41] N. Fujiwara, Y. Takiguchi, and J. Ohtsubo, "Observation of the synchronization of chaos in mutually injected vertical-cavity surface-emitting semiconductor lasers," *Opt. Lett.*, vol. 28, pp. 1677–1679, sep 2003.

[42] R. Vicente, S. Tang, J. Mulet, C. R. Mirasso, and J. M. Liu, "Synchronization properties of two self-oscillating semiconductor lasers subject to delayed optoelectronic mutual coupling," *Physical Review E - Statistical, Nonlinear, and Soft Matter Physics*, vol. 73, p. 047201, apr 2006.

[43] H. Shimizu and Y. Nakano, "First demonstration of TE mode nonreciprocal propagation in an InGaAsP/InP active waveguide for an integratable optical isolator," *Japanese Journal of Applied Physics, Part 2: Letters*, vol. 43, pp. L1561–L1563, nov 2004.

[44] P. E. Morrissey, W. Cotter, D. Goulding, B. Kelleher, S. Osborne, H. Yang, J. O'Callaghan, B. Roycroft, B. Corbett, and F. H. Peters, "On-chip optical phase locking of single growth monolithically integrated slotted fabry perot lasers.," *Optics express*, vol. 21, pp. 17315–23, jul 2013.

[45] P. E. Morrissey, W. Cotter, J. O'Callaghan, H. Yang, B. Roycroft, D. Goulding, B. Corbett, and F. H. Peters, "Multiple coherent outputs from single growth mono-

lithically integrated injection locked tunable lasers," in *Conference Proceedings - International Conference on Indium Phosphide and Related Materials*, pp. 281–284, IEEE, aug 2012.

[46] P. J. Winzer and R. J. Essiambre, "Advanced modulation formats for high-capacity optical transport networks," *Journal of Lightwave Technology*, vol. 24, no. 12, pp. 4711–4728, 2006.

[47] L. Chrostowski, C. Chang, and C. J. Chang-Hasnain, "Reduction of relative intensity noise and improvement of spur-free dynamic range of an injection locked VCSEL," *Lasers and Electro-*, 2003.

[48] L. Chrostowski and W. Shi, "Monolithic injection-locked high-speed semiconductor ring lasers," *Journal of Lightwave Technology*, vol. 26, no. 19, pp. 3355–3362, 2008.

[49] A. Hohl, A. Gavrielides, T. Erneux, and V. Kovanis, "Localized synchronization in two coupled nonidentical semiconductor lasers," *Physical Review Letters*, vol. 78, no. 25, pp. 4745–4748, 1997.

[50] A. Hohl, A. Gavrielides, T. Erneux, and V. Kovanis, "Quasiperiodic synchronization for two delay-coupled semiconductor lasers," *Physical Review A - Atomic, Molecular, and Optical Physics*, vol. 59, no. 5, pp. 3941–3949, 1999.

[51] K. Otsuka, R. Kawai, S. L. Hwong, J. Y. Ko, and J. L. Chern, "Synchronization of mutually coupled self-mixing modulated lasers," *Physical Review Letters*, vol. 84, no. 14, pp. 3049–3052, 2000.

[52] T. Heil, I. Fischer, W. Elsässer, J. Mulet, and C. R. Mirasso, "Chaos synchronization and spontaneous symmetry-breaking in symmetrically delay-coupled semiconductor lasers," *Physical Review Letters*, vol. 86, pp. 795–798, jan 2001.

[53] E. Wille, M. Peil, I. Fischer, and W. Elsäßer, "Dynamical scenarios of mutually delay-coupled semiconductor lasers in the short coupling regime," in *Semiconductor Lasers and Laser Dynamics* (D. Lenstra, G. Morthier, T. Erneux, and M. Pessa, eds.), vol. 5452, p. 41, sep 2004.

[54] H. Erzgräber, D. Lenstra, B. Krauskopf, E. Wille, M. Pzeil, I. Fischer, and W. Elsäßer, "Mutually delay-coupled semiconductor lasers: Mode bifurcation scenarios," *Optics Communications*, vol. 255, no. 4-6, pp. 286–296, 2005.

[55] N. Gross, W. Kinzel, I. Kanter, M. Rosenbluh, and L. Khaykovich, "Synchronization of mutually versus unidirectionally coupled chaotic semiconductor lasers," *Optics Communications*, vol. 267, pp. 464–468, nov 2006.

[56] D. A. Arroyo-Almanza, A. N. Pisarchik, I. Fischer, C. R. Mirasso, and M. C. Soriano, "Spectral properties and synchronization scenarios of two mutually delay-coupled semiconductor lasers," *Optics Communications*, vol. 301-302, pp. 67–73, 2013.

[57] I. Reidler, M. Nixon, Y. Aviad, S. Guberman, A. A. Friesem, M. Rosenbluh, N. Davidson, and I. Kanter, "Coupled lasers: phase versus chaos synchronization.," *Optics letters*, vol. 38, pp. 4174–7, oct 2013.

[58] M. Yousefi, Y. Barbarin, S. Beri, E. A. J. M. Bente, M. K. Smit, R. Nötzel, and D. Lenstra, "New role for nonlinear dynamics and chaos in integrated semiconductor laser technology," *Physical review letters*, vol. 98, no. 4, p. 44101, 2007.

[59] M. P. Vaughan, I. Henning, M. J. Adams, L. J. Rivers, P. Cannard, and I. F. Lealman, "Mutual optical injection in coupled DBR laser pairs.," *Optics express*, vol. 17, pp. 2033–41, feb 2009.

[60] D. Liu, C. Sun, B. Xiong, and Y. Luo, "Nonlinear dynamics in integrated coupled DFB lasers with ultra-short delay," *Optics Express*, vol. 22, pp. 5614–5622, mar 2014.

[61] F. Rogister, D. Pieroux, M. Sciamanna, P. Mégret, and M. Blondel, "Anticipating synchronization of two chaotic laser diodes by incoherent optical coupling and its application to secure communications," *Optics Communications*, vol. 207, pp. 295–306, jun 2002.

[62] J. Mulet, C. Masoller, and C. R. Mirasso, "Modeling bidirectionally coupled single-mode semiconductor lasers," *Physical Review A - Atomic, Molecular, and Optical Physics*, vol. 65, no. 6 A, pp. 638151–6381512, 2002.

[63] S. Yanchuk, K. R. Schneider, and L. Recke, "Dynamics of two mutually coupled semiconductor lasers: Instantaneous coupling limit," *Physical Review E*, vol. 69, no. 5, p. 056221, 2004.

[64] H. Erzgräber, D. Lenstra, B. Krauskopf, and I. Fischer, "Dynamical properties of mutually delayed coupled semiconductor lasers," in *Semiconductor Lasers and Laser Dynamics* (D. Lenstra, G. Morthier, T. Erneux, and M. Pessa, eds.), vol. 5452, p. 352, sep 2004.

[65] H. Erzgräber, B. Krauskopf, and D. Lenstra, "Mode structure of delay-coupled semiconductor lasers: Influence of the pump current," *Journal of Optics B: Quantum and Semiclassical Optics*, vol. 7, pp. 361–371, nov 2005.

[66] H. Erzgräber, S. Wieczorek, and B. Krauskopf, "Dynamics of two semiconductor lasers coupled by a passive resonator," *Physical Review E - Statistical, Nonlinear, and Soft Matter Physics*, vol. 81, may 2010.

[67] E. Clerkin, S. O'Brien, and A. Amann, "Multistabilities and symmetry-broken one-color and two-color states in closely coupled single-mode lasers," *Physical Review E - Statistical, Nonlinear, and Soft Matter Physics*, vol. 89, p. 032919, mar 2014.

[68] M. Seifikar, A. Amann, and F. H. Peters, "Dynamics of two identical mutually delay-coupled semiconductor lasers in photonic integrated circuits," *Applied Optics*, vol. 57, pp. E37–E44, aug 2018.

[69] F. M. Dubois, M. Seifikar, A. H. Perrott, and F. H. Peters, "Modeling mutually coupled non-identical semiconductor lasers on photonic integrated circuits," *Applied Optics*, vol. 57, pp. E154–E162, aug 2018.

[70] D. C. Byrne, J. P. Engelstaedter, W. H. Guo, Q. Y. Lu, B. Corbett, B. Roycroft, J. O'Callaghan, F. H. Peters, and J. F. Donegan, "Discretely tunable semiconductor lasers suitable for photonic integration," *IEEE Journal on Selected Topics in Quantum Electronics*, vol. 15, no. 3, pp. 482–487, 2009.

[71] N. P. Kelly, M. Dernaika, L. Caro, P. E. Morrissey, A. H. Perrott, J. K. Alexander, and F. H. Peters, "Regrowth-Free Single Mode Laser Based on Dual Port Multimode Interference Reflector," *IEEE Photonics Technology Letters*, vol. 29, pp. 279–282, feb 2017.

[72] W. Silfvast, *Laser Fundamentals*. USA: Cambridge University Press, 2^{nd} ed., 2004.

[73] S. Wieczorek, B. Krauskopf, T. B. Simpson, and D. Lenstra, "The dynamical complexity of optically injected semiconductor lasers," 2005.

[74] P. Morrissey, *Photonic Integrated Circuits for the Generation of Coherent Optical Signals, PhD Thesis*. Cork, Ireland: University College Cork, 2014.

[75] A. Hurtado, A. Quirce, A. Valle, L. Pesquera, and M. J. Adams, "Nonlinear dynamics induced by parallel and orthogonal optical injection in 1550 nm Vertical-Cavity Surface-Emitting Lasers (VCSELs).," *Optics express*, vol. 18, pp. 9423–9428, apr 2010.

[76] K. Balakier, M. J. Fice, F. van Dijk, G. Kervella, G. Carpintero, A. J. Seeds, and C. C. Renaud, "Optical injection locking of monolithically integrated photonic source for generation of high purity signals above 100 GHz," *Optics Express*, vol. 22, pp. 29404–29412, dec 2014.

[77] B. Lingnau, A. H. Perrott, M. Dernaika, L. Caro, F. H. Peters, and B. Kelleher, "Dynamics of On-Chip Asymmetrically Coupled Semiconductor Lasers," *Optics Letters*, vol. 45, pp. 2223–2226, mar 2020.

[78] F.Dubois, *Mutually Coupled Lasers in Photonic Integrated Circuits, PhD Thesis*. Cork, Ireland: University College Cork, 2019.

[79] M. Dernaika, L. Caro, N. P. Kelly, J. K. Alexander, F. Dubois, P. E. Morrissey, and F. H. Peters, "Deeply Etched Inner-Cavity Pit Reflector," *IEEE Photonics Journal*, vol. 9, feb 2017.

Appendix A

Automated Coupling

The results presented in this thesis could not have been obtained if all the experimental data had to have been recorded by hand. Therefore, much time and effort was put into writing LabView programs to automate the setup.

The main current sources used were Keithleys, which were easily programmed to apply a particular current or voltage and measure the resulting voltage or current. LabView programs were used to record a trace of a particular span and resolution from the ESA, OSA and HSO. The introduction of a programmable optical switch allowed a program to be written that could record an ESA, OSA and HSO trace from both lensed fibres i.e. from both lasers on the straight/curved/S-bend VOA PICs.

The main challenge was presented by the U-bend VOA PICs; both lasers were on the same facet therefore, the switch could no longer be used to record the output from both of the lasers. However, one of the lensed fibre manipulators on the probe station was controlled via motor and nanotrak piezo controllers. These were LabView programmable, therefore a program was written to automate the coupling of the fibre to the laser and to move the fibre to the second laser and couple to it.

The motors allowed the fibre to move in the x-, y- and z-directions, see Figure A.1. The nanotrak was programmed to track the maximum power in the y-z plane over a 2 μm range. The following steps describe how the program for automated coupling was written:

1. The fibre was manually positioned approximately 0.5 mm from the facet of one of the lasers.
2. The beam power in the y- and z-directions was recorded, the peak power was found and the fibre was moved to this position.
3. The fibre was moved ∼0.3 mm towards the facet and step 2 was repeated.
4. These two positions were used to determine the vector corresponding to the peak power.

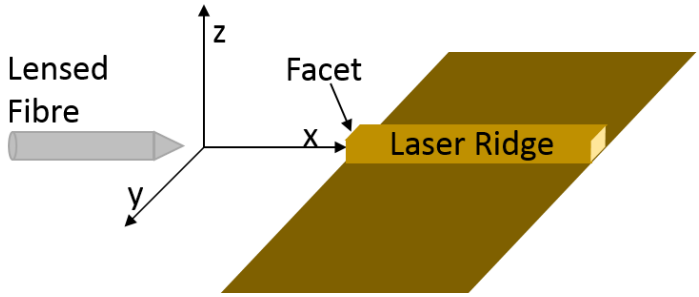

Figure A.1: Schematic of the automated coupling setup.

5. The nanotrak was set to tracking and the fibre was moved along the vector until the maximum power was obtained (when the power dropped the fibre was moved back a step). At each step the nanotrak was allowed to find the peak power and the fibre was moved to this position. The nanotrak was then allowed to find the peak power again (in case the peak had been outside its 2 μm range) before the fibre was moved forward.
6. The position of the fibre in the x-, y- and z-directions was recorded.
7. The fibre was then moved "home" to its original position.
8. The fibre was moved in the y-direction to the second laser (distance known from design of PIC).
9. Steps 2 to 6 were repeated to couple to the second laser.
10. The fibre was then moved home.
11. The fibre was moved to the saved position for the first laser, moving only 90% of the distance in x. Step 5 was repeated to recouple the laser from there. (The saved position was used to move the fibre most of the way to the facet to save time.) The new position was then saved.
12. The ESA, OSA and HSO traces were recorded.
13. The fibre was then moved home.
14. The fibre was then moved to the second laser and step 11 was repeated to recouple to the laser.
15. The ESA, OSA and HSO traces were recorded.
16. The fibre was then moved home.
17. The biases were changed and steps 11 to 16 were repeated for each change in the experimental parameters.

This LabView program meant that coupling to each laser was maintained at a maximum through out the experiment and the output of each laser was recorded during the sweep. The program was able to handle the drift that occurred overnight due to change in temperature, humidity, etc. in the lab when the air-conditioning was turned off. Therefore, sweeps could be run for days without loss of coupling. LabView was also programmed to use a Matlab script to plot the data once the sweep was complete.